The Event-Mixing Technique
for Modeling the $t\bar{t}$ Background in a Search for
Supersymmetry in the Di-Lepton Channel

Dissertation

zur Erlangung des Doktorgrades

des Department Physik

der Universität Hamburg

vorgelegt von

Hannes Schettler

aus Tübingen

Hamburg

2013

Abstract

In this thesis a search for Supersymmetry in the opposite-sign same-flavor di-lepton channel is presented. Data recorded by the CMS detector at the LHC accelerator corresponding to an integrated luminosity of $12.2\,\text{fb}^{-1}$ at a center-of-mass energy of $8\,\text{TeV}$ is analyzed. Events with at least two muons or two electrons with opposite charge, a significant transverse momentum imbalance, and at least one or at least two jets are selected. Supersymmetric particle decays are expected to form an edge-like structure in the di-lepton mass spectrum. The main background from Standard-Model processes is $t\bar{t}$ pair production. This background is estimated in a data-driven way using the event-mixing technique. Since event mixing is novel to estimate $t\bar{t}$ events, the method is validated in detail.

In the analyzed data no significant excess w. r. t. the event-mixing prediction is observed. In a counting experiment as well as in a fit of the shape of the distribution the data is in agreement with the expectations from the Standard Model. Hence, exclusion limits are calculated in terms of number of events forming an edge in the di-lepton mass spectrum. Additionally, the results are interpreted within a simplified model spectrum, assuming direct gaugino production and a decay chain like $\tilde{\chi}_2^0 \to \tilde{\ell}^{\pm}\ell^{\mp} \to \tilde{\chi}_1^0\ell^+\ell^-$. Limits are set on the masses of the supersymmetric particles.

Kurzfassung

In dieser Arbeit wird eine Suche nach Supersymmetrie im Zwei-Leptonen-Kanal mit gegensätzlichen Vorzeichen und gleichem Flavor vorgestellt. Daten, aufgezeichnet vom CMS-Detektor am LHC-Beschleuniger, entspechend einer integrierten Luminosität von $12.2\,\text{fb}^{-1}$ bei einer Schwerpunktsenergie von $8\,\text{TeV}$, werden analysiert. Ereignisse mit mindestens zwei Myonen oder zwei Elektronen gegensätzlicher Ladung, einer signifikanten Imbalance des transversalen Impulses und mindestens ein oder mindestens zwei Jets werden selektiert. Von supersymmetrischen Teilchenzerfällen wird erwartet, dass sie eine kantenförmige Struktur im zwei-Leptonen-Massenspektrum bilden. Der Hauptuntergrund an Standard-Modell-Prozessen ist $t\bar{t}$-Paarproduktion. Dieser Untergrund wird Daten getrieben abgeschätzt mithilfe der Event-Mixing-Technik. Da Event-Mixing erstmalig zur Abschätzung von $t\bar{t}$-Ereignissen benutzt wird, wird die Methode detailliert validiert.

In den analysierten Daten wird keine signifikante Abweichung zur Event-Mixing-Vorhersage beobachtet. Sowohl in einem Zählexperiment als auch in einem Fit der Form der Verteilung sind die Daten in Übereinstimmung mit den Erwartungen des Standard-Modells. Daher werden Ausschlussgrenzen auf die Anzahl der Ereignisse errechnet, die eine Kante im Zwei-Leptonen-Massenspektrum bilden. Zusätzlich werden die Ergebnisse innerhalb eines „simplified model spectrum" interpretiert, das von direkter Gaugino-Produktion und einer Zerfallskette wie $\tilde{\chi}_2^0 \to \tilde{\ell}^{\pm}\ell^{\mp} \to \tilde{\chi}_1^0\ell^+\ell^-$ ausgeht. Die Ausschlussgrenzen werden auf die Massen der supersymmetrischen Teilchen gesetzt.

Contents

1. Introduction

Symmetry considerations have always been a fruitful source of inspiration grasping the principles of nature and its constituents. Ancient natural philosophers assumed the most symmetric polyhedrons – the Platonic solids – to be the basic entity of matter. Plato associated each element (fire, air, water, and earth) with one regular solid. Even though todays understanding of nature is less idealistic, the concept of symmetry is still an important guideline, in an aesthetic sense but especially in particle physics also in a mathematical sense.

The key principle of the theoretically very clear and experimentally extremely well confirmed Standard Model of particle physics is the mathematical invariance under a local gauge transformation. Assuming such symmetries lead to the three interactions that are described by the Standard Model. Gauge invariance is an undoubted, established principle; the Standard Model, however, seems to be incomplete. Gravity is not included in the model, the cosmological observation of Dark Matter is unexplainable, and from a theoretical point of view the model is believed to be low-energy approximation of a more general underlying theory.

An additional symmetry is a promising candidate to generalize the Standard Model in a way that many of its issues are solved. This symmetry is named Supersymmetry. It predicts invariance under a transformation between fermions and bosons. Since this fermion-boson symmetry does not exist between the particles of the Standard Model, new particles have to be introduced.

With the Large Hadron Collider an accelerator was built probing collision energies that are expected to show effects of physics beyond the Standard Model. The Compact Muon Solenoid is one of the detectors that records the products of the collisions, its data is analyzed in this thesis. A search for supersymmetric particles is performed in $12.2\,\mathrm{fb}^{-1}$ of integrated luminosity at $8\,\mathrm{TeV}$ center-of-mass energy. The invariant di-lepton mass spectrum of events with at least two muons or two electrons, little hadronic activity, and a significant imbalance among the momenta of all particles is studied. Since leptons are relatively rare in proton-proton collisions and reliably identifiable, they are ideal candidates to search for new phenomena. In Supersymmetry decay cascades are expected that result in two kinematically correlated leptons. Like a resonance produces a peak in a two-particle spectrum, from these correlated leptons an edge-shaped distribution is expected.

Finding something new requires a good knowledge of the established. Hence, the main challenge of a search analysis is a reliable description of the background of Standard-Model processes. In the search channel of this analysis $\mathrm{t\bar{t}}$ pair production is the main background. A new way to predict this background from the data itself has been found in the event-mixing technique. This data-driven background-determination method has a long history in nuclear and particle physics, mainly in searches for hadronic resonances. It exploits the difference in kinematic correlation between the signal and the background. In this thesis it is validated and utilized in a search for Supersymmetry.

The analyzed data is in agreement with the event-mixing prediction. Hence, no evidence for new particles predicted by Supersymmetry has been found. Since Supersymmetry is not one model with one set of predictions, but a principle that can be realized in many models, exclu-

sion limits are set. Two kinds of limits are calculated. Very generically limits on the number of events forming an edge-shape in the di-lepton spectrum are set. Additionally within a so-called simplified model spectrum limits on the masses of the involved supersymmetry particles are given.

This thesis is structured as follows. After a short overview of the theoretical concepts and selected recent measurements, including the Standard Model and its supersymmetric extension in Chapter 2, the LHC and its experiments will be described in Chapter 3. In particular the CMS detector will be emphasized, since this thesis is based on CMS data. In Chapter 4 will be explained how physics objects are reconstructed from the measurements of the detector. Also the event selection will be addressed and the distributions of basic quantities will be compared to simulation. Chapter 5 introduces the event-mixing technique as a novel technique to estimate the di-lepton mass spectrum of the $t\bar{t}$ background in a data-driven manner. The technique will be studied in detail using simulated events. Possible problems will be addressed and their impact estimated. In Chapter 6 the results of the search for a deviation from the Standard-Model expectations are summarized and systematic uncertainties are discussed. In Chapter 7 these results will be interpreted. First, the agreement of the data with the prediction will be quantified, secondly, signal scenarios will be tested and exclusion limit on the number of new-physics events will be presented.

2. Concepts and Recent Observations in Particle Physics

In this chapter a short overview of the theoretical concepts of elementary particle physics is given, as well as a summary of selected recent achievements of experimental particle physics. In Section 2.1 the Standard Model of particle physics is described. In Section 2.2 the supersymmetric extension of the Standard Model is introduced.

The following is based on several textbooks [1–4] and the reviews in Ref. 5. Additional publications [6–9] are used for the overview of Supersymmetry.

2.1. The Standard Model of Particle Physics

The Standard Model of particle physics is a very successful and theoretically clear description of most phenomena and observations in the sub-atomic world. The model is built on the principle of local gauge invariance. With the electromagnetic, strong, and weak interactions three of the four interactions between elementary particles are described as quantum field theories based on local gauge symmetry. Only gravity, the weakest force, is not explained in the framework of the Standard Model.

Three groups of elementary particles are described by the Standard Model. The fermions carry spin 1/2 and form matter. The gauge bosons are the quanta of the gauge fields. They mediate the interactions between the fermions, their spin is one. And finally, the Higgs boson with spin zero is predicted.

The Higgs mechanism explains the mass of a particle less as an intrinsic property of the particle itself, but of the interaction between the particle and the Higgs field. The masses of the gauge bosons emerge in the electro-weak symmetry breaking. The fermions interact with the Higgs field via Yukawa couplings, i.e. the fermion masses are proportional to the coupling constants.

2.1.1. Particle Content of the Standard Model

An attractive feature of the Standard Model is the small number of elementary particles that are sufficient to explain the plenty of experimental measurements. Additionally, they can be ordered in a clear system.

The fermions can be further divided into quarks and leptons. Up to now, six different particles of each type are known, they can be grouped into three generations. The stable matter surrounding us is made of particles from the first generation. Protons and neutrons in atomic nuclei consist of up and down quarks, electrons form the atomic shell. The last particle of the first generation is the electron neutrino. It interacts only weakly and is thus not bound to matter.

In Tables 2.1 and 2.2 several quantities of all known quarks and leptons are summarized. The first generation comprises the lightest particles. The second and third generations can

Table 2.1.: The quarks of the Standard Model, their electric charges and their masses. From all quarks only the mass of the top quark can be directly measured because it decays before it hadronizes. Hence, the listed values are estimates of the free quark masses. In bound states the effective masses are higher [5].

	Quark		Charge [e]	Mass [MeV]
First generation	down	d	$-1/3$	5
	up	u	$2/3$	2
Second generation	strange	s	$-1/3$	95
	charm	c	$2/3$	1275
Third generation	bottom	b	$-1/3$	4180
	top	t	$2/3$	173 500

Table 2.2.: The leptons of the Standard Model, their electric charges and their masses. The established Standard Model assumes neutrinos to be massless. However, several experiments showed that neutrino flavors oscillate, which is only possible if neutrinos have non-zero masses [5].

	Lepton		Charge [e]	Mass [MeV]
First generation	electron	e	-1	0.511
	e neutrino	ν_e	0	
Second generation	muon	μ	-1	106
	μ neutrino	ν_μ	0	
Third generation	tau	τ	-1	1777
	τ neutrino	ν_τ	0	

be understood as heavier copies of the first generation. The stability of the first generation particles can be explained as a consequence of this mass hierarchy. Heavy particles can decay into lighter particles but not vice versa due to energy conservation. In addition to all particles of the first generation, all neutrinos are stable, which is related to the flavor conservation of leptons[1]. In every decay the total number of leptons of each generation is conserved (i.e. $N(e) + N(\nu_e) = \text{const}$, $N(\mu) + N(\nu_\mu) = \text{const}$, and $N(\tau) + N(\nu_\tau) = \text{const}$). The anti-particles count negative in the sums. An example is the decay $\mu^- \rightarrow \nu_\mu e^- \bar{\nu}_e$, which is the by far dominant decay channel of muons.

In the case of quarks the situation is slightly more complicated: The number of quarks of one generation is not strictly conserved. Quark decays within one generation are favored but other decays are possible. The mass eigenstates of the quarks can be understood as superpositions of

---

[1]The established Standard Model assumes neutrinos to be massless and stable. Several recent measurements strongly indicate that neutrinos oscillation between different flavor states, what also requires them to be massive. However, no observation contradicts flavor conservation in a decay.

Interaction	Boson	Charge [e]	Mass [MeV]
Strong	8 gluons g	0	0
Electromagnetic	photon γ	0	0
Weak	$W^\pm$	± 1	81 000
	Z^0	0	92 000

Table 2.3.: The gauge bosons of the Standard Model. The limited reach of the weak interaction is a consequence of the massive gauge bosons. The "confinement" of the color charge causes the same effect for the strong interaction [5].

gauge eigenstates, which are strictly conserved within one generation.

The Cabibbo-Kobayashi-Maskawa matrix V_{CKM} transforms between the mass and the gauge eigenstates:

$$\begin{pmatrix} d' \\ s' \\ b' \end{pmatrix} = V_{\mathrm{CKM}} \begin{pmatrix} d \\ s \\ b \end{pmatrix}, \tag{2.1}$$

where d', s', and b' are the gauge eigenstates and d, s, and u are the mass eigenstates. The numeric values of the matrix elements have been determined experimentally[2] [5]:

$$V_{\mathrm{CKM}} = \begin{pmatrix} 0.97425 \pm 0.00022 & 0.2252 \pm 0.0009 & 0.00415 \pm 0.00049 \\ 0.230 \pm 0.011 & 1.006 \pm 0.023 & 0.0409 \pm 0.0011 \\ 0.0084 \pm 0.0006 & 0.0429 \pm 0.0026 & 0.89 \pm 0.07 \end{pmatrix}. \tag{2.2}$$

The preference for decays within one generation is reflected by the fact that the diagonal elements are close to one. The mixing between the first and second generations is much larger than with the third generation. Theoretically, the CKM matrix is determined by three mixing angles and one phase.

The mixing of the "down-type" quarks d, s, and b rather than the "up-type" quarks u, c, and t is just a matter of convention. The same result would be achieved, if the differentiation between mass and gauge eigenstates was made for the up-type quarks.

Already shortly after the quark model was established in elementary particle physics, an apparent violation of the Pauli principle in baryons lead to an additional quantum number, called color charge. The Δ^{++} baryon is comprised of three u quarks in the ground state. A composition of three identical spin-1/2 particles in the ground state is clearly forbidden by Fermi statistics. A new quantum number resolves the problem by making the quarks distinguishable.

Each quark carries one of the colors red, green, or blue, each anti-quarks carries an anti-color, i. e. anti-red, anti-green, or anti-blue. Comparisons of branching fractions (e. g. $e^+ e^- \rightarrow \mu^+ \mu^-$ compared to $e^+ e^- \rightarrow q\bar{q}$) show an enhancements of the quark channel by a factor of three and thus experimentally confirm the number of three colors. The number of degrees of freedom (i. e. the number of colors) is connected with the charge of the quarks. Divergences in triangle loops

---

[2]The given values are independent measurements of the elements. These values can be further processed in a common fit making use of additional Standard Model assumptions, such as the unitarity of the matrix.

cancel only, if the charge sum within one particle generation is zero:

$$-1 \quad + \quad 0 \quad + \quad \mathbf{3} \quad \cdot \, (\quad \tfrac{2}{3} \quad - \quad \tfrac{1}{3} \quad) = 0$$

$$\text{electron} \qquad \text{neutrino} \qquad \textbf{colors} \qquad \text{up quark} \qquad \text{down quark}$$

The factor of three is exactly necessary to adjust the quark contribution in this sum to the lepton charge.

The color charge is like the electric charge a conserved quantum number. And like the electric charge enables a particle to interact electromagnetically, all color charged particles can participate in strong interactions.

In analogy to visible color, combinations of colors can be "white", i. e. color neutral: Neutral two-quark bound states can be formed from a quark with a certain color and an anti-quark with the same anti-color, such compositions are called *mesons*. Neutral bound states of three quarks can be achieved by combining all three colors (or anti-colors) to so-called *baryons* (or anti-baryons).

The concept of *color confinement* forbids free colored particles. All observable *hadrons* (quark compositions) are color neutral. Hence, only the combinations qqq, $\bar{q}\bar{q}\bar{q}$, and q$\bar{q}$ are allowed, but not e. g. qq$\bar{q}$ or qq. Other possible color-neutral composites like q$\bar{q}$q$\bar{q}$ (*tetraquarks*) or qqqq$\bar{q}$ (*pentaquarks*) are subjects to many searches, e. g. recently at the e^+e^- collider experiments Belle [10] and BESIII [11]. Also bound states including gluons can be color neutral. So-called *glueballs* are theoretically expected, but not undoubtedly observed yet [12].

The interactions are transmitted by exchange of bosons with spin 1. Some properties of these bosons are summarized in Tab. 2.3. The photon γ couples to all electrically charged particles and transmits the electromagnetic force. The strong interaction is carried by the gluons. They couple to all particles with color charge. Gluons themselves are color charged, carrying a combination of a color and an anti-color. In that way a gluon can couple to a quark and an anti-quark, carrying the color from the quark and the anti-color from the anti-quark. In Tab. 2.3 eight gluons are mentioned; they correspond to different combinations of color and anti-color. The weak interaction is carried by the massive gauge bosons Z^0 and $W^\pm$. As discussed later, the electromagnetic and the weak interactions are unified in the Standard Model to the *electroweak* interaction. Thus, the mass eigenstates γ, Z^0, and $W^\pm$ are formulated as superpositions of the gauge eigenstates B^0 and $W^{1,2,3}$.

2.1.2. Gauge Interactions

All interactions in the Standard Model are formulated as quantum field theories. Requiring local gauge invariance necessitate additional fields, which can be identified as gauge fields of the interactions.

In classical mechanics the Lagrange function L is defined as the difference of kinetic energy T and the potential energy U

$$L = T - U. \tag{2.3}$$

The equations of motion are obtained by solving the Euler-Lagrange equation

$$\frac{d}{dt}\left(\frac{\partial L}{\partial \dot{q}_i}\right) = \frac{\partial L}{\partial q_i}, \tag{2.4}$$

where q_i are the generalized coordinates.

This can be adopted to a field theory by replacing the Lagrange function L by the Lagrange density $\mathscr{L}$, with the trivial relation

$$L = \int \mathscr{L}\, \mathrm{d}^3 x. \tag{2.5}$$

Commonly, $\mathscr{L}$ is referred to as *Lagrangian*. The coordinates in classical mechanics are replaced by the fields ϕ_i. The derivatives are w.r.t. time and spatial coordinates, written as the vector $x_\mu = (t, x, y, z)$, with the abbreviation:

$$\partial_\mu \phi_i \equiv \frac{\partial \phi_i}{\partial x^\mu}. \tag{2.6}$$

The Euler-Lagrange equation in the field theory becomes consequently

$$\partial_\mu \left(\frac{\partial \mathscr{L}}{\partial(\partial_\mu \phi_i)} \right) = \frac{\partial \mathscr{L}}{\partial \phi_i}. \tag{2.7}$$

The field of a spin-1/2 particle is written as a Dirac Spinor ψ. The Lagrangian of such a particle with mass m in absence of any interaction is

$$\mathscr{L} = \bar{\psi}(i\gamma^\mu \partial_\mu - m)\psi \tag{2.8}$$

with $\bar{\psi} \equiv \psi^\dagger \gamma^0$. For simplification natural units are used in this thesis where speed of light c and Planck's constant $\hbar$ are set to 1.

The γ matrices originally occurred when Dirac quantized the relativistic energy-momentum relation $p^\mu p_\mu = m^2$ for particles with spin 1/2. He found that four coefficients γ^0, γ^1, γ^2, and γ^3 are necessary that fulfill the anti-commutation relation

$$\{\gamma^\mu, \gamma^\nu\} = 2g^{\mu\nu}, \tag{2.9}$$

where $g^{\mu\nu}$ is the Minkowski metric.

This is only possible if γ^μ are matrices of a size of at least 4×4. The actual numerical values of the matrices are subject to a certain arbitrariness. Widely common is the Bjorken-Drell convention:

$$\gamma^0 = \begin{pmatrix} 1 & 0 & 0 & 0 \\ 0 & 1 & 0 & 0 \\ 0 & 0 & -1 & 0 \\ 0 & 0 & 0 & -1 \end{pmatrix} \quad \text{and} \quad \gamma^i = \begin{pmatrix} 0 & \sigma^i \\ -\sigma^i & 0 \end{pmatrix}, \quad i = 1, 2, 3, \tag{2.10}$$

where σ^i are the three 2×2 Pauli matrices.

Quantum Electrodynamics (QED)

The relativistic wave equation of a spin-1/2 particle, the *Dirac equation*, without any interaction is given by

$$(i\gamma^\mu \partial_\mu - m)\psi(x) = 0 \tag{2.11}$$

The principle of local gauge invariance requires the invariance of the Dirac equation under the transformation

$$\psi \to \psi' = e^{i\theta(x)}\psi \tag{2.12}$$

where $\theta(x)$ is an arbitrary real function in space-time. In contrast, a "global" gauge transformation would be described by a θ independent from x. Putting ψ' into Eq. 2.11 leads to

$$(i\gamma^\mu \partial_\mu - m)\psi'(x) = -\gamma^\mu \partial\theta(x)\psi'(x) = q\gamma^\mu A'_\mu \psi'(x). \tag{2.13}$$

In the last step $A'_\mu = \frac{-1}{q}\partial_\mu\theta(x)$ is introduced to show that this could be read as the Dirac equation of a particle with charge q in an electromagnetic field with 4-potential A'_μ. Performing simultaneously the transformations Eq. 2.12 and

$$A_\mu \to A'_\mu = A_\mu - \frac{1}{q}\partial_\mu\theta(x) \tag{2.14}$$

and replacing the derivative ∂_μ by the covariant derivative $D_\mu = \partial_\mu + iqA_\mu$ finally leads to the required invariance of the Dirac equation $(i\gamma^\mu D_\mu - m)\psi(x) = 0$.

The electromagnetic field is a direct and necessary consequence of the requirement of local gauge invariance of the Dirac equation.

With the electromagnetic field tensor $F_{\mu\nu} = \partial_\mu A_\nu - \partial_\nu A_\mu$ the Lagrangian of a charged fermion within an electromagnetic field can be written as

$$\mathscr{L} = \bar{\psi}(i\gamma^\mu D_\mu - m)\psi - \frac{1}{4}F_{\mu\nu}F^{\mu\nu} \tag{2.15}$$

The discussed gauge transformation with a scalar phase $\theta(x)$ belongs to the unitary group U(1). $e^{i\theta}$ is considered as a unitary 1×1 matrix U, where *unitary* means that $U^\dagger U = 1$.

Quantum Chromo Dynamics (QCD)

In quantum chromodynamics there is not only one charge like in QED but three. Each color is conserved and therefore the Lagrangian has to be invariant under color transformations. The quarks are represented by color triplets of Dirac spinors

$$\psi = \begin{pmatrix} \psi_{\text{red}} \\ \psi_{\text{blue}} \\ \psi_{\text{green}} \end{pmatrix}. \tag{2.16}$$

With this color triplet ψ the Lagrangian of a free colored particle looks exactly like the Lagrangian of a free charged particles in Eq. 2.11:

$$\mathscr{L} = \bar{\psi}(i\gamma^\mu \partial_\mu - m)\psi. \tag{2.17}$$

The symmetry group of QCD must be slightly more complex in order to deal with three charges instead of one in the case of QED. The special unitary group $SU(3)$ was found to be appropriate (*special* indicates that the determinant is 1). As generators of $SU(3)$ usually the Gell-Mann matrices $\lambda_1, \lambda_2, \ldots \lambda_8$ are used. Each element SU of the group can be represented as a linear combination of the Gell-Mann matrices in the following way:

$$SU = e^{i\boldsymbol{\lambda}\cdot\boldsymbol{a}}, \tag{2.18}$$

where $\boldsymbol{\lambda}$ and $\boldsymbol{a}$ are the vectors of the Gell-Mann matrices and of eight real parameters $a_1(x)$, $a_2(x), \ldots a_8(x)$, respectively. The invariance is achieved by introducing a covariant derivative

following the same structure as in QED:

$$D_\mu = \partial_\mu + iq_s \boldsymbol{\lambda} \cdot \boldsymbol{A}_\mu \tag{2.19}$$

where the vector $\boldsymbol{A}_\mu$ contains eight gauge fields. The infinitesimal transformation of $\boldsymbol{A}_\mu$ is given by

$$\boldsymbol{A}_\mu \to \boldsymbol{A}'_\mu = \boldsymbol{A}_\mu - \partial_\mu \frac{1}{q_s} \boldsymbol{a} - 2(\boldsymbol{a} \times \boldsymbol{A}_\mu) \tag{2.20}$$

The cross product is defined by

$$(\boldsymbol{a} \times \boldsymbol{A}_\mu)_i = \sum_{j,k=1}^{8} f_{ijk} a_j A_\mu^k, \tag{2.21}$$

where f_{ijk} are the structure constants of $SU(3)$, defined by the commutator of the group generators:

$$[\lambda_i, \lambda_j] = i f_{ijk} \lambda_k. \tag{2.22}$$

The fact that f_{ijk} are non zero causes an additional term in the field tensor compared to QED, which also appears in the Lagrangian. Groups with not commuting generators are called non-Abelian.

The gluon term in the Lagrangian can be formulated analogue to QED as

$$\mathscr{L}_{\text{gluon}} = -\frac{1}{4} \boldsymbol{F}^{\mu\nu} \cdot \boldsymbol{F}_{\mu\nu} \tag{2.23}$$

with

$$\boldsymbol{F}^{\mu\nu} = \partial^\mu \boldsymbol{A}^\nu - \partial^\nu \boldsymbol{A}^\mu - 2q_s(\boldsymbol{A}^\mu \times \boldsymbol{A}^\nu) \tag{2.24}$$

using the same cross product as defined in Eq. 2.21.

The complete Lagrangian for the color charged particle in a "color field" is finally:

$$\mathscr{L} = \bar{\psi}(i\gamma^\mu \partial_\mu - m)\psi - \frac{1}{4} \boldsymbol{F}^{\mu\nu} \cdot \boldsymbol{F}_{\mu\nu} - (q_s \bar{\psi}\gamma^\mu \boldsymbol{\lambda}\psi)\boldsymbol{A}_\mu \tag{2.25}$$

Using the covariant derivative this equation has exactly the same form as the QED Lagrangian in Eq. 2.15. An important strength of the Standard Model is that the two very different interactions electromagnetism and strong interaction are described using the same formalism. Like the photon field is derived from invariance under $U(1)$ transformation, the $SU(3)$ invariance leads to eight massless gauge fields representing the eight gluons. The additional term in the Lagrangian that arises from the non-zero commutators (Eq. 2.22) accounts for the gluon self-interaction. Gluons are color charged themselves, and hence couple to gluons.

Electroweak Interaction

Fermi's model is an early theory of the weak interaction. Enrico Fermi assumes a direct one-to-three interaction for the β decay of the neutron (n $\to$ p$^+$e$^-\bar{\nu}_{\text{e}}$) introducing G_F as coupling constant. Up to energies in the order of the W$^\pm$ mass and on tree level, Fermi's model works well as an effective theory. But not only by the experimental reach of higher energies, also by theoretical considerations, the model is ruled out to be valid in energy regimes above the masses of the weak bosons.

In the Standard Model the weak interaction is not described by its own but as part of the Glashow-Salam-Weinberg-Model, which is a unified theory of QED and weak interaction. The combined electroweak interaction is based on an $SU(2) \times U(1)$ symmetry. The structure of QED is conserved in the $U(1)$ symmetry, the actual implementation, however, is different. The $SU(2)$ group is characteristic for the weak interaction. It acts only on *left-handed* fermions (and right-handed anti-fermions[3]), why it is often denoted as $SU(2)_L$.

Handedness or *chirality* describes the direction of the spin of a particle relative to the direction of its momentum. For massless particles chirality is identical with helicity h, which is the projection of the spin $\boldsymbol{s}$ onto the direction of momentum $\boldsymbol{p}/|\boldsymbol{p}|$:

$$h = \boldsymbol{s} \cdot \frac{\boldsymbol{p}}{|\boldsymbol{p}|} \tag{2.26}$$

A particle with positive helicity ($\boldsymbol{s}$ and $\boldsymbol{p}$ point to the same direction) is called right-handed, a particle with negative helicity ($\boldsymbol{s}$ and $\boldsymbol{p}$ point to opposite directions) is called left-handed.

The chiral states of a Dirac spinor can be written with the $\gamma^5 = i\gamma^0\gamma^1\gamma^2\gamma^3$ matrix:

$$\psi_L = \frac{1}{2}(1 - \gamma^5)\psi \quad \text{and} \quad \psi_R = \frac{1}{2}(1 + \gamma^5)\psi \tag{2.27}$$

The "charge" of the weak interaction is the spin-like quantum number *isospin*. The left-handed version of each fermion participates in weak interaction[4]. The magnitude of the isospin is for all left-handed fermions $1/2$, the third component I_3 is $+1/2$ for neutrinos and up-type quarks and $-1/2$ for the charged leptons and down-type quarks. Here, "down-type" refers to the gauge eigenstates (or *isospin eigenstates*) of the quarks as introduced in Eq. 2.1. The left-handed particles are grouped to isospin doublet

$$\begin{pmatrix} \nu_e \\ e^- \end{pmatrix}_L \quad \begin{pmatrix} \nu_\mu \\ \mu^- \end{pmatrix}_L \quad \begin{pmatrix} \nu_\tau \\ \tau^- \end{pmatrix}_L \quad \begin{pmatrix} u \\ d' \end{pmatrix}_L \quad \begin{pmatrix} c \\ s' \end{pmatrix}_L \quad \begin{pmatrix} t \\ b' \end{pmatrix}_L,$$

where the upper particles have positive isospin state. ($I_3 = +1/2$) and the lower particles have negative isospins ($I_3 = -1/2$)[5].

Since the electroweak $U(1)$ is not identical but similar to the QED $U(1)$, also the charge of the former is a modification of the electric charge q. It is called *hypercharge Y*, defined by

$$q = I_3 + \frac{Y}{2}. \tag{2.28}$$

In order to distinguish between the two $U(1)$ groups, the newly introduced electroweak group is commonly referred to as $U(1)_Y$.

The phenomenology of the electroweak interaction in more complex than QED or QCD. That can already be seen from the particles that mediate the forces. In QED there is only the photon;

---

[3]In the following it will not be explicitly stated, but everything that applies to left-handed fermions, applies for right-handed anti-fermions, too.

[4]In the established Standard Model neutrinos are always left handed. However, a non-zero neutrino mass requires the existence of right-handed neutrinos as well. These right-handed neutrinos would not participate in any interaction (except gravity).

[5]Since the right-handed fermions carry no isospin ($I = 0$), each of them forms an isospin singlet: $e_R^-, \mu_R^-, \tau_R^-, (\nu_R^e, \nu_R^\mu, \nu_R^\tau), u_R, c_R, t_R, d_R, c_R, b_R$. For the right-handed quarks the differentiation between mass eigenstate and isospin eigenstate has no meaning.

in QCD though there are 8 gluons, they differ only by their color charge. The electroweak force is transmitted by three very different bosons: the massless photon, the massive and neutral Z^0 boson, and the massive and electrically charged $W^\pm$ boson. The difference in electric charge is referred to in the differentiation between *charged current* and *neutral current*.

Following the same strategy as in QED and QCD a covariant derivative accounting for $SU(2)_L$ and $U(1)_Y$ symmetries can be written as

$$D_\mu = \partial_\mu - ig'\frac{1}{2}YB_\mu - ig\boldsymbol{T}\boldsymbol{W}_\mu, \tag{2.29}$$

with two couping constants g and g', the gauge field B_μ and the 3-vector of gauge fields $\boldsymbol{W}_\mu$. The components of the vector $\boldsymbol{T}$ are the Pauli matrices $T_i = \sigma_i/2$, $i = 1, 2, 3$. The Pauli matrices transform the isospin doublets. The right-handed fermions, which do not form isospin doublets are not effected by the $\boldsymbol{W}_\mu$ field.

For the complete Lagrangian tensors for the new fields are necessary. $B_{\mu\nu}$ is equivalent to $F_{\mu\nu}$ in QED:

$$B_{\mu\nu} = \partial_\mu B_\nu - \partial_\nu B_\mu. \tag{2.30}$$

$\boldsymbol{W}_{\mu\nu}$ has a similar structure like the field tensors of QCD:

$$\boldsymbol{W}_{\mu\nu} = \partial_\mu \boldsymbol{W}_\nu - \partial_\nu \boldsymbol{W}_\mu - g(\boldsymbol{W}_\mu \times \boldsymbol{W}_\nu). \tag{2.31}$$

With this ingredients the full Lagrangian of the electroweak interaction can be written:

$$\mathscr{L} = \bar{\psi}(i\gamma^\mu D_\mu - m)\psi - \frac{1}{4}\boldsymbol{W}_{\mu\nu}\boldsymbol{W}^{\mu\nu} - \frac{1}{4}B_{\mu\nu}B^{\mu\nu}. \tag{2.32}$$

In total four gauge fields B_μ, W_μ^1, W_μ^2, and W_μ^3 have been introduced, but they are not identical with the particles γ, W^+, W^-, and Z^0. The mass eigenstates are linear combinations of the isospin eigenstates that occur in the Lagrangian in the following way:

$$\begin{pmatrix} \gamma \\ Z^0 \end{pmatrix} = \begin{pmatrix} \cos\theta_W & \sin\theta_W \\ -\sin\theta_W & \cos\theta_W \end{pmatrix} \begin{pmatrix} B \\ W^3 \end{pmatrix} \tag{2.33}$$

and

$$W^\pm = W^1 \pm iW^2 \tag{2.34}$$

θ_W is referred to as the electroweak mixing angle or Weinberg angle. This parameter also determines the coupling constants in the covariant derivative (Eq. 2.29):

$$g = \frac{e}{\sin\theta_W} \quad \text{and} \quad g' = \frac{e}{\cos\theta_W} \tag{2.35}$$

There are no mass terms for the gauge fields in the Lagrangian of the electroweak interaction (Eq. 2.32). In fact such terms would destroy the invariance of the Lagrangian. Experimentally it is known that only the photon is massless, $W^\pm$ and Z^0 have masses of $80.385 \pm 0.015\,\text{GeV}$ and 91.1876 ± 0.0021 [5], respectively.

Also the fermion masses are not properly explained by the model how it is described previously. The fermion mass m appears in the Lagrangian in Eq. 2.32 and does not disturb gauge invariance. However, the masses of the particles combined to one isospin doublet must be identical. Obviously, experimental observations clearly contradict this requirement. Neither do
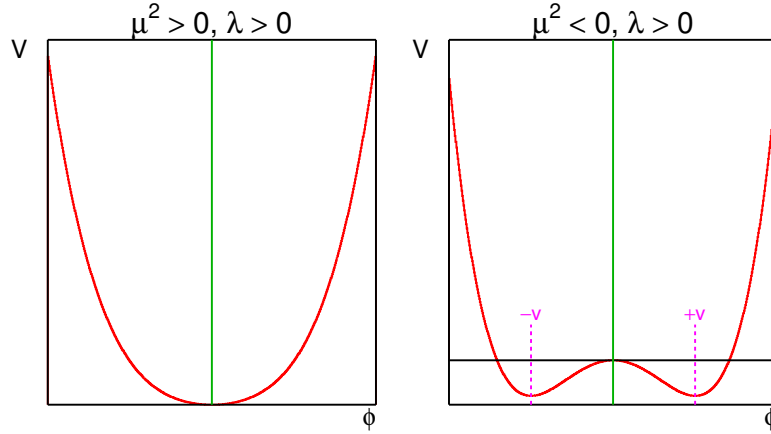
Figure 2.1.: Sketch of the Higgs potential in one dimension. Left: For a real μ the potential is symmetric, the ground state is at zero. Right: If $\mu^2 < 0$ the whole potential is still symmetric, but in ground state the symmetry is hidden. Below a certain energy the system freezes in one of the asymmetric minima. Hence, the expectation of the Higgs field in the vacuum (i.e. ground state) differs from zero [13].

charged leptons have the same mass as the neutrinos nor do up- and down-type quarks.

Both, the boson masses and the different fermion masses in a isospin doublet can be explained by a mechanism called "spontaneous symmetry breaking".

2.1.3. Higgs Mechanisms

The last experimentally open question of the Standard Model was the origin of particle masses. A theoretical explanation is given by the Higgs mechanism. A new field is introduced that is characterized by spontaneous symmetry breaking. As quantum of the field the Higgs boson was predicted. In 2012 the two large LHC experiments ATLAS and CMS claimed discovery of a new boson with properties that are expected for the Standard Model Higgs boson.

The symmetry of a system's potential is call "spontaneously broken", if the whole potential shows the symmetry, but not the ground state. Hence, in an excited state the system can be symmetric, only below a certain energy threshold the symmetry breaks.

In the Higgs mechanism the spontaneous symmetry breaking leads to non-vanishing vacuum expectation value of the Higgs field. As a simple potential that shows this feature, the Higgs potential can be written as

$$V = \mu^2 \mathbf{\Phi}^\dagger \mathbf{\Phi} + \lambda (\mathbf{\Phi}^\dagger \mathbf{\Phi})^2. \qquad (2.36)$$

The simplest structure of the Higgs field $\mathbf{\Phi}$ that is able to explain the masses of the $\mathrm{W}^\pm$ and Z^0 bosons but keeps the photon massless is a complex isospin doublet:

$$\mathbf{\Phi} = \begin{pmatrix} \phi^+ \\ \phi^0 \end{pmatrix} \qquad (2.37)$$

Figure 2.1 shows the schematic shape of the Higgs potential given in Eq. 2.36 in one dimension

(e. g. the real part of one of the fields). If $\mu^2 < 0$ the ground state of V is

$$|\boldsymbol{\Phi}|^2 = \frac{1}{2} \left(\left(\text{Re}\phi^+ \right)^2 + \left(\text{Im}\phi^+ \right)^2 + \left(\text{Re}\phi^0 \right)^2 + \left(\text{Im}\phi^0 \right)^2 \right) = \frac{-\mu^2}{2\lambda}. \tag{2.38}$$

Since the potential is symmetric between ϕ^+ and ϕ^0 and between the real and imaginary parts, the minimum is a manifold of points of which one can be chosen by setting all components to zero except the real part of the neutral field:

$$\text{Re}\phi^+ = \text{Im}\phi^+ = \text{Im}\phi^0 = 0, \quad \text{Re}\phi^0 = \sqrt{\frac{-\mu^2}{\lambda}} \equiv v. \tag{2.39}$$

Now, the Higgs field can be parametrized in terms of deviations from that minimum:

$$\Phi = \exp\left(\frac{i\boldsymbol{\xi} \cdot \boldsymbol{\sigma}}{2v} \right) \begin{pmatrix} 0 \\ (v + \text{H})/\sqrt{2} \end{pmatrix}, \tag{2.40}$$

where $\boldsymbol{\xi}$ is the vector of three real ξ_i fields, which account for deviations in the components that was set to zero in Eq. 2.39. $\boldsymbol{\sigma}$ is the vector of the Pauli matrices. H is the fourth real field, which is the only one that actually sees a change of the potential. By expanding the field w. r. t. this ground state, the two complex fields (Eq. 2.37) are substituted by four real field with a vanishing vacuum expectation value. The quanta of the ξ_i fields are massless scalars, called *Goldstone bosons*. Their appearance is a general feature of spontaneous breaking of a continuous symmetry [14].

The Higgs doublet was introduced as isospin doublet. Of course, also the re-parametrized formulation in Eq. 2.40 is a isospin doublet, which should be invariant under a $SU(2)$ gauge transformation. The phase factor in Eq. 2.40 (including the fields of the Goldstone bosons) can be eliminated by the gauge transformation. Doing so, the ξ fields and the connected degrees of freedom seem to simply disappear from the Lagrangian. In fact, at the same time the masses of the gauge bosons are generated. Hence, the degrees of freedom reappear, since each massive field gains one degree of freedom due to the additional transverse polarization.

Finally, the interaction of the electroweak gauge bosons (in terms of the mass eigenstates) with the Higgs field can be written as

$$\mathscr{L} = \frac{1}{2}(\partial \text{H})^2 + \frac{1}{4}g^2\text{W}^+\text{W}^-(v + \text{H})^2 + \frac{1}{8}g_Z^2\text{ZZ}(v + \text{H})^2 - V\left[\frac{1}{2}(v + \text{H})^2 \right]. \tag{2.41}$$

Expanding this Lagrangian leads to two terms proportional to v^2, which can be identified as mass terms with the values

$$M_\text{W} = \frac{1}{2}gv \quad \text{and} \quad M_\text{Z} = \frac{1}{2}g_Z v = \frac{M_\text{W}}{\cos\theta_W} \tag{2.42}$$

The higher mass of the Z boson compared to the W is a consequence of the mixing between the W_μ^3 and the B_μ fields. Also the Higgs boson itself becomes massive. From the Higgs potential in Eq. 2.36 $M_\text{H}^2 = -2\mu^2$ can be extracted, why μ is referred to as the Higgs mass parameter.

Since the Higgs field has been introduced as a field with isospin but without color charge, and the electrically neutral field was chosen to be non-zero in the vacuum, only the weak bosons interact with it and get masses while the photon and the gluon remain massless.

The masses of the fermions arise from Yukawa couplings with the Higgs field. Each fermion
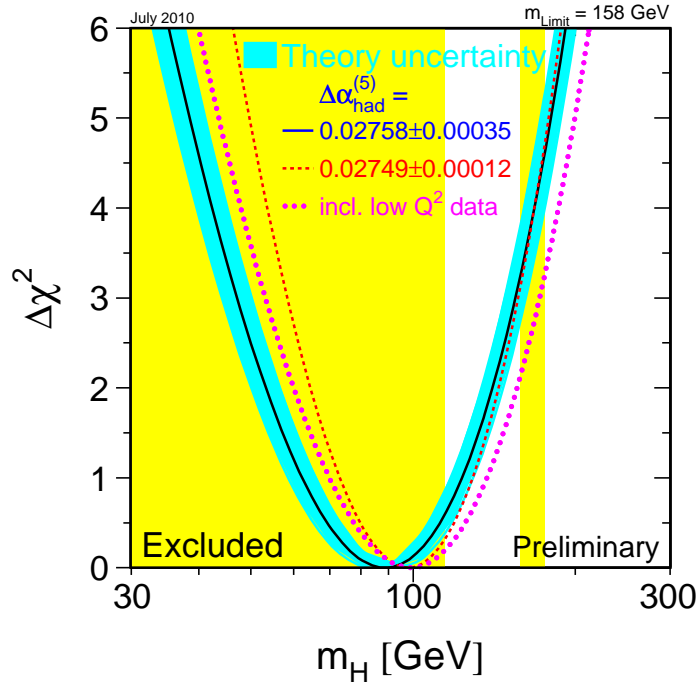
Figure 2.2.: Experimental constraints on the Higgs mass before the measurements of the LHC experiments. The wide yellow region on the left ($M_{\mathrm{H}} < 114\,\mathrm{GeV}$) is excluded by direct LEP measurements, the yellow strip on the right ($158 < M_{\mathrm{H}} < 175\,\mathrm{GeV}$) by the Tevatron experiments. The parabolic lines are results of global Standard-Model fits. Plotted is the $\Delta\chi^2 = \chi^2 - \chi^2_{\min}$ w. r. t. the Higgs boson mass. $\Delta\alpha^{(5)}_{\mathrm{had}}$ denote the light quark contribution to the uncertainty of the electromagnetic coupling constant $\alpha(m_{\mathrm{Z}^0})$ [15].

has a coupling constant proportional to its mass. Therefore a mechanism for the masses is provided but their values remain as free parameters of the model, which have to be determined experimentally. Also the coupling of the fermions to the Higgs boson is proportional to the masses of the fermions, which is relevant for experimental searches for the Higgs. A decay $\mathrm{H} \to \mathrm{e^+e^-}$ is highly suppressed, while decays to $\tau^+\tau^-$ or heavy quarks are much more likely.

Discovery of a Higgs-Like Particle at LHC

Already in the 1960s and 1970s the Higgs model was developed and established in the Standard Model. Since then at several collider experiments it was searched for hints for the Higgs boson without success. Most sensitive for direct Higgs discovery in the pre-LHC era were the $\mathrm{e^+e^-}$ ring collider LEP at CERN, the $\mathrm{e^+e^-}$ linear collider SLC at SLAC, and the $\mathrm{p\bar{p}}$ collider Tevatron at Fermilab. In Fig. 2.2 the experimental knowledge about the mass of the Higgs boson is summarized as of July 2010 [15]. The limit of the direct searches at LEP and Tevatron are shown as well as results of global fits of Standard-Model parameters. These fits utilize the fact that also many known parameters of the Standard Model, such as top, $\mathrm{W^\pm}$, and $\mathrm{Z^0}$ masses and widths, are sensitive to the Higgs mass, since the Higgs boson virtually contributes via high-order loop corrections. The measured values of several Standard-Model parameters and the unconstrained Higgs mass are fitted simultaneously.
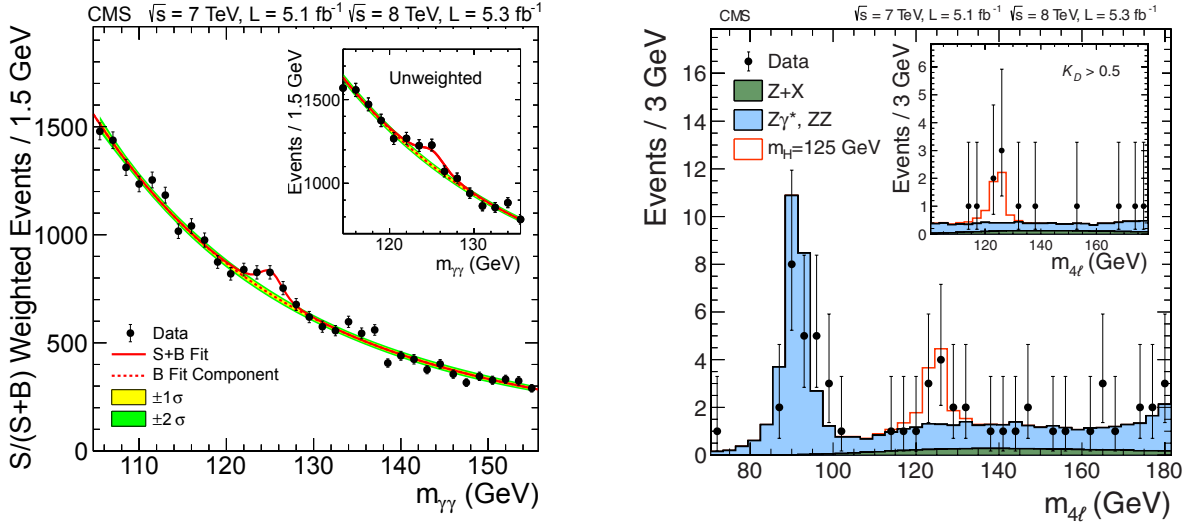
Figure 2.3.: Signatures of the newly discovered boson in the $\gamma\gamma$ (left) and Z^0Z^0 (right) mass spectra. These two channels have the best mass resolution among all studied decay modes [16].

The best fit value of the Higgs boson mass results between $90\,\mathrm{GeV}$ and $100\,\mathrm{GeV}$ (depending on the data that is included and the value of the hadronic corrections to the electromagnetic coupling constant). However, this mass region was already excluded by direct LEP searches. The upper limit at 95% confidence level from the fit is given at $M_\mathrm{H} = 158\,\mathrm{GeV}$. Together with the direct exclusion from LEP the mass of the Higgs boson was assumed to be in the region of $114\,\mathrm{GeV}$ to $158\,\mathrm{GeV}$.

That was the situation when the LHC was launched. After slightly more than two years of data taking at $7\,\mathrm{TeV}$ and $8\,\mathrm{TeV}$ center-of-mass energies, the two multipurpose experiments ATLAS and CMS announced discovery of a new particle that might be the Higgs boson. Independently both experiments found an excess with a local significance of about 5σ at a mass of around $125\,\mathrm{GeV}$ [16, 17]. The cross section of the new process is in agreement with the predictions for Higgs boson production, as well as the appearance of the excess in several channels that fit to the different decay channel expected for the Higgs boson. The analyzed channels are $\gamma\gamma$, Z^0Z^0, W^+W^-, $\tau^+\tau^-$, and $b\bar{b}$.

Figure 2.3 displays the invariant mass spectra of the two most sensitive channels $\gamma\gamma$ and Z^0Z^0 as measured in CMS. The di-photon mass distribution is composed of a smoothly falling background spectrum plus a clear bump around $125\,\mathrm{GeV}$, interpreted as the signal of the new boson. In the $Z^0Z^0 \rightarrow \ell^+\ell^-\ell^+\ell^-$ channel the situation is very different. Only very few events survive the selection, and the excess is formed from a handful of events. A significant accumulation of entries is found at the same mass region. From these two channels a value of the mass is extracted to $m = 125.3 \pm 0.4(\mathrm{stat.}) \pm 0.5(\mathrm{syst.})\,\mathrm{GeV}^6$.

---

[6]Very similar plots are published by the ATLAS collaboration. The excess observed by the ATLAS experiment is most significant at a mass of $126.0 \pm 0.4(\mathrm{stat.}) \pm 0.4(\mathrm{syst.})\,\mathrm{GeV}$ [17].

Many further analyses are necessary before conclusions can be drawn whether the observed boson is the Standard-Model Higgs boson or not. There are hints that the Standard Model is not a complete description of the sub-atomic world (cf. Section 2.2.1). If the Standard Model has to be extended, e. g. by Supersymmetry (cf. Section 2.2), also the Higgs sector is effected. In that sense, studying the new particle can either reinforce the Standard Model, suggest an extension of it, or lead to a completely new understanding of particle physics.

Both, CMS and ATLAS already performed many analyses in order to understand the properties of the new particle. Figure 2.4 shows two plots by CMS concerning the production and decay rates of the new boson w. r. t. the prediction of the Standard Model. On the left the measured cross sections relative to the expected Higgs cross section are plotted for the analyzed decay channels. The results are given in terms of signal strength, i. e. relative to the Standard Model cross section $\mu = \sigma/\sigma_{\mathrm{SM}}$. The signal strengths of the different channels are spread around one, with a slight preference to smaller values. Therefore the combination of all channels results in $\mu = 0.80 \pm 0.14$. However, a striking deviation from the Standard Model prediction is not visible in any channel. On the right the production mechanism is analyzed. Again the signal strength μ is the used variable. On the x axis the signal strengths of fermionic production modes ("ggH": gluon-gluon fusion via a top loop, "ttH": Higgs production is association with $t\bar{t}$) is given, on the y axis μ of the bosonic modes ("VBF": vector-boson fusion, "VH": Higgs production associated with $W^{\pm}$ or Z^0). Because of the different event content, the different decay channels are more or less sensitive to the production modes. The uncertainties are still too large to interpret the results as confirmation of the Standard-Model Higgs boson, but a significant deviation is not visible either [18].

In the Standard Model a scalar Higgs boson (spin $s = 0$) is predicted. The $s = 1$ hypothesis is already strongly disfavored by the observation of the excess in the $\gamma\gamma$ channel. In Fig. 2.5 the $s = 0$ and the $s = 2$ hypotheses are confronted with ATLAS measurements. The logarithm of the likelihood ratio testing the two hypotheses is plotted w. r. t. the production fraction of $q\bar{q}$ annihilation. Over the whole range the data strongly supports the Standard Model hypothesis. However, as alternative hypothesis a specific model predicting a CP-even $s = 2$ boson is used. That model can be excluded at 99.9% confidence level [19].

Further investigations of the new boson are undoubtedly necessary. Additional answers are expected from ongoing analyses of the already recorded data, but also from studies at higher center-of-mass energies in the upcoming running period of the LHC accelerator.

2.2. The Supersymmetric Extension of the Standard Model

The success of the Standard Model is a success of symmetry. The interactions are described as consequences of symmetries: The invariance of the Lagrangian under a certain symmetry group require the gauge fields. Applying Noether's Theorem conservation laws can be directly derived from the symmetries: From the invariance under $U(1)$ transformation follows conservation of a simple additive quantum number. In the case of QED this additive quantum number can be identified as electric charge. Similarly leads the $SU(2)_L$ to conservation of isospin and the $SU(3)$ invariance to conservation of color.

The supersymmetric extension of the Standard Model predicts a symmetry between fermions and bosons, i. e. particles with half-integer and integer spin. Since spin is a property in space, Supersymmetry (SUSY) can be understood as a generalization of space-time symmetry. The Coleman-Mandula theorem [20] actually forbids such non-trivial combinations of space-time
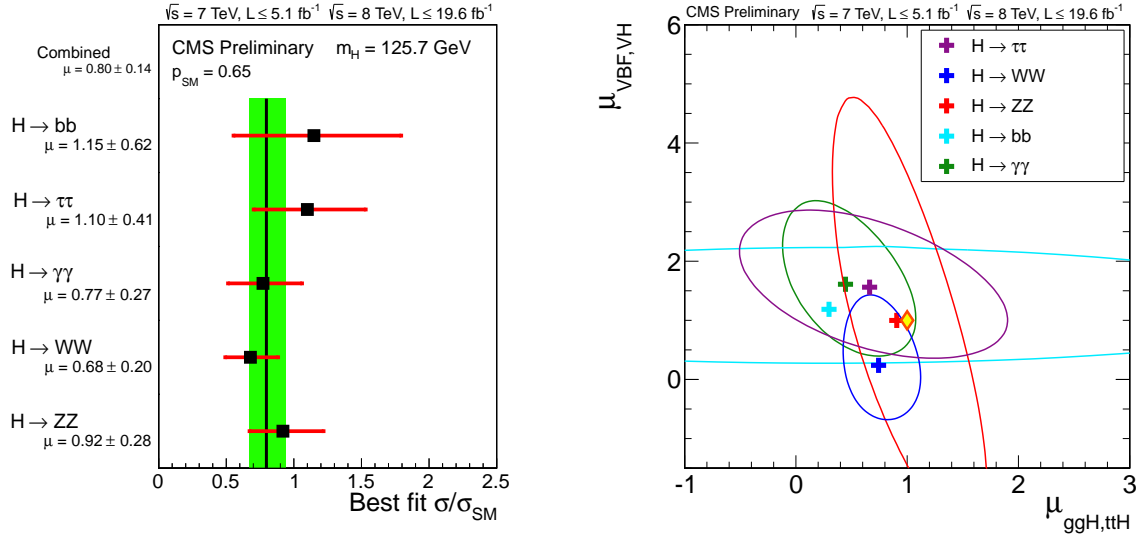
Figure 2.4.: Production and decay of the newly discovered boson in the light of the Higgs boson predicted by the Standard Model as measured in 7 TeV and 8 TeV datasets recorded by CMS. On the left the "signal strength" $\mu = \sigma/\sigma_{SM}$ is plotted for several decay channels. On the right two classes of production mechanisms are investigated. The crosses mark the best fit point of the channel, the ellipses the 68% CL contours, the diamond shows the Standard-Model prediction [18].
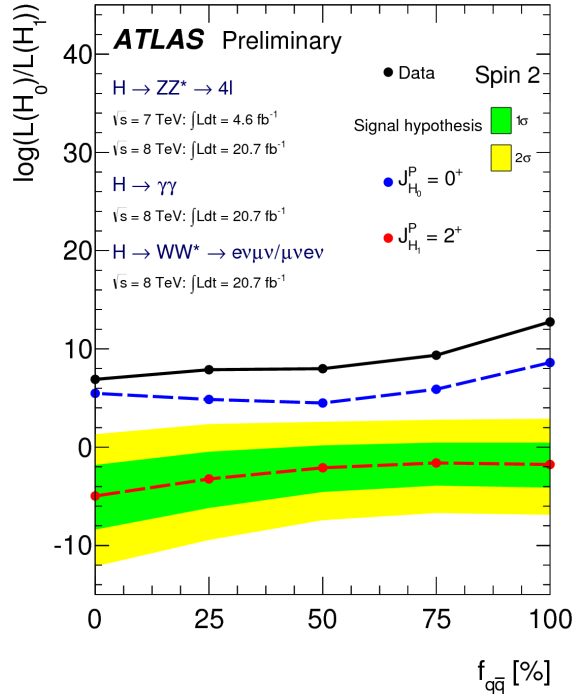

Figure 2.5.: Spin of the newly discovered boson measured in 7 TeV and 8 TeV datasets recorded by ATLAS. The $s = 0$ hypothesis (Standard Model) is favored over the $s = 2$ hypothesis. Since the analysis is sensitive to the production mechanism, the fraction of q$\bar{\text{q}}$ annihilation is varied from 0% to 100% on the x axis [19].

and internal symmetries with only one exception [21], and that is Supersymmetry.

The generator of the new symmetry Q transforms a fermionic state into bosonic state and vice versa

$$Q \left| \text{boson} \right\rangle = \left| \text{fermion} \right\rangle \quad \text{and} \quad Q \left| \text{fermion} \right\rangle = \left| \text{boson} \right\rangle, \tag{2.43}$$

Each particle of the Standard Model becomes part of a *supermultiplet* together with new particles called *superpartners*. Supersymmetry requires now these particles to have identical quantum numbers with exception of the spin that differs by 1/2. This means that also the masses of the particles in each supermultiplet should be the same. Obviously this is not the case since light superpartners with the same couplings as the known Standard-Model particles would have been discovered easily. Consequently the symmetry must be broken.

2.2.1. Problems of the Standard Model and Possible Solutions

Besides the fact that symmetries have been very fruitful in physics and the unique possibility to introduce this new symmetry, there are more particular reasons why Supersymmetry is promising and desirable extension of the current theory of particle physics.

As outlined in the previous sections the Standard Model of particle physics has been very successful. There is no direct deviation found in any experiment. Discoveries and precision measurements at the high energy frontier (LEP, HERA, Tevatron, LHC, and others), but also at low energies confirmed all predictions. With the discovery of a boson that could be the Higgs boson, it seems that also the last Standard-Model prediction could become a great success of the theory. But nevertheless, some issues remain.

Inclusion of Gravity An obvious problem of the Standard Model is that it provides no description of gravity. In the energy and mass regions reachable in current collider experiments, gravitational interactions play no role at all. The same can actually be said about any collider experiment for the foreseeable future. The gravitational attraction between elementary particles are expected to become relevant only at the Planck's scale of $M_P \approx 10^{19}$ GeV. However, a fundamental theory should also hold possibilities of answers to questions that can not be tested experimentally. The formalism performing that well in describing electromagnetic, electroweak, and strong interaction, fails in explaining gravity.

Supersymmetry does not deliver an elaborated quantum field theory of gravity, but it may lead a way: The space-time-like character of the symmetry requires to include a gravitation field as soon as Supersymmetry should become a local symmetry. Hence, the model of local Supersymmetry is called *Supergravity*. The implementation of gravity is still an open question, but a link between the world of quantum field theories and General Relativity is a remarkable by-product.

The Hierarchy Problem The maybe strongest indication for the incompleteness of the Standard Model is know as the hierarchy problem. If there is no new phenomena between the electroweak scale and the Planck's scale (where the Standard Model fails anyhow because of the missing description of gravity), an extreme fine-tuning of the Higgs mass parameter would be necessary.

The Higgs boson is assumed by the Standard Model to be a scalar spin-0 particle, which couples to all massive particles. The first studies of the new boson found at LHC tentatively
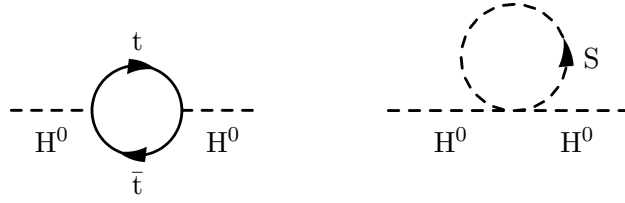
Figure 2.6.: Loop diagrams of particles that couple to the Higgs boson contribute to its mass. Due the large coupling especially loops of top quarks are relevant in the Standard Model (left). In Supersymmetry the top quark is accompanied a scalar stop, which compensates the top contribution by the loop at the right.

confirm the spin. The observation of the excess in several decay channels and via different production processes indicates agreement with the required couplings.

The mass of the Higgs boson is not constant over the energy range. Also other particles have so-called *running masses*, for example the electron. The measurable mass of the electron is understood as the sum of its *bare mass* and photon loop corrections. Although these loop corrections diverge with the energy scale, by means of renormalization the measurable mass remains stable. Due to the spin and the couplings of the Higgs boson very large mass corrections can be expected. Whereas the electron mass correction scales logarithmically with the energy, the corrections to a spin-0 particle scale quadratically. Especially loops of top quarks, as illustrated on the left in Fig. 2.6, contribute because of the large coupling. The corrections to the mass parameter μ^2 of the Higgs boson by such a process is given by

$$\Delta\mu^2 = \frac{|\lambda_\mathrm{t}|^2}{16\pi^2} \left(-2\Lambda_\mathrm{UV}^2 + 6m_\mathrm{t}^2 \ln(\Lambda_\mathrm{UV}/m_\mathrm{t}) + \cdots \right), \tag{2.44}$$

where λ_t is the coupling constant of the top quark to the Higgs boson and Λ_UV is an ultraviolet momentum cutoff. The higher the considered energy scale the higher the cutoff has to be chosen. This cutoff can be understood as an upper limit of the energy range in which the theory is valid. Since the loop correction is proportional to the square of this cutoff the Higgs mass diverges quadratically with the energy scale. At the Planck's scale for example the correction to μ^2 is about 30 orders of magnitude larger than μ^2 at the electroweak scale itself.

Although there is a possibility to cancel the squared divergence within the Standard Model this would require an extreme fine-tuning of the underlying parameter with an accuracy of the order of 10^{-26} in each order of perturbation theory.

Neither a strong dependency of the mass of a particle from the energy scale nor an extreme fine-tuning of some parameters is desirable for fundamental physical theory.

Supersymmetry solves the hierarchy problem in a very natural way. The top quark gets a scalar superpartner. This scalar top contributes to the Higgs mass via a loop as sketched on the right in Fig. 2.6. The correction to the Higgs boson mass is

$$\Delta\mu^2 = \frac{\lambda_\mathrm{S}}{16\pi^2} \left(\Lambda_\mathrm{UV}^2 - 2m_\mathrm{S}^2 \ln(\Lambda_\mathrm{UV}/m_\mathrm{S}) + \cdots \right). \tag{2.45}$$

Comparing this contribution with the one from Standard-Model top quark in Eq. 2.44 there is a relative minus sign at the squared cutoff Λ_UV. Hence, automatically the terms quadratic in Λ_UV
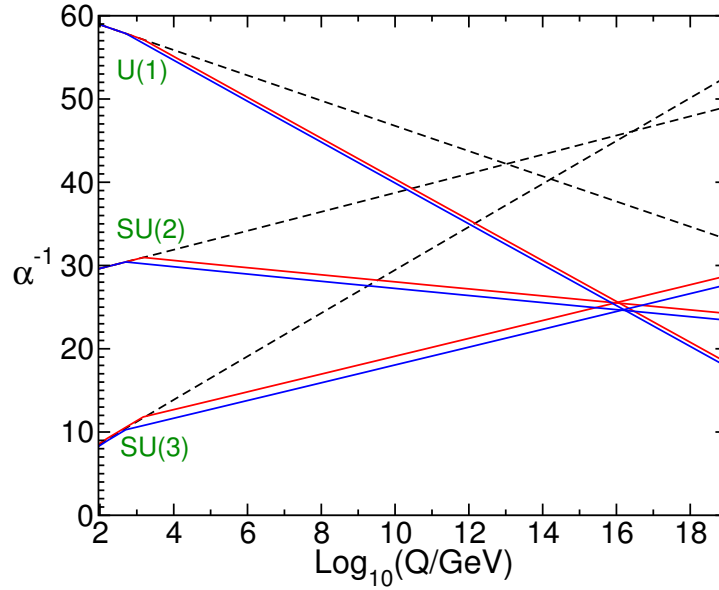
Figure 2.7.: Running of the inverse coupling constants with the energy scale: While in the Standard Model the constants miss each other, in Supersymmetry they meet at one point [6].

cancel, since the Yukawa couplings λ_S and λ_t are the same[7]. What remains is the logarithmic dependency, which would only cancel if the masses m_t and m_S were the same. However, as long as the mass difference is not too large, say $m_S \lesssim 1\,\mathrm{TeV}$, the situation is similar to the running electron mass and the Higgs boson mass is "renormalizable".

Grand Unification From an aesthetic point of view the many free parameters of the Standard Model are considered as problematic. Particle masses, coupling constants, the elements of the CKM matrix, and some more add up to 19 parameters that are not predicted by the theory, but have to be determined experimentally. Also other arbitrarinesses of the model such as the mass hierarchy of the particle families can be mentioned.

Obviously, Supersymmetry is not an extension to the Standard Model that reduces its number of parameters. Instead, new particles with masses and mixings add parameter to the theory. However, many supersymmetric models need only very few new parameters, by assuming the plenty of parameters at the electroweak scale to be unified at a higher scale. An example is the *constrained minimal supersymmetric Standard Model* (CMSSM), which is determined by four numeric parameters and one sign.

Almost accidentally Supersymmetry does lead to a reduction of free parameters in a very crucial area. The coupling constants of the electromagnetic, weak, and strong interaction change with the energy scale. Similar to masses also the strengths of interactions are effected by loop corrections.

Figure 2.7 shows the evolution of the inverse coupling constants with the energy scale in the Standard Model as dashed lines. At a scale of about $10^{14}\,\mathrm{GeV}$ the interaction strengths become similar. If also supersymmetric particles are considered in the loop corrections, the slopes in

---

[7]The factor of 2 between Eq. 2.44 and Eq. 2.45 is compensated in Supersymmetry since a fermion has two scalar superpartners. One is the partner of the left-handed, the other of the right-handed fermion.

Fig. 2.7 change to the solid lines. Whenever the energy scale reaches a threshold where new particle loops contribute, the lines get a link. As long as these threshold, i.e. the masses of the supersymmetric particles, are not much larger than 1 TeV the slopes get changed in such a way that all three constants meet at one point at a scale of approximately 10^{16} GeV. Hence, the three interaction could be described by one parameter and the different strength at low energies is just an effect of different loop corrections.

This very pragmatical argumentation via the number of free model parameters can be restated as a large step towards a "Grand Unified Theory" (GUT). In the 19$^{\text{th}}$ century electricity and magetism that was found to be two manifestations of the same interaction. In Grand Unified Theories all three interactions of the Standard Model are assumed to show only different aspects of one single underlying interaction. A unified coupling constant could be an essential element of unification of the interactions.

Dark Matter A final problem can even be interpreted as experimental evidence against the Standard Model: The theory that is supposed to describe all fundamental particles, holds no particle that is suitable to form the Dark Matter observed in the universe. Also the Dark Energy can not be explained by the model.

Recent cosmological observations found the following composition of the universe [22]

4.9%	Ordinary matter
26.8%	Dark Matter
68.3%	Dark Energy

Hence, only 5 percent of the universe can be explained by the Standard Model. Especially the missing explanation for the Dark Matter is embarrassing for the Standard Model. Massive neutrinos seem to fulfill the requirement of Dark Matter since they are neither electrically nor color charged. But the masses are very small, i.e. neutrinos are typically relativistic. Model calculations show that the masses are too small to account for the huge amount of Dark Matter, and that relativistic particles would form other patterns. In particular, rotation curves of galaxies and gravitational sensing indicate a agglomeration of Dark Matter in halos around galaxies. Relativistic neutrinos are not appropriate for such a behavior.

Supersymmetry provides a perfect candidate for Dark Matter. In many supersymmetric models the lightest supersymmetric particle (LSP) is stable, massive and only weakly interacting. The stability of the LSP is associated with the stability of the proton. In general, the baryon and lepton number conservation can be violated in Supersymmetry without disturbing gauge invariance.

The experimental lower limit on the proton lifetime is of order of 10^{30} years [5]. This is a strong argument why baryon number should also be conserved in Supersymmetry. To achieve this a new quantum number is introduced: the R parity defined by

$$R = (-1)^{3B+L+2S}, \tag{2.46}$$

where B is the baryon number, L the lepton number, and S the spin. All Standard Model particles have $R = 1$ while all SUSY particles have $R = -1$. The conservation of R leads to a stable proton and to a stable LSP.

2.2.2. Particle Content of Supersymmetric Models

The number of new particles predicted by a supersymmetric extension depends on the actual model. The only constrain given is that the number of fermionic and the number of bosonic degrees of freedom in each supermultiplet must be the same. So-called *minimal supersymmetric extension of the Standard Models* (MSSM) introduce the minimal amount of the particles: for each known particle the least possible number of superpartners. For each spin-1/2 fermion of the Standard Model two scalars are introduced, each as partner of one helicity state of the fermion[8]. Each gauge boson is accompanied by a supersymmetric fermion[9].

In supersymmetric models the Higgs sector has to be slightly modified. The Standard Model Higgs doublet would lead to triangular anomalies. The cancellation of diverging triangle loops in the Standard Model is mentioned in Section 2.1.1. The fermionic superpartner of the Higgs boson would also contribute to the loop, and hence cause a divergence. Therefore a second Higgs doublet has to be introduces. In order to restore the cancellation the two Higgs supermultiplets must have opposite hypercharge. Moreover, in a supersymmetric environment two Higgs doublets a necessary, one generating the masses of up-type quarks, the other of down-type quarks and charged leptons. From the two complex Higgs doublets five Higgs bosons are expected, labeled as h^0, H^0, $H^\pm$, and A_0.

The naming scheme of the supersymmetric particles distinguishes scalars from fermions. The scalars (which are the partners of the Standard Model fermions) get an 's' in front of the Standard Model particle's name: The partner of the quark is called squark, the partner of the lepton is the slepton and so on. The fermionic superpartners end with '-ino', for example gluino or higgsino. The common notation is a tilde over the symbol. Therefore the selectron for example is written as $\tilde{e}$.

The mass eigenstates of the supersymmetric partners are not constructed analogue to the Standard Model. In the Standard Model the Higgs boson has a spin of 0, the gauge bosons have a spin of 1. Their superpartners, however, have all a spin of 1/2. Hence the electrically neutral superpartners agree in all quantum numbers and they can mix to mass eigenstates. Four neutral particles called *neutralinos* $\tilde{\chi}_1^0$, $\tilde{\chi}_2^0$, $\tilde{\chi}_3^0$, $\tilde{\chi}_4^0$ (ordered with increasing mass) are linear combinations of the fermionic gaugino and higgsino fields $\tilde{B}^0$, $\tilde{W}^0$, $\tilde{H}_u^0$, $\tilde{H}_d^0$. The mixing matrix is given by:

$$
M_{\tilde{\chi}^0} = \begin{pmatrix} M_1 & 0 & -\frac{1}{2}g'v_d & \frac{1}{2}g'v_u \\ 0 & M_2 & \frac{1}{2}gv_d & -\frac{1}{2}gv_u \\ -\frac{1}{2}g'v_d & \frac{1}{2}gv_d & 0 & -\mu \\ \frac{1}{2}g'v_u & -\frac{1}{2}gv_u & -\mu & 0 \end{pmatrix},
\tag{2.47}
$$

where M_1 and M_2 are the gaugino mass parameters, μ is the higgsino mass parameter, g and g' are the coupling constants, and $v_u = \langle H_u^0 \rangle$ and $v_d = \langle H_d^0 \rangle$ are the vacuum expectation values of the neutral components Higgs fields. The two vacuum expectation values are related via

$$
v_u^2 + v_d^2 = \frac{2m_{Z^0}^2}{(g^2 + g'^2)};
\tag{2.48}
$$

---

[8]The degrees of freedom are counted before the electroweak symmetry breaking. Hence, the particles are massless and do not have a transverse spin degree of freedom.

[9]In the massless case there is no difference in the numbers of degrees of freedom between spin-1 and spin-1/2 particles.

	Supersymmetry eigenstates	mass eigenstates
Squarks	$\tilde{u}_L, \tilde{u}_R, \tilde{d}_L, \tilde{d}_R$ $\tilde{s}_L, \tilde{s}_R, \tilde{c}_L, \tilde{c}_R$ $\tilde{t}_L, \tilde{t}_R, \tilde{b}_L, \tilde{b}_R$	$\tilde{t}_1, \tilde{t}_2, \tilde{b}_1, \tilde{b}_2$
Sleptons	$\tilde{e}_L, \tilde{e}_R, \tilde{\nu}_e$ $\tilde{\mu}_L, \tilde{\mu}_R, \tilde{\nu}_\mu$ $\tilde{\tau}_L, \tilde{\tau}_R, \tilde{\nu}_\tau$	$\tilde{\tau}_1, \tilde{\tau}_2, \tilde{\nu}_\tau$
Neutralinos	$\tilde{B}^0, \tilde{W}^0, \tilde{H}_u^0, \tilde{H}_d^0$	$\chi_1^0, \chi_2^0, \chi_3^0, \chi_4^0$
Charginos	$\tilde{W}^\pm, \tilde{H}_u^+, \tilde{H}_d^-$	$\chi_1^\pm, \chi_2^\pm$
Gluino	$\tilde{g}$	

Table 2.4.: Superpartners introduced by MSSM. In the third generation and the gaugino sector the mass eigenstates, i.e. the experimentally observable particles, are mixed states of the eigenstates w.r.t. SUSY transformation.

commonly the ratio of both is used as free parameter, traditionally denoted as $\tan\beta = v_u/v_d$.

Also the charged gauginos and higgsinos $\tilde{W}^+$, $\tilde{W}^-$, $\tilde{H}_u^+$, and $\tilde{H}_d^-$ mix to mass eigenstates $\tilde{\chi}_{1,2}^\pm$, called *charginos*, defined by the matrix

$$M_{\tilde{\chi}^\pm} = \begin{pmatrix} M_2 & \frac{1}{\sqrt{2}}gv_u \\ \frac{1}{\sqrt{2}}gv_d & \mu \end{pmatrix}. \tag{2.49}$$

Also in the scalar particle sector the mass eigenstates can be superpositions of the Supersymmetry eigenstates. In most scenarios the superpartners of the left and right handed fermions of the first and second generations are nearly mass generated, i.e. mixing is not relevant. However, in the third generation due the large Yukawa couplings, the mass splitting can be large and thus the mixing. The mass eigenstates are subscripted with 1 and 2, by convention 1 labels the lighter particle.

In Table 2.4 the particles of the minimal supersymmetric extension of the Standard Model are listed.

2.2.3. Breaking Mechanism of Supersymmetry

The basic problem of the Supersymmetry model is the absence of observation of any superpartner in a collider experiment. The postulated particles with masses and couplings like the known Standard-Model particles should have been produced and detected in large numbers at many experiments.

A possible and promising way out is the known concept of spontaneous symmetry breaking.

Similar to the spontaneous symmetry breaking in the model of the electroweak interaction (cf. Section 2.1.3), the Lagrangian itself remains invariant under Supersymmetry transformation, while in the ground state of the superpotential the symmetry is broken.

Due to severe difficulties in building a model that breaks the symmetry only with the particles of the MSSM, commonly a *hidden sector* is introduced. The symmetry breaking takes place in the hidden sector, which is invisible for MSSM particles. In the Lagrangian the breaking terms are explicitly added. This type of symmetry breaking is called *soft Supersymmetry breaking.*

The connection between the hidden sector and the visible physics can be accomplished in different ways. One possibility is that gravitation mediates between the sectors. Such a model is the minimal Supergravity Model (mSUGRA, also called constrained MSSM, CMSSM). The huge amount of new parameters that is introduced by Supersymmetry is reduced to five: The gauginos have a unified mass parameter at the GUT scale ($m_{1/2}$). Therefore their different masses at low energy scales are no free parameters anymore. They can be calculated by considering all occurring radiative corrections. In the same way all sfermion masses unify to m_0. Additionally, the ratio of the vacuum expectation values of the two Higgs doublets $\tan \beta = v_\mathrm{u}/v_\mathrm{d}$ is a free parameter, the trilinear coupling A_0 which is also unified at high energy scales, and the sign of the higgsino mass parameter μ.

Another breaking scenario of Supersymmetry if formulated in gauge-mediated Supersymmetry breaking models (GMSB). Here the gauge interactions of the Standard Model are responsible for the breaking terms in the superpotential.

2.2.4. Searches for Supersymmetry

Generally, the supersymmetric particles are expected to be heavier than the Standard Model particles. In a collider experiment they can be produced if the center-of-mass energy is high enough and the couplings reasonable. If R parity is conserved supersymmetric particles can only be produced in pairs. Then, the massive particles decay – possibly via intermediate states of lighter SUSY particles – emitting quarks, leptons, gluons, or gauge bosons into the lightest supersymmetric particle (LSP), which is stable and only weakly interacting. R parity prevents a decay of a supersymmetric particle into Standard Model particles only.

In the detector the LSP behaves like a massive neutrino, a particle that interacts neither electromagnetically nor strongly can not be detected by current collider experiments. For this reason the main signature of events containing SUSY particles is missing energy. In addition the heavy masses of the expected new particles produce a lot of kinetic energy in the events. Therefore high-energetic jets or leptons can be hints to supersymmetric events.

The plenty of searches performed the LEP, Tevatron, and many previous experiments will not be discussed here, Instead, a very short summary of the searches at the LHC experiments ATLAS and CMS is given.

In summary, up to now a supersymmetric signal has not been discovered. Both experiments performed many analyses searching in various channels and probing different models. The channels are characterized by the observable event content (the *final state*), whether only jets are measured or also leptons or photons. In the case of two (or more) leptons it could make sense to distinguish further according to electric charge and lepton flavor. In the hadronic sector bottom-quark jets can be experimentally distinguished from "light" jets (cf. Section 4.2.3). Hence, also the b-jet multiplicity is used to define search channels. The different channels are sensitive to different models of Supersymmetry, but differ also in the amount, composition, and characteristics of events from Standard Model processes, called *background.* Large effort is put
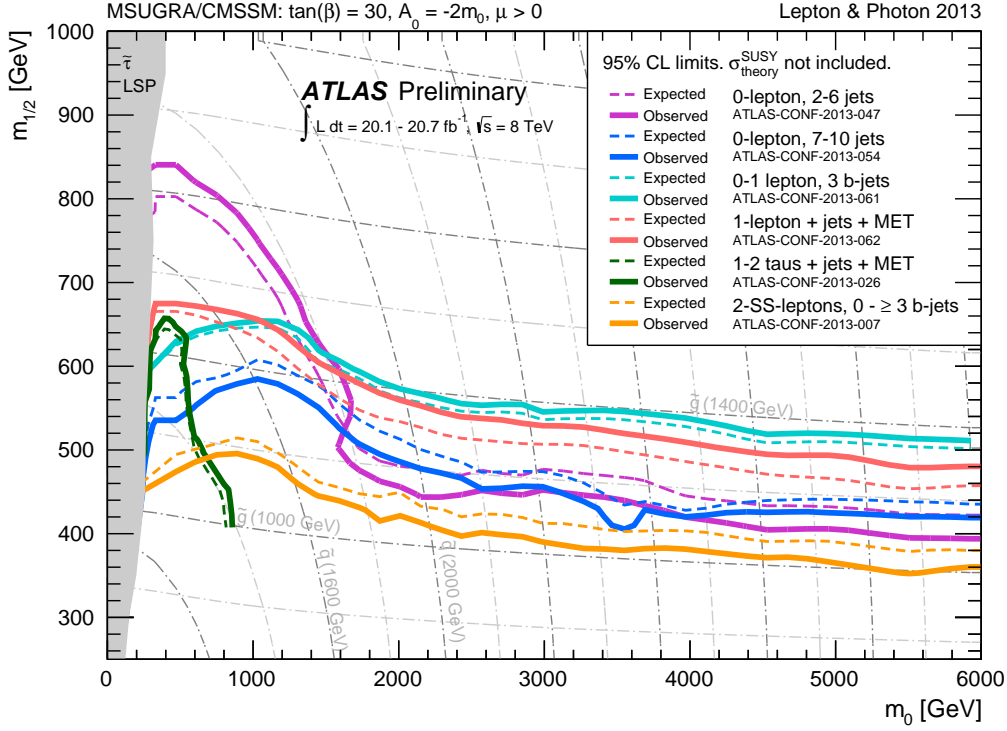
Figure 2.8.: A summary of analyses performed by the ATLAS collaboration probing the CMSSM model. From the five model parameter, $\tan\beta$, A_0, and the sign of μ are set to values that are in agreement with the assumption that the found excess is a Higgs boson. The mass parameters m_0 and $m_{1/2}$ are scanned. The trilinear coupling A_0 is not fixed but proportional to m_0. The parameter space below a line is excluded to 95% confidence level by the stated analysis. Lines of constant light squark and gluino masses are drawn dash-dotted [23].

into reliable and convenient estimations of the backgrounds.

If the measurements agree with the expectations from Standard Model events, signal model assumptions can be used to test, whether a deviation should be seen if that particular model was realized in nature. Supersymmetric signal events are simulated by Monte-Carlo programs and (together with estimations on background events) compared to the measurements. In that way models or parameter regions of models can be excluded by the observation. Exclusion limits are typically given with a confidence level of 95%.

Figure 2.8 gives an overview of several analyses performed by ATLAS probing the CMSSM model. Assuming that the discovered boson is a Higgs boson (cf. Section 2.1.3), implications on possible supersymmetric models are expected. Parts of the whole parameter space can be already excluded, since the predicted Higgs boson mass does not agree with the measured one. Here, the model parameters are set to values that are still allowed under the assumption of the Higgs-boson discovery. The signature with only hadronic event activity ("0-lepton") and the one-lepton signature are most sensitive in this scenario. Within the model assumptions gluino masses up to almost 1400 GeV can be excluded and squark masses up to slightly more than 1700 GeV.
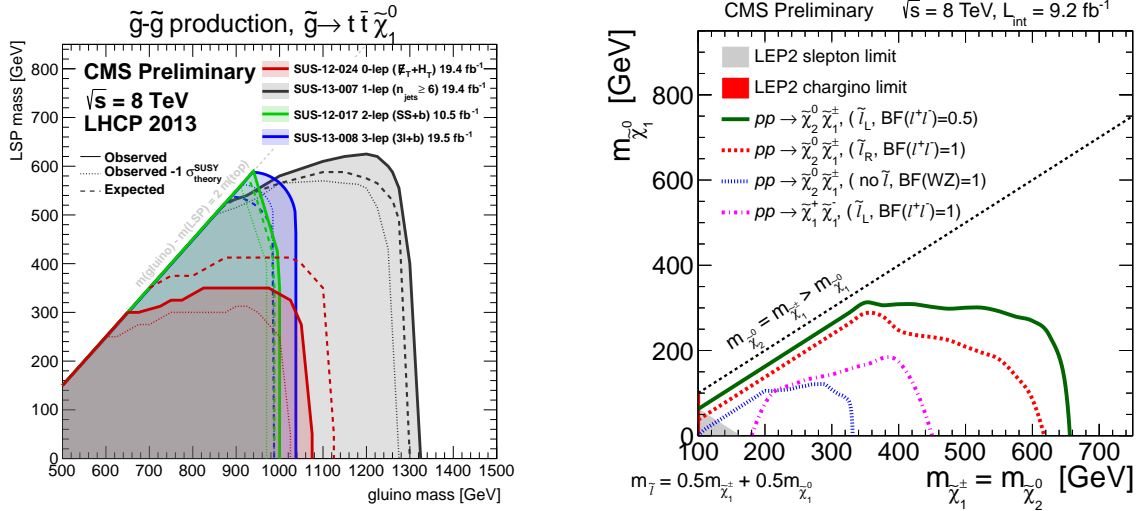
Figure 2.9.: Exclusion limits on simplified models derived from CMS analyses. On the left gluino-gluino production with four top quark in the final state is tested. The shaded areas are excluded by the stated analysis. At parameter points above the diagonal line the two top quarks in each branch can not be on-shell. On the right, direct neutralino and chargino production is tested. The first chargino $\tilde{\chi}_1^\pm$ and the second neutralino $\tilde{\chi}_2^0$ are assumed to be mass degenerated. The mass of the intermediate slepton is assumed to be exactly in the middle between the LSP and neutralino-chargino mass. The area above the diagonal dashed line is kinematically forbidden [24].

A more general and model independent approach makes use of *simplified models spectra* (SMS) [25, 26]. Here, no specific model of Supersymmetry is assumed, but generically specific production and decay processes are tested. The masses of the involved particles act as parameters.

On the left in Fig. 2.9 a supersymmetric particle cascade is tested that starts with gluino-gluino production. Both gluinos decay via a three-body decay into a $t\bar{t}$ pair and the LSP $\tilde{\chi}_1^0$. Third-generation scenarios are of special interest since the hierarchy problem is only solved by Supersymmetry if the superpartner of the top quark, the *stop*, is not too heavy. The three-body decay can be understood as cascade with an off-shell stop. The two parameters of the process are the mass of the gluino and the mass of the LSP. In events with four top quarks there is a reasonable probability that at least one lepton can be found in the final state. Hence, the one-lepton analysis shows the best sensitivity[10]. Independent of the LSP mass gluinos decaying in such a way can be excluded up to a mass of about 950 GeV. For light LSPs the gluino mass exclusion reaches up to 1300 GeV.

On the right in Fig. 2.9 electroweak production of supersymmetric events is tested. Here, the plotted exclusion limits do not correspond to different final states but to slightly different models as stated in the legend. Most of the lines are combinations of a same-sign di-lepton and

---

[10]The same-sign di-lepton analysis requiring b jets "2-lep (SS+b)" is performed with only half of the available dataset. With the full dataset its sensitivity is expected to increase.

the 3-lepton analysis having the best sensitivity.

Since neutralinos and charginos are mixed states, the actual mixing has an influence on the couplings. Different scenarios are tested. If the gauginos couple mainly via weak interaction, the superpartner of the left-handed lepton ($\tilde{\ell}_L$) is preferred. The extreme case with only $\tilde{\ell}_L$ is tested. Although only half of the branching fraction (BF) is available to the 3-lepton analysis because also decays with sneutrinos contribute, for that scenario the best limit can be set. On the other hand, if the higgsino contribution in the gaugino mixing dominates, not the weak interaction but the Yukawa couplings rule the decay. Hence, $\tilde{\ell}_R$ appear in the cascade, but no sneutrinos. Since the Yukawa couplings are proportional to the lepton mass, the tau superpartner is strongly preferred. Therefore the analysis is less sensitive although there is no branching fraction loss due to neutrinos.

If the slepton is heavier than the $\tilde{\chi}_2^0$ ($\tilde{\chi}_1^\pm$), the latter preferably decay into the LSP emitting a Z^0 ($W^\pm$) boson. Here, the weakest limit can be set from all tested scenarios. The last tested model is direct $\tilde{\chi}_1^+ \tilde{\chi}_1^-$ production. The most sensitive search channels, same-sign di-lepton and 3-lepton, are not suitable for this scenario. Instead, for a non-resonant overshoot of events in opposite-sign di-lepton channel is searched.

A comprehensive summary of the CMS results in the SMS framework is given in Fig. 2.10. For many production and decay processes the observed limits on the mass of the primarily produced SUSY particle are illustrated. In cascades with only two SUSY particles two limits a stated: one under the assumption that the LSP is massless (which is typically the strongest limit) and one assuming the LSP to be 200 GeV lighter than the primary particle. In cascades with an intermediate state, its mass is varied in three steps relative to the masses of the other particles.

Due to the larger cross sections, on strongly produced particles the harder limits can be set. In the gluon-rich environment of the LHC especially the limits on gluino masses are leading.

Ongoing analyses as well as studies at a center-of-mass energy of 13 TeV in the upcoming LHC run are essential in order to answer the question if nature decided for Supersymmetry to be a true concept of elementary particles. The main challenge is and will be reliable descriptions of the Standard Model background. Only then possible deviations could become measurable. If a significant deviation is measured, many studies will be necessary to determine the nature of the deviation. Also further accelerator and detector upgrades and even a new accelerator like a linear e^+e^- machine will be imperative to find a better description of the sub-atomic world.
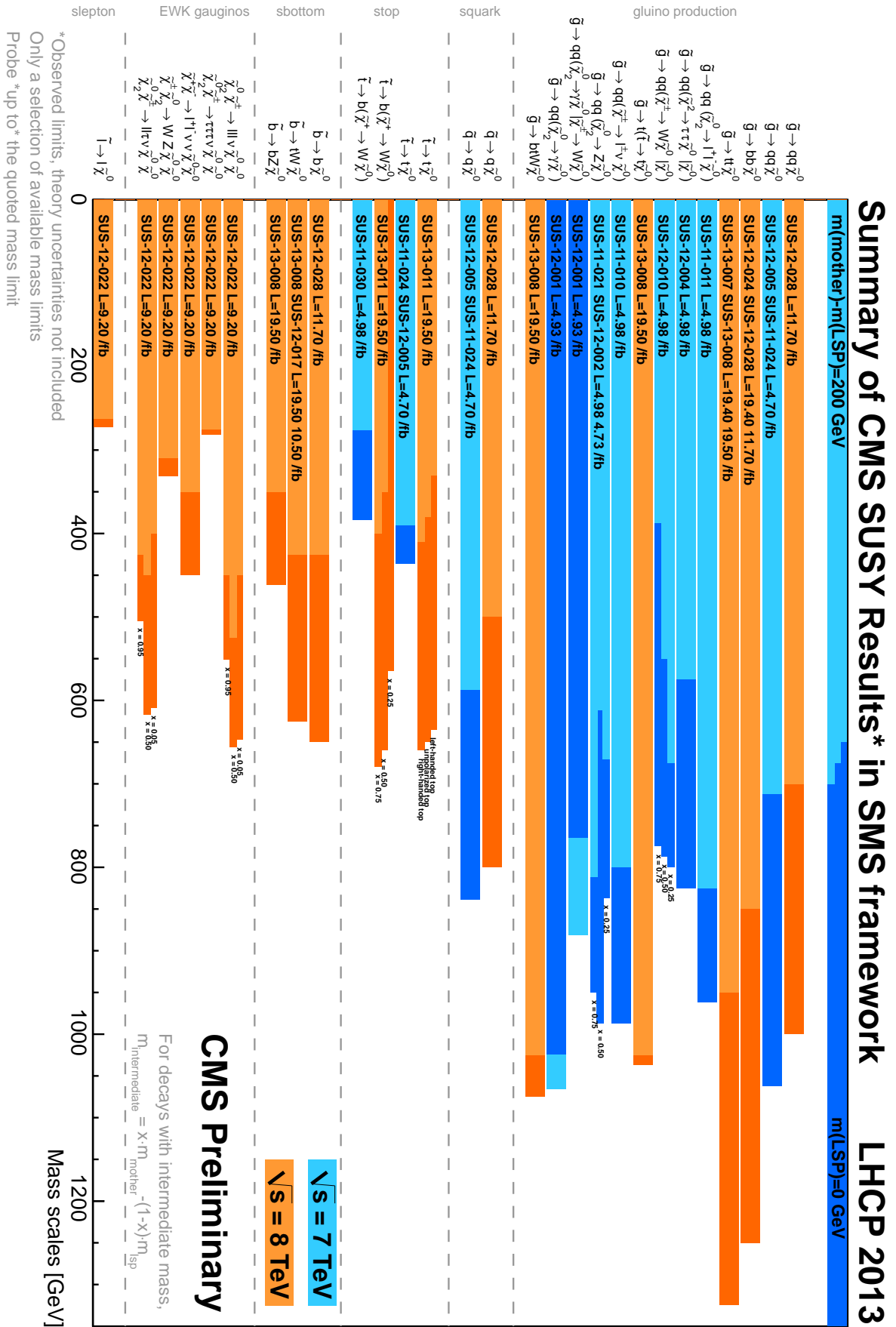
Figure 2.10.: Summary of SMS exclusion limits observed at CMS [24].

3. The LHC and the CMS Experiment

In this chapter the experimental setup is described. Section 3.1 introduces the LHC accelerator, its pre-accelerators, and its experiments. In the Section 3.2 the CMS detector and its components are described.

3.1. The Large Hadron Collider

Between the Jura Mountains and Lake Geneva, at the Swiss-French border, the particle physics laboratory CERN (Conceil Européen pour la Recherche Nucléaire – European Organization for Nuclear Research) operates the world largest particle accelerator, the LHC (Large Hadron Collider) [28–31]. This machine is large, both in terms of size with a circumference of $27\,\mathrm{km}$ and in terms of energy with a design center-of-mass energy of $14\,\mathrm{TeV}$. The collider is housed in the tunnel that was built for the Large Electron-Positron Collider (LEP). LEP was shut down in 2000 and the construction of the LHC was started. Figure 3.1 shows a schematic view of the CERN accelerator complex including the LHC, its main experiments, and its pre-accelerators.

The event rate that is achieved in a particle collider can be split in two components, one depends exclusively on machine and beam quantities, the other on the interaction process. The former is called luminosity L, the latter is the cross section σ_X:

$$r_X = L\sigma_X \tag{3.1}$$

is the event rate of the process X. The luminosity combines all relevant beam parameters:

$$L = \frac{N_{\mathrm{b}}^2 n_{\mathrm{b}} f_{\mathrm{rev}} \gamma_{\mathrm{r}}}{4\pi\epsilon_{\mathrm{n}}\beta^*}F, \tag{3.2}$$

where N_{b} is the number of particles per bunch, n_{b} the number of bunches per beam, f_{rev} the revolution frequency, γ_{r} the relativistic gamma factor, ϵ_{n} the normalized transverse beam emittance, β^* the beta function, and F accounts for the reduction due to the beam crossing angle.

In the main operation mode the LHC accelerates two contradirectional beams of protons, which can be brought to collision at four points along the ring. 2808 particle bunches circulate at the design luminosity of $L = 10^{34}\,\mathrm{cm}^{-2}\,\mathrm{s}^{-1}$, each containing about 10^{11} protons. The bunch crossing rate for the experiments under these conditions is $40\,\mathrm{MHz}$ ($25\,\mathrm{ns}$ bunch spacing). In 2012, when the data for this analysis was taken, the center-of-mass energy was $8\,\mathrm{TeV}$, the maximum peak luminosity was $L = 8 \times 10^{33}\,\mathrm{cm}^{-2}\,\mathrm{s}^{-1}$, and the bunch spacing was $50\,\mathrm{ns}$.

On September 10th, 2008 the first proton beam surrounded the whole accelerator, but an electrical failure in the cooling system delayed the first collisions to November 23rd, 2009. In 2010 and 2011 the LHC ran with a beam energy of $3.5\,\mathrm{TeV}$ in proton-proton collisions, in 2012 the energy was increased to $4\,\mathrm{TeV}$. Current plans foresee a restart in 2015 with a beam energy of $6.5\,\mathrm{TeV}$.
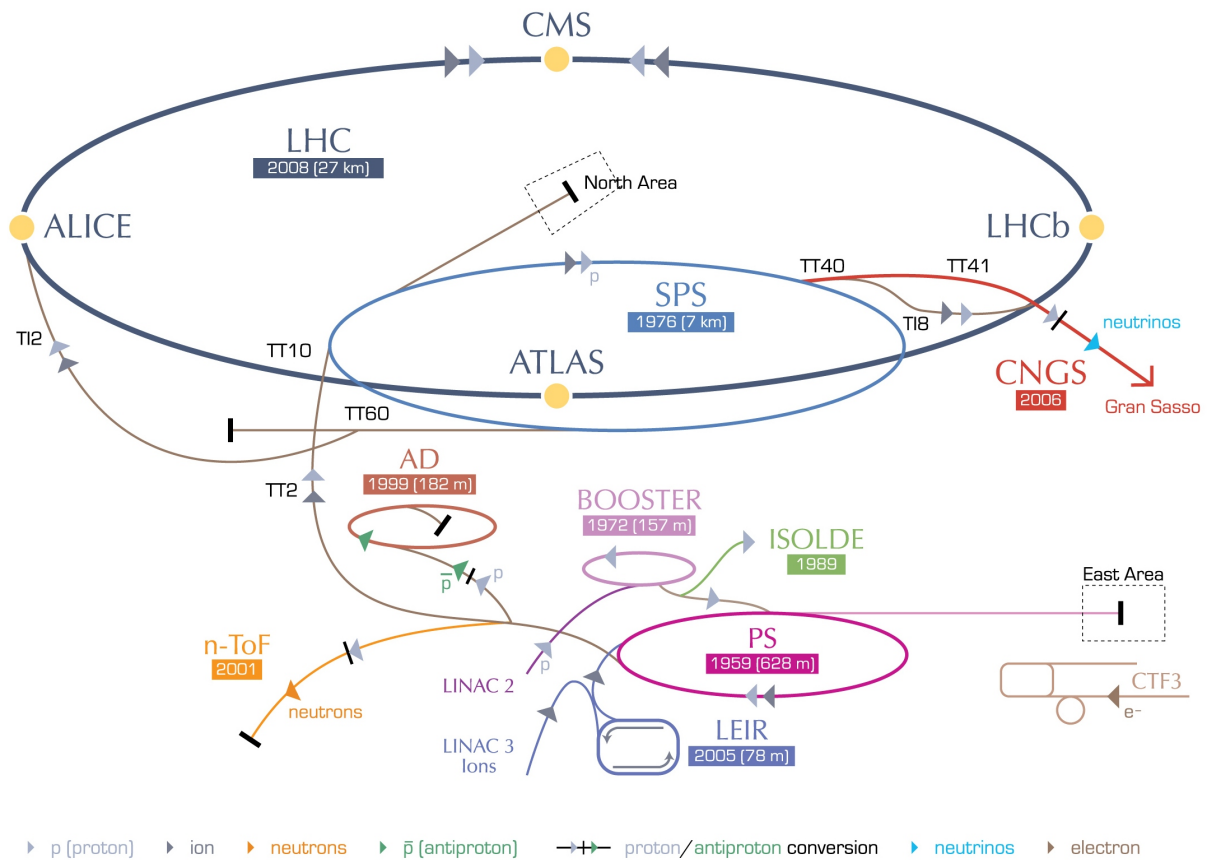
Figure 3.1.: Schematic view of the CERN accelerators including LHC and its pre-accelerators. The CMS detector is located at the top of this scheme. Following the beam pipe clock-wise, the other large LHC experiments are LHCb, ATLAS and ALICE. The LHC protons start at LINAC 2, going through Booster, PS, and SPS until they are injected into the LHC. The given numbers at each accelerator indicate the years of initial operation and the circumferences of the accelerators [27].

In a second operation mode the LHC accelerates and collides heavy ions. Two beams of lead ions ($^{208}\text{Pb}^{+82}$) were brought to collision for a few weeks in 2010 and 2011; proton-lead collisions were performed in the beginning of 2013. The design energy of the lead ion beams is 2.76 TeV per nucleon, which corresponds to a Pb-Pb center-of-mass energy of 1148 TeV.

3.1.1. The LHC Cavities and Magnets

The three main tasks of a particle collider are keeping the beams on their circular track, accelerating the particles, and bringing them to collision in a way that maximizes the probability of a hard interaction. The first task is done by dipole magnets. A total of 1 232 superconducting niobium-titanium magnets bend the two beams on their circular path. The superconductivity requires an operation temperature of 1.9 K, which is achieved by a complex cooling system based on superfluid helium. At design energy a magnetic field of 8.3 T is necessary. In contrast to LEP and Tevatron, the two beams can not be bent by the same dipole field: In LEP and
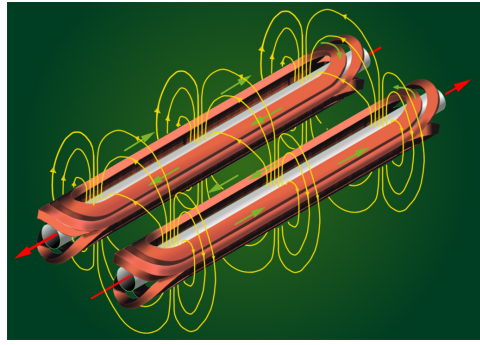
Figure 3.2.: Scheme of the magnetic field in the LHC dipoles: A common field provides an opposite magnetic flux in the two beam pipes. The red ovals represent the conductors, the direction of current is indicated, as well as the direction of the protons in the beam pipes [32].

Tevatron the beams were formed from particles with opposite charge (e^+e^- and $p\bar{p}$, resp.), which leads together with the opposite direction of movement to the same Lorentz force in a magnetic field, whereas the two proton beams in the LHC would be affected by Lorentz forces with opposite directions and therefore diverge.

The problem can be solved by working with two separate beam infrastructures like it was done for the electron and proton beams at HERA. But there are two main drawbacks: It is more expensive and it needs more space. The space consumption was actually found to be a serious problem: Especially the spatial limitations in the arc segments of the LEP tunnel (where the dipole magnets have to be placed) requires a more sophisticated solution: The LHC dipoles are constructed in such a way that a connected field provides an opposite magnetic flux for the two beams, as illustrated in Fig. 3.2.

The acceleration itself is achieved by 16 superconducting niobium sputtered copper single cell cavities. The 400 MHz cavities are all placed at *Point 4*, which is located between the CMS and the ALICE experiments. The cavities do not solely accelerate the proton beams but also squeeze the bunch length in beam direction. Particles in the front part of a bunch are affected by a weaker electric field, particles in the back part by a stronger field. In that way the front particles get less accelerated, while the rear particles get more accelerated.

Focusing the beams in the transverse plane is achieved by several series of quadrupole and sextupole magnets. Sextupole and octupole magnets are additionally used for beam corrections.

3.1.2. The Pre-Acceleration Chain

Several accelerators that already had existed at CERN when the LHC was built are combined to a chain of pre-accelerators, as sketched in Fig. 3.1. At Linac 2 hydrogen atoms get stripped and the bare protons get accelerated by a linear accelerator. Then they are injected to the Proton Synchrotron Booster (PSB), followed by the Proton Synchrotron (PS) and the Super Proton Synchrotron (SPS), increasing the energy at each stage. The SPS accelerates the protons to 450 GeV, which is the injection energy of the LHC.

3.1.3. The Experiments at LHC

At the LHC ring the two multi-purpose experiments ATLAS and CMS are located diametrally. LHCb and ALICE are between them, but closer to ATLAS. TOTEM and LHCf are situated in the same caverns as CMS and ATLAS, resp.

CMS (Compact Muon Solenoid) is a multi-purpose detector, described in Section 3.2.

ATLAS (A Toroidal LHC Apparatus) is the other multi-purpose detector [33]. The successful tradition of having two competitive detectors at a particle collider (e. g. CDF and D0 at Tevatron or ZEUS and H1 at HERA) is continued at the LHC. CMS and ATLAS have very similar conditions but slightly different ways of measuring the particle collisions. In that way possible discoveries can gain in confidence if both experiments confirm each other. The most obvious difference of the ATLAS detector compared to CMS is the toroidal magnetic field in the outer part of the detector that complements the solenoid magnet in the center. The calorimeters are mainly based on liquid argon as active detector material.

The scientific program of ATLAS is very similar to that of CMS. The observation of a Higgs-like boson in parallel to CMS is mentioned in Section 2.1.3. A summary of some results in searches for Supersymmetry is given in Section 2.2.4.

LHCb (the "b" indicates the emphasis on b physics) is dedicated to analyze the CP violation in the decay of b mesons [34]. In contrast to typical detectors at particle colliders, LHCb is very asymmetric and detects only particles close to the beam axis. This special geometry is owned to the fact that b hadrons are predominantly produced in the forward direction. The CP violation is directly connected to the asymmetry between matter and anti-matter in the universe.

An achievement of the LHCb experiment is the first measurement of CP violation in the charm sector [35]. An additional success, which is also relevant in the context of Supersymmetry, was achieved in searches for $B^0_s \to \mu^+\mu^-$ and $B^0 \to \mu^+\mu^-$ decays [36, 37]. The muonic $B^0_{(s)}$ decay is only possible via a flavor changing neutral current, which is highly suppressed in the Standard Model. New particles, such as SUSY particles, could open new decay modes and thus increase the branching fraction. Upper limits have been set for both decays, the $B^0_s \to \mu^+\mu^-$ decay has been observed with a significance of 3.5σ.

ALICE (A Large Ion Collision Experiment) is a special detector for heavy-ion runs at LHC [38]. The experiment analyzes the quark-gluon plasma that is produced in the collisions of lead nuclei. The quark-gluon plasma is supposed to be a model of the universe right after the Big Bang. By measuring its features and properties a deeper understanding of the evolution of the universe is expected. Especially the confinement of colored particles (cf. Section 2.1.1) is suspended in this extremely dense and hot state of matter.

An early measurement of the ALICE collaboration was the *elliptic flow* in Pb-Pb collisions [39]. The elliptic flow is an event shape variable that measures the anisotropy of the energy flow, it can be used to proof the presence of a quark-gluon plasma in the collisions.

TOTEM (Total Elastic and Diffractive Cross Section Measurement) is dedicated to provide a better understanding of QCD, using a different approach [40]. The experiment shares the

interaction point with CMS and studies the decay products of collisions scattered with a very small angle. Conclusions can be drawn from such measurements concerning the structure of the proton (described by parton distribution functions) and the total proton-proton cross section independent of the luminosity. Due to this independency the measurement can be used to calibrate the luminosity measurement at LHC.

Results of a proton-proton cross-section measurements at center-of-mass energies of $7\,\mathrm{TeV}$ and $8\,\mathrm{TeV}$ have been published [41,42]. The elastic cross section at $8\,\mathrm{TeV}$ is $\sigma_\mathrm{el} = (27.1\pm1.4)\,\mathrm{mb}$, the inelastic cross section is $\sigma_\mathrm{inel} = (74.7 \pm 1.7)\,\mathrm{mb}$.

LHCf (LHC forward) uses the collisions at the ATLAS interaction point to measure neutral particles in the very forward region ($|\eta| > 8.4$) [43]. To reach this very small scattering angles two detectors are installed at a distance of $140\,\mathrm{m}$ from the interaction point in both directions along the beam axis. The motivation for the measurement is providing a calibration for cosmic ray experiments. These experiments suffer from uncertainties in the hadron interaction models and can gain from a better understanding of cosmic ray air showers.

A measurement of the neutral pion spectrum in the very forward region has been performed with 2010 data and compared to the hadronic interaction models that are used in cosmic ray experiments [44].

3.2. The CMS Experiment

The Compact Muon Solenoid (CMS) is one of the two multi-purpose experiments at the LHC. The analysis presented here is based on data recorded with the CMS detector.

The coordinate system used in CMS has its origin in the center of the detector at the nominal interaction point. In Cartesian coordinates the x-axis points radially to the center of the LHC ring, the y-axis points upwards, and the z-axis points tangentially w. r. t. the beam line towards the Jura Mountains. In spherical coordinates the azimuth ϕ refers to the angle in the projection on the x-y-plane, with $\phi = 0 \Leftrightarrow y = 0$. Thus, θ refers to the angle w. r. t. the z-axis.

However, the most commonly used coordinate system is specific for a hadron collider: The exact energy is known for the colliding protons, but not for the colliding partons within the protons. Especially the momentum balance between the two partons is not known as well. To account for the missing knowledge about the z momentum component of the initial state of the interaction, coordinates with a certain invariance are widely used: As a measure for the momentum of a particle the transverse component $p_\mathrm{T} = \sqrt{p_x^2 + p_y^2}$ is used. Its direction is given by the azimuth ϕ and a quantity called pseudorapidity $\eta = -\ln \tan \theta/2$. As indicated by the name, the pseudorapidity is related to the rapidity known from special relativity with the main difference that the pseudorapidity depends only on the angle θ, but not on the energy of the particle. In case of massless particles or in the limit $E \gg m$, the pseudorapidity converges with the rapidity. The decay products of hard interactions are more or less evenly distributed in pseudorapidity, and differences in pseudorapidity are invariant under a Lorentz boost in z direction.

In the following the onion-like structure of the detector is described starting from the interaction point in the center.

CMS DETECTOR

Total weight   : 14,000 tonnes
Overall diameter : 15.0 m
Overall length   : 28.7 m
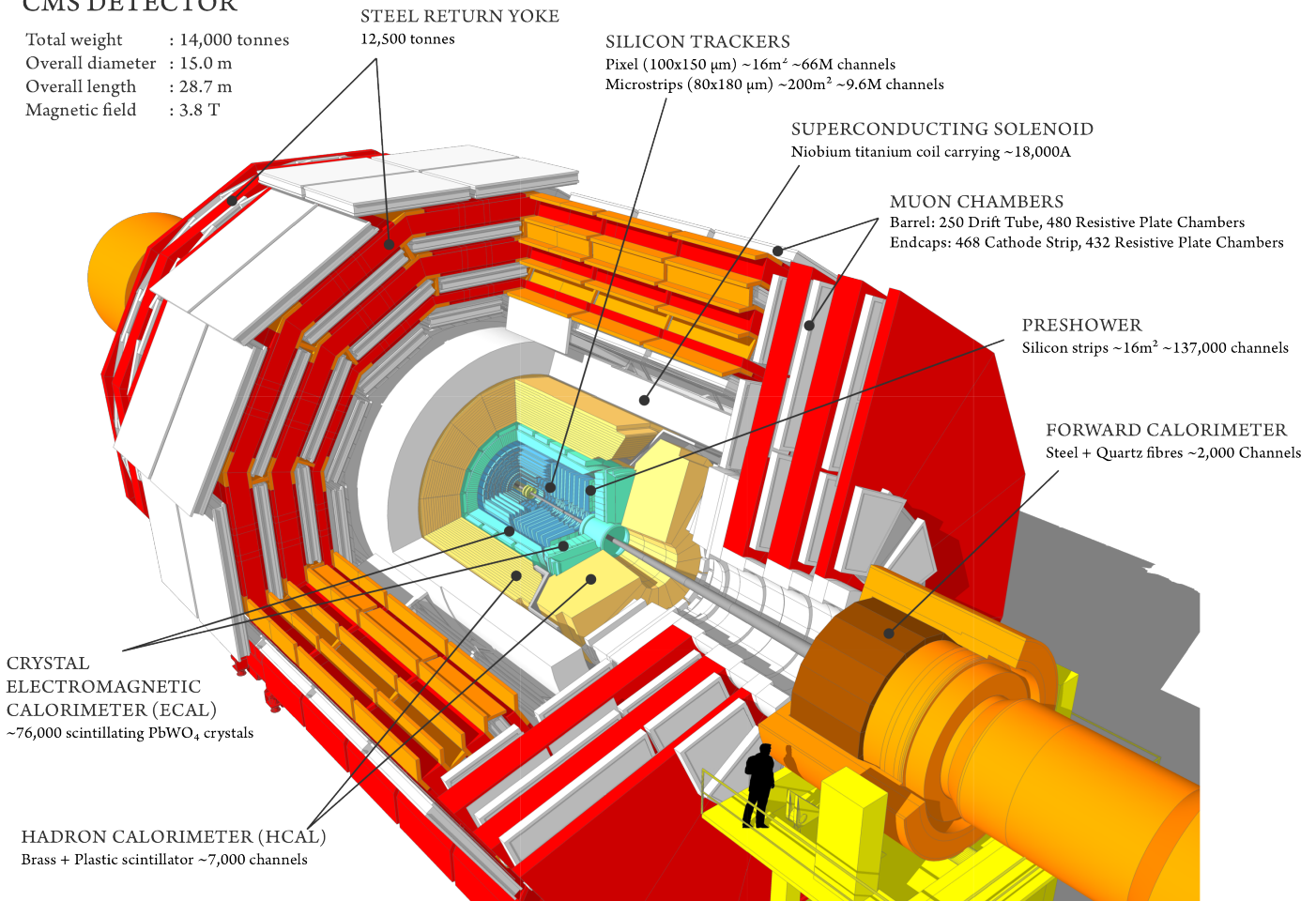Magnetic field   : 3.8 T

STEEL RETURN YOKE
12,500 tonnes

SILICON TRACKERS
Pixel (100x150 μm) ~16m² ~66M channels
Microstrips (80x180 μm) ~200m² ~9.6M channels

SUPERCONDUCTING SOLENOID
Niobium titanium coil carrying ~18,000A

MUON CHAMBERS
Barrel: 250 Drift Tube, 480 Resistive Plate Chambers
Endcaps: 468 Cathode Strip, 432 Resistive Plate Chambers

PRESHOWER
Silicon strips ~16m² ~137,000 channels

FORWARD CALORIMETER
Steel + Quartz fibres ~2,000 Channels

CRYSTAL
ELECTROMAGNETIC
CALORIMETER (ECAL)
~76,000 scintillating PbWO₄ crystals

HADRON CALORIMETER (HCAL)
Brass + Plastic scintillator ~7,000 channels

Figure 3.3.: Schematic view of the CMS detector. The onion-like structure starts close to the interaction point with the tracker, enclosed by the electromagnetic and hadronic calorimeters, enclosed by the super-conducting solenoid magnet. The outermost part consists of alternate layers of muon detectors and iron plates that act as absorbers and as return yoke for the magnetic field [45].

3.2.1. The Tracking System

The innermost part of the detector is dedicated to measure the momenta of charged particles. The all-silicon tracker is composed of a pixel detector enclosed by a silicon strip detector. The radius of the whole cylinder-shaped tracker is about 110 cm, the length is approximately 540 cm [46]. Originally a three-layered tracker system was envisaged for application in CMS: A silicon pixel detector, a silicon strip detector, and a micro strip gas chamber tracker (MSGC) [47]. Due to doubts in the robustness of the MSGCs and increased availability of silicon strip sensors, the plan was changed towards an all-silicon tracker [48].

The Pixel Tracker

The main challenge of the pixel tracker, as the detector that is closest to the interaction region, is to measure the origins of tracks with high precision. There are several areas where such a
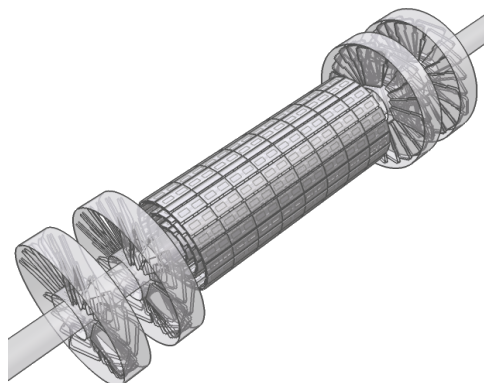
Figure 3.4.: A drawing of the pixel detector with three cylindric layers in the barrel and two windmill-structured endcaps on each side [45].

measurement is crucial, such as b tagging, separating prompt electrons from converted photons, and handling pile-up events by reconstructing distinct vertices. In LHC environments with high luminosities and particle densities this requires a high resolution and a first measurement of the track as close as possible to the interaction region. At the same time radiation hardness of both the sensors and the front-end readout electronics is required.

The pixel detector consists of a barrel part of three concentric cylindric layers and two endcap disks on each side. The barrel cylinders are 53 cm long and have radii of 4.4 cm, 7.3 cm, and 10.2 cm. The endcaps are rings with an inner radius of 6 cm and an outer radius of 15 cm, their position along the beam axis is at ± 34.5 cm and ± 46.5 cm (measured from the center of the detector).

The barrel consists of 768 pixel modules in total, the endcaps of 672 modules, each pixel has a surface of $100 \times 150\,\mu\mathrm{m}^2$. The blades carrying the pixel modules in the endcaps are arranged in a windmill-like structure as illustrated in Fig. 3.4.

Due to the close distance to the interaction region, the pixel tracker is exposed to the highest particle flux in the detector of about 10^7/s at $r = 10$ cm. The expected radiation dose under design conditions for an integrated luminosity of $500\,\mathrm{fb}^{-1}$ was calculated to 840 kGy at $r = 4$ cm and 190 kGy at $r = 11$ cm. An efficient cooling reduces the radiation damages to the material.

The pixel tracker is planned to be replaced during the long LHC shutdown in 2017 in order to be prepared for increased luminosities ($2 \times 10^{34}\,\mathrm{cm}^{-2}\mathrm{s}^{-1}$) [49]. Then, the innermost barrel layer will be even closer to the beam axis and there will be a fourth layer in the barrel and a third disk on each side. Also cooling and readout will be further improved.

The Silicon Strip Tracker

Figure 3.5 shows the layout of the tracker. The pixel tracker in the very central detector region is enclosed by the silicon strip tracker, which consists of several subsystems itself: Two cylindric barrels, the tracker inner barrel (TIB) and the tracker outer barrel (TOB), and two endcaps on each side, the tracker inner disks (TID) and the tracker endcap (TEC). The TIB is 130 cm long, the TOB 220 cm. The first TEC disks have a distance of 120 cm from the detector center ($z = \pm 120$ cm), the outer most disks are at $z = \pm 280$ cm. The gap between the TIB and the TEC is filled with the TID. The whole silicon strip tracker comprises 15 400 modules, recording
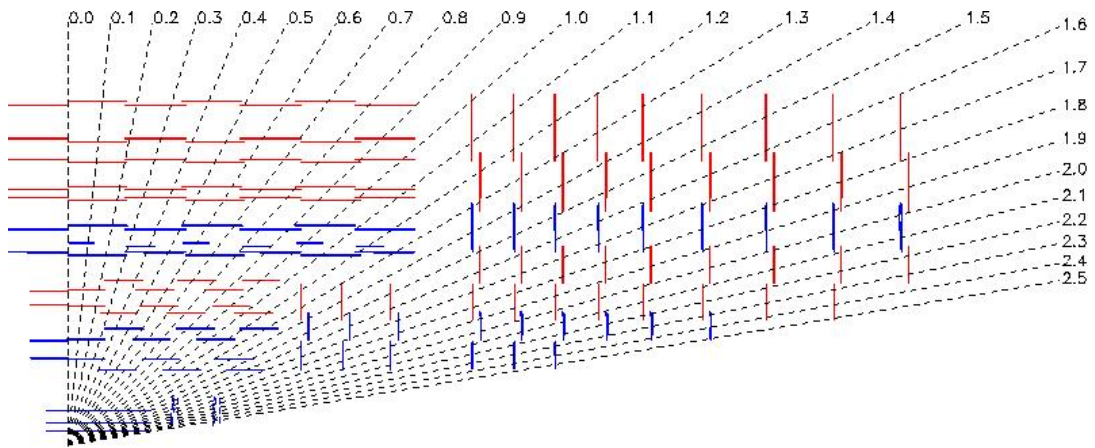
Figure 3.5.: Elevation of a quarter of the CMS tracker. The interaction point is at the bottom left, the beam axis goes horizontally. The dashed lines indicate different values for the pseudorapidity η. Closest to the interaction point the three layers of the pixel barrel are drawn as horizontal lines. The vertical lines next to them represent the pixel endcaps. The next parts are the tracker inner barrel (TIB) and tracker inner disks (TID) followed by the tracker outer barrel (TOB) and tracker endcaps (TEC) [46].

tracks at an operation temperature of $-20\,°C$.

The TIB consists of four layers of silicon sensors, of which the inner two are made of so-called stereo modules providing a two dimensional measurement in ϕ and in z. The sensors in the TIB have a thickness of $320\,\mu m$. Since the radiation level decreases with the radius a thickness of $500\,\mu m$ is sufficient in the TOB. Additionally the strip pitches increase with the radius. In the TIB it varies from $80\,\mu m$ to $120\,\mu m$, in the TOB from $120\,\mu m$ to $180\,\mu m$. The first two of the six TOB layers are also made of stereo modules.

The endcaps on each side comprise nine disks (TEC) plus three smaller disks called TID. Stereo modules are used for the first two rings of the TID and the first, second, and fifth ring of the TEC. The thiner $320\,\mu m$ sensors are used for the TID and the first three TEC disks. The outer TEC rings are made of $500\,\mu m$ sensors.

3.2.2. Calorimetry

One special feature of the CMS detector is that the whole calorimetry takes place inside the solenoid (besides the HO, that acts as a tail catcher in the central η region). This strategy has both a big advantage and some disadvantage: The advantage is that the energy loss of the particles passing the material of the solenoid is avoided, the disadvantage is the spatial limitation for the calorimeters.

The basic idea of a calorimeter is to stop the particles in the detector material, in order to measure their energies. As typical for a particle detector, the CMS calorimeter consists of an inner detector responsible for measuring (mainly) electromagnetically interacting particles, and an outer detector measuring hadronically interacting particles. This order is due to the fact that for absorbing hadronically interacting particles very dense materials are necessary.
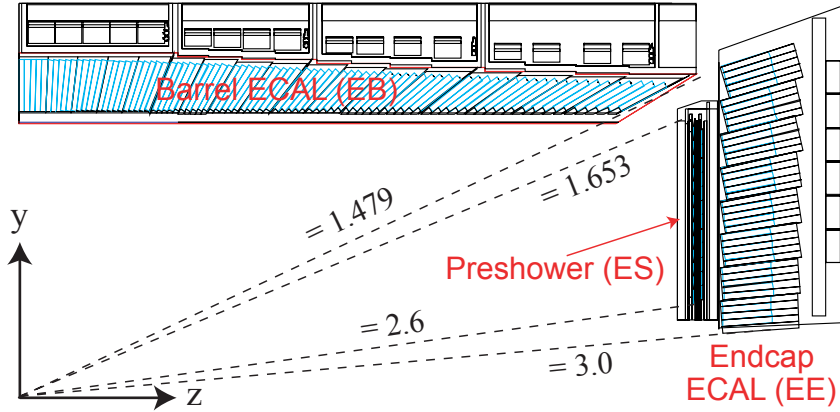
Figure 3.6.: A sketch of a quadrant of the CMS electromagnetic calorimeter. The quasi-projective orientation of the crystals is visible. The dashed lines indicate trajectories at the given values of the pseudorapidity η [46].

Electromagnetic Calorimeter

The task of the electromagnetic calorimeter (ECAL) is to measure the energy of electromagnetically interacting particles such as photons and electrons and to a smaller extent charged hadrons. The CMS ECAL uses the principle of scintillation. A crossing particle excites the material molecules, which then leads to light emission. The relevant numbers to quantify a material are the Molière radius, describing the transverse expansion of the shower, and the radiation length, quantifying the depth until the electron energy is reduced to $1/e$ of the original energy. Muons are of course also electromagnetically interacting particles, but since they are minimal ionizing in the relevant energy range, they deposit only a small fraction of their energy in the ECAL. An entire detector component is dedicated to measure muon momenta (cf. Section 3.2.4).

The scintillation material of the CMS ECAL is lead tungstate ($PbWO_4$), which combines several advantages: The very short radiation length ($X_0 = 0.89\,cm$) allows a compact design without energy losses, the small Molière radius of $2.2\,cm$ allows a good spatial resolution. Furthermore, the material is very resistant to radiation and allows a good time resolution (80% of the light is emitted within $25\,ns$, i. e. the minimal time of two bunch crossings).

The ECAL barrel consists of $61\,200$ crystals, the endcaps of 7324 crystals on each side. One barrel crystal is $230\,mm$ long and has a front face cross-section of about $22 \times 22\,mm^2$, slightly increasing up to $26 \times 26\,mm^2$ at the rear face. In η-ϕ parametrization this corresponds to a size of 0.0174×0.0174. The crystal shapes vary slightly with η. The endcap crystals have a larger cross-section ($28.62 \times 28.62\,mm^2$ to $30 \times 30\,mm^2$) and are a bit shorter ($220\,mm$).

The orientation of the crystals is *quasi-projective*. Each barrel crystal is tilted by $3°$ w. r. t. the line pointing to the nominal interaction point. The radiant geometry ensures that an electromagnetic shower is optimally captured within one crystal, while the tilt avoids particle trajectories going along the crack between two crystals. In the endcaps the same effect is achieved by arranging all crystals pointing to a focus $1.3\,m$ beyond the nominal interaction point.

In order to gain in discrimination power between photons and neutral pions in the forward region, a preshower detector (PS) is installed in the eta range of $1.653 < |\eta| < 2.6$. In Fig. 3.6 an overview of the ECAL components is depicted.
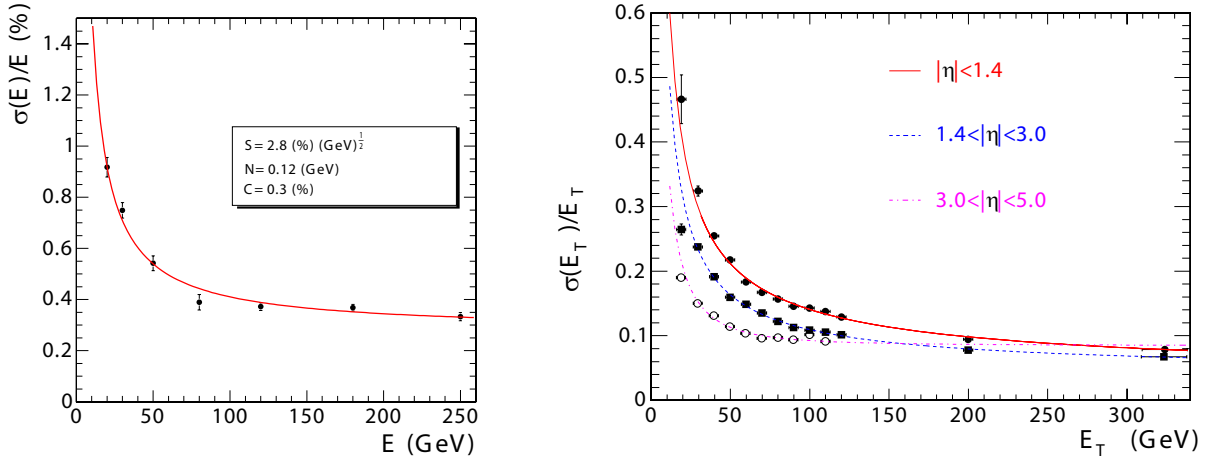
Figure 3.7.: Relative energy resolution of the calorimeter measurements. Left: ECAL resolution as a function of the electron energy in a test-beam measurement. The given numbers are the fit parameters referred to as stochastic (S), noise (N), and constant (C) term (see text and Eq. 3.3). Right: The transverse energy resolution for measured jet energies for barrel, endcap, and forward jets, which is mainly driven by measurements in the HCAL [50].

At the beginning of data taking in 2010 99.3% of all barrel channels and 98.94% of all endcap channels have been working [51]. The energy resolution was determined in test beam measurements with electrons. The left plot in Fig. 3.7 shows the result of this measurement and a fit of the function

$$\left(\frac{\sigma}{E}\right)^2 = \left(\frac{S}{\sqrt{E}}\right)^2 + \left(\frac{N}{E}\right)^2 + C^2, \tag{3.3}$$

where σ is the resolution, E is the energy of the electron, S is the stochastic term (determined to $2.8\%\sqrt{\mathrm{GeV}}$), N is the noise term ($0.12\,\mathrm{GeV}$), and C is the constant term (0.3%).

Hadronic Calorimeter

The ECAL energy measurement is complemented by the hadronic calorimeter (HCAL) determining the energies of hadrons. The HCAL measurements act as key ingredients for clustering jets and for determining the unmeasurable energy in the event. When the CMS detector was designed, it was one of the main challenges to construct a hadronic calorimeter featuring a sufficient depth (in terms of interaction lengths λ_I), but though small enough to fit between the ECAL and the solenoid. One consequence of this constraint is the decision for a tail catcher outside the magnet coil, called HCAL Outer (HO).

The other subcomponents of the HCAL are the barrel part (HB), the endcaps (HE), and the HCAL Forward (HF), as illustrated in Fig. 3.8. The HB covers an η region from -1.4 to $+1.4$, the HE covers $1.3 < |\eta| < 3.0$, the HF goes from $|\eta| = 3.0$ up to $|\eta| = 5.2$. The HO covers the central η regions from -1.26 to $+1.26$. The crack between the HB and the HE houses all cooling, power, readout etc. connections for the tracker and the ECAL.

The HCAL is a sampling calorimeter using brass as absorber material. Brass has a short interaction length and is not ferromagnetic, which is very important since it is installed inside
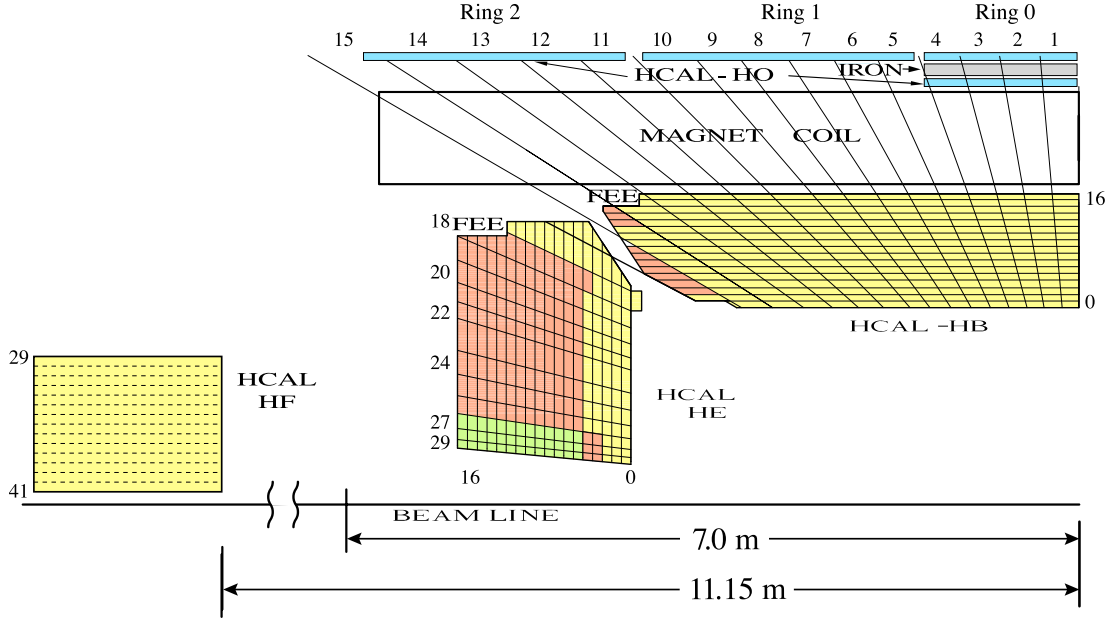
Figure 3.8.: A sketch of a quadrant of the CMS hadronic calorimeter, the interaction region is in the lower right corner. The barrel (HB), endcap (HE), and outer (HO) parts of the HCAL are sketched, as well as the forward calorimeter (HF) on the very left. The distance between the forward calorimeter and the other components is not drawn to the scale, between them the muon endcap is placed. The single calorimeter cells are stacked to *towers* in a projective geometry. The cells in most towers in the barrel are combined and have only one readout channel. Towers with cells of different colors have two or even three readout channels: Cells of one color are combined to one readout channel [52].

the solenoid. Plastic scintillators are used as active medium. Wavelength-shifting fibers are embedded for the readout. This technology allows a very compact design.

The barrel consists of 2304 towers with an η-ϕ segmentation of 0.087×0.087. The layer sequence going from inside to outside starts with a 5 mm thick scintillator plate, followed by 15 iterations of 5 cm brass and 3.7 mm scintillator. The depth of the HB varies between 5.82 interaction lengths for orthogonal particle crossing and $10.6\,\lambda_I$ for trajectories with $\eta = \pm 1.3$. The energy loss of hadrons in the ECAL adds $1.1\,\lambda_I$ to the total calorimeter depth.

In the endcaps the segmentation in ϕ is 5°, decreased to 10° for larger $|\eta|$, the η segmentation varies between 0.087 and 0.35. A longitudinal segmentation within the towers is implemented in the radiative harsh region close to the beam pipe to be prepared for scintillator degradation (see Fig. 3.8). When it will become necessary, specific corrections will be applied to the separate readout channels to restore the energy resolution.

The HO is the only calorimeter part of the CMS barrel that is outside of the magnet coil. The coil itself acts as an absorber with a θ dependent thickness of $1.4 \sin^{-1} \theta\,\lambda_I$. For geometrical reasons the smallest depth of the calorimeter is in the very central region. Therefore two HO layers are installed for $|\eta| < 0.35$ with a 19.5 cm iron absorber between them, and one layer in the remaining η range. The HO elements are mounted on the five rings of the muon system. In

combination with the HO the minimum calorimeter depth adds up to 11.8 interaction lengths (except for the transition region between the barrel and the endcap).

The forward calorimeter (HF) is exposed to a huge energy and particle flux, which leads to the decision to use quartz fibers as active medium. The Cherenkov light generated by charged shower particles is detected. The absorbers are made of steel. A longitudinal segmentation in the readout allows the early-showering electrons and photons to be distinguished from hadrons with a typically more evenly distributed shower.

Figure 3.7 shows on the right a performance plot of the HCAL in terms of the transverse energy resolution in jet measurements for different η regions corresponding to the different HCAL components.

3.2.3. The Solenoid

The heart and eponymous part of the CMS detector is the 6 m in diameter and 12.5 m long superconducting solenoid, designed to produce a magnetic field of 4 T. The four-layer winding is made of niobium-titanium. The return flux is channeled by a 10 000 tons iron yoke, segmented in five wheels and two endcaps, which are used as absorbers for the muon system.

In operation the solenoid produces a field of 3.8 T. The slightly lower value w. r. t. the maximum has little impact on physics measurements, but is appropriate as additional safety margin in the view of the envisioned lifetime of the magnet [53].

3.2.4. The Muon system

As implied by its name, the muon detector is of central importance for the CMS experiment. Three different types of detectors are used in CMS to measure muons: drift tube (DT) chambers in the central barrel region ($|\eta| < 1.2$), cathode strip chambers (CSC) in the endcaps ($0.9 > |\eta| > 2.4$), and resistive plate chambers (RPC) in barrel and endcaps ($|\eta| < 1.6$). The positions of the muon detectors are illustrated in Fig. 3.9.

DTs are chosen for the central part since the muon and background rates are small. Furthermore the magnetic field is channeled in the iron yoke and therefore small in the interstices where the DTs are placed. Another aspect favoring DTs is the cost issue considering the large surface that has to be covered. Between the yoke plates four DT *stations* are installed, the first three stations measure the track position in ϕ as well as in z, the fourth layer performs only the ϕ measurement.

In the endcaps both the muon and the background rate is higher and there is a larger and non-uniform magnetic field. In this environment CSCs are suitable, they are installed similar to the DTs in four stations between the plates of the return yoke.

Due to the emphasis on muon measurements in the CMS experiment, as a complementary system of muon detection the RPCs are installed. RPCs do not reach the spatial resolution of DTs and CSCs, but have a very good time resolution. Therefore this detector component is especially dedicated to muon triggering. Two layers are placed in each of the first two stations in the barrel, and one layer each in the third and fourth barrel station and in the first three endcap stations.

Not only the muon system is used for determining the muon momentum, but also the inner tracker (cf. Section 4.2.1). The redundancy leads to a high efficiency and accuracy in the identification and measurement of muons.

The performance of the muon detectors in proton-proton collisions is studied in Ref. 54.
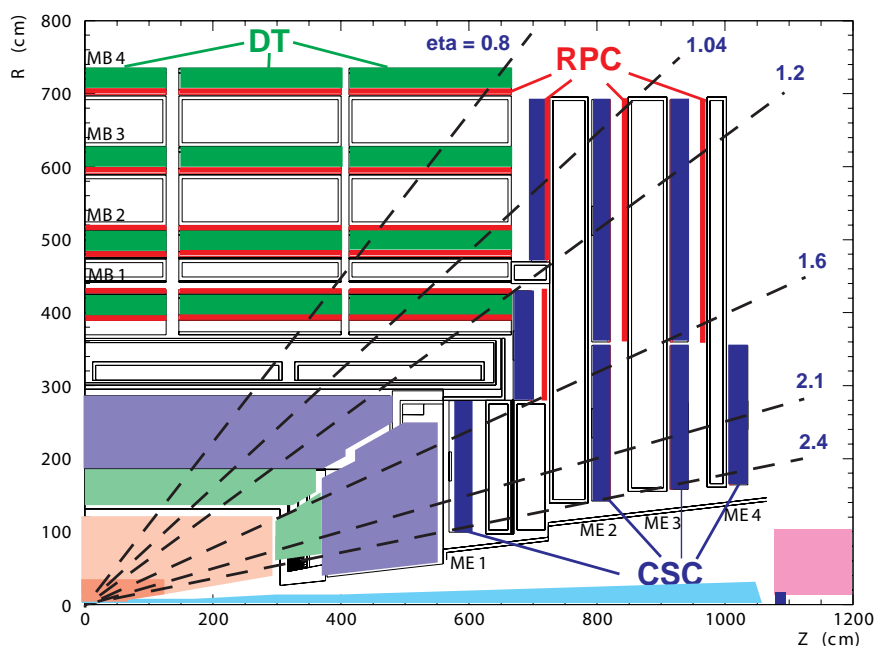
Figure 3.9.: The sketch shows a quadrant of the CMS detector with the muon detectors labeled. The shaded areas in the lower left corner show position and size of the other detector components, such as pixel and strip tracker, ECAL, and HCAL. The magenta square in the lower right corner represents the forward calorimeter. From the dashed lines the η ranges of the different components of the muon system can be read [46].

3.2.5. Triggering and Data Acquisition

The trigger system takes the decision whether an event is worth storing it or whether it can be rejected. The trigger and data acquisition in CMS is designed to handle an event rate of 40 MHz, which is the maximal bunch crossing rate at the LHC [55, 56]. When the system was developed, the maximal rate, at which events can be stored, was assumed to be about 100 Hz. In fact, in 2012 the rate of recorded and reconstructed events was 300 Hz to 350 Hz. Although the rate was already higher than intended, the limit in storing data was still not reached. The actual bottleneck is not storing but the reconstruction of the events. In this situation CMS decided for a *data parking* strategy [57]. With an additional rate of 300 Hz to 350 Hz events were recorded, awaiting for reconstruction when computing resources are available (i. e. most probable during the LHC shut down in 2013/2014).

But still, the event rate has to be drastically reduced from the bunch crossing rate to the rate that can be recorded. The trigger and data acquisition system of CMS consists of four parts: the detector electronics, the level-1 trigger, the readout network, and finally the high-level trigger (HLT).

The level-1 trigger is the first gate keeper designed to reduce the event rate from 40 MHz to 100 kHz. The main challenge is the time issue. Until the decision is made whether an event is stored or not, the event information has to be buffered. The longer the decision takes, the more events the buffer has to be able to hold. For the whole procedure – including the transit of the signals between the detector and the trigger logic – 3.2 μs are allocated. The level-1 trigger

decision is based on information from the calorimeters and from the muon system, including correlations between them. From that a rough version of objects such as photons, electrons, muons, and jets (*trigger primitives*), but also sums of E_T and $E_\mathrm{T}^\mathrm{miss}$ are formed, and checked if given thresholds are surpassed. Due to the strict time constraint the trigger logic is manifested in custom hardware processors.

The HLT software runs on a computing farm of about one thousand commercial processors. An event that passed the level-1 trigger is transferred to one of the processors, where the whole event information and a more sophisticated object reconstruction give rise to the final decision if an event might be interesting for further analysis. Within the HLT procedure sub-levels can be differentiated. In order to avoid wasting computing time, the event objects are reconstructed sequentially. As soon as the reconstructed information is sufficient for taking the decision, the reconstruction stops and the event is either stored or discarded.

The Data Acquisition (DAQ) system runs an *event builder* that combines all detector information to form events. With the output rate of the level-1 trigger (100 kHz) the signals of almost 500 sources and 10^8 electronic channels are gathered and presented to the HLT system. Accepted events are stored at a local storage with a capacity of 300 TB, from where the data is transferred to the Tier-0 computing center at the CERN main site [58]. At the Tier-0 the full reconstruction takes place and the data is permanently stored. A copy of the data is transferred to each of the worldwide 7 Tier-1 centers, stored there, and further distributed to the Tier-2 centers, where the main part of the actual physics analyses is performed.

3.2.6. Data Quality Monitoring

The CMS detector is a very complex machine, which can be affected by many kinds of problems and malfunctions. To ensure that only data that was taken under "good detector conditions" and is well reconstructed, is used for physics analyses and to spot detector or software problems as early as possible, a two-level data quality monitoring system (DQM) is established in CMS [59].

The first monitoring takes place in parallel to the data taking (*online DQM*), the second quality check is performed after the full event reconstruction (*offline DQM*). Both steps are done by trained CMS members in a shift system. The online shifter works in the CMS control room at *Point 5* (at the surface above the CMS cavern), the offline shifts are done in three CMS centers: at CERN, at Fermilab (near Chicago, USA), and at DESY (in Hamburg, Germany), making use of the time shift between Europe and the USA.

A web based graphical user interface is used to examine several control plots of each subdetector (at offline DQM reconstructed objects are monitored as well). Based on this information the shifter decides whether the respective run should enter the physics analyses or not; or if there is even the need to involve an expert to solve a severe problem. The information about the condition of each sub-detector is recorded for each run in a database (*Run Registry*).

3.2.7. The Scientific Program and Results Achieved so far

A broad scientific program is the driving force for the design and the operation of the CMS detector [60]. The indubitable first objective was an understanding of the nature of the electroweak symmetry breaking. The LHC was built to probe the energy region where the question was assumed to be answered, if a Higgs boson exists or what other mechanism is responsible for the large masses of the gauge bosons.
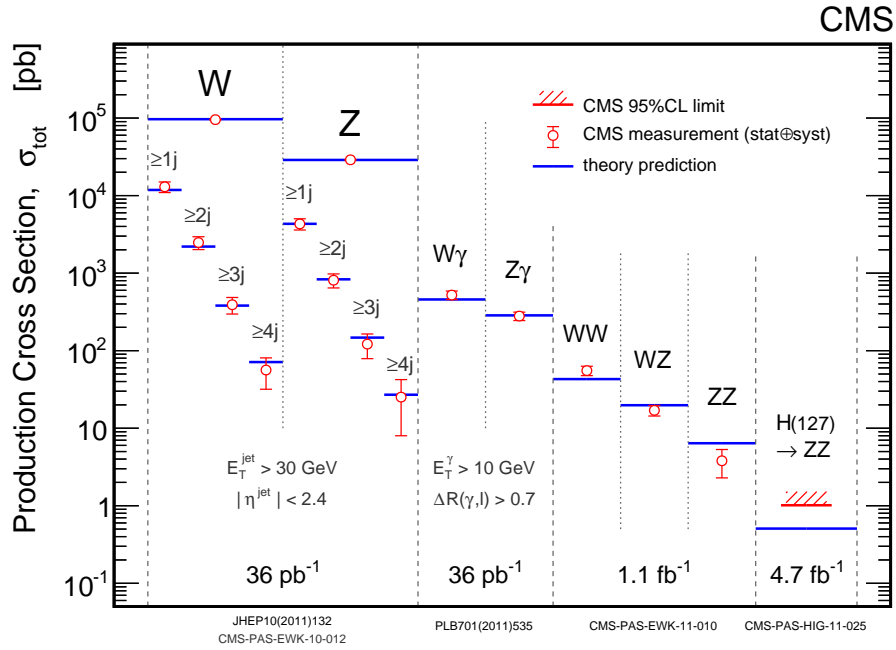
Figure 3.10.: Summary of cross sections of electroweak processes as measured by CMS compared to Standard Model predictions at 7 TeV [61–64]. The plot is available online [65].

Even if the particle zoo of the Standard Model was completed with a Higgs, there are good reasons to expect signatures of *physics beyond the Standard Model* (BSM physics) in the LHC collisions. And finally also known Standard Model particles and processes are an exciting field of research at the LHC.

In the detector design the emphasis on lepton and photon measurements is manifest: There is a large magnetic field and an excellent tracking system (both, the inner silicon detector and the muon chambers as outermost layers) for a precise momentum determination, and the outstanding electromagnetic calorimeter for energy measurement and particle identification.

Generally, the emphasis on the non-hadronic event content makes sense in an environment that is dominated by the hadronic background from QCD processes. In particular, the search for the Higgs boson seemed most promising in channels like

- $H \to \gamma\gamma$

- $H \to ZZ^* \to e^+e^-e^+e^-$ or $\mu^+\mu^-\mu^+\mu^-$

- $H \to WW^* \to e^+\nu\,e^-\bar{\nu}$ or $\mu^+\nu\,\mu^-\bar{\nu}$.

Rediscovery of the Standard Model

The Standard Model of particle physics is the basis of whatever is and will be measured at the LHC. Hence, the first and ongoing task of the CMS experiment is to measure Standard Model processes and compare the results with the expectations. Before new physics can be discovered, it has to be understood how already known processes behave in the new energy range.
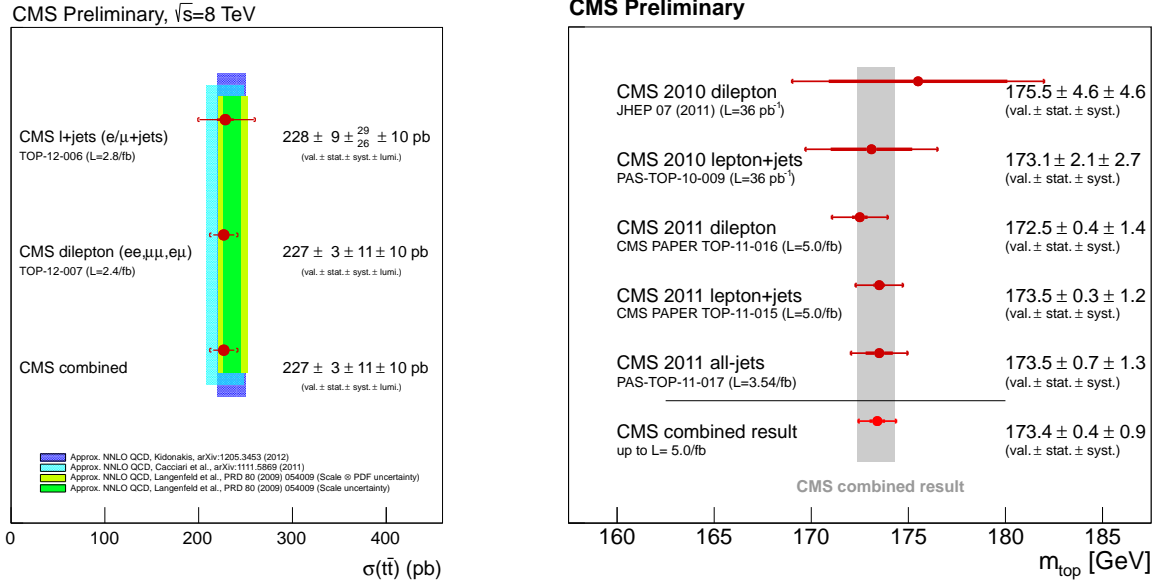
Figure 3.11.: Summary of CMS measurements in the top sector. Left: The $t\bar{t}$ cross section determined in the semi-leptonic [66] and di-leptonic [67] channel at 8 TeV in comparison to several theoretical predictions [68–70]. Right: Results of top mass measurements performed in several decay channels [71–75]. Both plots are available online [76].

Not just the physics is tested, but also the detector. Many Standard Model processes provide a unique opportunity to validate the understanding of the detector measurements. An example is the Z^0 boson. Events involving $Z^0 \rightarrow \ell^+\ell^-$ decays can be used to investigate the lepton reconstruction, since the mass of the Z^0 is very well known. If the Z^0 is produced in association with jets, the hadronic energy measurements can be studied, too.

Furthermore, Standard Model events play a significant role in searches for new processes as they occur as background events. The sensitivity for a potential discovery depends on the understanding of the background.

Figure 3.10 shows a summary of cross-section measurements at 7 TeV center-of-mass energy. The production rate of one or two gauge bosons, in the former case also in association with up to four jets, is compared to theoretical calculations. The cross sections agree very well through more than four orders of magnitude[1].

Since LHC is only the second collider (after Tevatron) that has enough energy to produce $t\bar{t}$ pairs, top physics plays naturally a crucial role at CMS. In Fig. 3.11 a summary of some of the measurements in the top sector is presented. Most top analyses concentrate on one specific channel defined by the decay of the tops, that can include a lepton ($t \rightarrow Wb \rightarrow \ell\nu b$) or only quarks ($t \rightarrow Wb \rightarrow q\bar{q}b$). Hence, three main channels can be defined: di-leptonic, semi-leptonic (or lepton + jets), and full-hadronic (or all-jets).

---

[1]At the time this plot was made, the Higgs-like boson was not yet discovered. Therefore only an upper limit on the Higgs cross section is stated.
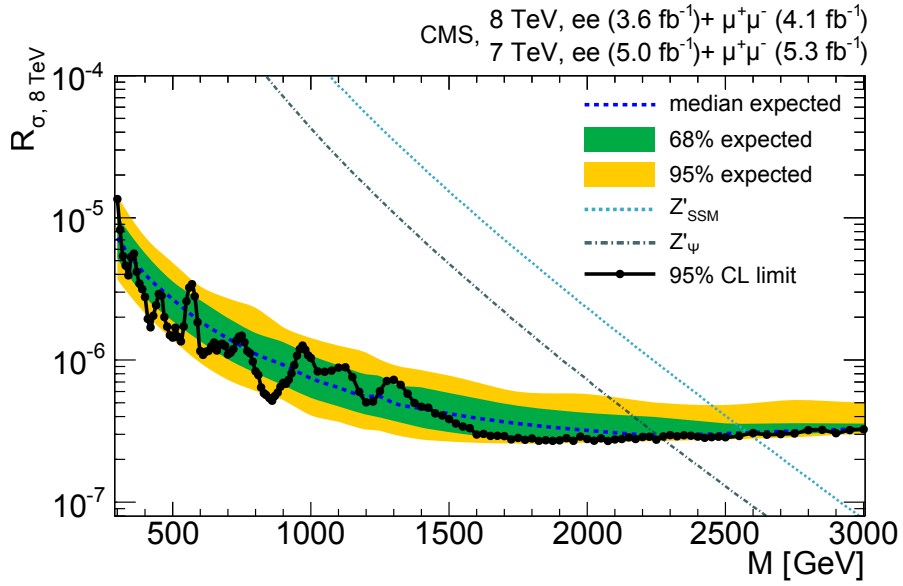
Figure 3.12.: Exclusion plot from a Z' search combining $7\,\mathrm{TeV}$ and $8\,\mathrm{TeV}$ data. R_σ is a measure for the cross section, its exact definition is given in the text. The black dots mark the upper limit on R_σ w.\,r.\,t. the mass of the hypothesized Z'. The expected R_σ for two different Z' models are shown as dotted and dashed-dotted lines. The highest mass that can be excluded is derived from the crossing point of these lines with the measured upper limit [77].

A Higgs-Like Boson

The main achievement of CMS so far is undoubtedly the discovery of a new particle [16]. In the combination of $7\,\mathrm{TeV}$ and $8\,\mathrm{TeV}$ data (each dataset comprises slightly more than $5\,\mathrm{fb}^{-1}$) an excess with a local significance of 5σ is found at a mass of around $125\,\mathrm{GeV}$. The discovery is discussed in the context of the Higgs mechanism in Section 2.1.3.

Searches for Supersymmetry and Other BSM Signatures

Up to now no signatures hinting at BSM processes have been found in the recorded data. Many analyses have been conducted searching for new particles that could help solving the shortcomings of the Standard Model.

In many studies supersymmetric models are tested and exclusion limits on the model parameter have been set. Several results are briefly summarized in Section 2.2.4.

Among the plenty of BSM studies besides Supersymmetry as an example the result from a Z' analysis is shown in Fig. 3.12. The upper limit (at 95% C.L.) is plotted in terms of relative cross section w.\,r.\,t. the Standard Model Z^0 cross section, taking also into account the specific branching fraction into e^+e^- and $\mu^+\mu^-$: $R_\sigma = (\sigma_{Z'} \cdot \mathrm{BF}_{Z' \to \ell\ell})/(\sigma_{Z^0} \cdot \mathrm{BF}_{Z^0 \to \ell\ell})$. The observed limit agrees very well with the Standard-Model-only expectation. Lower limits are set on the mass of the Z' issuing from two different models:

- Sequential Standard Model Z': $M(Z'_{\mathrm{SSM}}) > 2590\,\mathrm{GeV}$

- superstring-inspired Z': $M(Z'_\psi) > 2260\,\mathrm{GeV}$

All CMS Publications

The CMS results presented here are a personal and non-representative selection of the achievements of the collaboration. All published results from CMS can be found at a web page [78].

4. Object Reconstruction and Event Selection

In this chapter the physics objects that are used in this analysis are described as well as the event selection requirements. Section 4.1 introduces the particle-flow algorithm, in Section 4.2 the reconstruction of muons, electrons, jets, and missing transverse energy is described. The last part (Section 4.3) summarizes the event selection defining the dataset that is analyzed in this study.

4.1. Particle Flow

In the previous chapter the CMS detector has been briefly described. It is a very compleX system that can measure different properties of different particles with a very high resolution and accuracy. Particle flow is the attempt to derive the most benefit from this plenty of information [79].

In particular, due to the large silicon tracker and the high granularity of the electromagnetic calorimeter, the CMS detector is an appropriate machine to identify specific particles and not only abstract energy deposits. With a sophisticated combination of the measurements of all sub-detectors, the particle-flow algorithm is able to identify electrons, muons, photons, charged hadrons, and neutral hadrons. For obvious reasons the main challenge is to reconstruct the hadrons, whereas electron and especially muon identification is relatively easy.

The muon and electron reconstruction is discussed in Section 4.2. In this section the emphasis is placed on the reconstruction of the hadronic event content, which is crucial for jets. Although the jets themselves play an inferior role in this analysis, they are very important for calculating the transverse imbalance of the event. This imbalance is used as a measure for invisible particles. Like in many Supersymmetry searches, also in this analysis the missing transverse energy is a key variable to enrich the data with possible signal events, as described in the event selection section (4.3).

The particle-flow algorithm starts with so-called *elements*, which are the basic entities the detector can measure:

Tracks formed from hits in the silicon tracker   The charged particle trajectories in the tracker are reconstructed using an iterative tracking approach, which is designed to achieve a high efficiency and a low fake rate at the same time. In the first iteration very strict quality criteria are imposed for the hits to obtain a first set of tracks with almost no fake tracks. In the following iterations hits are removed from the found tracks and simultaneously the quality criteria are loosened. The removal of hits that are already assigned to tracks reduces the probability of finding accidentally tracks built from noise etc. ("fake tracks"). Consequently the efficiency increases due to the loosened criteria, but the fake rate can be kept very low.

Clusters of energy deposits in the calorimeters A three-step algorithm clusters energy deposits in the calorimeters. It is done separately in the sub-systems of the calorimeters (ECAL barrel, ECAL endcap, HCAL barrel, HCAL endcap, PS first layer, PS second layer, see Section 3.2.2). The first step is the seeding of clusters by calorimeter cells with local maxima in measured energy. In the second step *topological clusters* are formed by combing the cells within the cluster with neighboring cells that exceed a given energy threshold, starting with the seeds. Several topological clusters can "grow" together, but in the third step each topological cluster is split again in as many particle-flow clusters as it contains seeds. In an iterative process the energy is shared between the particle-flow clusters according to distance between the cell and the cluster center.

Tracks formed from hits in the muon system The muon tracks are reconstructed tracks in the muon detectors.

In the next step, these building blocks are connected by a link algorithm. According to the different kinds of elements there are different kinds of links: A track measured in the silicon tracker is extrapolated to the PS, the ECAL and the HCAL. If this extrapolation hits a calorimeter cluster this track is linked to that cluster. The bremsstrahlung emitted by an electron is also taken into account by extrapolating tangents to the track to the ECAL. All clusters found by this procedure are also linked to the track. Links between different calorimeter clusters are set in a similar way. If the position (measured in ϕ and η) of a cluster of a more granular calorimeter is within the envelope of a cluster in a less granular calorimeter the clusters are linked. The linking between tracks in the silicon tracker and the muon system is done by a global fit. If a given threshold on the χ^2 of the fit is not exceeded, the link is established (*global muon*).

The directly or indirectly linked elements form *blocks*, typically containing not more than three elements. All detector signals within one block are assumed to originate from one crossing particle. The final challenge of the particle-flow event reconstruction is the identification of these particles. For the purpose of physics analysis not the abstract detector measurements are relevant but the physics particles. This task is done by the actual particle-flow algorithm.

The philosophy of this algorithm is to start with the identification of the most unequivocal objects, and proceed with objects in the order of increasing ambiguity. Consequently, the first objects to identify are muons. For each global muon, the momentum obtained from the global fit trajectory is compared to the momentum calculated only from the track in the silicon tracker. If these two numbers agree within three standard deviations, the first particle-flow object, a *particle-flow muon* is found. The tracks identified as muon tracks are not available to be part of any other object. In addition, small energy deposits in the calorimeters along the trajectory can be assigned to each muon. These values are estimated to 3 GeV in the HCAL and 0.5 GeV in the ECAL from cosmic-ray measurements.

Electrons are identified as tracks pointing to an energy deposit in the ECAL, and by their tendency to emit Bremsstrahlung in the tracker material. In Section 4.2.2 the electron specifics in tracking (Gaussian-sum filter) and energy clustering (ECAL supercluster) is briefly described. Again, the detector signals identified to be caused by an electron, including the track, the main ECAL cluster and all ECAL clusters that originate from bremsstrahlung photons, are removed from the list of elements for further object identification.

The identification of the light leptons is relatively easy due to the excellent tracker, the

electromagnetic calorimeter, and the muon system of the CMS detector. The particle-flow algorithm is not necessary to identify and reconstruct them. The main purpose why these particles are included in the particle-flow procedure at all, is to remove their signals from the event. The detector signals that remain must come from photons and hadrons (note, that taus either decay leptonically $\tau \to \ell \nu_\ell \nu_\tau$ or hadronically $\tau \to q\bar{q}\nu_\tau$, leading either to a light lepton or to a hadronic signature).

Again, the procedure starts with the component that can be measured best by the detector, namely tracks. Since all tracks are now expected to be caused by charged hadrons, a special quality criterion is applied: Only those tracks are further considered that have a smaller uncertainty on p_T than the expected energy resolution in the calorimeter. On the one hand fake tracks with large uncertainties are rejected, on the other hand the redundancy in the energy measurement of charged hadrons is exploited: If the accuracy of the momentum measurement is surpassed by the calorimeter measurement, the latter one is used for that specific particle.

Calorimeter clusters undergo an energy calibration before hadrons and photons are reconstructed. For identifying charged hadrons, tracks linked to calorimeter clusters are considered. The energy measured in the calorimeters is compared to the momentum measured in the tracker. If more than one track is linked to a calorimeter cluster, the track momenta are summed. If instead one track can be linked to more than one cluster, it is only compared to the closest one.

If this comparison results in a excess of energy in the calorimeter, this additional energy is assumed to originate from neutral particles (photons or neutral hadrons). By this procedure it is possible to separate the energy from charged and neutral particles even if they are very close together. Charged hadrons are formed from the tracks matched to calorimeter deposits. an excess in energy in the ECAL is used to construct photons, additional energy in the HCAL gives rise to neutral hadrons. The clear priority of photons over neutral hadrons in the ECAL energy is justified by the observation that only 3% of the jet energy is deposited by neutral hadrons in the ECAL, whereas 25% of the jet energy is carried by photons.

After the here sketched procedure all different kinds of particles the CMS detector is able to measure are available. Thus it is possible to apply very specific corrections to the measurements and improve the overall understanding of an event. Especially the quality of tau, jet and $E_\mathrm{T}^\mathrm{miss}$ measurements benefit from that.

4.2. Physics Objects

In this section the reconstruction and identification of physics objects are described, such as muons, electrons, jets, and the missing transverse energy. Taus and photons are not considered since they play no role in the presented analysis.

4.2.1. Muons

Muons have a unique feature among the particles produced in the LHC collisions. They are detectable at the very outside of the detector. The reason is that they are long-lived enough not to decay inside the detector, additionally they are minimal ionizing at the relevant energy scales, i.e. they are not stopped in the detector material. Only a small fraction of the muon energy is deposited in the calorimeters, but since muons are charged, they leave a track in the tracker, and since they traverse the detector material without a significant energy loss, they are still measurable at the very outside where another tracker, the muon system, is placed.
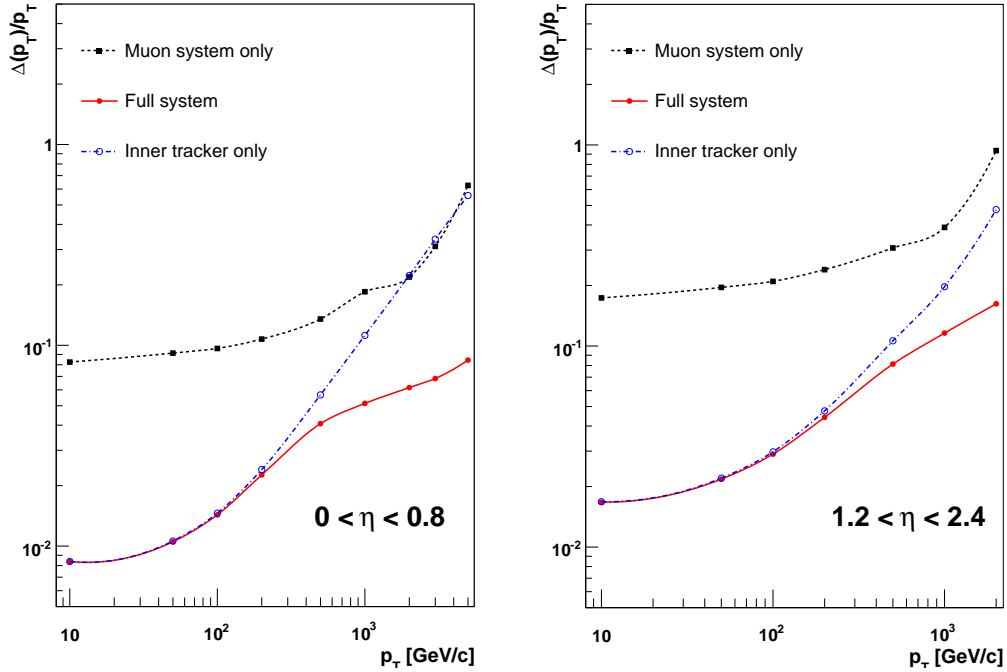
Figure 4.1.: Resolution of the muon momentum measurement for particles passing through all barrel layers (left) and passing through all endcap layers (right). Up to more than 100 GeV the tracker resolution surpasses the muon system by around one order of magnitude. A combination of both measurements (global fit) yields in the best performance for higher energies [50].

Two algorithms are implemented to reconstruct muons that leave hits both in the inner tracker and in the muon detectors [46,80]: the global muon reconstruction and the tracker muon reconstruction. The former method starts with hits in the muon chambers and extrapolates to the inner tracker, the latter one goes the opposite way, starting from inner tracks and extrapolating to the muon system. A third type of muons is the standalone muon, which consists only of a track in the muon detector. Standalone muons play an inferior role in physics analyses (so as in the here presented study), but are important for the trigger.

The track reconstruction in the muon detectors uses a Kalman-filter technique. It is seeded by track segments in the innermost chambers. Thereon an iterative procedure extrapolates the existing track to the next sensitive layer and updates the track parameters considering the measurement on this layer.

The tracker muon reconstruction starts from tracks in the inner detector, using the Kalman-filter tracking algorithm. Considering the magnetic field and the (small) energy loss of a muon in the calorimeters, the track is extrapolated to the muon detectors. If the extrapolation hits a muon segment, a tracker muon is found. The loose requirements for the track in the muon system guarantee a high efficiency for the reconstruction of low-energetic muons.

The global muon reconstruction starts from muon tracks and extrapolates them (accounting for energy loss and multiple scattering) to the silicon tracker. If a matching is possible, a global track is fitted including tracker and muon hits. This track is referred to *global muon track*.

Most muons that are produced in the proton-proton collision are reconstructed as both,

tracker and global muons. The resolution of momentum measurement is dominated by the precision of the silicon tracker. Only high-energetic particles ($p_{\mathrm{T}} \gtrsim 200\,\mathrm{GeV}$) can benefit from the global muon fit, as illustrated in Fig. 4.1.

In Section 4.3 the selection requirements for the muons used in this study are summarized and additional variables are introduced that are suitable to identify a well measured muon.

4.2.2. Electrons

The electron measurement in CMS is based on the outstanding performances of the silicon tracker and the electromagnetic calorimeter. The basic signature of an electron in the detector is a track in the inner tracker pointing to an energy cluster in the electromagnetic calorimeter.

The electron track is reconstructed with a Gaussian-sum filter algorithm (GSF), which accounts for energy loss due to bremsstrahlung [81]. The default tracking algorithm in CMS is the Kalman filtering approach. Here, the energy loss of a particle in the tracker material is assumed to be well modeled by a Gaussian probability density function. A generalization of the Kalman filter is the Gaussian-sum filter that allows a mixture of Gaussians to be used to model the energy loss.

The Bethe-Heitler model [82][1] describes the energy loss of electrons due to bremsstrahlung by the probability density function (PDF)

$$f(z) = \frac{(-\ln z)^{c-1}}{\Gamma(c)}, \quad \text{with} \quad c = t/\ln 2, \tag{4.1}$$

where z is the fraction of remaining energy and t is the path length in units of radiation lengths. In the GSF approach this highly non-Gaussian PDF can be approximated by a weighted sum of Gaussians, which then can be used in the track finding and fitting algorithm. The tracking algorithm itself is identical to the default Kalman filter based tracking: Starting from a seed of at least two pixel hits that are compatible with a given beam spot, iteratively the track is extrapolated to the next detector layer and updated with the measurement that is found on that layer. The only difference is the model that is used to describe the energy loss between two measurements.

The actual material thickness an electron passes before it reaches the ECAL depends on η. For $\eta = 0$ it is about 0.35 radiation lengths (X_0); for increasing $|\eta|$ the thickness increases until the maximum of $1.4\,X_0$ is reached in the transition region between the ECAL barrel and endcaps; for larger $|\eta|$ it decreases again ($0.8\,X_0$ for $|\eta| = 2.5$) [83]. Figure 4.2 shows the bremsstrahlung energy of electrons as fraction of the initial electron energy E^{e} for $E^{\mathrm{e}} = 10\,\mathrm{GeV}$, $E^{\mathrm{e}} = 30\,\mathrm{GeV}$, and $E^{\mathrm{e}} = 50\,\mathrm{GeV}$. Obviously, if only the energy of the electron was measured in the ECAL, the initial energy of the electron would be underestimated by a large factor.

Instead, the so-called super-clustering algorithm [84] tries to collect all energy deposits originating from bremsstrahlung photons and add them to the electron energy. In the magnetic field the electron trajectories are bent in ϕ direction, and the bremsstrahlung photons are emitted tangentially to the track. Hence, it is expected that the true electron energy is spread across a strip of ECAL deposits, extended in ϕ. In order to cluster the whole electron energy, at first ECAL energy clusters are formed (as described in the context of particle flow in Section 4.1). Hereon, superclusters are built as clusters of clusters in a very similar way. High energetic clusters act as seeds and are associated with nearby clusters to superclusters.

---

[1]qtd. in [81]
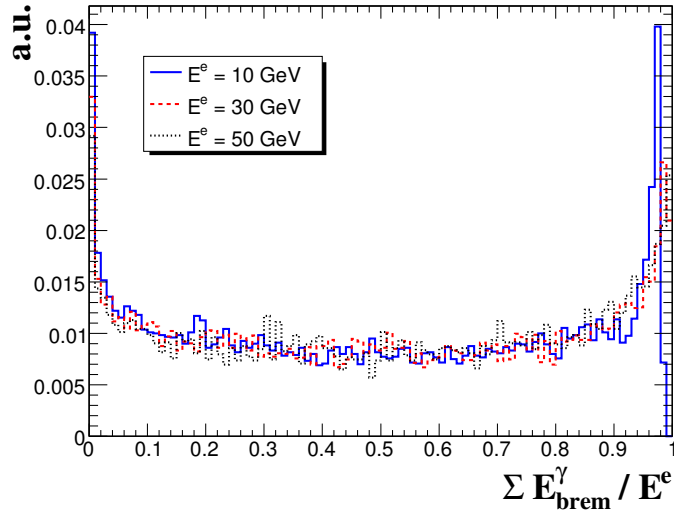
Figure 4.2.: Histogram of the fraction of energy an electron loses due to bremsstrahlung before it enters the ECAL crystals for three different initial electron energies [83].

The superclusters can also be used to drive the track finding algorithm. The actual trajectory of the particle can be estimated from the orientation and shape of the strip. The radiation projects the helix-like trajectory onto the calorimeter surface. With this information the number of possible seeds for electron tracks in the pixel detector can be drastically reduced.

Finally, electron candidates are formed from GSF tracks pointing to ECAL superclusters. A geometrical match as well as an agreement between the measured momentum and the measured energy is required in this step. Due to the equivalence of momentum and energy measurement the combination of both results in a significant improvement of the resolution as demonstrated in Fig. 4.3.

The electron selection for this analysis is described in Section 4.3, including further electron identification and quality variables.

4.2.3. Jets

Due to color confinement (cf. Section 2.1.1) quarks and gluons cannot be observed directly. They almost immediately fragment into bundles of colorless hadrons, which are reconstructed as jets within the detector. The challenge of jet reconstruction is to collect all energies that originate from the quark or the gluon, to preserve the direction of the parton, and to end up with the same number of jets as partons in the event. In this analysis jets are clustered with the anti-k_T algorithm using particle-flow objects as input.

Basically there are two approaches of clustering measured energies to jets:

- cone algorithms and

- sequential algorithms.

Cone algorithms assume all energies within a certain area to originate from the parton. The energies are summed up, and the axis of the cone is taken as jet direction. How the cones actually are drawn, is handled differently and it separates different algorithms. Widely used methods are iterative cone, midpoint cone, or SIS cone [85]. The midpoint algorithms can be
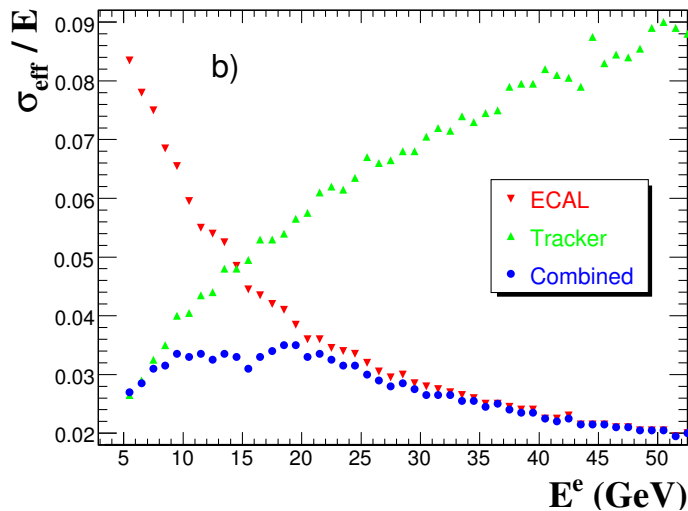
Figure 4.3.: The relative energy resolution w. r. t. the true electron energy as it is measured in the tracker (momentum) and in the ECAL. While the momentum measurement decreases in accuracy with the energy the calorimeter measurement increases [46].

seen as a subclass of the iterative cone algorithm. Both methods start in the first iteration with seeds for a first set of cones. Due to this procedure they suffer from not being infrared safe or collinear safe.

Infrared safety is a feature, that prevents the result of the jet algorithm from depending on very low energetic objects in the event. If a seeded algorithm has no threshold for objects that could act as a seed, even very low energetic radiation can seed a jet. The typical scenario to illustrate the problem of infrared unsafety contains two hard objects with an angular distance close to the cone size. The iterative cone algorithm would reconstruct two jets, where each of the hard objects would be in the center of one of the cones. If there was another soft particle right in the middle of the hard objects, the result would be only one jet, seeded by the additional particle. This is clearly an unwanted behavior, as the presence or absence of very low energetic objects in the event should have only a very small effect on the result of the algorithm.

On the other hand, if a threshold on the seed is required, the resulting jet collection could differ, whether two close objects (both below threshold) are handled as one object (above threshold). There is often an ambiguity if a certain signature in the detector is counted as two objects or one. In particular it could depend on the granularity of the detector. This issue is called collinear unsafety.

Several techniques have been developed to overcome these problems or at least reduce their impact on the final jet collection. E. g. the iterative cone algorithm (which was widely used during the first run period at CMS and also later on trigger level). Here the procedure starts with the hardest object, clustering nearby objects, looking for a stable cone. All clustered objects are removed and the next-hardest remaining object is taken to seed the next jet. This procedure avoids the infrared issue, but splitting one hard object into two collinear weaker objects changes the order and therefore potentially the result. It is clearly an improvement to the scenario described above, but still the collinear issue is not solved.

One approach to avoid both problems at the same time is the seedless infrared safe cone jet algorithm (SIS cone [85]). By avoiding seeds at all, the ambiguity in the seed properties is

avoided as well. Instead, all possible cones are taken into account by this method. An algorithm, which does that in an efficient way, is described in Ref. 85.

The second family of jet clustering algorithms sequentially combines the two closest objects into one (*proto-jet*). For these methods no seeds are necessary and not even a fix geometrical cone. What is needed instead is a definition of "close", i. e. a distance measure, and a truncation criterion, otherwise all objects in the event would always be combined into one jet. The distance measure between object i and object j can be defined by

$$d_{i,j} = \min\left(k_{\mathrm{T},i}^{2p}, k_{\mathrm{T},j}^{2p}\right) \frac{\Delta_{i,j}^2}{R^2}, \tag{4.2}$$

where k_{T} is the transverse momentum of the object, $\Delta_{i,j}^2 = (\Delta\phi)^2 + (\Delta y)^2$ is the angular distance, measured in the azimuth ϕ and the rapidity y. R is the distance parameter that takes over the role of the cone radius in the cone algorithms. There exist three different flavors of sequential clustering algorithm: the k_{T} [86–88], the Cambridge-Aachen, and the anti-k_{T} [89] algorithm. In this nomenclature the parameter p distinguishes between these flavors:

+1: k_{T}

0: Cambridge-Aachen

−1: anti-k_{T}

The second ingredient is the stop criterion, given by the distance to the beam line:

$$d_{i,B} = k_{\mathrm{T},i}^{2p} \tag{4.3}$$

All $d_{i,j}$ and all $d_{i,B}$ are calculated in each iteration. If the smallest value is a $d_{i,j}$, i and j are combined to one object by adding the Lorentz vectors, if it is a $d_{i,B}$ the object i is taken as a final jet and removed from the list. This procedure is continued until the list is empty.

The different flavors use different "momentum weightings" of the angular distance. While the Cambridge-Aachen algorithm is a pure geometrical one, a positive momentum weight is used in the k_{T} algorithm. The actual value of p is less important, as long as $p > 0$ the clustering algorithm behaves similar [89]. The idea is, that the probability of combining two hard objects is reduced, whereas a soft object is more likely to be clustered to both another soft object or a more energetic one. Since only $\min\left(k_{\mathrm{T},i}^{2p}, k_{\mathrm{T},j}^{2p}\right)$ appears in the distance definition in Eq. 4.2, only the energy of the weaker object counts.

The negative exponent used by the anti-k_{T} algorithm might be counterintuitive and needs a closer look. Again, the actual number -1 is less relevant, the behavior does not change drastically for all $p < 0$ [89]. First, note that the angular distance is not weighted by the inverse of the minimal k_{T}, but by the minimal of the inverse k_{T}, i. e. if i is harder than j $d_{i,j} = 1/k_{\mathrm{T},i}^2 \Delta_{i,j}^2/R^2$. The k_{T} algorithm prefers to cluster soft particles to harder ones, the anti-k_{T} algorithm takes the perspective of the hardest proto-jets and clusters from that point of view the surrounding softer objects. The k_{T} method tends to start with clustering soft objects, the anti-k_{T} method prefers harder objects. The anti-k_{T} algorithm turned out to be stable against soft radiation both in direction and shape of jets.

Besides the clustering algorithm there are several possibilities what objects to use as an input. At CMS there are mainly three types [91]:
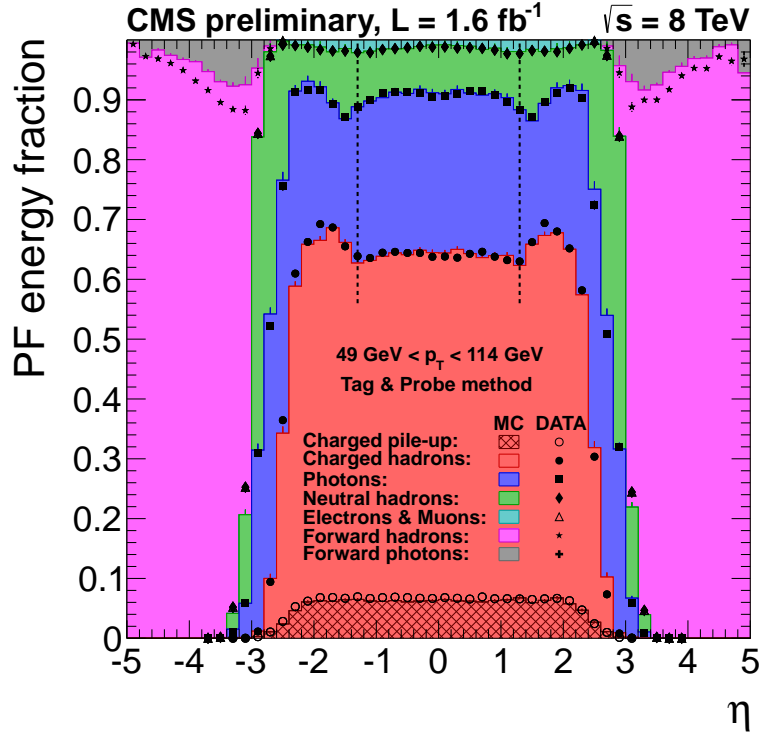
Figure 4.4.: Particle composition of particle-flow jets w.r.t. η in terms of the mean energy fraction they carry from the whole jet, as it was measured in the early 8 TeV data. Charged hadrons, electrons, muons, photons, and neutral hadrons, can only be identified in the coverage range of the tracker, muon system, electromagnetic and hadronic calorimeter, respectively. That explains the successive drop of these particles with increasing $|\eta|$. In the forward region ($|\eta| \gtrsim 3$), there is only the forward calorimeter left, which can distinguish between hadrons and electromagnetic interacting particles. [90].

Calorimeter jets: The energy deposits in the electromagnetic and the hadronic calorimeter are used for calorimeter jets. As described in Section 3.2.2, the CMS calorimeter is segmented in *towers*, each consisting of ECAL crystals and HCAL cells. The measured energy in the towers and their positions are the objects for the jet clustering algorithm.

Jet-Plus-Tracks: The jet-plus-track algorithm is an extension to pure calorimeter jets. The momenta of reconstructed tracks of charged particles are used to correct the energy measurement in the calorimeters. Also tracks that point to the jet close to the interaction region, but are bent in the magnetic field in such a way that they do not hit the calorimeters inside the jet cone, can be added to the jet. The procedure can change both the energy and the position of the jet w.r.t. the original calorimeter jet.

Particle-Flow jets: Particle-flow jets are the most sophisticated jets in CMS. As the name suggests, they are clustered from particle-flow objects. The particle-flow technique itself is described in Section 4.1. Figure 4.4 shows the particle composition of jets, as it was measured
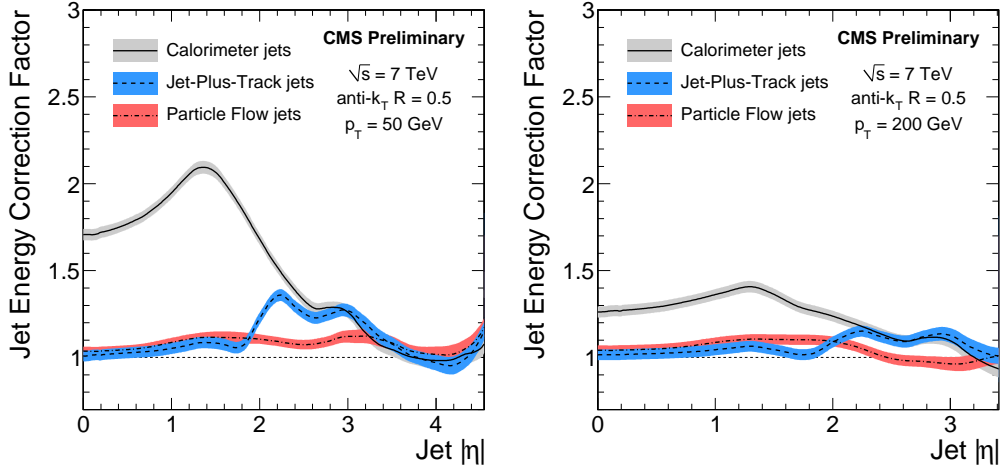
Figure 4.5.: Jet energy correction factors for $7\,\mathrm{TeV}$ data w. r. t. the pseudorapidity for $50\,\mathrm{GeV}$ jets (left) and $200\,\mathrm{GeV}$ jets (right). Compared to calorimeter jets the factors for particle-flow jets are rather constant both w. r. t. p_T and η [92].

in the early $8\,\mathrm{TeV}$ data recorded by CMS in terms of the energy fraction they carry.

In this analysis particle-flow jets are used and the clustering is done by the anti-k_T algorithm with a distance parameter $R = 0.5$. The selection requirements are discussed in Section 4.3.

Jet Energy Correction

The ideal jet has the same direction and the same energy as the initial quark or gluon. The clustering algorithm takes care of assigning the jet fragments to single jet objects. Additionally, energy corrections are necessary, mainly to compensate for non-uniformity and non-linearity in the detector response. Due to the corrections the measured energy is related to the energy of the true particle jet [92,93]. Most necessary are the corrections for calorimeter jets, because the energy deposits in the calorimeters are directly taken as input of the jet algorithm. Whereas the constituents of the particle-flow jets are already energy corrected (cf. Section 4.1) and the corrections on the jet energy are relatively small.

The jet energy corrections are applied as a factor C to the "raw" energy, i. e. to the components of the Lorentz vector P^μ:

$$P^\mu_{\text{corrected}} = C \cdot P^\mu_{\text{uncorrected}}, \tag{4.4}$$

where C depends on the raw p_T and the pseudorapidity of the jet, $C = C(p_\mathrm{T}, \eta)$. Figure 4.5 shows the correction factor including uncertainties w. r. t. η for two different values of p_T. The factor for calorimeter jets changes strongly with p_T and η, the particle-flow jets need to be corrected by a smaller amount, which is also almost independent from the jet kinematics.

The correction factor itself is composed of several factors, each compensating for a specific effect:

$$C = C_{\text{PU}}(p_\mathrm{T}^{\text{raw}}, \eta) \cdot C_{\text{rel}}(p_\mathrm{T}', \eta) \cdot C_{\text{abs}}(p_\mathrm{T}'') \cdot C_{\text{res}}(\eta), \tag{4.5}$$

where p_T' and p_T'' are the jet p_T with the previous corrections applied, i. e. $p_\mathrm{T}' = C_{\text{PU}} \cdot p_\mathrm{T}^{\text{raw}}$ and $p_\mathrm{T}'' = C_{\text{rel}} \cdot p_\mathrm{T}'$.
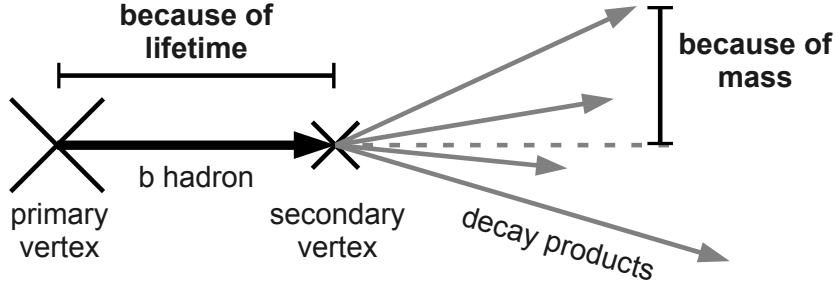
Figure 4.6.: Sketch of how b hadrons can cause secondary vertices: Because of the lifetime the b hadron decay is displaced w. r. t. the primary vertex of the event, and because of the mass the decay products have a non-zero momentum component perpendicular to the momentum of the b hadron.

$C_{\mathbf{PU}}$ removes the energy coming from pile-up interactions and instrumental noise.

$C_{\mathbf{rel}}$ corrects for non-uniformity of the detector response w. r. t. η. The correction is *relative* because different η regions are equalized without taking care of the absolute scale.

$C_{\mathbf{abs}}$ restores the absolute energy scale and corrects for the p_{T} dependent detector response.

$C_{\mathbf{res}}$ corrects for small differences between data and simulation. This factor is only applied in data.

The relative and the absolute correction factors are derived from Monte Carlo, but cross-checked in data using the event balance in di-jet, γ+jets, and $Z^0(\to \ell\ell)$+jets events. From these data-driven studies it emerged that there is a small difference in the jet energy response between data and simulation. In terms of minimizing the uncertainties the best procedure turned out to stick to the simulation-based corrections, but multiply another factor in data that compensates for the difference. This additional factor is the *residual* correction C_{res}.

Further corrections are available in CMS, e. g. flavor dependent correction factors, but in this analysis only the described default correction sequence is applied.

b-Jet Identification

Due to the hadronization of colored particles, the detector signatures of all quarks and gluons look very similar. Indeed, distinguishing between jets originating from an u, d, and s quark is close to impossible, and from gluons it is very hard. Only jets initiated by bottom quarks ("b jets") and (to a smaller extent) charm quarks can be identified with a satisfying reliability. Accepting a misidentification rate of e. g. 10%, an efficiency of 85% can be achieved, where the former is the probability that a jet that is identified as a b jet truly is a u, d, or s quark or gluon jet ("light jet") and the latter is the probability to correctly identify a b jet [94].

The differences between b and light jets that are utilized to identify b jets are the typically larger masses and the longer lifetimes of hadrons formed with b quarks. Several algorithms are used in CMS to identify b jets, exploiting observables like the impact parameters of tracks, the properties of secondary vertices, and the presence or absence of leptons. At one point of
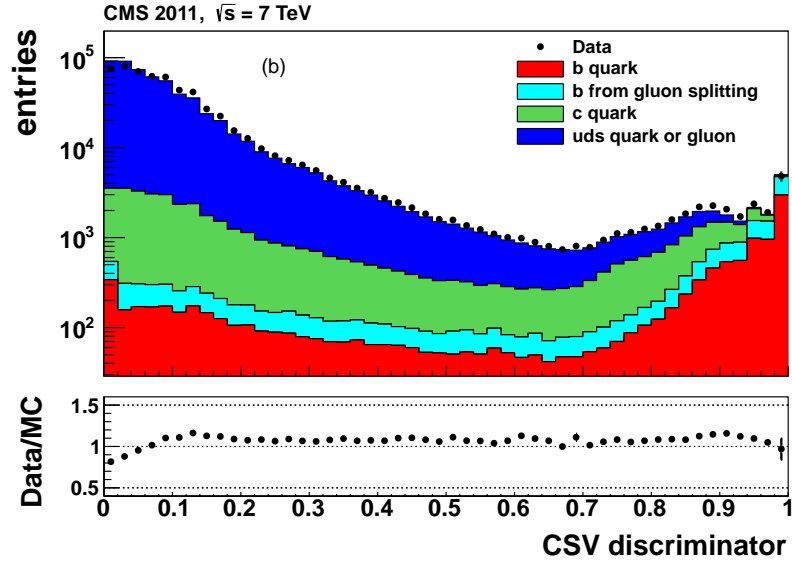
Figure 4.7.: Distribution of the discriminator produced by the combined secondary vertex algorithm. 7 TeV data comprising $2.3\,\text{fb}^{-1}$ is compared to MC simulation.

this analysis b jets play a role, and the *combined secondary vertex* (CSV) algorithm is used to identify them. Therefore the discussion here is limited to the CSV algorithm, a more complete picture is given in Ref. 94.

Both the lifetime and the mass of the b hadrons allow the reconstruction of a second vertex at the point where the b hadron decays. The lifetime causes the distance to the primary vertex, the mass gives the decay products (i. e. including the tracks) a significant momentum transverse to the hadron's momentum. Only due to the latter it is possible to differentiate these tracks from the tracks originating in the primary vertex, as sketched in Fig. 4.6.

The CSV algorithm combines several variables describing the secondary vertex to construct a discriminator variable. To increase the efficiency it is advisable to also include jets, for which no secondary vertex successfully can be fitted. For that purpose variables describing the impact parameters of tracks are additionally considered in the discriminator. Figure 4.7 displays the distribution of the discriminator in 7 TeV data in comparison to simulated events split into several cases whether the jet under consideration is a true b jet, a b jet from gluon splitting, a c jets, or a light jet.

CMS-wide there are three working points defined, i. e. values for the discriminator. If the discriminator for a certain jet exceeds this value, the jet is referred to as *b tagged* according to this working point. Here, the medium working point is used, which is defined to obtain a misidentification rate for light jets of 1%. The value of the discriminator where the cut has to be placed to achieve this performance is found to be 0.679.

4.2.4. Missing Transverse Energy

The transverse energy balance in an event is an important observable for most studies searching for supersymmetric particles. The basic assumption is that the initial state (i. e. the colliding partons) has no significant boost orthogonal to the beam axis. Parallel to the beam axis this is
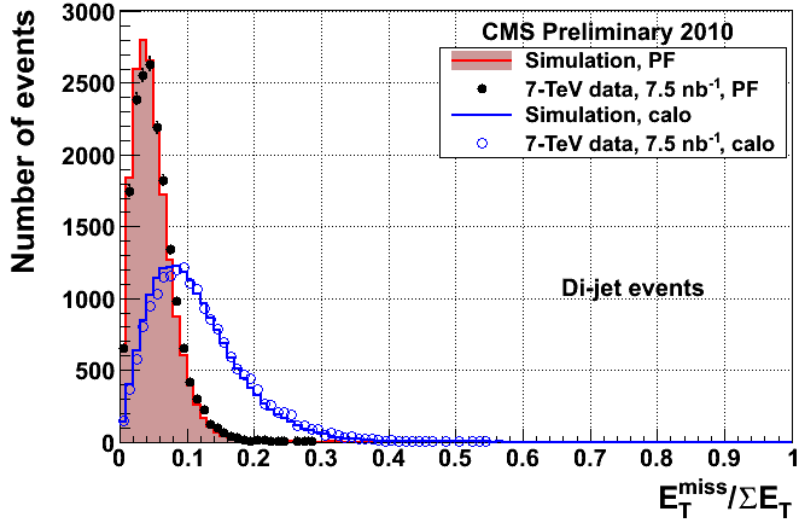
Figure 4.8.: Distribution of the relative E_T^{miss} in di-jet events based on calorimeter measurements and on particle-flow objects. Both histograms are compared to the simulated distributions. The di-jet events are expected to be dominated by QCD events with no unmeasurable particles. In this case the E_T^{miss} is expected to be caused by the detector resolution and by possible mismeasurements [95].

surely not true, since the momentum fraction one parton carries from its proton is in general different from the second parton. Knowing that, the vectorial sum of all momenta in the final state should also have no significant transverse component. Consequently, if there is a transverse component, one or more particles of the final state are either measured wrongly or not measured at all. The latter one is expected for neutrinos and possible new physics particles like the LSP in Supersymmetry (see 2.2.1). The momentum that is missing in the event to be transversely balanced is called missing transverse momentum $\vec{p}_T^{\,miss}$. Its magnitude is typically referred to as missing transverse energy E_T^{miss}.

$$\vec{p}_T^{\,miss} = - \sum_{\substack{\text{all} \\ \text{objects}}} \vec{p}_T \tag{4.6}$$

$$E_T^{miss} = \left| \vec{p}_T^{\,miss} \right| \tag{4.7}$$

There are several experimental possibilities which objects to take in order to calculate E_T^{miss}. Similar to the jets, in CMS basically three different E_T^{miss} flavors are realized:

Calo-E_T^{miss}: The energy measured in the calorimeter towers and their geometrical position act as input of the E_T^{miss} calculation.

TC-E_T^{miss}: The calorimeter measurements are corrected using information from the tracker. The additional information improves the E_T^{miss} resolution.
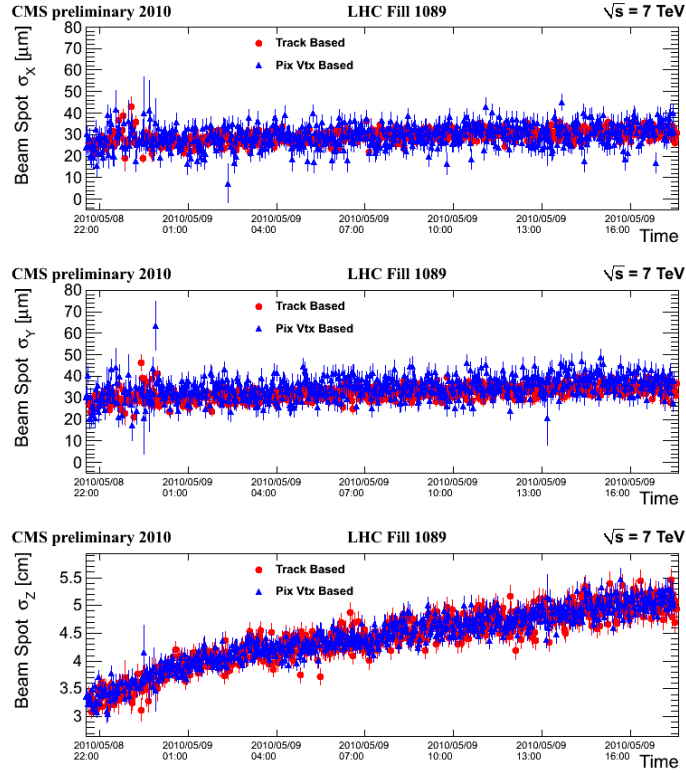
Figure 4.9.: The width of the beam in the CMS interaction region in x, y, and z and the evolution during one LHC fill of about 20 hours in 2010. While the transverse width (σ_x and σ_y) increases only very little, the longitudinal width (σ_z) gets significantly larger. Two methods are used for the measurements: One is based on vertex determinations using tracks, for the other method only measurements in the pixel detector are used [96].

PF-$E_{\mathrm{T}}^{\mathrm{miss}}$: The event imbalance is calculated from particle-flow objects. Using the particle-flow algorithm the most benefit is derived from all measurements of the CMS detector.

In this study the PF-$E_{\mathrm{T}}^{\mathrm{miss}}$ is used. Although it is supposed to be the closest possible approach to the true transverse energy of the unmeasured particles, also this observable is very sensitive to many kinds of mismeasurements.

In Fig. 4.8 the PF-$E_{\mathrm{T}}^{\mathrm{miss}}$ is compared to the calorimeter $E_{\mathrm{T}}^{\mathrm{miss}}$ in di-jet events taken during the very first 7 TeV runs. The di-jet event sample is completely dominated by QCD interactions. Since all strongly interacting particles can be measured by the detector, $E_{\mathrm{T}}^{\mathrm{miss}}$ should be zero. Due to the finite resolution of every detector measurement and possible mismeasurements, a non-zero $E_{\mathrm{T}}^{\mathrm{miss}}$ is observed. The plot shows the distribution of the $E_{\mathrm{T}}^{\mathrm{miss}}$ relative to the sum of all energies in the event. This observable accounts for the fact that the absolute energy resolution increases with energy. The comparison is an impressing demonstration of the improvement gained due to the particle-flow algorithm.
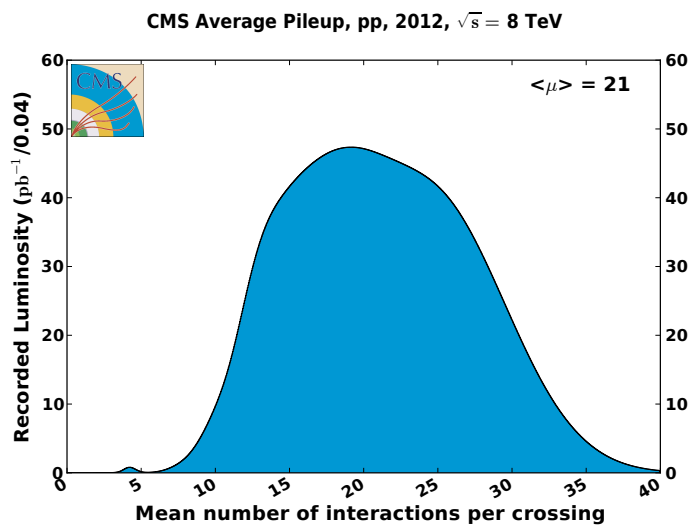
Figure 4.10.: The recorded luminosity of data w. r. t. the mean number of pile-up interactions per bunch crossing in 2012. From a constant luminosity the number of interactions is expected to be Poisson distributed. Since the luminosity changed during the year, the result is accumulation of several Poisson distributions [97].

4.2.5. Vertices and Pile-up

The – literally – central object of every event in CMS is the vertex, the spot where the parton-parton interaction takes place. The transverse position of the vertex is well constrained due to the small transverse bunch size in the interaction region (several 10 μm). Whereas the longitudinal extension of the interaction region is quite large due to the lengths of the bunches (a few cm). To reduce this area, the beams cross with a certain angle. At CMS each beam enters the detector with an angle of 150 μrad w. r. t. the z axis. But still, as shown in Fig. 4.9 the size of the luminous region is transversely very narrow, but longitudinally a few centimeter extended.

The strong transverse focusing together with the long way the bunches traverse each other, lead to an effect called pile-up. On average in every bunch crossing not only two protons collide but 10s of them. It is a sacrifice that has to be made in order to increase the probability of interactions where something interesting happens. This is directly correlated to the instantaneous luminosity. Figure 4.10 shows the distribution of interactions per bunch crossing in terms of the recorded luminosity in 2012. During the year several beam parameters were changed to increase the luminosity, the distribution can be understood as a sum of Poisson distributions, where each distribution represents a certain luminosity with an integral that corresponds to the integrated luminosity that was taken under these conditions.

Each vertex that is caused by a proton-proton interaction is called primary vertex. A secondary vertex – as it is discussed in the context of b tagging in Section 4.2.3 – is caused by the decay of a particle, which is displaced from the primary vertex where it was produced. In that terminology there are ideally as many primary vertices as proton-proton interactions per bunch crossing, but only very few of them have an associated secondary vertex or even more of them.

The reconstruction of the primary vertex starts with a set of selected tracks [96]. They have

to fulfill several quality criteria to make sure that they originate directly in a p-p collision and are well reconstructed. These tracks are clustered based on the z position of the closest approach to the beam axis. A cluster is handled as vertex candidate if it is separated in z by at least 1 cm from the next closest candidate. Hereon all vertices containing at least two tracks undergo the fitting procedure.

In CMS an adaptive vertex fitter [98] is preferred to a Kalman filter because of the higher robustness against outliers [99]. Every track is weighted according to its distance to the vertex, and its influence on the position of the vertex is relative to this weight. Since the vertex position changes with the weights, in an iterative approach the final vertex coordinates are found. From the final track weights w a number of degrees of freedom is defined that is used to select reliable vertices:

$$N_{\text{dof}} = 2 \sum_{i=1}^{\# \text{ tracks}} w_i - 3. \tag{4.8}$$

It is a measure for the number of tracks that are in good agreement with the vertex. In this study – like in most CMS analyses – at least one vertex in an event is required fulfilling:

$$N_{\text{dof}} > 4 \tag{4.9}$$

$$\Delta z < 24\,\text{cm} \quad \text{w.r.t. nominal interaction point} \tag{4.10}$$

$$\Delta \rho < 2\,\text{cm} \quad \text{w.r.t. nominal interaction point, with } \rho = \sqrt{x^2 + y^2}. \tag{4.11}$$

4.3. Event and Object Selection

In the previous section the reconstruction of all event objects that are relevant for this study are described. Here, the selection based on this reconstruction is discussed. Two main ideas drive the selection requirements. First, they should make sure that only those objects and events are further considered where a reliable reconstruction were possible and that are not affected by an error or malfunction of the detector or the reconstruction algorithms. Secondly, the selection should reject events with Standard Model processes ("background") while keeping events that could include supersymmetric partner particles ("signal").

The signal that is searched for contains at least two muons or two electrons of opposite charge. Furthermore, a certain amount of $E_{\text{T}}^{\text{miss}}$ is expected in addition to some hadronic activity (measured in terms of jets and H_{T}).

In Chapter 5 it is shown that this analysis aims for a prediction of the main background, formed from events where a $t\bar{t}$ pair decays into two leptons and jets. Other background processes are Z^0 production associated with jets or di-boson events such as Z^0Z^0, $Z^0W^{\pm}$, and $W^{\pm}W^{\mp}$. Especially the former has a large cross section and could fake a signal as demonstrated in Section 5.3.3. Special emphasis is therefore put on the rejection of these events. The di-boson events are more likely to pass the selection since they might contain real $E_{\text{T}}^{\text{miss}}$ due to $Z^0 \to \nu\nu$ or $W^{\pm} \to \ell\nu$ decays.

4.3.1. Lepton Definition

The leptons are the main object in the presented analysis. Only electrons and muons will be considered and referred to as leptons. The reconstruction of taus is difficult and much less reliable due to their very short lifetime. Nevertheless, events with taus might survive the event

selection if the taus decay leptonically ($\tau^- \to e^- \bar{\nu}_e \nu_\tau$ or $\tau^- \to \mu^- \bar{\nu}_\mu \nu_\tau$ or τ^+ accordingly) and the light leptons pass the acceptance and quality cuts. Another wording convention concerns particles and anti-particles. In cases with no need to distinguish them, if "leptons" is said also anti-leptons are meant. In the same way "electrons" include positrons, "muons" include anti-muons, "b quarks" include $\bar{b}$ quarks, etc.

Similar to the event selection in general, also the purpose of the lepton definition is twofold: First, the selection acts as a second-layer identification. It has to be made sure, that only real leptons survive the selection, but also leptons within jets or from heavy flavor decays should not be considered. Secondly, for the background prediction the full kinematic properties of the leptons are exploited (see Chapter 5). Therefore they have to be measured reliably.

Muons

The muons in this analysis must be reconstructed as global muons and as tracker muons (cf. Section 4.2.1). Further cuts are applied to reject fake or badly reconstructed muons such as a minimal number of hits in the tracker and the muon system, and the normalized χ^2 of the track fit must be smaller than 10. To reject muons from cosmic ray, pile-up collisions, and secondary vertices the extrapolated track is required to pass the primary vertex of the event closer than $1\,\text{mm}$ in z-direction and closer than $0.2\,\text{mm}$ in x-y-direction.

In addition, the muons should by isolated from other activity in the event: Within a cone of $\Delta R = \sqrt{(\Delta\phi)^2 + (\Delta\eta)^2} < 0.3$ around the muon track the energies of all objects reconstructed as charged hadrons, neutral hadrons and photons by the particle-flow algorithm are summed up. Then an average energy expected from pile-up interactions is subtracted. If the remaining energy exceeds 15% of the muon energy, the muon is rejected. An isolation requirement is very efficient against muons produced inside a hadronic shower.

Finally, the spacial acceptance is restricted to $|\eta| < 2.4$, and the minimal transverse momentum p_T is required to be at least $10\,\text{GeV}$. Each event must contain at least one lepton with a p_T larger than $20\,\text{GeV}$. These cuts are motivated by the detector geometry and performance, but also by the trigger.

Electrons

The strategy of selecting electrons is very similar to selecting muons, but the difficulties to separate good from fake or badly measured objects are different. One source of unwanted electrons are photons that decay in the presence of the detector material into electron-positron pairs. Electrons from such processes are called converted photons or simply conversions.

The electron selection starts with a CMS-wide predefined identification flag, which is constructed to have an efficiency of 90%, the so-called *loose ID*. This ID covers shape variables of the shower in the electromagnetic calorimeter selecting the typical "footprint" of an electron and several other observables as sketched in the following.

For a well measured electron the momentum measured by the tracker and the energy measured by the calorimeter should agree. This motivates the cut on the reverse difference of $|1/E - 1/p| < 0.05/\text{GeV}$.

The hadronic fraction of the measured energy must not exceed 12%, otherwise jets could be mis-interpreted as electrons. For the same reason and to reject real electrons produced inside jets, the considered electrons must be spatially isolated from other activity in the event. Like in the muon case, the energies of all charged and neutral hadrons and photons (reconstructed

by the particle-flow algorithm) inside a cone around the electron track are summed and an amount of energy that could be expected from pile-up interactions is subtracted. The result is required to be maximally 15% of the energy of the electron itself. The pile-up subtraction uses the event-wise energy density and the η dependent effective area of the isolation cone.

As mentioned, a rejection of converted photons is necessary: From such an object it is expected that the track does not start at the collision point, but the photon converts inside the detector material. Therefore, at the innermost layers of the pixel detector there are typically no hits. This is utilized by allowing not more than one missing hit in the pixel tracker. Furthermore, a vertex fit of the electron track is performed. If the electron comes from a conversion, a kink is expected and the track does not point to the vertex. The latter one is complemented by a hard cut on the distance of the extrapolated track to the vertex. The same numbers are used as for muons, $\Delta z < 1\,\mathrm{mm}$ and $\Delta xy < 0.2\,\mathrm{mm}$.

Since muons can deposit a little energy in the calorimeters, they can mimic electrons. Hence, a cross cleaning is performed. If an electron is within a cone defined by $\Delta R < 0.1$ around any global or tracker muon it is rejected.

The η acceptance is restricted to the region where both the tracker and the electromagnetic calorimeter show a good performance, $|\eta| < 2.4$. The transition region between the barrel part and the end-cap part of the calorimeter $(1.4442 < |\eta| < 1.566)$ is omitted to ensure that only well measured electrons are considered. The p_T requirement for electrons is the same as for muons: at least $10\,\mathrm{GeV}$ for all electrons and at least $20\,\mathrm{GeV}$ for the leading.

Further details on electron reconstruction and identification are given in Ref. 100.

4.3.2. Jets and Hadronic Energy

Besides the leptons also the hadronic event activity is used to enrich a possible signal in the data sample. As described in Section 4.2.3, the jets to be used in this analysis are clustered from particle-flow objects using the anti-k_T algorithm with a distance parameter of 0.5. Like it is the case for electrons, also for jets an *ID* is defined centrally in CMS [91]. Here, the *loose ID* is used, its basic task is it to avoid detector noise to be considered as a jet.

The loose ID comprises the following selection steps: A jet clustered from only one constituent is rejected. The neutral hadronic and neutral electromagnetic energy each must not exceed 99% of the total energy. Jets in the region $|\eta| < 2.4$ additionally have to have a charged hadronic energy fraction, at least one track, and a charged electromagnetic fraction below 99%. The latter restriction on the central η region can be understood from Fig. 4.4, in the forward region charged particles can not be identified.

The p_T of a jet is required to be larger than $40\,\mathrm{GeV}$, its axis has to be within $|\eta| < 3$.

This jet definition is very generic, hence, leptons can also be reconstructed as jets. Having the lepton defined as explained above (especially including the isolation), these objects are very reliable. Consequently, jets are rejected that are close to a selected lepton $(\Delta R(\mathrm{lepton}, \mathrm{jet}) < 0.4)$.

An event-wise variable for the hadronic activity is the scalar sum of all jet p_T's, typically called H_T. In this study all jets fulfilling the requirements mentioned above are considered in this sum:

$$H_\mathrm{T} = \sum_{i=1}^{\#\,\mathrm{jets}} p_\mathrm{T} \qquad (4.12)$$

4.3.3. Event Selection

In the previous sections the objects that are used in this work are defined. Here, the final event selection based on these objects is stated.

Triggering

The trigger strategy for this study is naturally di-leptonic. At trigger level two leptons are required, for the signal search they have to have the same flavor. As a control sample events with at least one electron and one muon are used.

The di-muon trigger has thresholds of 17 GeV for the p_{T} of the most energetic muon and 8 GeV for the p_{T} of the second muon. The muons have to be global muons as defined on HLT level. Additionally a second trigger is used that allows also an HLT tracker muon for the less energetic. Either of the two triggers has to fire to accept the event[2]. The contribution of the second trigger in addition to the first one is expected to be small since the fully reconstructed muons have to be both global and tracker.

In contrast to the muon collection the electron collection contains much more fakes from QCD events. In order to keep the trigger rate of the di-electron trigger at a reasonable level, further selection criteria have to be applied already in the HLT step. The p_{T} thresholds are also at 17 GeV and 8 GeV, in addition HLT versions of the electron ID on calorimeter and tracker measurements are required, and the electrons have to be isolated both in the calorimeter and in the tracker[3].

The combined muon-electron trigger uses the same objects as mentioned above. Also the p_{T} thresholds at 17 GeV and 8 GeV are the same, but two triggers are necessary, one requiring the higher p_{T} for the muon, the other for the electron[4].

Noise Cleaning

Analyses dealing with $E_{\mathrm{T}}^{\mathrm{miss}}$ are particularly exposed to noisy detector cells, mismeasurements, and malfunctions. All these effects typically lead to an imbalance in the event. Either because particle energies are wrongly measured, or because additional energies are detected that are not caused by a crossing particle, or because particles are missing. Thus, even if only a very small number of events are effected, after requiring a large $E_{\mathrm{T}}^{\mathrm{miss}}$ their fraction could be reasonably large.

Within the CMS collaboration, a lot of effort has been spent on the development of filters that reject events suspected to suffer from detector or reconstruction malfunctions. In this event selection several filters are applied.

Final Selection

Finally, per event at least two muons or two electrons are required to have opposite charge. To surpass the trigger thresholds the leading lepton p_{T} must exceed 20 GeV, the sub-leading 10 GeV. This *opposite-sign same-flavor* (OSSF) signature defines the search region of the here

---

[2]in terms of CMS trigger names: `HLT_Mu17_Mu8` or `HLT_Mu17_TkMu8`

[3]the full CMS trigger name is
`HLT_Ele17_CaloIdT_CaloIsoVL_TrkIdVL_TrkIsoVL_Ele8_CaloIdT_CaloIsoVL_TrkIdVL_TrkIsoVL`

[4]the full CMS trigger names are
`HLT_Mu17_Ele8_CaloIdT_CaloIsoVL_TrkIdVL_TrkIsoVL` and
`HLT_Mu8_Ele17_CaloIdT_CaloIsoVL_TrkIdVL_TrkIsoVL`

Table 4.1.: The main selection steps and the number of MC background events that pass the cuts. The numbers are scaled to the integrated luminosity of the analyzed data ($12.2\,\mathrm{fb}^{-1}$). The details of the MC samples are given in the text. The summed contributions of all di-boson and all tri-boson processes are labeled as VV and VVV, respectively.

selection step	$t\bar{t}$	s. top	$t\bar{t}V$	Drell-Yan	VV	VVV
trigger, cleaning	181 017	9 483	3 028	14 207 240	36 042	345
one $\ell^+\ell^-$ pair	39 940	2 484	706	9 759 944	24 278	157
$E_{\mathrm{T}}^{\mathrm{miss}} > 160\,\mathrm{GeV}$	1 285	68	46	122	251	11
at least one jet	1 255	64	45	122	191	10
at least two jets	983	44	37	62	88	6

presented analysis. Most of the QCD background is rejected by the di-lepton requirement. The invariant di-lepton mass is required to exceed 15 GeV to reject low-mass resonances.

An $E_{\mathrm{T}}^{\mathrm{miss}}$ cut on 160 GeV is used to enrich possible signal events in the dataset. The lightest supersymmetric particles (LSP) typically causes a significant amount of $E_{\mathrm{T}}^{\mathrm{miss}}$ in the signal events. But several Standard Model processes – in particular Drell-Yan – have no intrinsic $E_{\mathrm{T}}^{\mathrm{miss}}$, and get effectively rejected.

Finally, some hadronic event activity is required to reduce background events that have two OSSF leptons and intrinsic $E_{\mathrm{T}}^{\mathrm{miss}}$, e.g. several di-boson processes. The main search strategy of this analysis aims for a signal characterized by colored SUSY particle production. Hence, jets are expected in the signal. That is accounted for by requiring at least two jets per event.

Although the cross sections for production of colored SUSY particles is generally higher in LHC collisions than for color-neutral particles, a signal process with electroweak SUSY production is used through this analysis for illustrative reasons and for demonstrating the sensitivity of the analysis. Since jets are expected is such scenarios only as initial state radiation, the jets requirement is reduced to at least one jet.

4.4. Event Numbers and Basic Distributions

In Table 4.1 the numbers of expected events from all relevant Standard Model processes are listed. Due to the very good lepton identification in the CMS detector, processes with no real leptons (QCD, except $t\bar{t}$) or only one lepton ($W^\pm$) are negligible although their cross sections are high.

As expected from a opposite-sign same-flavor event selection initially the majority of the events are Drell-Yan processes. More than 99% of the event sample are Drell-Yan events before the $E_{\mathrm{T}}^{\mathrm{miss}}$ cut. The $E_{\mathrm{T}}^{\mathrm{miss}}$ cut, however, rejects them almost completely. Then, di-leptonic $t\bar{t}$ events are dominant. The requirement for at least one jet reduces mainly di-boson backgrounds. The selection up to this step will be used for the search for electroweakly produced SUSY particles. Requiring at least a second jet rejects half of the remaining di-boson and Drell-Yen events. After the final selection approximately 80% of the simulated events are $t\bar{t}$ events.

Table 4.2.: The same selection as listed in Table 4.1, but here the sum of all background MC samples is compared to data and two different parameter points of a signal model with electroweak SUSY production as described is Section 7.2.2. Model 1 has the parameters $M_{\tilde{\chi}_1^\pm, \tilde{\chi}_2^0} = 150\,\text{GeV}$, $M_{\tilde{\chi}_1^0} = 50\,\text{GeV}$, $x_{\tilde{\ell}} = 0.5$, model 2 is defined by $M_{\tilde{\chi}_1^\pm, \tilde{\chi}_2^0} = 500\,\text{GeV}$, $M_{\tilde{\chi}_1^0} = 25\,\text{GeV}$, $x_{\tilde{\ell}} = 0.5$. The E_T^miss requirement rejects many of the low-mass signal events, the jet requirements reduce both signals. After the whole selection chain a good agreement between the numbers of measured and expected events is observed.

selection step	background MC	signal MC 1	signal MC 2	data
trigger, cleaning	14 437 154	11 586	86	10 900 197
one $\ell^+\ell^-$ pair	9 827 509	10 092	71	10 540 449
$E_\text{T}^\text{miss} > 160\,\text{GeV}$	1 782	310	46	1 770
at least one jet	1 686	142	24	1 670
at least two jets	1 221	52	7	1 219

In the following the relevant background processes are listed including information about the MC samples that are used through this analysis:

t$\bar{\text{t}}$ simulated with POWHEG (MADGRAPH and MC@NLO samples are used to spot differences, the MADGRAPH sample includes only di-leptonic events), is the main background.

single top simulated with MADGRAPH, possible via s, t, and $t\text{W}$ channel, of which the latter is by far the dominant since both the top an the $\text{W}^\pm$ can decay leptonically.

t$\bar{\text{t}}$V simulated with MADGRAPH, t$\bar{\text{t}}$Z^0, t$\bar{\text{t}}\gamma^*$, t$\bar{\text{t}}$W$^\pm$, t$\bar{\text{t}}$W$^+$W$^-$, tbZ^0, dominated by t$\bar{\text{t}}$Z$^0/\gamma^*$

Drell-Yan simulated with MADGRAPH with $M_{\ell\ell} > 50\,\text{GeV}$ and binned in jet multiplicities from one to four. After the event selection the low $M_{\ell\ell}$ region is negligible, as well as events with no additional jet. Additionally an inclusive sample (including also Drell-Yan events with no jet) and a sample with $10\,\text{GeV} < M_{\ell\ell} < 50\,\text{GeV}$ are available and used if it is appropriate.

di-boson simulated with MADGRAPH, Z^{0}Z^0, Z^{0}W$^\pm$, W$^+$W$^-$, most important are the processes W$^+$W$^- \to \ell^-\bar{\nu}\ell^+\nu$ and Z^{0}W$^\pm \to \ell^+\ell^-\ell\nu$, with small contributions from Z^{0}Z$^0 \to \ell^+\ell^-\nu\bar{\nu}$.

tri-boson simulated with MADGRAPH, Z^{0}Z^{0}Z^0, Z^{0}Z$^0\gamma^*$, Z^{0}Z^{0}W$^\pm$, Z^{0}W$^+$W$^-$, W$^+$W$^-$W$^\pm$, nearly negligible due to small cross sections.

The event selection steps can be illustrated by so-called "$n-1$ plots". A variable is plotted after all cuts are applied except the cut on that variable. In Fig. 4.11 such plots are shown comparing the measured data to simulated events. The latter are scaled according to the expected cross section of the process to the integrated luminosity of the analyzed data.
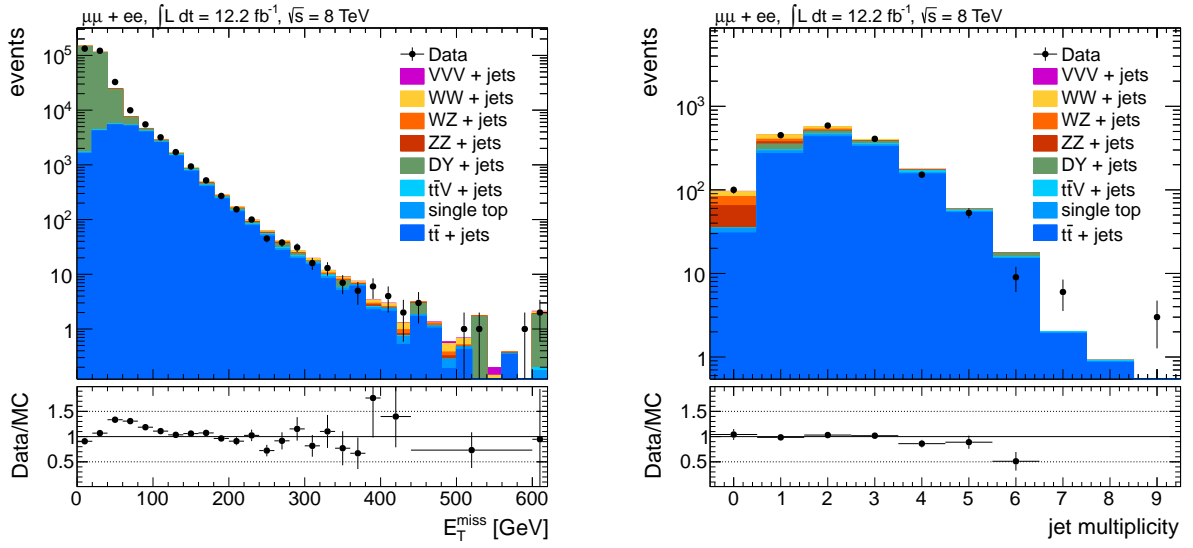
Figure 4.11.: Distribution of E_T^{miss} and jet multiplicity in data and Monte Carlo. For the left plot all event selection cuts are applied except the E_T^{miss} cut, for the right plots the requirement on the jet multiplicity is skipped. The disagreement in the low E_T^{miss} region is due to a not-matching simulation of the jet resolutions. The E_T^{miss} cut on 160 GeV clearly rejects most Drell-Yan background. The cut on a certain number of jets effectively reduces the di-boson contamination; also the Drell-Yan background gets further reduced.
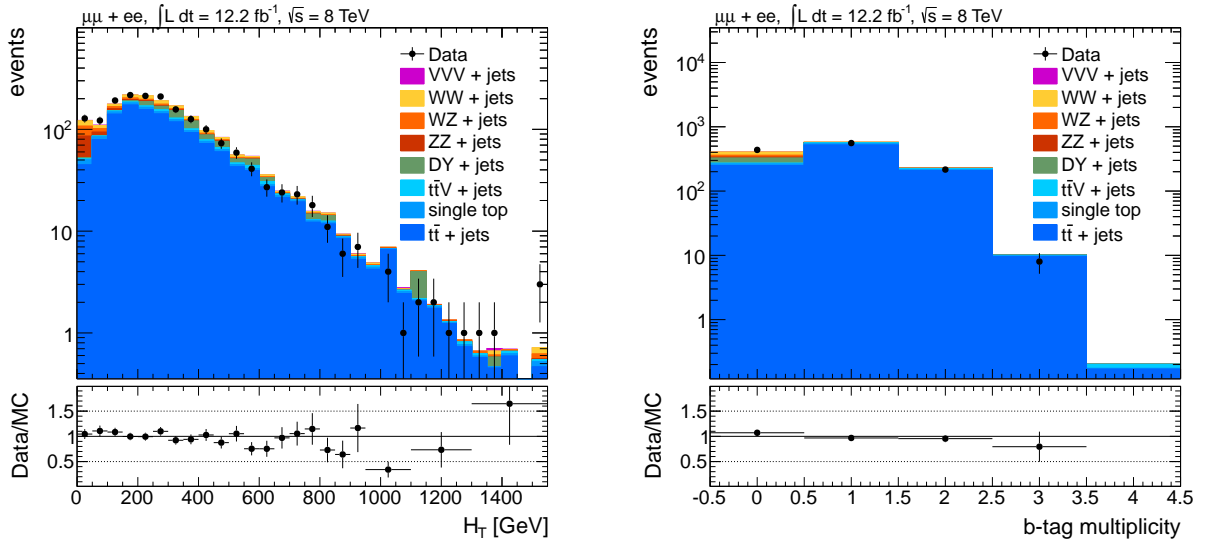
Figure 4.12.: The scalar sum of the selected jets (H_T) and b tag multiplicity in data compared to simulation. The left plot is done omitting cut on the jet multiplicity. Also here the accumulation of di-boson events at low or no hadronic activity is visible. The right plot shows the number of b tags per events after the whole selection chain. With a b-tag requirement the remaining Drell-Yan and di-boson background can be further reduced.

In the low-$E_\mathrm{T}^\mathrm{miss}$ region a clear deviation between data and Monte Carlo is visible. The reason was found to be the simulation of jet resolution, which is better then actually observed in data. In particular the distribution of Drell-Yan events is expected to be shifted, since in most of these event the jet resolution is the main source of $E_\mathrm{T}^\mathrm{miss}$. Hence, a realistic jet resolution in the simulation would shift the Drell-Yan distribution to larger values of $E_\mathrm{T}^\mathrm{miss}$ and the Monte Carlo prediction would fit to the measured data. The distribution of jet multiplicity shows a very good agreement between data and Monte Carlo.

In Fig. 4.12 two additional distributions are shown. The H_T distributions shows a good agreement, however, the simulated distributions seems to be slightly shifted to higher values of H_T w. r. t. the data. The b-tag multiplicity is an interesting variable for a further discrimination of the backgrounds and for characterizing a potential signal. After the presented event selection the number of b tags per event in data is similar to the simulation.

Figure 4.13 shows the distribution of the main variable in the analysis, the di-lepton invariant mass. Again, the expectations form Monte-Carlo simulation is drawn in comparison to the measurements. No striking deviation is visible. The number of events in the first bin of the spectrum is slightly underestimated, in the following two bins a slight overestimation can be observed. This and other minor deviations can be expected from statistical fluctuations.

Figure 4.14 shows the same distribution after the 1-jet selection. The Z^0 peak is large due to increased contributions from di-boson events, but the simulation describes the data. Additionally the signal Monte-Carlo sample with the parameters $M_{\tilde{\chi}_1^\pm, \tilde{\chi}_2^0} = 150\,\mathrm{GeV}$, $M_{\tilde{\chi}_1^0} = 50\,\mathrm{GeV}$, $x_{\tilde{\ell}} = 0.5$ is drawn. It shows a clear edge in the region of $100\,\mathrm{GeV}$.

The distributions of the Lorentz-vector components are given in Appendix A.
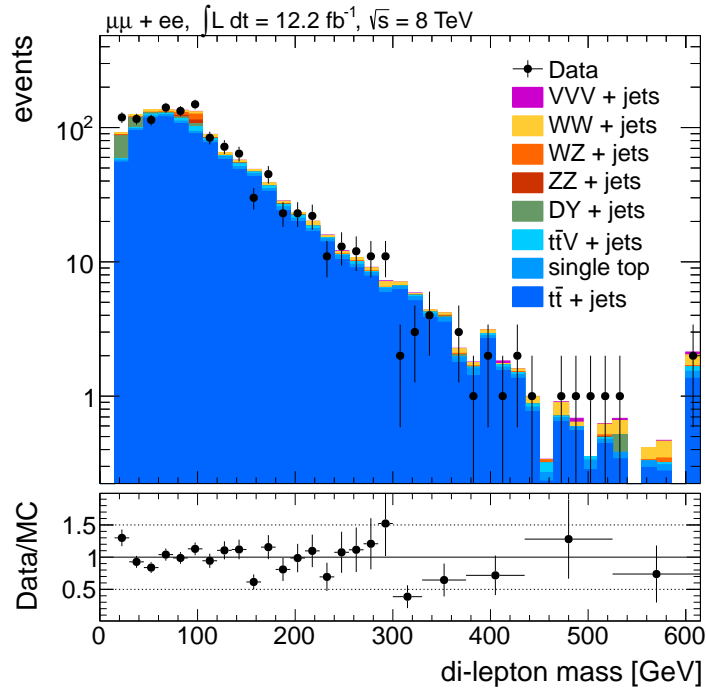
Figure 4.13.: Distribution of the di-lepton mass in data compared to Monte-Carlo simulation after the whole event selection. In the very first bin more data events are measured than expected, followed by a slight downward fluctuation in the following two bins.
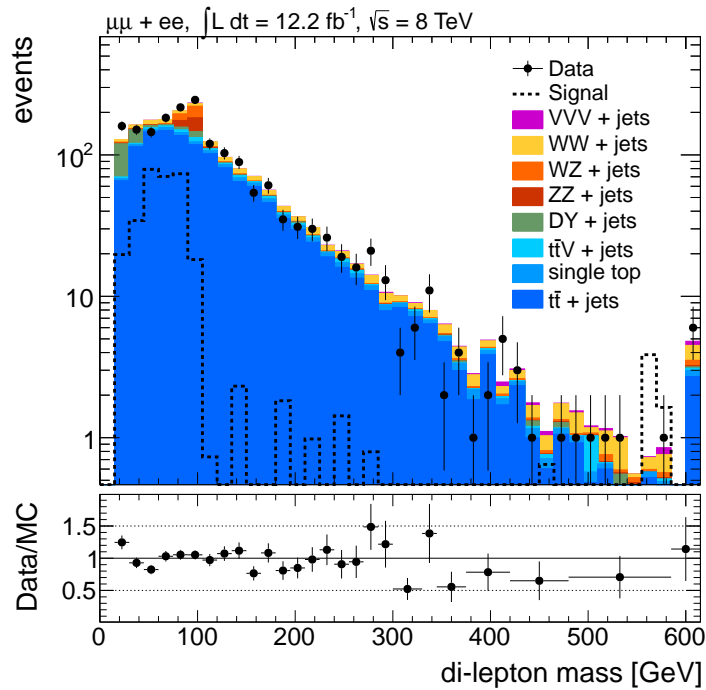
Figure 4.14.: Distribution of the di-lepton mass in data compared to Monte-Carlo simulation after the 1-jet event selection. In addition to the MC background the signal model 1 (cf. Table 4.2) is shown.

5. The Event-Mixing Method

In this chapter the event-mixing technique is described and how it can be used to estimate the background formed from $t\bar{t}$ events. In Section 5.1 the general idea of a search for an edge in the di-lepton mass spectrum is motivated, in Section 5.2 the concept of event mixing is introduced. In Section 5.3 the validation of this technique on simulated events is shown. In Section 5.4 an alternative way of performing the event mixing is presented.

5.1. Kinematic Endpoints in Supersymmetric Decay Cascades

In particle physics it is a very common approach to search in the invariant-mass distribution of two measured particles for hints of a new particle. The most famous successful examples of such an analysis might be the discovery of the Z^0 boson in the di-lepton mass spectrum at the SPS collider at CERN. An observed excess of events with an invariant di-lepton mass in the region of $90\,\text{GeV}$ to $95\,\text{GeV}$ was the first direct experimental hint leading to the discovery of one of the crucial particles in the Standard Model [101, 102]. Another field of intense use of two-particle masses was the discoveries and analyses of meson and baryon resonances.

The interesting feature of a two-particle mass is its invariance under a common Lorentz transformation. No matter what momentum the Z^0 boson has, the invariant mass of its decay products, $M = \sqrt{(P_1 + P_2)^2}$ (where P_1 and P_2 are the Lorentz vectors of the daughter particles) reflects the rest mass of the Z^0. Although the Z^0 itself decays promptly, its mass can be measured by studying the decay products.

In Supersymmetry many heavy-weighted short-living particles are expected. They might be produced in the proton-proton collisions at the LHC, and decay each via a cascade into particles, of which most can be measured by the detector. Since the invariance of the mass holds also for more than two daughter particles, it is also possible to search for supersymmetric particles in invariant mass distributions of measured particles.

One important difference to the Z^0 boson or the hadronic resonances is caused by the conservation of R parity, which is assumed in many SUSY models, as described in Section 2.2.1. As one consequence, it is not expected that all decay products of a SUSY particle can be measured. At least one particle – in most models the lightest SUSY particle (LSP) – is expected to escape the detector unseen. If the invariant mass of the measurable particles is formed, it is not possible to obtain the true mass of the mother particle, as a certain energy fraction is missing, carried away by the LSP.

What remains as an invariant observable is an upper bound on the invariant mass. In the rest frame of the decaying particle the mass of this particle is the available energy. The energy of the measurable particles is maximal if the invisible particle is produced at rest.

This analysis is designed for SUSY models that predict a reasonable production of the second-lightest neutralino ($\tilde{\chi}_2^0$), either directly or from a squark decay, decaying further into the lightest neutralino ($\tilde{\chi}_1^0$, the LSP) and two leptons. Because of charge and flavor conservation the two leptons have to be opposite charged and of the same flavor. From now on to these particles will
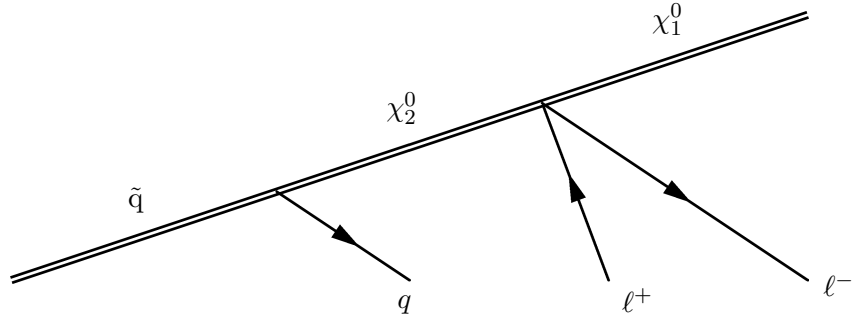
Figure 5.1.: The easiest scenario is the three-body decay of a neutralino into a lepton pair and the LSP. The total measurable energy is maximized if the $\tilde{\chi}_1^0$ is produced at rest and contribute only with its mass to the true total energy. The cut-off in the di-lepton mass spectrum is at the difference of the $\tilde{\chi}_2^0$ and the $\tilde{\chi}_1^0$ mass (Eq. 5.1).
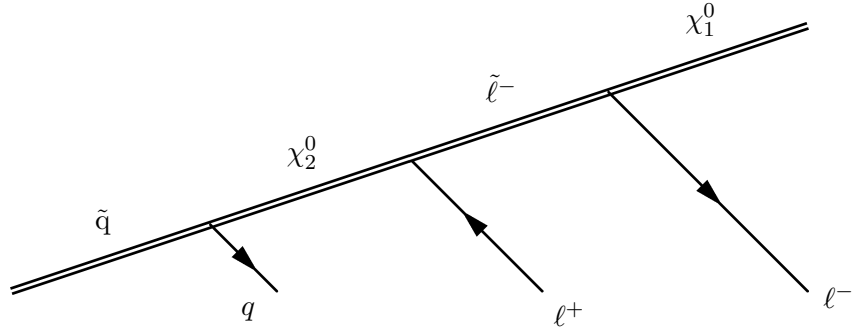
Figure 5.2.: If the mass hierarchy of the SUSY particles allows an on-shell $\tilde{\ell}$ between the $\tilde{\chi}_2^0$ and the $\tilde{\chi}_1^0$, these two subsequent two-body decays are expected to be the main process. The meaning of the mass edge in this case is given by Eq. 5.2.

be referred – although the main ideas and methods are more general and applicable to many other new physics models since most of the utilized features depend only on kinematics. In this sense, $\tilde{\chi}_2^0$ stands for any massive new particle that decays into two leptons of opposite charge and same flavor and a not-measurable particle, represented by $\tilde{\chi}_1^0$.

However, what matters for the proper interpretation of the endpoint in the di-lepton mass distribution is the actual mode the decay takes place. The easiest case is a three-body decay as illustrated by the Feynman diagram in Fig. 5.1. This decay is expected to be dominant if other on-shell decays are not reachable. The maximal di-lepton mass is simply the mass difference of the mother particle and the LSP:

$$M_{\ell\ell}^{\max} = M_{\tilde{\chi}_2^0} - M_{\tilde{\chi}_1^0} \tag{5.1}$$

This result can be easily derived from the extreme case, when $\tilde{\chi}_1^0$ is at rest in the rest frame of $\tilde{\chi}_2^0$, as shown in Appendix B.1.

The on-shell process involving a slepton is expected to be dominant if the $\tilde{\ell}$ mass is located well between the $\tilde{\chi}_2^0$ mass and the $\tilde{\chi}_1^0$ mass. Figure 5.2 shows the Feynman graph for this decay

chain. The maximal di-lepton mass depends again only on the masses of the involved particles:

$$M_{\ell\ell}^{\max} = \sqrt{\left(M_{\tilde{\chi}_2^0}^2 - M_{\tilde{\ell}}^2\right)\left(M_{\tilde{\ell}}^2 - M_{\tilde{\chi}_1^0}^2\right)} \Big/ M_{\tilde{\ell}} \tag{5.2}$$

A sketch of a derivation is shown in Appendix B.2, the full calculation can be found in Ref. 103.

A third possibility of the decay involves an on-shell Z^0. If the mass difference of the $\tilde{\chi}_2^0$ and the $\tilde{\chi}_1^0$ is larger than the Z^0 mass, the three-body decay will be mainly replaced by this on-shell decay. The di-lepton mass will then show a Z^0 peak. Since this analysis is not aiming for estimating the Standard-Model Z^0 background, signals involving on-shell Z^0's are not distinguishable from Standard-Model Z^0 events.

5.2. Concept of the Event-Mixing Method

Event mixing is a technique to decorrelate observables that can be combined to one quantity. A typical example is the kinematic correlation between particles that originate from the decay of one on-shell intermediate state. The Lorentz vectors are the observables, the two-particle mass is the combined quantity.

The correlation between the Lorentz vectors is measured by comparing the two-particle mass spectrum with a second artificial mass spectrum that is obtained from taking one particle from one event and the other particle from another event. These cross-event particle combinations are called *mixed events*.

Assuming a correlated signal and an uncorrelated background, by comparing the real two-particle mass distribution with the mixed one, the background distribution is reproduced by the mixed events, and the signal contribution within the event sample should become visible. The difference between the spectra can be quantified with shape comparison methods like maximum likelihood ratio, χ^2, or Kolmogorov test.

5.2.1. History of Event-Mixing Techniques

The event-mixing technique has a quite long history in particle and nuclear physics. The idea came up in the 1970s in the field of meson physics. One of the first publications mentioning it comments on the correlation in interference analyses with di-pion sources [104]. The density distribution calculated from two pions from different events is proposed to be used as a model for the non-interfering contribution to the real event-wise density distribution.

A fruitful area of applying event-mixing techniques have early been found in modeling the combinatorial background in invariant two-particle mass spectra. At the ISR proton-proton storage ring at CERN, for example, it was used to extract ρ and ω resonances from the di-pion spectrum [105]. Event mixing was used to find a description of the background taking into account detector acceptance and combinatorial issues. In addition, the technique provided background predictions in several other di-particle mass spectra (including kaons, protons, and pions) searching for further resonances and setting limits [106].

Another experiment, also searching for hadronic resonances (at the Fermilab hybrid spectrometer) found that event mixing is not a suitable method for describing the background [107]. Both, the ISR and the Fermilab group used the same-sign di-pion mass as a control sample to validate the method, but came to different results.
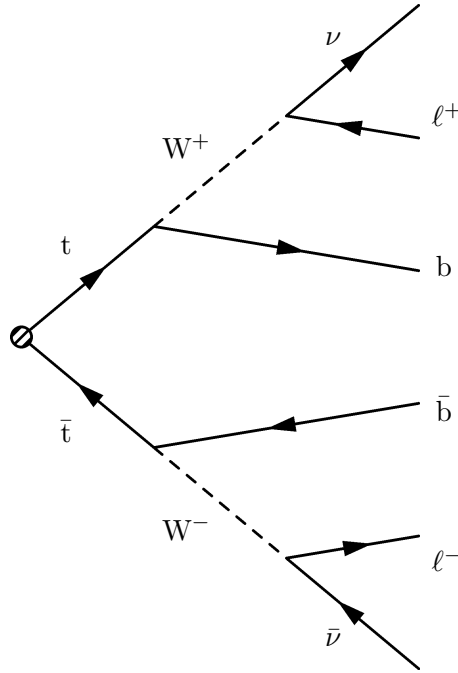
Figure 5.3.: Feynman graph of a t$\bar{\text{t}}$ decay, with both W bosons decaying leptonically. While in the signal decays (Figs. 5.1 and 5.2) the two lepton originate from one chain, here they are expected to be much less kinematically correlated.

In Ref. 108 an overview of using event-mixing methods is given. The authors claim that the technique is especially then suitable, if the expected signal peak sits on top of an also (but broader) peaking background distribution. While in cases with simple falling or rising background shapes its estimation with an analytical function is easier and sufficient. Furthermore, it is pointed out that the kinematic restrictions induced by the experimental setup and the event selection is a potential problem and can lead to wrongly estimated backgrounds. This is found to be an issue in this analysis as well. In Section 5.3.5 the effects of acceptance and event selection cuts are studied.

In a more recent publication, the mixed events are called bi-events and the background subtraction based on them is introduced as *BEST* (bi-event subtraction technique) [109]. In the ATLAS collaboration event mixing was found to be suitable to predict the background in lepton-jet mass spectra that can be used for SUSY mass measurements [110]. Also at the BELLE experiment the method is used in several studies to predict the contribution from event-wise uncorrelated events [111, 112].

In CMS studies that analyze angular correlations, the event-mixing technique is applied. One example is the analysis of the long-range near-side angular correlation in proton-proton collisions [113]. The uncorrelated background is estimated from data with mixed events. Another study investigates the angular correlation between b and $\bar{\text{b}}$ hadrons. The simulated events are validated using event mixing [114].

5.2.2. $t\bar{t}$ Background Prediction based on Event Mixing

The event-mixing method is a novel technique to emulate the Standard-Model background in the Supersymmetry discovery channel that is characterized by two opposite-sign same-flavor leptons, jets, and missing transverse energy ($E_{\mathrm{T}}^{\mathrm{miss}}$). This background is mainly composed of $t\bar{t}$ events with both the top and the anti-top decaying leptonically. The final states of these background events consist of two opposite-sign leptons, two neutrinos (i. e. $E_{\mathrm{T}}^{\mathrm{miss}}$), two b-quarks, and possible further jets from initial or final state radiation. The Feynman graph of the di-leptonic $t\bar{t}$ decay is given in Fig. 5.3.

The event-mixing method utilizes an important difference between the signal and the background events: In signal events both leptons originate from the same decay branch (as described in Section 5.1), whereas in the $t\bar{t}$ background events the lepton comes from the anti-top decay and the anti-lepton comes from the top decay, as illustrated in Fig. 5.3. This leads in signal events to a clear correlation between the two leptons, which is much weaker in $t\bar{t}$ events.

The question of how large the correlation between the two leptons in $t\bar{t}$ events actually is, is the key issue of this analysis and is addressed in the following.

Given that the leptons are not correlated, event mixing should reproduce the shape of the measured di-lepton mass distribution.

The invariant di-lepton mass $M_{\ell\ell}$ is calculated as:

$$M_{\ell\ell} = \sqrt{(P_{\ell^+} + P_{\ell^-})^2}, \tag{5.3}$$

where the P's are the Lorentz vectors. The mixed di-lepton mass can be written as

$$M_{\ell\ell}^{\mathrm{mix}} = M_{\ell\ell}^{\mathrm{AB}} = \sqrt{\left(P_{\ell^+}^{\mathrm{A}} + P_{\ell^-}^{\mathrm{B}}\right)^2}, \tag{5.4}$$

where A and B indicate the different events. The lepton of one event can be combined with the anti-lepton of all other events. In this way from n real events $n(n-1)$ mixed events can be generated. Due to this large number of mixed events a smooth distribution is obtained for the background prediction.

5.3. Method Validation with Simulated Events

In this section simulated events are used to study the validity and reliability of the above described method to estimate the $t\bar{t}$ background in di-lepton events with missing transverse energy. In Section 5.3.1 the relevant kinematic issues are addressed, especially the question, if the distribution of the mixed events reproduces the original invariant mass spectrum without a bias. In Section 5.3.2 the effects of spin correlation in $t\bar{t}$ events are discussed. In the following sections it is studied how other background events affect the prediction (Section 5.3.3) and also how contamination from signal influence the prediction (Section 5.3.4). In Section 5.3.5 the effects of the event selection cuts are studied. In Section 5.3.6 the method is cross-checked with samples that are simulated with other Monte-Carlo programs.

5.3.1. Event Kinematics in the Simulated $t\bar{t}$ Background

Figure 5.4 shows the proof-of-principle of the method. The event-mixing technique is applied to reproduce the di-lepton mass shape in simulated $t\bar{t}$ events. Only those events that fulfill the
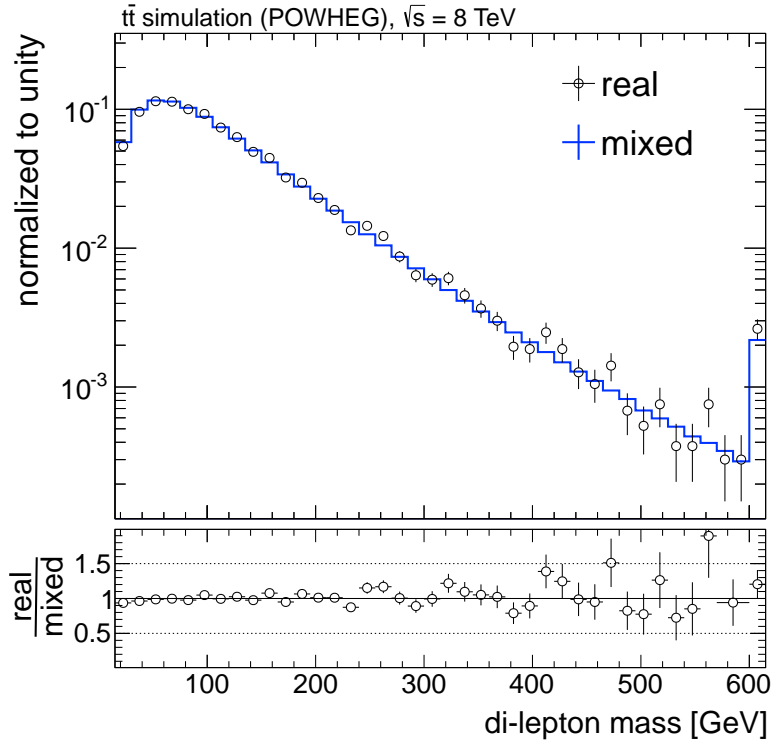
Figure 5.4.: Proof-of-principle with simulated $t\bar{t}$ events (POWHEG Monte Carlo) after the default event selection. The "real events" are lepton anti-lepton combinations that occur in one event, "mixed events" are lepton combinations from different events. The mixed distribution is scaled to the number of real events. The error bars indicate the statistical uncertainty.

selection criteria discussed in Section 4.3 enter this plot. The mixed distribution is scaled by integral to the number of real events. Clearly both spectra agree very well across the whole energy range. A very small deviation might be visible at small di-lepton masses where the number of real events is slightly overpredicted by the mixed events. The Monte-Carlo event generator POWHEG is used here.

For the mixed distribution all event combinations are considered fulfilling the requirement $\Delta R(\ell^+, \ell^-) > 0.4$. ΔR is a measure for the angular distance, it is defined as $\sqrt{(\Delta\phi)^2 + (\Delta\eta)^2}$, where ϕ is the azimuth angle and η the pseudorapidity. In the real events the two leptons need to have a minimal distance to be separately reconstructed as isolated objects. The ΔR requirement is applied to have such a minimal distance also in the mixed events. The value of 0.4 is chosen because this is the size of the isolation cone, but it is varied to study its behavior as a potential source of a systematic uncertainty (cf. Section 6.2.2). Another requirement on the mixed events is $M_{\ell\ell}^{\mathrm{mix}} > 15\,\mathrm{GeV}$ as it is done in the real events as well (cf. Section 4.3).

The basic assumption of the event-mixing method is that the two leptons are kinematically independent from each other in $t\bar{t}$ events. Under this condition, the mixed events would perfectly reproduce the measured di-lepton mass spectrum and a potential signal would clearly stand out. Unfortunately there is a slight correlation. Although the leptons come from different decay branches, they still share a common production process with its kinematic properties.
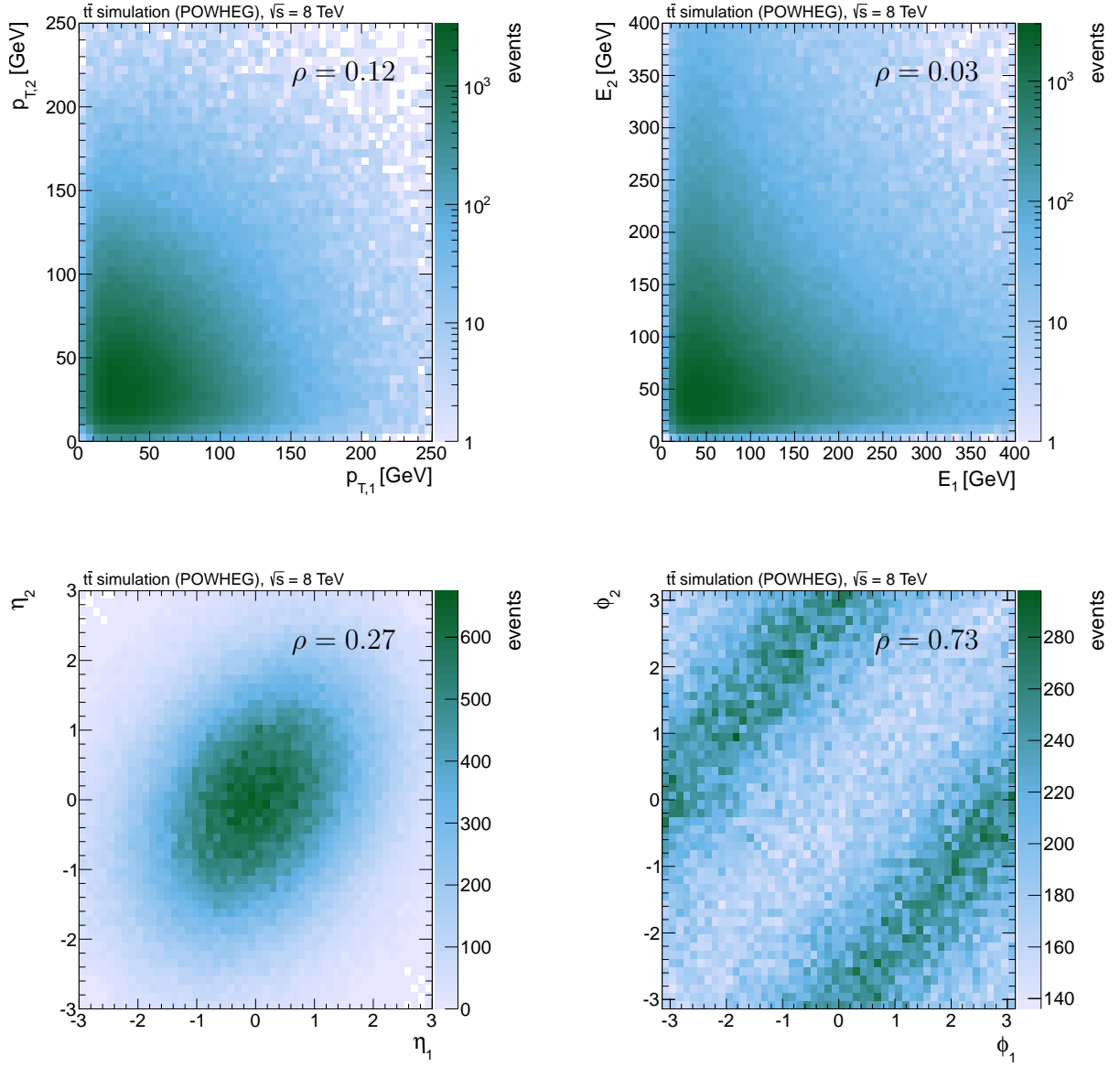
Figure 5.5.: The correlation between the Lorentz vectors of the two leptons in $t\bar{t}$ MC events before the event selection. For each component of the vector in the usual parametrization the correlation plots is given together with the value of the linear correlation coefficient ρ, as defined in Eq. 5.5. Especially the angular components show a clear correlation. The correlation coefficient between the ϕ components is calculated with ϕ_2 shifted by π as illustrated in Appendix C.1, which also shows how the 2π invariance of the ϕ component is used in order to construct a sensible correlation coefficient. The absolute number for the ϕ correlation is biased to higher values by this procedure, but a reasonable comparison between ϕ correlations is possible.

The actual correlation of the Lorentz-vector components is shown in Fig. 5.5. The pseudorapidity is slightly positive correlated, if one lepton has a certain value the probability is increased that the other lepton in the event has a similar value. The azimuth angle is also correlated. Here, a distance of π between the leptons is the preferred topology.

As a measure of the correlation between two random variables a and b the correlation coefficient ρ is defined by:

$$\rho = \frac{\sum (a_i - \bar{a})(b_i - \bar{b})}{\sqrt{\sum (a_i - \bar{a})^2 \sum (b_i - \bar{b})^2}}, \tag{5.5}$$

where $\bar{a}$ and $\bar{b}$ are the mean values. It is a measure for the linear correlation of two variables. $\rho = 0$ means that the variables are not linearly correlated, $\rho = (-)1$ is the result for two strictly linear (negatively) correlated variables, i. e. $a = (-)x \cdot b$. For two reasons the plain ρ would not be a suitable measure of the ϕ correlation. The limited range of $\pm\pi$ causes problems at the edges: A large difference in ϕ does not necessarily correspond to a large distance in space. Additionally, the visible correlation does not follow the structure of a simple dependency ("if ϕ_1 is small, ϕ_2 is typically small/large"), but a certain distance is preferred. In Appendix C.1 it is shown, how these two problems are overcome and how the stated ρ is calculated.

Two causes of correlation have been found, both depending on the energies of the colliding partons but with opposite effects: The initial boost of the $t\bar{t}$ system and the di-top mass.

Initial Boost of the $t\bar{t}$ System

In many events the whole $t\bar{t}$ system is boosted in z direction (i. e. along the beam axis), caused by an imbalance of energies of the colliding partons. In transverse direction no net boost of the whole event is expected, but the $t\bar{t}$ system can still be boosted if it is recoiled by initial-state radiation. However, the main direction of the boost is along the beam axis.

Of course, such a boost induces a lepton-lepton correlation: The $t\bar{t}$ boost is inherited by all daughter particles including the lepton, causing a correlation. In Fig. 5.5 this effect is visible for the η component of the Lorentz vectors: the two leptons tend to be in the same forward-backward hemisphere.

The actual effect on the mixing can be described from a kinematic point of view: Assuming a scenario with only highly boosted $t\bar{t}$ event, the leptons are typically high energetic and close together. The event mixing results in a collection of mixed events with, of course, also high energetic leptons but no angular relation between them. Since the two-particle mass is larger for higher energies and smaller for smaller angles the spectrum of the mixed events are shifted to higher mass w. r. t. the spectrum of the real events.

In another notation of the di-lepton mass the effects of angular and energetic properties are more clear:

$$M_{\ell\ell} = \sqrt{2E_{\ell^+} E_{\ell^-}(1 - \cos\theta_{\ell\ell})}, \tag{5.6}$$

where $\theta_{\ell\ell}$ is the lepton-lepton opening angle. It directly shows, why the two-particle mass is invariant under common boosts: The larger the boost, the larger the energy, but the smaller the opening angle. They compensate exactly and lead to the well known invariance. But, of course, only in the real events and not in the mixed events.

Figure 5.6 shows the effect of the boost on the estimation power of the mixed spectrum. There is no doubt, the boost has a strong influence. In event samples with only small boosts the method would not predict the shape of the spectrum correctly, as it would not in event samples with highly boosted events only.
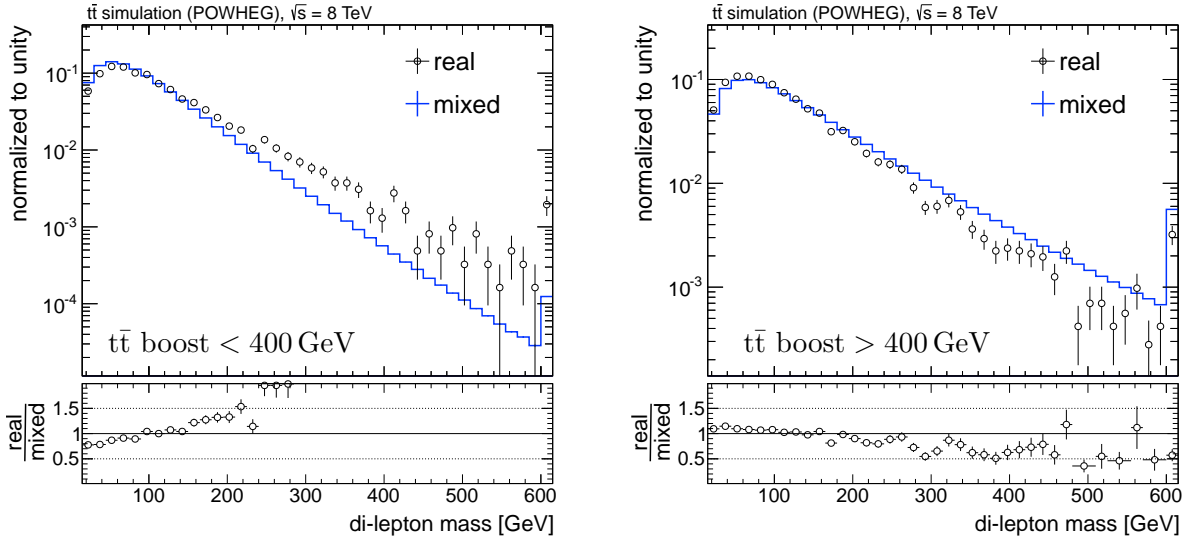
Figure 5.6.: Effect of initial $t\bar{t}$ boost on the event-mixing prediction. The left plot shows the real and the mixed distribution using events with small boosts only, the right plot is done with highly boosted events only. While the real distributions in both plots are very similar (the event-wise di-lepton mass is invariant under the boost), the low boost mixed spectrum is too soft and the high boost mixed spectrum is too hard. The default event selection is applied.

Di-Top Mass

A second reason for a correlation is found in the center-of-mass energy of the $t\bar{t}$ system. This energy can be interpreted as the di-top mass. Although there is no resonance in the mass spectrum, there is a certain structure in the center-of-mass frame of the hard interaction: At the lower end there is a threshold at two times the top mass, the upper tail is governed by the typically reached energies in the parton-parton collisions (depending on the proton energies and the parton density functions). The leptons as descendants of the tops carry parts of their kinematics and therefore remnants of the di-top mass. Since both leptons in an event are affected by the same di-top mass, a correlation is induced. In the mixed events the correlation is broken and the spectrum of the di-lepton mass is generally expected to differ from the spectrum in the real events.

The other point of view is again purely kinematic: The higher the energy in the $t\bar{t}$ rest frame the stronger the back-to-back topology of the whole event is realized. In events with two high energetic back-to-back tops, the leptons inherit the kinetic energy and have preferably also larger opening angles. In Fig. 5.5 the ϕ_1-ϕ_2 correlation shows that the back-to-back structure is favored. In the mixed events there is again no angular preference. The same argument that explains the harder spectrum of $M_{\ell\ell}^{\text{mix}}$ for highly boosted event, holds also for the di-top mass, but in the opposite direction. The higher the di-top mass, the softer the $M_{\ell\ell}^{\text{mix}}$ spectrum (compared to the real events) and vice versa. But in this case also the distribution of the real events depends on the energy.

In Fig. 5.7 the effect on the mixing is illustrated. The MC event sample is split into a low di-top mass and a high di-top mass subsample, and the real and the mixed di-lepton mass
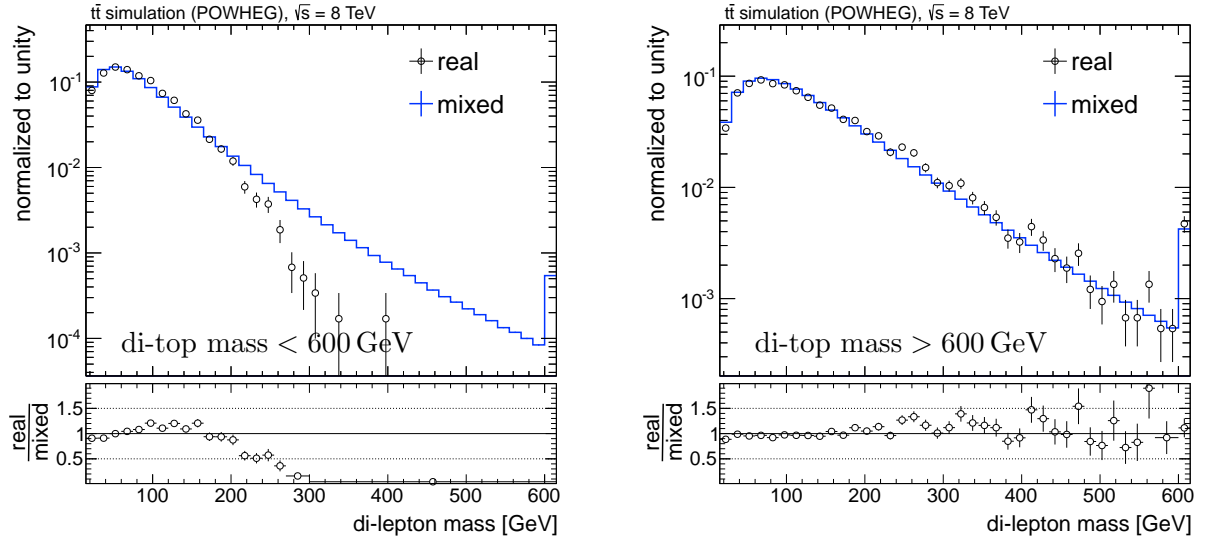
Figure 5.7.: Effect of the di-top mass on the event-mixing prediction. For the left plot only events are used with a low di-top center-of-mass energy, the high energetic events enter the distributions in the right plot. Both the real and the mixed spectrum differ strongly between both plots. Here, the real distributions show an even stronger discrepancy. The events are selected according to the default requirements.

shape is compared separately. As in the boost case, there are mismatches in both subsamples, especially in the low di-top sample.

Figure 5.8 displays how the opening angle between the two leptons is differently distributed for different $t\bar{t}$ boosts and different di-top masses. Both figures confirm the explanations given above: A large $t\bar{t}$ boost decreases the lepton-lepton opening angle, while a large di-top mass has the opposite effect.

Since the kinematic correlation is the reason for the mismatch between the real MC distributions and the predictions in Figs. 5.6 and 5.7, the correlation coefficients between the components of the Lorentz vectors can help to understand the behavior. Figure 5.9 shows how the correlations change with the $t\bar{t}$ boost and with the di-top mass. Since the effects of the boost and the di-top mass can compensate or enhance each other, in Appendix C.2 the correlation coefficients are given in 2-D bins of both event energies. In this context also the correlation between the $t\bar{t}$ boost and the di-top mass itself might be interesting. In Appendix C.3 it is shown that the variables are slightly positive correlated.

As expected, the boost has a strong influence on the η correlation. For small boosts the correlation is negative: A forward top is likely to be balanced by a backward anti-top, and leptons that tend to follow the top directions show the same topology. For higher boosts the boost energy prevails and the two lepton are more likely to be in the same hemisphere. The energy correlation shows the opposite effect, for small boosts it is small positive, for large boosts the correlation becomes negative. From Fig. C.3 in the Appendix clearly can be concluded that this evolution is due to events with high di-top masses. If the back-to-back topology due to the high di-top mass is boosted in one direction, it is likely that one lepton gains energy while the other loses energy, thus the correlation is negative. The correlations between the transverse
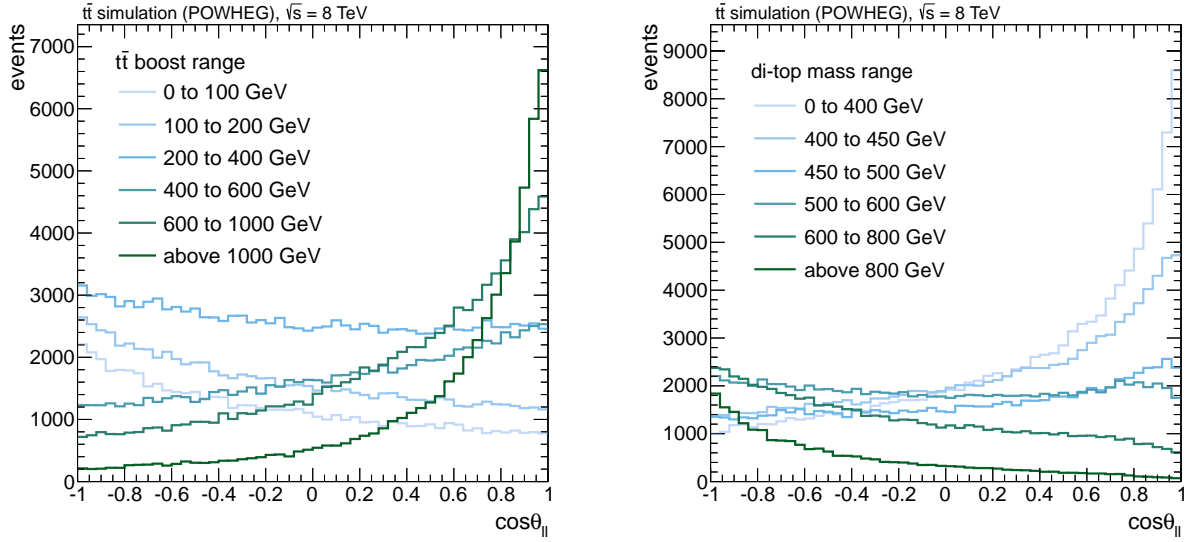
Figure 5.8.: Dependence of the lepton-lepton opening angle on the initial t$\bar{\text{t}}$ boost (left) and the di-top mass (right). The plots are not normalized and show all di-leptonic t$\bar{\text{t}}$ MC events without any selection. The effects are obvious: the larger the boost, the closer the leptons ($\cos\theta_{\ell\ell} \to +1$); the larger the di-top mass, the larger the opening angle ($\cos\theta_{\ell\ell} \to -1$)

components p_{T} and ϕ is expectedly independent of the t$\bar{\text{t}}$ boost.

The di-top mass has a reasonable influence on the correlations of all vector components. Here, the η_1 vs. η_2 correlation is large and positive for small energies and gets negative for large di-top masses. In the low di-top-mass bins the t$\bar{\text{t}}$ boost can by expected to be the dominant event energy, i. e. the η correlation is positive large. The higher the di-top mass the stronger the back-to-back topology is pronounced. The negative correlation in the highest bins indicates that here the di-top mass prevails the boost and even in forward-backward direction the back-to-back topology is preferred. Also the energy correlation shows a decreasing evolution. The explanation is given in the previous discussion of the influence of the t$\bar{\text{t}}$ boost. The p_{T} correlation is close to zero for small di-top masses and increases slightly with higher values. The transverse momentum does not interfere with the t$\bar{\text{t}}$ boost like the total lepton energy. Thus, the p_{T} correlation can be understood more easily: The higher the di-top mass, the more energy the leptons inherit from their tops. The correlation between the ϕ components slightly increases with the di-top mass, which is expected from the back-to-back event topology.

Simulation of the t$\bar{\text{t}}$ Boost and the Di-Top Mass

The proof-of-principle demonstrated in Fig. 5.4 is only as valid as far as the simulation of the t$\bar{\text{t}}$ boost and the di-top mass can be trusted. In the Monte-Carlo sample used here the extreme scenarios depicted in Figs. 5.6 and 5.7 are obviously well balanced, and in the whole sample the method works well.

Both variables, the t$\bar{\text{t}}$ boost and the di-top mass are not easily accessible in data events. The di-leptonic t$\bar{\text{t}}$ decay comprises two neutrinos, which makes the event-by-event reconstruction
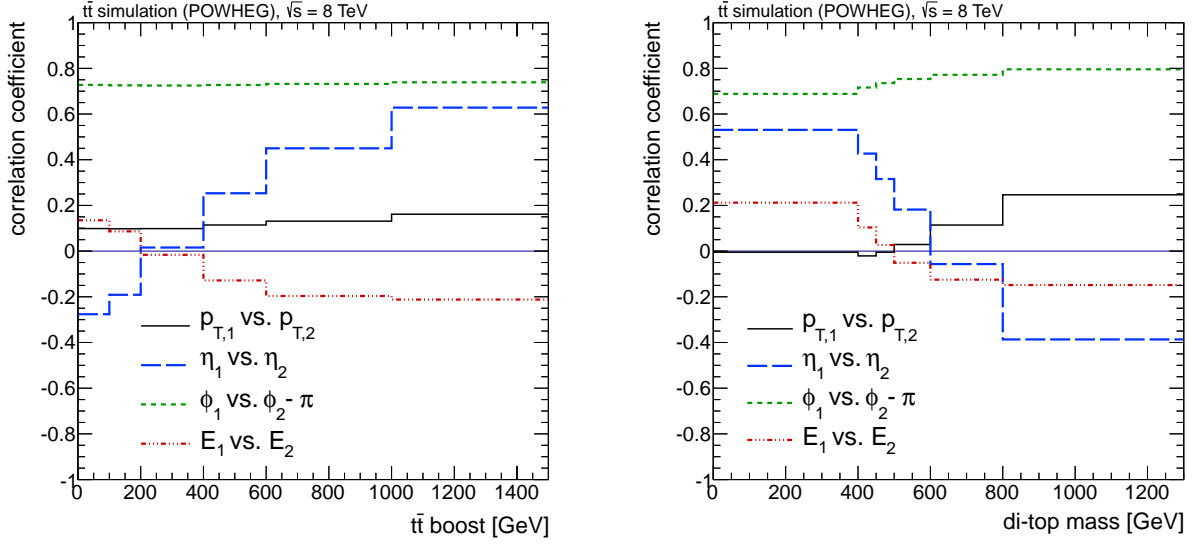
Figure 5.9.: The correlation coefficients of the Lorentz-vector components w. r. t. the $t\bar{t}$ boost (left) and the di-top mass (right). The simulated events are split in bins ρ is calculated separately in each bin.

of the full $t\bar{t}$-pair kinematics impossible without further assumptions. But if the validation of the method on simulated events should generate confidence that it can be applied on data, the simulation of these two quantities needs to be tested.

As already discussed, both effects depend on the energies of the colliding partons. Since the energies of the protons are identical and constant, the parton energy is quantified as fraction of the proton energy, the Bjørken-x. The $t\bar{t}$ boost $b_{t\bar{t}}$ is the energy difference of the partons

$$b_{t\bar{t}} = E_1 - E_2 \tag{5.7}$$

$$= x_1 \frac{\sqrt{s}}{2} - x_2 \frac{\sqrt{s}}{2} \tag{5.8}$$

$$= \frac{1}{2}(x_1 - x_2)\sqrt{s}, \tag{5.9}$$

with $\sqrt{s}$ being the proton-proton center-of-mass energy, and x_1 and x_2 the Bjørken variables of the partons. This $b_{t\bar{t}}$ is actually not the full boost, but the dominant fraction. Another boost is caused by colliding partons that have a significant momentum fraction transverse to the beam line, typically due to initial-state radiation. In this work the full boost is studied, defined as $\vec{b}_{t\bar{t}}^{\text{full}} = \vec{p}_t + \vec{p}_{\bar{t}}$.

The di-top mass $M_{t\bar{t}}$ can be written in terms of the same quantities

$$M_{t\bar{t}} = \sqrt{2E_1 E_2(1 - \cos\theta)} \tag{5.10}$$

$$= \sqrt{2x_1 \frac{\sqrt{s}}{2} x_2 \frac{\sqrt{s}}{2} 2} \tag{5.11}$$

$$= \sqrt{x_1 x_2 s}. \tag{5.12}$$
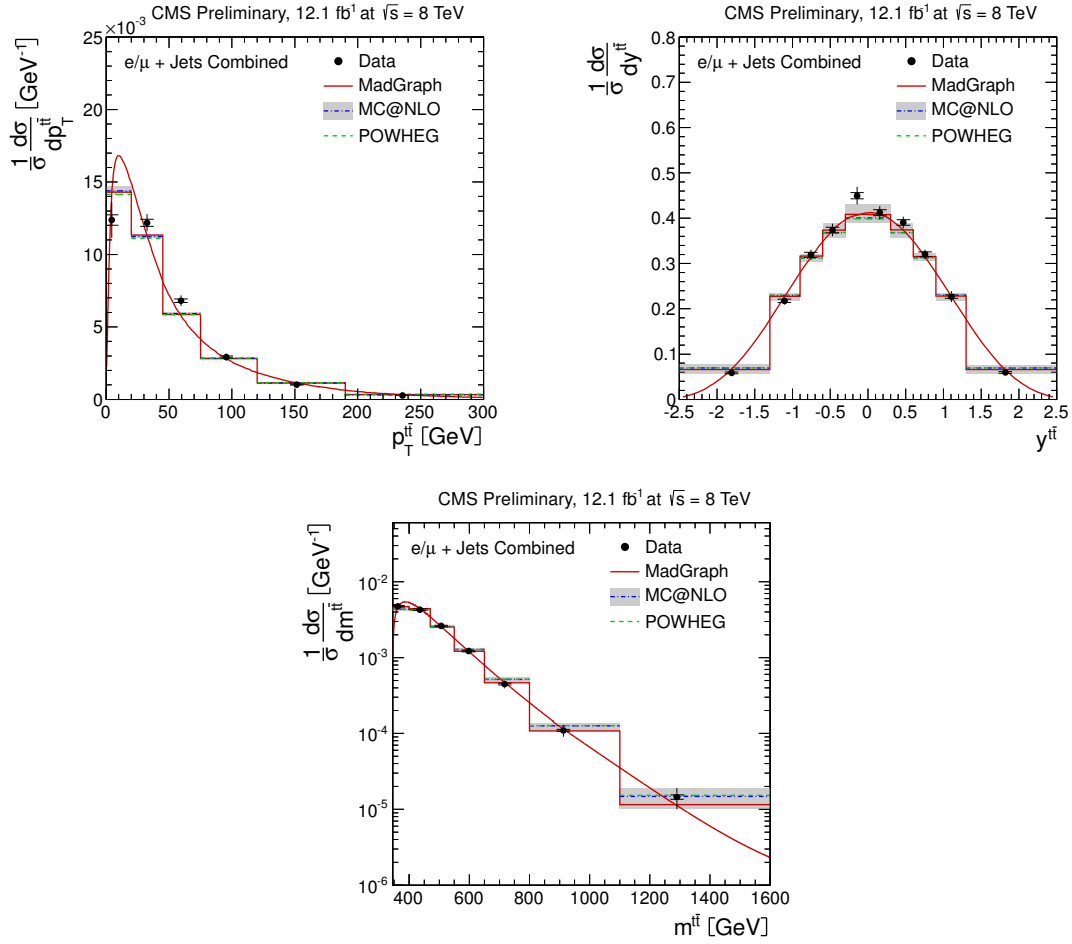
Figure 5.10.: Kinematic quantities of semi-leptonically decaying $t\bar{t}$ pairs in terms of differential cross sections. The simulations from three Monte-Carlo programs (MadGraph, mc@nlo, and powheg, the first one is drawn as histogram and as curve) agree well with the measurements in 8 TeV data [115].

Hence, both variables are proportional to the center-of-mass energy, but depend in different ways on the Bjørken-x. The distributions of the Bjørken-x's for different partons are described by the parton density functions (PDFs).

In order to gain confidence in the Monte-Carlo simulation several checks are performed.

Full $t\bar{t}$ reconstruction Top physics is a very active field of research in the CMS collaboration. A lot of effort is invested in reconstructing the full kinematic information of $t\bar{t}$ pairs. With a system of equations, each representing one kinematic constraint, such as p_T balance or particle masses along the decay chain, the components of the missing neutrino Lorentz vectors are calculated, or a fit can be performed by varying all measurements within their uncertainties [115–117].

For this purpose events from the semi-leptonic decay mode combine two advantages: Due to the lepton they are easier to distinguish from QCD events than full-hadronically decaying $t\bar{t}$
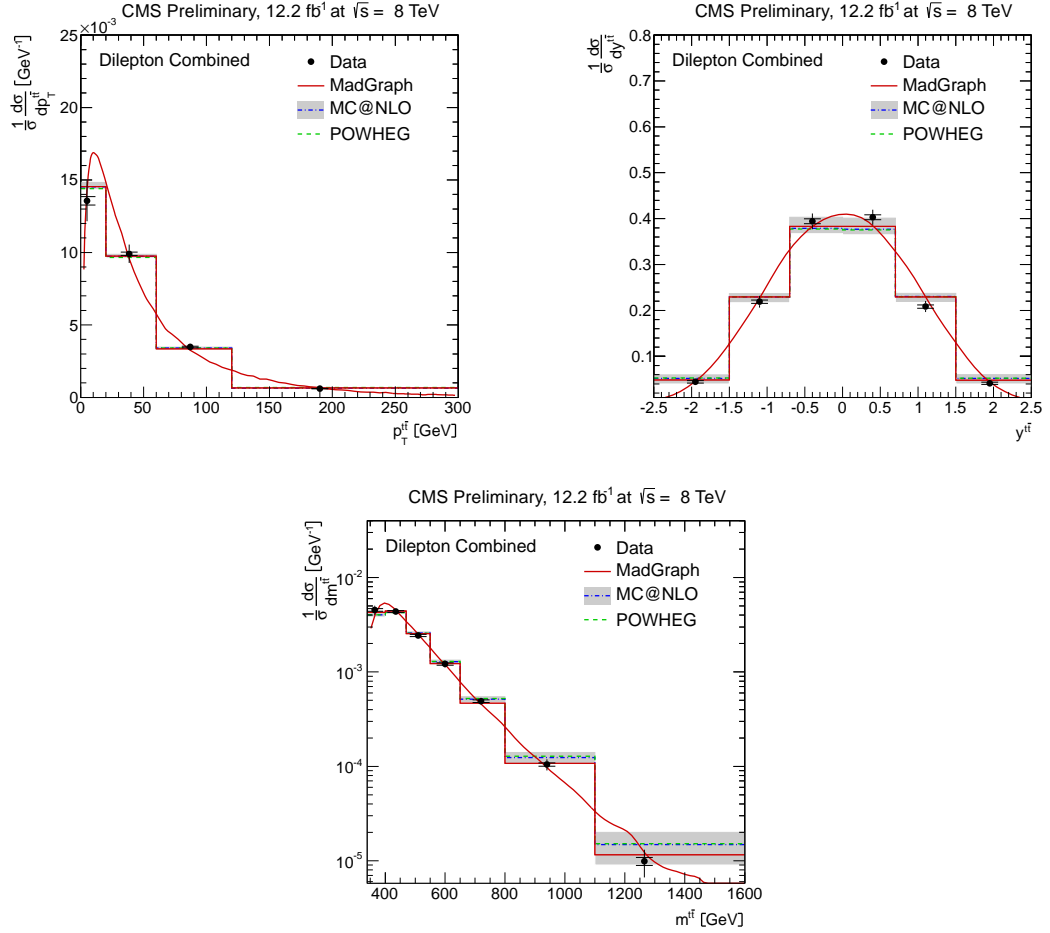
Figure 5.11.: Kinematic quantities of di-leptonically decaying $t\bar{t}$ pairs in terms of differential cross sections. The simulations from three Monte-Carlo programs (MADGRAPH, MC@NLO, and POWHEG, the first one is drawn as histogram and as curve) agree well with the measurements in 8 TeV data [116].

pairs; and since there is only one neutrino per event, the system of equations can be solved event-by-event. Figure 5.10 shows the kinematic variables obtained from the semi-leptonic $t\bar{t}$ reconstruction compared to several Monte-Carlo generators. The transverse momentum, the rapidity, and the di-top mass show a very good agreement between data and all three Monte-Carlo samples. The $t\bar{t}$ boost is not directly studied in the cited analyses, but indirectly via the transverse momentum and the rapidity.

In the di-leptonic case the situation is different. Two particles cannot be measured, and thus the system is underconstrained, i.e. not uniquely solvable. A sophisticated procedure extracts the most probable solution, making use of additional assumptions concerning the p_T spectrum of the neutrinos [116]. The results are presented in Fig. 5.11 and again, the simulations meet the measurements.

The comparison in both decay modes increases confidence that the observations from simulated events hold also for data.
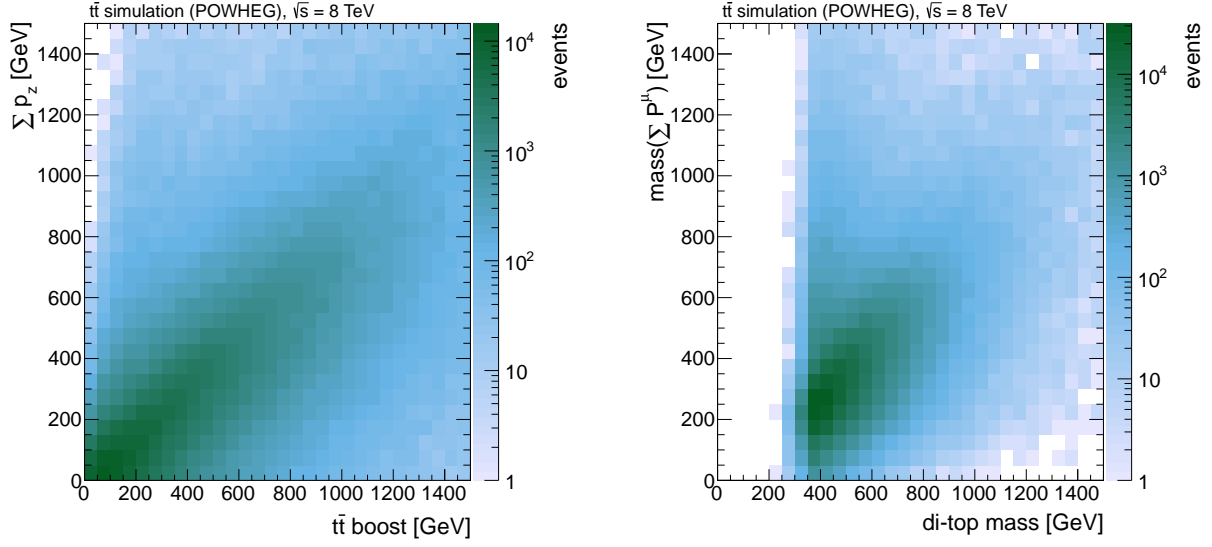
Figure 5.12.: Correlation plots between the interesting variables and the surrogate observables. Left: $t\bar{t}$ boost versus the p_z sum of the selected objects (jets and leptons) in the event. Right: di-top mass versus the invariant mass of the selected objects. For these plots no selection cuts are applied.
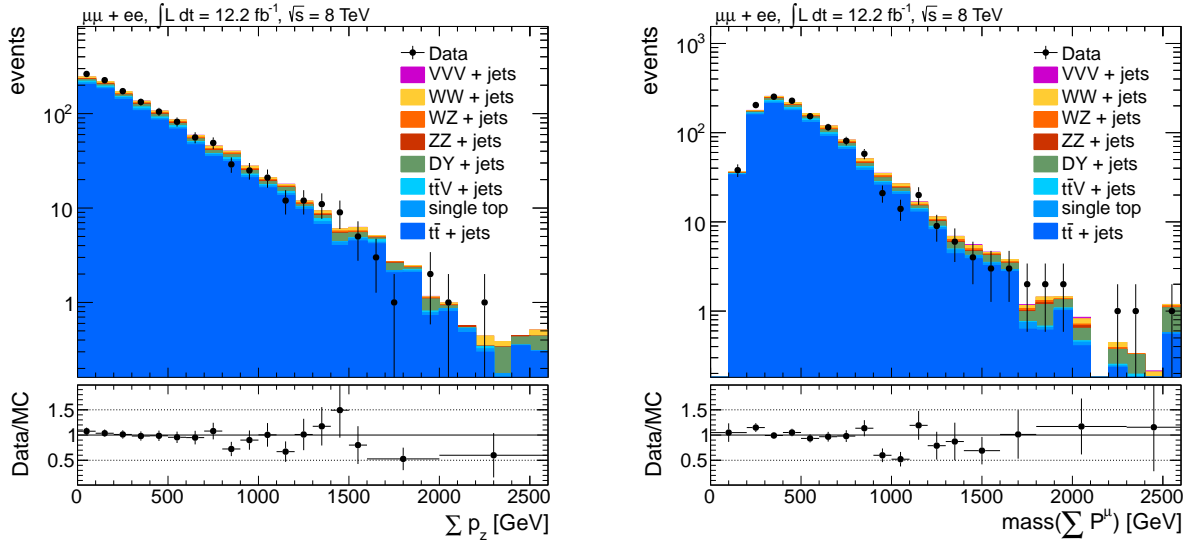
Figure 5.13.: Comparison between data and simulation in the two observables correlated with the critical quantities $t\bar{t}$ boost and di-top mass, which are the p_z sum of all selected objects (jets and leptons) in the event (left), and the invariant mass of all selected objects (right), respectively. Both variables are well modeled in the simulation.

tt̄ boost and mass surrogate observables   For a second check, observables are constructed that are strongly correlated with the tt̄ boost and the di-top mass. On the one hand this surrogate variables do not measure the variables that are of interest as good as it can be done with the full tt̄ reconstruction. On the other hand, however, results can be retrieved with exactly the same event selection as used throughout this analysis. Especially since all decay products of the tops (besides the neutrinos) have to be well measured, and since the reconstruction fails for about 11% of the events [117], a systematic bias w. r. t. the analysis event sample is possible. In that sense the two approaches are complementary.

The surrogate observables are constructed by ignoring the neutrino and any other particles that are out of acceptance or not fulfilling the reconstruction and selection requirements:

$$b_{t\bar{t}} \quad \longrightarrow \quad \left| \sum_i p_{z,i} \right| \tag{5.13}$$

$$M_{t\bar{t}} \quad \longrightarrow \quad \sqrt{\left(\sum_i P_i \right)^2}, \tag{5.14}$$

where p_z is the z component of the momentum and P is the Lorentz vector. The index i runs over the two selected leptons plus two jets that are selected depending on the event content. The jets that should be included in the sums are the b-jets from the top decays. But since b-tagging has its inefficiencies, it is not guaranteed that they can be identified as b-jets. Depending on the number of b-tags in the event, the jets are selected applying the following rules:

if #b-tags ≥ 2 $\quad \rightarrow \quad$ select two leading b-tagged jets
if #b-tags $= 1$ $\quad \rightarrow \quad$ select b-tagged jet plus leading non-tagged jet
if #b-tags $= 0$ $\quad \rightarrow \quad$ select two leading jets

Figure 5.12 illustrates the validity of the replacement. Clearly both pairs of variables are correlated in the Monte-Carlo sample, but also a distortion is visible. The missing energy of the neutrinos can explain the population below the diagonal ($b_{t\bar{t}} > |\sum_i p_{z,i}|$, $M_{t\bar{t}}^2 > (\sum_i P_i^\mu)^2$). Results above the diagonal can be expected in events where the wrong objects are picked in the sums, e. g. an initial-state radiation jet instead of the b-jet from the top decay. In the case of the tt̄ boost, initial-state radiation can lead to an additional effect. On the level of measured objects only the z components of the momenta are summed, but initial-state radiation can cause a significant boost that is not along the beam line.

In Fig. 5.13 the agreement of the surrogate observables between data and simulation is demonstrated. Also the second performed check is not giving rise to doubt in the reliability of the simulation in this specific case.

Variation of the parton density functions   In a third and final check the underlying cause is studied. Both the tt̄ boost and die di-top mass are governed by the energy fractions of the colliding partons. In the Monte-Carlo simulation parton density functions (PDFs) are used to model these energy fractions, separately for gluons and the different quark flavors. Several research groups (e. g. CT [118], MSTW [119], and NNPDF [120]) define sets of PDFs based on theoretical calculation and measurements in different kinds of experiments probing the structure of the proton (e. g. LHC, Tevatron, HERA, and fixed target experiments).

The available PDF sets differ slightly and each of it has uncertainties. Experimental limitation and uncertainties as well as the incompleteness of the theoretical description of the
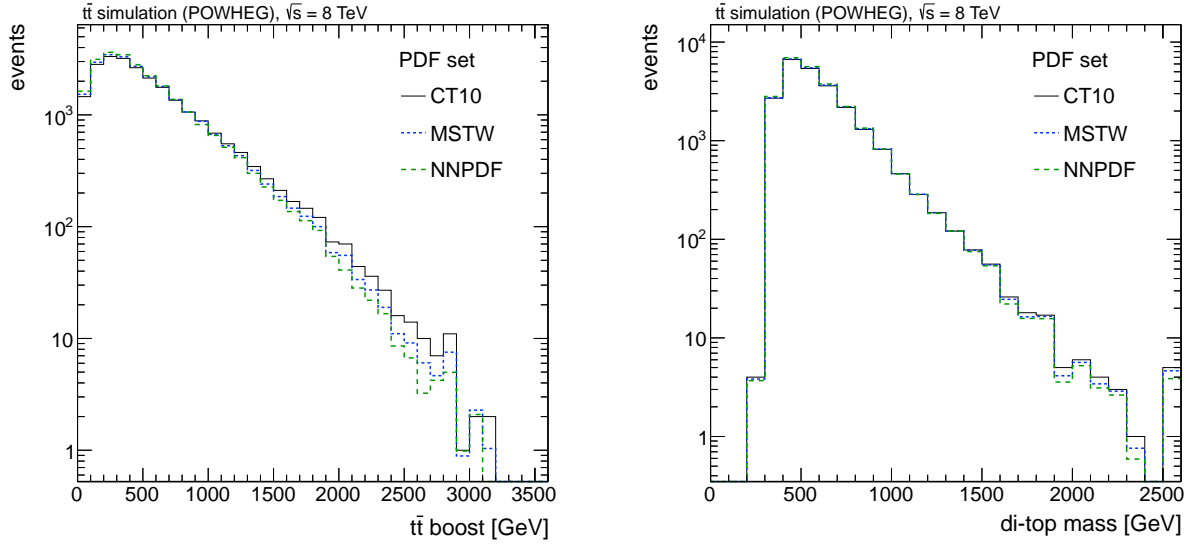
Figure 5.14.: The Effect of the PDF set on the distributions of the $t\bar{t}$ boost and di-top mass. The MC sample is generated assuming the CT10 PDF set, the distributions for the PDF sets MSTW 2008 and NNPDF2.1 are obtained by reweighting the events. The $t\bar{t}$ boost distributions show a systematic deviation between the three PDF sets, while the simulation of the di-top mass is almost independent of the PDFs.

proton (all mentioned groups provide PDF sets calculated including next-to-next-to-leading order QCD corrections) lead to uncertainties on the actual shape of the PDFs. But also different approaches by the groups (e. g. depending on which experimental measurements are included) cause different results [121, 122], all having their advantages and disadvantages.

The best way to account for these uncertainties would be to simulate many event samples, each using one of the available PDF sets, and additional samples to cover the uncertainty range of each PDF set. In a much more effective and for most cases sufficient procedure, only one Monte-Carlo sample is generated using the nominal distributions from one PDF set. After that, event weights are calculated to mimic the 1σ uncertainty variation of the production PDF, but also to reproduce distributions like they would be obtained if another PDF set was used in the production [123].

Here, a $t\bar{t}$ Monte-Carlo sample is used that is produced with the CT10 PDF set. To study the influence of the PDF, the weighting method is used to simulate the distribution of the relevant quantities for two different PDF sets, namely NNPDF2.1 and MSTW 2008. Figure 5.14 shows how the $t\bar{t}$ boost and the di-top mass distributions change: The spectrum of the $t\bar{t}$ boost, which is driven by $\sqrt{x_1 x_2}$ (cf. Eq. 5.9), is systematically different for the three PDF sets. CT10 predicts on average a stronger boost than NNPDF, while the MSTW distribution is between these two. The di-top mass, governed by $x_1 - x_2$ (cf. Eq. 5.12), is very similar for all three PDF sets. Only a very small deviation is found which is similar to the deviation in the boost: CT10 predicts the hardest spectrum and NNPDF the softest.

The importance of the boost and the invariant mass of the $t\bar{t}$ system has been discussed. The cited results from the full $t\bar{t}$ reconstruction, as well as the approach replacing the quantities by

observables, show a convincing agreement between data and simulation. Only the reweighting to different parton density functions shows a deviation that might effect the prediction power of the event-mixing procedure. The difference between the PDF sets can be understood as an uncertainty since it is not known, which of the PDF set describes the data the best. In Section 6.2.7 a systematic uncertainty is derived from the reweighting to account for that potential bias of the prediction.

5.3.2. t$\bar{\text{t}}$ Spin Correlation

In the previous section the t$\bar{\text{t}}$ production and decay process was considered only with regard to their kinematic properties. The correlations found so far were due to energies in the t$\bar{\text{t}}$ production. From that point of view, if the top and anti-top were produced in rest (in the laboratory frame) and decayed isotropically, the leptons would be uncorrelated.

From the electroweak interactions it is known that there is a spin dependency leading together with a correlation between the spins of the top and the anti-top to a kinematic correlation between the leptons. For the purpose of this analysis, only a rough overview of spin correlation and its effects is given, details can be found elsewhere [124].

The relevant conclusions for this analysis are:

- The effects of spin correlation on the decay products is a special feature of the top quark, it is related to its very short life-time. All other quarks hadronize before they decay and the spin correlation gets destroyed. Only the top quark's life-time is short enough that it decays before QCD interactions significantly affect the spin, thus the spin correlation is propagated to the W$^{\pm}$ bosons.

- The correlation between the spins of the top and the anti-top depends on the production process: At the LHC gluon-gluon fusion is dominant since anti-quarks with high x are rare in proton-proton collisions.

- The spin configuration of the t$\bar{\text{t}}$ system depends on the initial state. At low di-top masses the fusion of like-helicity gluons is dominant leading to an aligned t$\bar{\text{t}}$ spin configuration ($\uparrow\uparrow$ or $\downarrow\downarrow$). At higher di-top masses pairs of unlike-helicity gluons play a more important role and the preferred t$\bar{\text{t}}$ spin configuration is anti-aligned ($\uparrow\downarrow$ or $\downarrow\uparrow$).

- The weak decays t $\rightarrow$ W^+b and W$^+ \rightarrow \ell^+\nu$ (and for $\bar{\text{t}}$ accordingly) are spin-dependent, in particular the lepton direction of flight in the top rest frame is directly connected to the top spin, since its "sister", the (anti-)neutrino, couples only left (right) handed to the W. Actually, this makes the lepton to an ideal candidate to probe the spin correlation.

- The explicit effect of spin correlation on the lepton kinematics can be summarized as follows:
  top spins parallel ($\uparrow\uparrow$) $\Longrightarrow$ W spins parallel ($\uparrow\uparrow$) $\Longrightarrow$ ℓ momenta anti-parallel ($\Uparrow\Downarrow$)
  top spins anti-parallel ($\uparrow\downarrow$) $\Longrightarrow$ W spins anti-parallel ($\uparrow\downarrow$) $\Longrightarrow$ ℓ momenta parallel ($\Uparrow\Uparrow$)

Since Monte-Carlo simulated events are used for validation of the event-mixing method, the proper simulation of the spin correlation has to be verified.

As described above, the spin of the top determines the preferred momentum direction of the leptons. Of course, the momentum of the top interferes, since it introduces another preference direction caused by pure kinematics. This effect can be disentangled from the spin effect by studying the lepton direction in the rest frame of the top.
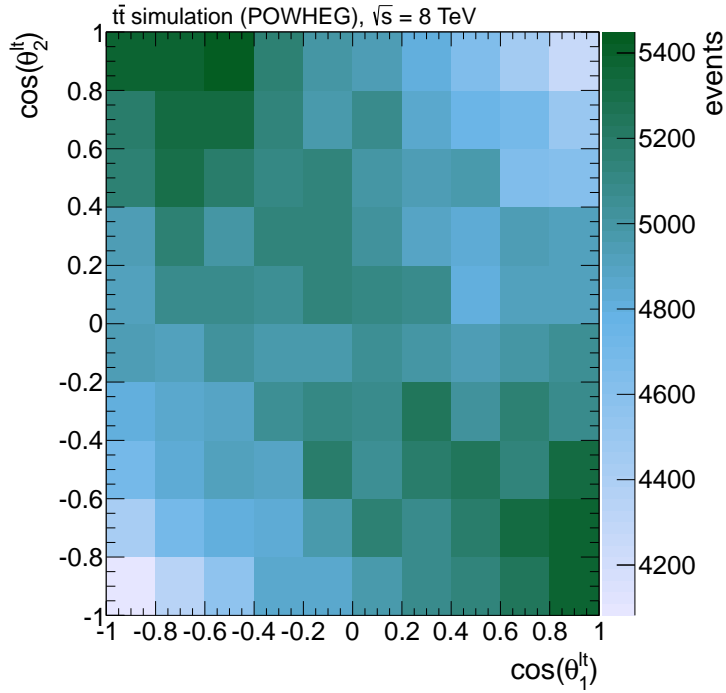
Figure 5.15.: An illustration of how the $t\bar{t}$ spin correlation influences the lepton kinematic in Monte-Carlo simulation. The angle of one lepton w.r.t. the momentum of the top quark from which it originates in the rest frame of this top is plotted against the same quantity of the second lepton. By evaluating these angles in the according top rest frames kinematic correlation effects are eliminated and the spin-correlation effects can be studied.

In data such a study is difficult as the top rest frame is a priori not known due to the missing neutrino momentum. But in simulated events the top momentum is completely known. The correlation of the top spins is visible in the correlation of the lepton angles w.r.t. the top momentum in the top rest frame. In Fig. 5.15 one can see that these angles are negatively correlated. From that observation one can conclude that for the top and the anti-top the aligned spin orientation is preferred: If the lepton momentum is parallel to the anti-top momentum the probability is increased that the anti-lepton's momentum is opposite to the momentum of the top in the according rest frames, and vice versa. Considering the fixed opposite chirality of the neutrinos, this is an indication for a preferred parallel spin configuration of the top quarks.

Another – experimentally more accessible – observable for $t\bar{t}$ spin correlation is the transverse projection of the lepton-lepton opening angle $\Delta\phi_{\ell^+\ell^-}$. In this variable there is of course the described interference between spin effects and kinematically preferred event topologies present. Both CMS and ATLAS performed analyses [125–127] using $\Delta\phi_{\ell^+\ell^-}$ as one of the sensitive observables. Figure 5.16 shows the comparison of the measurement with two simulated event samples, of which only one considers spin correlation. The results of both experiments are very similar: The $\Delta\phi_{\ell^+\ell^-}$ distribution is dominated by the kinematically preferred back-to-back event topology in the transverse projection. But the comparison between the Monte-Carlo samples with and without spin correlation suggests that the simulation with spin correlation is a very good description for the data measurements. A requirement for b tagged jets and a rejection
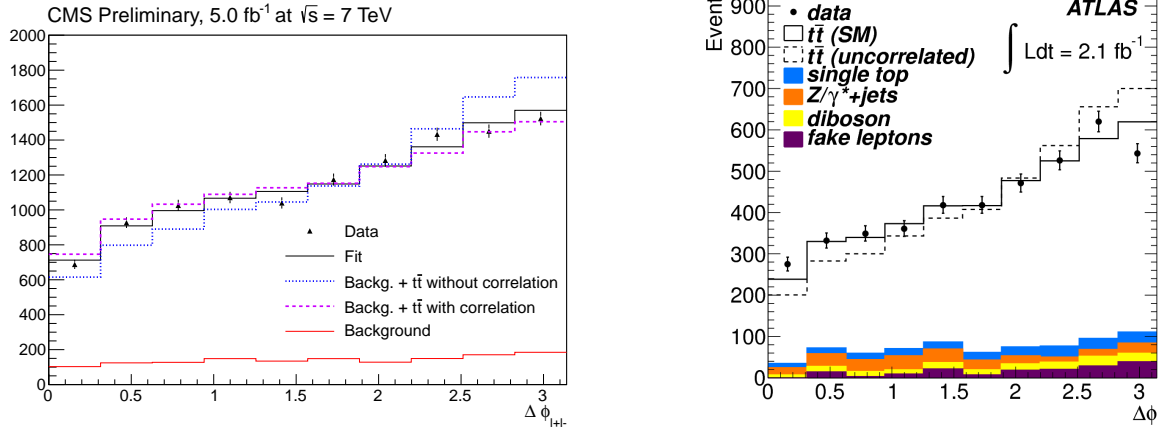
Figure 5.16.: Effect of spin correlation in $t\bar{t}$ events on the transverse angle between the two leptons is measured by CMS [125] and ATLAS [126] in 7 TeV data. Both experiments observe a tendency of the data to be better described by a MC sample that considers spin correlation than by the reference sample.
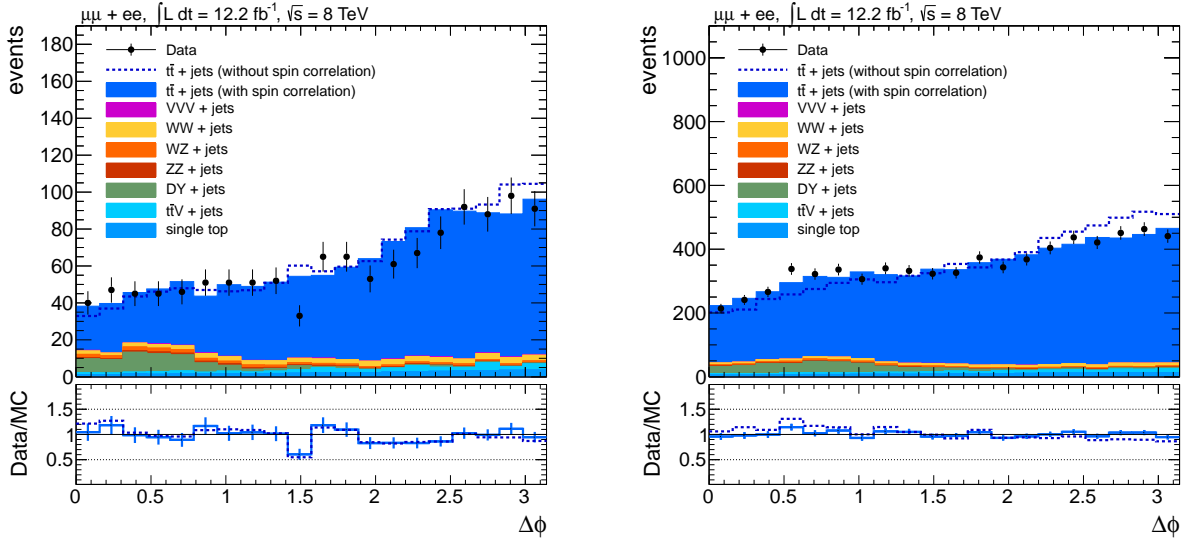
Figure 5.17.: Distribution of $\Delta\phi$ in data and Monte Carlo after the event selection that is used in this analysis. The filled $t\bar{t}$ histogram represents the MC@NLO simulation including Standard-Model spin correlation. The dashed line shows the spectrum in a MC@NLO sample with no spin correlation. The other processes are added to both distributions. Two ratio plots are shown with the different MC samples as denominators. On the left the default event selection is applied. The effect of spin correlation is hardly visible. On the right the $E_{\mathrm{T}}^{\mathrm{miss}}$ cut is relaxed from 160 GeV to 100 GeV. Here, the preference of the sample including spin correlation effects is obvious.
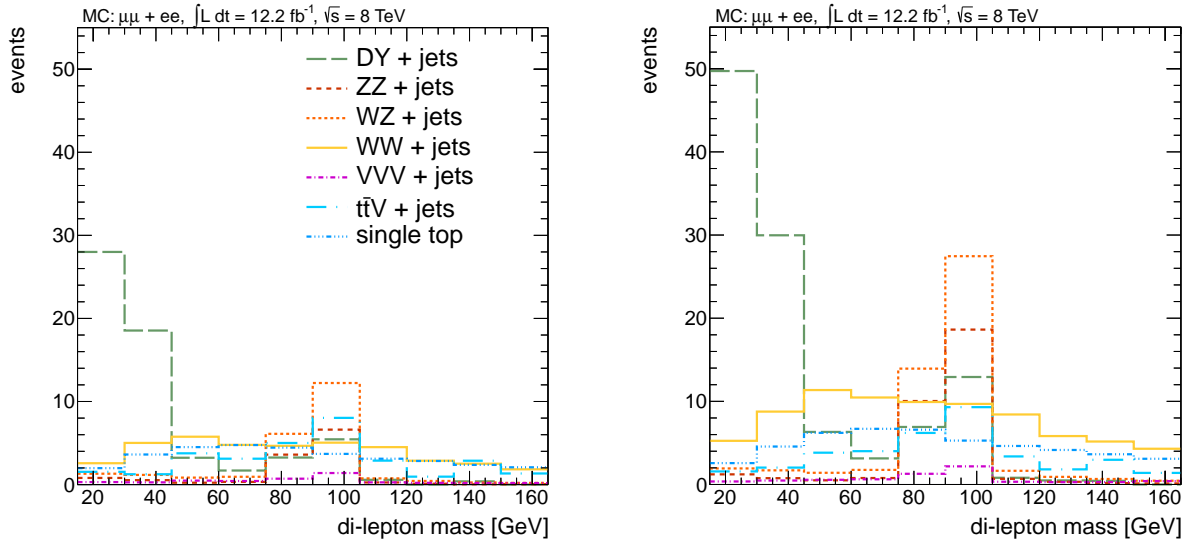
Figure 5.18.: After the event selection several other processes can be expected besides t$\bar{\text{t}}$ events. On the left the default selection cuts requiring at least two jets are applied, on the right only one jet is required. The latter is used searching for direct gaugino production.

of the di-lepton mass region around the Z^0 mass is applied in order to enrich the dataset with t$\bar{\text{t}}$ events.

In this analysis the dominance of t$\bar{\text{t}}$ processes is a result of the $E_{\text{T}}^{\text{miss}}$ requirement. Therefore, in Fig. 5.17 on the left the same distribution is shown after the selection that is used in this analysis and for 8 TeV data. There is almost no systematic difference between the two MC samples visible. For the right plot the $E_{\text{T}}^{\text{miss}}$ cut is changed from $E_{\text{T}}^{\text{miss}} > 160\,\text{GeV}$ to $E_{\text{T}}^{\text{miss}} > 100\,\text{GeV}$. This cut threshold is still high enough to suppress the electroweak backgrounds, but the difference between the simulated samples becomes visible. The data prefers the simulation that considers t$\bar{\text{t}}$ spin correlation.

The different behavior for different $E_{\text{T}}^{\text{miss}}$ thresholds is a consequence of the neutrino kinematics. Since $E_{\text{T}}^{\text{miss}}$ is mainly caused by the two neutrinos in di-leptonic t$\bar{\text{t}}$ events, an $E_{\text{T}}^{\text{miss}}$ requirement prefers certain neutrino topologies. Since the neutrino topology is exactly the reason why $\Delta\phi_{\ell^+\ell^-}$ is an observable of spin correlation, a high $E_{\text{T}}^{\text{miss}}$ cut can hide or interfere with the relatively small effect of spin correlation.

5.3.3. Contamination from Other Background Processes

In Section 4.3 the event selection is described, mentioning that special emphasis is placed on rejecting events containing Z^0 bosons. The background prediction method presented in this work distinguishes between events with a strong kinematic lepton-lepton correlation and events with no or only a weak correlation. The former class of events is assumed to be a supersymmetric signal, and the latter is treated as background.

Events containing $Z^0 \to \ell^+\ell^-$ decays clearly show a strong correlation between the lepton kinematics. In that sense these events behave like the signal. Simple Drell-Yan processes like
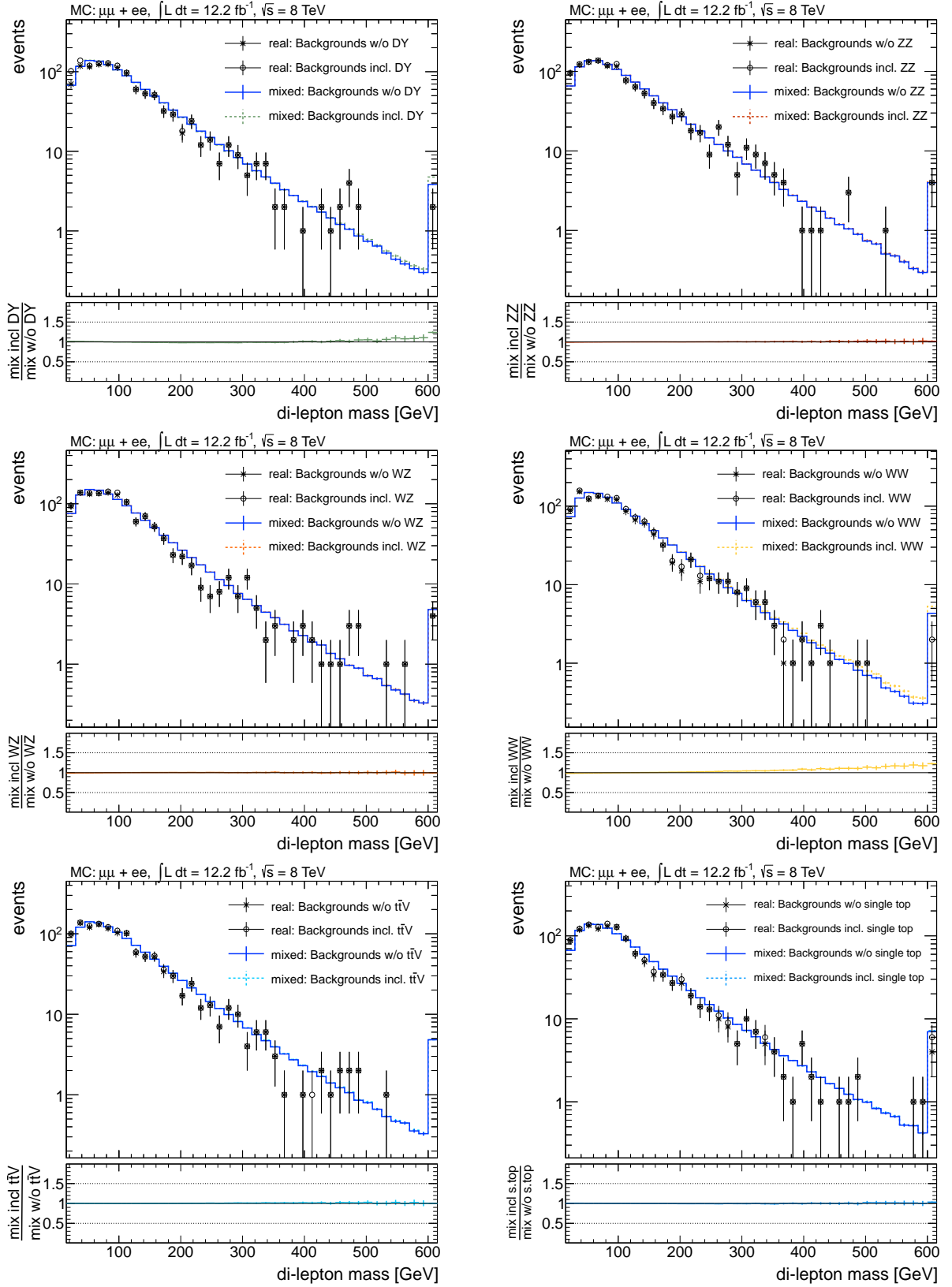
Figure 5.19.: Effect of background contamination on the event-mixing prediction. The real and mixed di-lepton mass spectra are separately shown with and without the contributions from Drell-Yan, Z^0Z^0, $W^{\pm}Z^0$, W^+W^-, $t\bar{t}V$, and single top processes.

$q\bar{q} \to Z^0 \to \ell^+\ell^-$ are effectively suppressed by the E_T^{miss} requirement but have a large cross section. Processes that contain genuine E_T^{miss} survive the selection to a large fraction, they matter although their cross sections are small. Figure 5.18 summarizes all relevant additional backgrounds for the default selection and for the 1-jet selection:

- A small Z^0 peak made from Drell-Yan events is present in both selection scenarios. The E_T^{miss} in these events is caused by mis-measurements and resolution effects mainly of jets recoiling the Z^0 boson.

- The much larger fraction of surviving Drell-Yan events contain $Z^0 \to \tau^+\tau^-$ decays, i.e. the visible di-lepton mass is below the Z^0 peak. Since a τ lepton can decay into a light lepton and two neutrinos, these events contain genuine E_T^{miss}.

- The Z^0 peak is dominated by Z^0Z^0 and $Z^0W^\pm$ events. The decay modes that survive the event selection are predominantly $Z^0Z^0 \to \ell^+\ell^-\nu\bar{\nu}$ and $Z^0W^\pm \to \ell^+\ell^-\ell\nu$.

- W^+W^- events show a broad distribution, as expected from the non-resonant lepton origin. These events survive the selection due to neutrinos as well.

- Events with $t\bar{t}$ in association with an additional vector boson show a combination of the small Z^0 peak and a broader spectrum, which reflects the different origins of leptons in these events.

- Most single top events that survive the di-lepton selection contain an additional $W^\pm$ (tW-channel). The lepton-lepton correlation is therefore similar to $t\bar{t}$ events.

- Tri-bosons event play no relevant role in this analysis due to their small cross sections.

In Fig. 5.19[1] the effect of these events on the event-mixing prediction is illustrated. In each plot the real and the mixed event distributions are shown twice, once with the process under consideration and once without. Below each plot the ratio between the two mixed shapes is plotted. Ideally the contributions from the studied processes do not change the shape of the prediction, i.e. the ratios should be flat. For $t\bar{t}V$ and single top this is the case: Since these events are very similarity to $t\bar{t}$ events, they behave similarly under event mixing. The increasing effect from Z^0Z^0 to $W^\pm Z^0$ to W^+W^- is a consequence of the increasing number of events that are expected from these processes. They all have a slightly harder lepton spectrum than $t\bar{t}$. Therefore, also the mixed distributions are slightly shifted to higher values.

The same effect can be observed from the Drell-Yan contribution. In the high-energetic tail the mixed distribution including Drell-Yan events is slightly higher. This effect is mainly driven by events with Z^0 bosons directly decaying into muons or electrons. The second class of Drell-Yan events containing $Z^0 \to \tau^+\tau^-$ decays leads to a very slight deviation in the low energetic part of the di-lepton mass spectrum. The lost energy of the neutrinos in the τ decays increases the number of mixed events with small di-lepton masses.

Although the observed effects are small, it is accounted for in terms of a systematic uncertainty as described in Section 6.2.8.

---

[1]The default event selection is applied for these plots. The same study for the selection requiring only one jet is summarized in Appedix D.
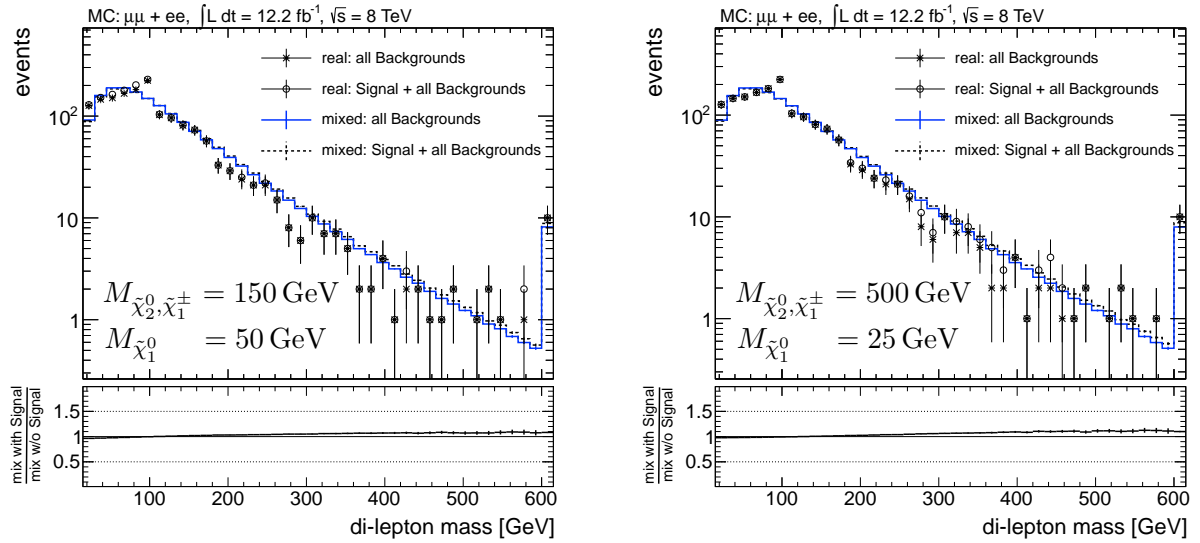
Figure 5.20.: Effect of a potential SUSY signal on the prediction of the $t\bar{t}$ background. The plots show the results of two different parameter points of the electroweakino model. The assumed masses are given in the plots. The $\tilde{\ell}$ mass is in both cases in the middle of the stated gaugino masses.

5.3.4. Signal Contamination and Prediction Correlation

Every data-driven background-estimation method must state how a potential signal would influence the result of the background prediction. Ideally, there should be no influence at all; if the background is correctly predicted, it is independent from the presence of signal events. However, in reality there are many possibilities how a signal can interfere with the background prediction – in particular because the properties of the signal are not known.

The classical data-driven method uses one or more background regions, from where some sort of extrapolation to a signal region is performed. The basic assumption is that these background regions are dominated by background events. In the optimal case, they are completely free of signal events. In reality this can typically not be guaranteed and the contamination of the background regions effects the prediction. Two cases can be distinguished: The presence of signal leads to an over-prediction of the background in the signal region or to an under-prediction. The former case is called *conservative*, since less signal events are measured compared to a situation knowing the correct amount of the background events.

This analysis is different. The same events are used for both, searching for a signal among them and extracting an estimation for the background. The signal is assumed to show the described kinematic correlation between the two leptons. Of course, one can also think of Supersymmetry events with two uncorrelated leptons. Such signal models would not be discovered by this analysis, the events would be treated as background events.

But also signal events that show the assumed correlation enter the mixing procedure and occur in the background prediction. The method, as it is used here, makes use of the shape of the distribution, whereas the number of events is irrelevant. In a perfect world, the mixed events containing SUSY events follow the same distribution as mixed events from only $t\bar{t}$ processes. One reason why this might not be the case, is a possibly different energy spectrum of the leptons.

In SUSY events the energy spectrum depends on the *mass splitting* of the intermediate particle: For example, if the masses of the $\tilde{\chi}_2^0$, the $\tilde{\ell}$, and the $\tilde{\chi}_1^0$ are very similar, the energy spectrum of the leptons is very soft. Such a signal would change the prediction for the $t\bar{t}$ background and the extracted number of signal events might be wrong.

The actual effect of signal contamination can not be answered in general, since it depends on the Supersymmetry model. But the issue is less serious as it might look like: If the kinematic properties of the signal events – and in particular those of the leptons – are similar to $t\bar{t}$ events, the effect of signal contamination is small. On the other hand, if the events and leptons are very different from the background, the prediction might be biased, but in this case there are easier ways to discover the signal. In other words: The harder it is to distinguish the signal from the background, the better works the event-mixing technique as background-estimation method.

In Fig. 5.20 the influences of two example signals on the prediction are illustrated in a similar way as it is done in the previous section with the contamination from other backgrounds. The real and the mixed distributions are shown once with and once without the signal. As signal samples two parameter points of direct gaugino production are used. The events are selected according to the 1-jet selection strategy.

From the signal a mass edge is expected with a position that depends on the involved particle masses, as discussed in Section 5.1. Consequently for the low-mass point on the left a slight excess of event below the Z^0 peak is visible. The right plot with the much higher mass difference shows SUSY events with di-lepton masses of several hundred GeV. Despite the large differences in parameters and di-lepton mass spectrum, the effects on the mixed event distribution are very similar. In both models the lepton energy spectrum is slightly harder than in $t\bar{t}$ events, thus the mixed di-lepton masses are also high due to signal contamination.

Related issues are statistical correlations between the real events and the mixed events and within the mixed events. Typically one is interested in a background estimation that follows the true underlying distribution, but is statistically independent from the measured distribution. Especially if the deviation between the data and the predicted spectrum should be statistically interpreted – e.g. by performing a χ^2 test – the correlation should vanish. Alternatively, if the correlation is known one can make use of the full covariance matrix to perform the χ^2 test instead of using the residuals only.

In the case of the event-mixing prediction the reason for the correlation between real and mixed events is trivial: The prediction is generated from the same events it is compared to. For example, if there is an upward fluctuation in the lepton energy in the real event sample, this upward fluctuation is still present in the mixed distribution. Additionally it is obvious that the mixed events can not be statistically independent from each other: From n real events up to $n(n-1)$ mixed events can be generated. Each real event is used in up to $n-1$ mixed events.

In principle the correct uncertainties and correlations can be calculated for the event-mixing technique [128]. For the purpose of this analysis, Monte-Carlo simulated event samples are used in order to interpret the result of a χ^2 test (cf. 7.1). Therefore, the χ^2 is not used as an absolute measure for the agreement of the distributions.

5.3.5. Effects of Event Selection Cuts

The object and event selection is presented in Section 4.3. Here, it is studied whether the capability of the event-mixing method to predict the $t\bar{t}$ background depends on the selection cuts. In particular, the effects of varying the actual cut threshold are addressed. Only the

kinematically relevant selection requirements are discussed here: lepton p_T, lepton η, $E_\mathrm{T}^\mathrm{miss}$, and jet multiplicity.

The event-mixing method exploits the full kinematic information of the leptons to generate the prediction for the di-lepton mass distribution. Therefore, every selection cut on a kinematic quantity is a potential source of a bias:

- Cuts on lepton p_T and η could bias the prediction, since these quantities directly enter the calculation of the di-lepton mass.

- In $t\bar{t}$ events the $E_\mathrm{T}^\mathrm{miss}$ is correlated with $p_\mathrm{T}^{\ell\ell}$ via the common origin from the W decays into a lepton and a neutrino ($E_\mathrm{T}^\mathrm{miss}$).

- Generally, cuts on variables that describe the event topology, such as $E_\mathrm{T}^\mathrm{miss}$ or number of jets, can also bias the lepton kinematics since these quantities are connected to the recoil of the di-lepton system.

To study the influence of these cuts the thresholds are varied and the proof-of-principle plot in Fig. 5.4 is redone.

Figures 5.21-5.23 show the results of the threshold variations of the most important cuts. In each row, the middle plot is done with the default cut value, i.e. all middle plots are identical. The left plot is done with the given cut threshold at a relaxed value, for the right plot the cut is tightened. All other cuts than the one explicitly stated are kept at their default value.

If the lepton p_T cut is increased (Fig. 5.21, right), a lot of events are lost in the low di-lepton mass region. The predicted distribution is also shifted to higher masses, but much less than the real one. The reason can be found in another correlation in $t\bar{t}$ events, which is illustrated in Fig. 5.24: Events with a high-p_T lepton tend to have a back-to-back structure. The effect of such an event topology was already discussed in the context of high di-top masses (Section 5.3.1): If there is a preference for large opening angles in the real event, the mixed events have on average smaller angles, which results in an underestimation of the di-lepton mass. If the p_T cut is decreased (Fig. 5.21, left), the opposite applies: In the very first bins of the spectrum the real distribution is slightly overpredicted.

The cut on the lepton η (Fig. 5.22) has a slight effect on the tail of the prediction. The tighter the cut, the lower the prediction in the tail compared to the real spectrum. The angular restriction enriches the mixed sample with events containing smaller opening angles leading to a tendency to smaller di-lepton masses.

Figure 5.23 shows that the variation of the $E_\mathrm{T}^\mathrm{miss}$ cut has a similar effect as the variation of the lepton-p_T cut: A weaker $E_\mathrm{T}^\mathrm{miss}$ cut leads to an over-prediction at very small di-lepton masses, a higher $E_\mathrm{T}^\mathrm{miss}$ cut causes the opposite in the same region. The reason can be found in the mentioned correlation between $p_\mathrm{T}^{\ell\ell}$ and $E_\mathrm{T}^\mathrm{miss}$ in $t\bar{t}$ events. Figure 5.25 illustrates the correlation between the $\ell\ell$ angular distance ΔR and $E_\mathrm{T}^\mathrm{miss}$. It is less pronounced than the correlation between ΔR and lepton p_T, and the right plot in Fig. 5.25 shows the presence of a contradirectional effect in the lower $E_\mathrm{T}^\mathrm{miss}$ bins, which can be understood from a purely kinematic point of view: The larger the $E_\mathrm{T}^\mathrm{miss}$, the more probable it is recoiling against both leptons.

The remaining selection cut on the jet multiplicity has only a very small effect. The according plots are shown in Appendix E.1.

The similarity between varying the lepton p_T and the $E_\mathrm{T}^\mathrm{miss}$ cut suggests to study not only the effect of changing one single cut threshold, but considering also correlations between the
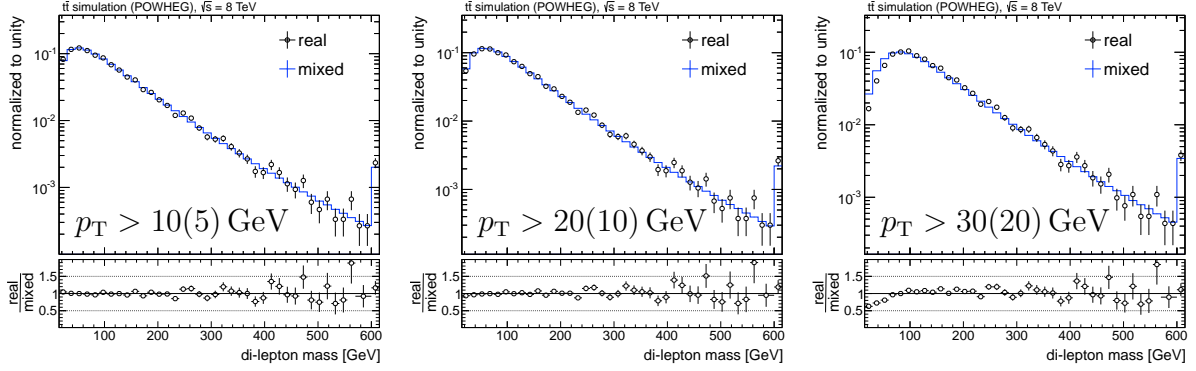
Figure 5.21.: Variation of the lepton p_T cut: The middle plot represents the nominal cut value, which in loosened on the left and tightened on the right.
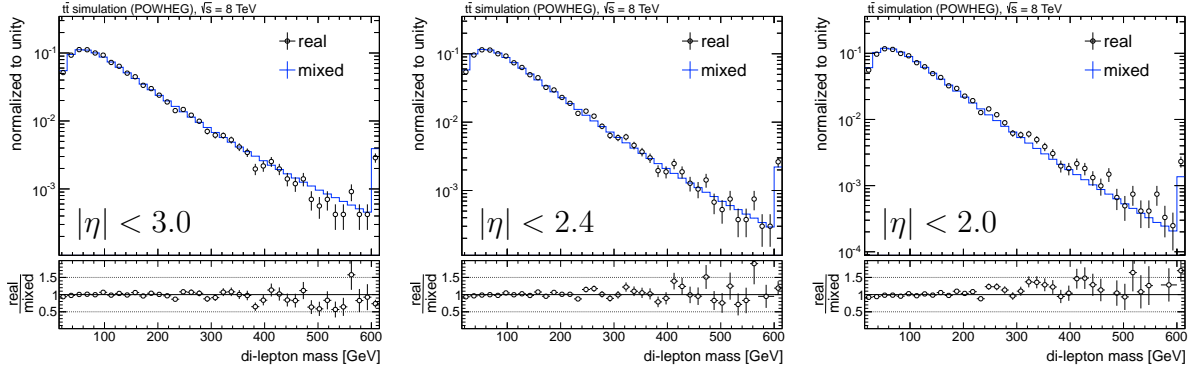
Figure 5.22.: Variation of the lepton η cut: The middle plot represents the nominal cut value, which in loosened on the left and tightened on the right.
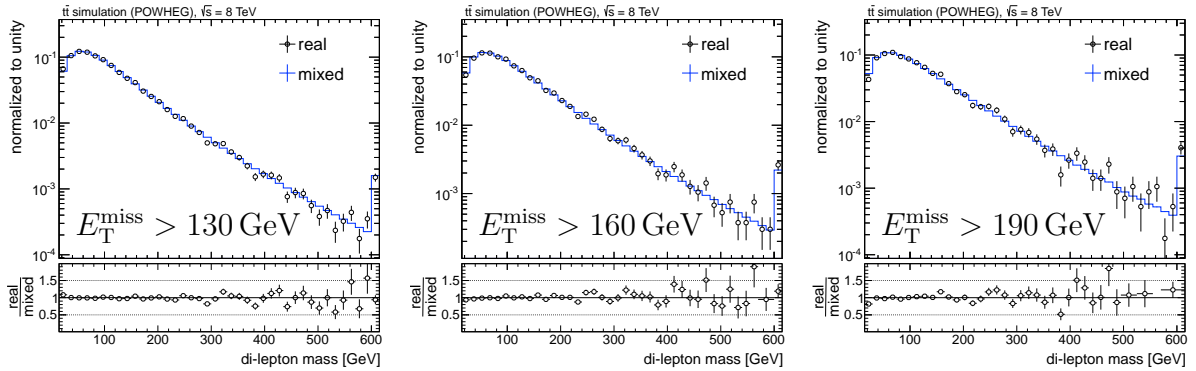
Figure 5.23.: Variation of the lepton E_T^{miss} cut: The middle plot represents the nominal cut value, which in loosened on the left and tightened on the right.
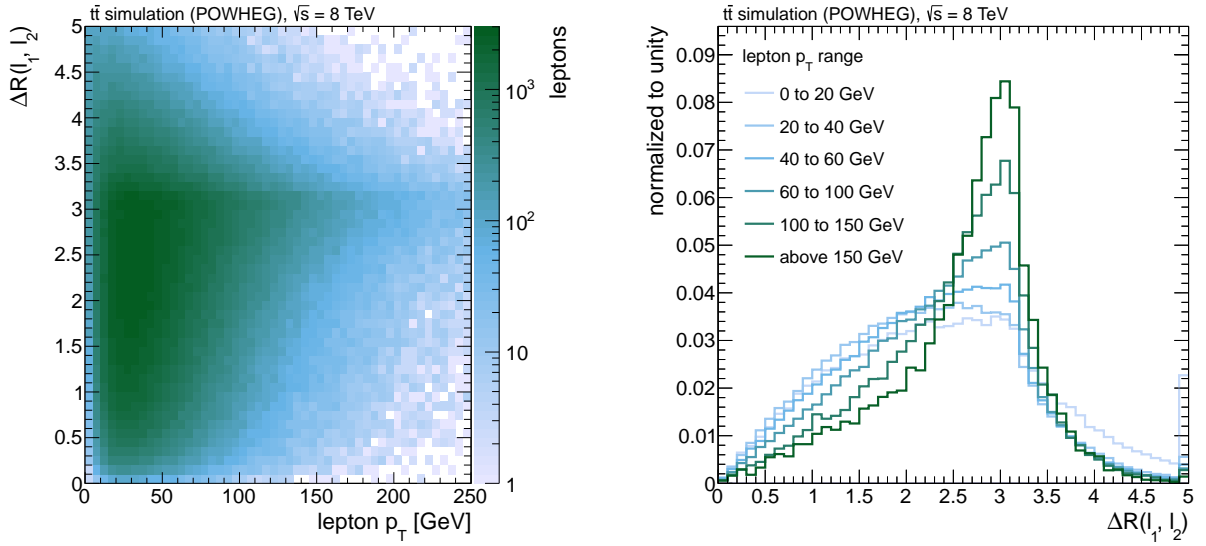
Figure 5.24.: Correlation between the lepton p_T and the lepton-lepton opening angle in simulated $t\bar{t}$ events. On the left the 2D histogram of ΔR versus lepton p_T is plotted. On the right the ΔR distribution binned in lepton p_T is shown, the histograms are normalized to unity to visualize shape differences. No selection cut are applied.
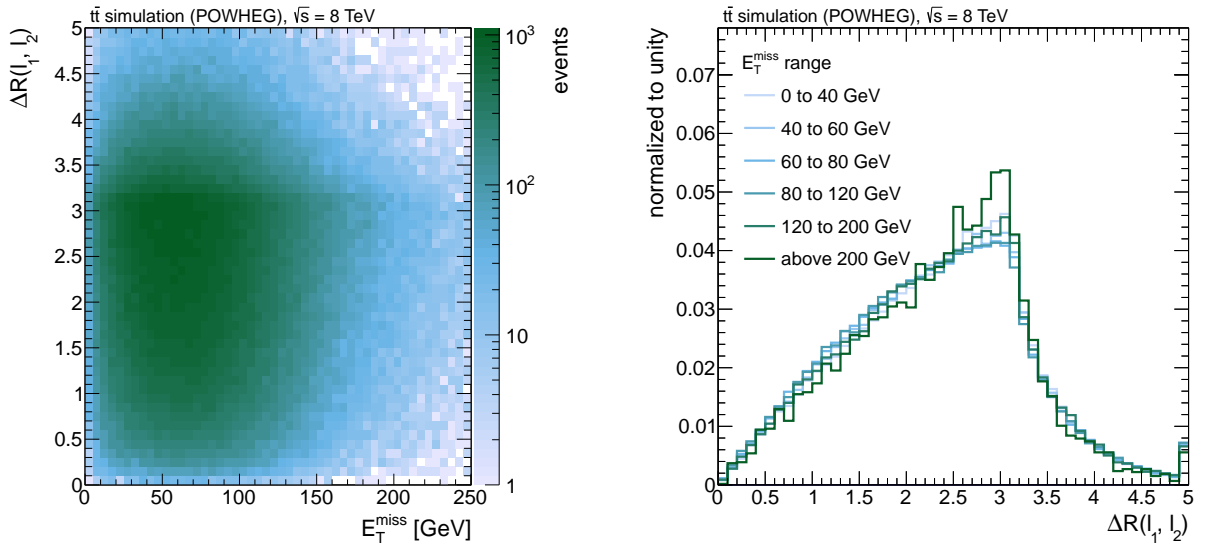
Figure 5.25.: Correlation between E_T^{miss} and the lepton-lepton opening angle in simulated $t\bar{t}$ events. On the left the 2D histogram of ΔR versus E_T^{miss} is plotted. On the right the ΔR distribution binned in E_T^{miss} is shown, the histograms are normalized to unity to visualize shape differences. The back-to-back topology ($\Delta R \approx \pi$) is most preferred in high-E_T^{miss} events, but also in events with very low E_T^{miss}.
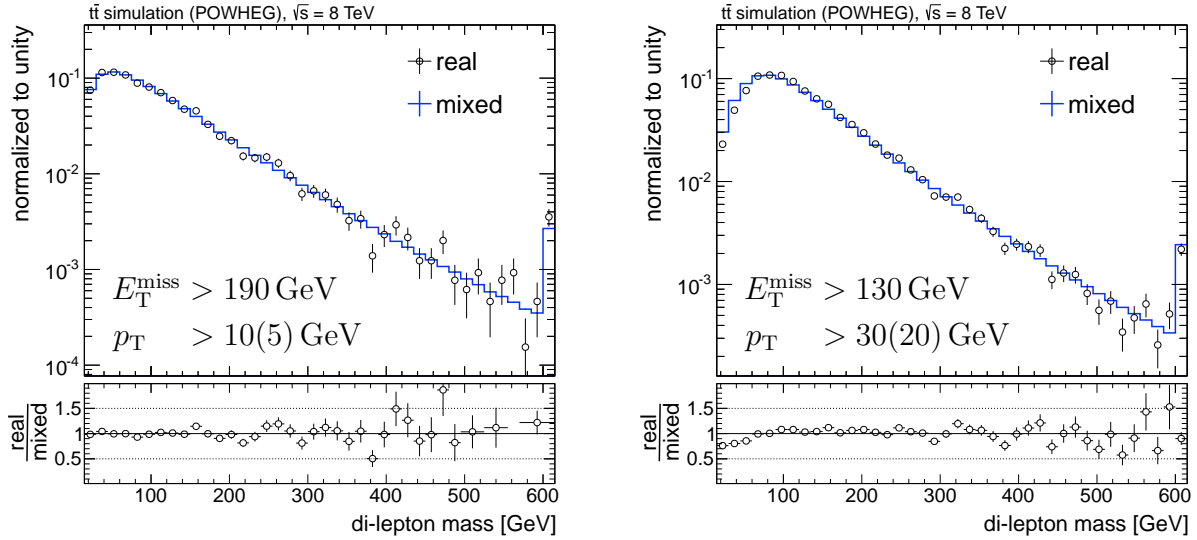
Figure 5.26.: Effect of two simultaneous cut variations: On the left the lepton p_T cut is lower than the default, the E_T^{miss} cut is tighter. On the right the lepton p_T cut is tighter and the E_T^{miss} cut threshold is lower.

cut thresholds. Additionally, stronger or weaker requirements on the total none-leptonic event content (E_T^{miss} and jet multiplicity) can show a different behavior than single cut variations. In Appendix E.2 all "2D" cut variations are shown. From these plots for most of the cut pairs no correlation can be concluded. Only the lepton p_T and E_T^{miss} thresholds show a dependency: In Fig. 5.26 the real di-lepton spectrum is compared to the predicted if simultaneously one cut is tightened while the other is loosened. The left plot indicates that a lower p_T cut can compensate for harder restrictions on E_T^{miss}, whereas the right plot shows that the opposite is not true.

5.3.6. Other MC Generators

Although the event-mixing method is purely data driven, the analysis relies on Monte-Carlo simulation, since it is tested and validated with simulated events. Also for the interpretation of the result MC input is needed. Events produced by different MC generators could behave differently under event mixing. This applies generally since many aspects of the event kinematics can influence the prediction power of the method.

The main $t\bar{t}$ Monte-Carlo sample in this work is simulated with POWHEG [129]. The hard production process is simulated in NLO accuracy by POWHEG, whereas the parton showering and hadronization is simulated with PYTHIA [130].

Here, the proof-of-principle is repeated with two samples produced with other Monte-Carlo generators: MADGRAPH [131, 132] and MC@NLO [133]. The former uses also PYTHIA for the showering and hadronization, the latter uses HERWIG [134]. In this way the method is tested with three different simulators of the matrix element and with two different simulators of the parton showering and hadronization. Figure 5.27 shows for the two samples the simulated di-lepton mass spectrum compared to the prediction derived from the event-mixing technique. Both plots show reasonable agreements, but also differences become visible. In the MADGRAPH sample the tail of the distribution is clearly underpredicted, whereas the small overprediction
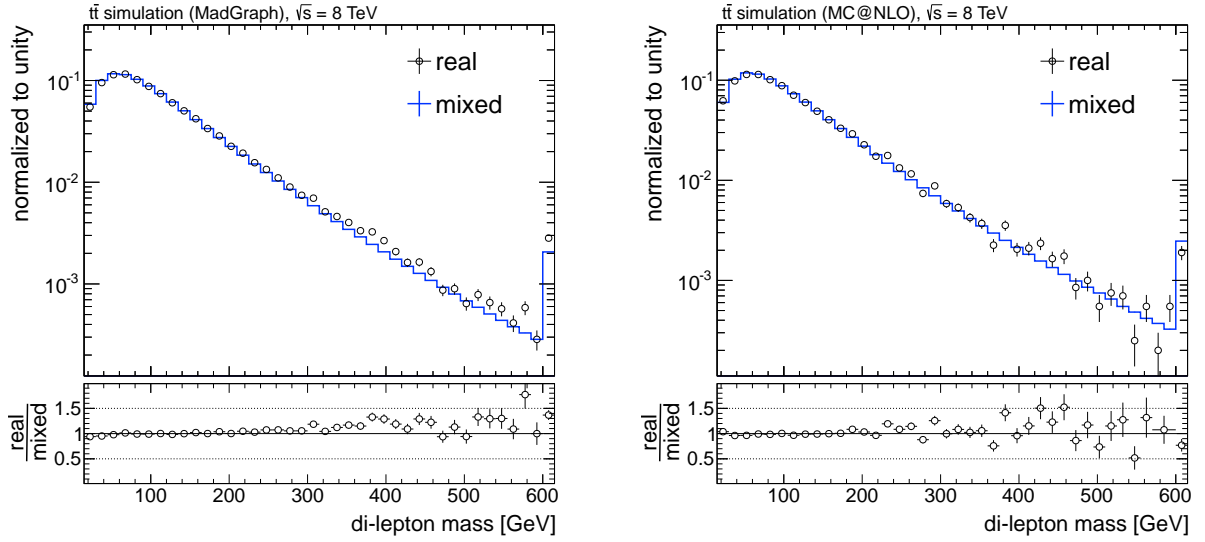
Figure 5.27.: The proof-of-principle plot in Fig. 5.4 is redone with events simulated with Monte-Carlo generators MADGRAPH and MC@NLO.

at very small di-lepton masses is similar to the POWHEG sample (cf. Fig. 5.4). In the MC@NLO sample the tail is correctly predicted, but the behavior at small masses is sightly different: The number of events in the first bin is slightly underestimated followed by a small dip in the ratio plot.

Figure 5.28 shows how the three Monte-Carlo programs simulate the $t\bar{t}$ boost and the di-top mass. These event energies were found to be relevant for the correlation between the leptons. Also here small differences are visible. For both variables MADGRAPH simulates a slightly softer spectrum than POWHEG and MC@NLO. Additionally the turn-on in the di-top mass shows small deviations.

The observations give rise to a systematic uncertainty on the result of this study. In Section 6.2.4 it is described how the three proof-of-principle plots are used to derive corrections to the data driven prediction.

5.4. Digression: Angle-Momenta Mixing

In this section another type of event mixing is presented. In the rest of this work the full Lorentz vectors of the leptons are mixed, suffering from risk of being prone to correlation effects. The effects of the correlation have been investigated in detailed in the previous sections. It was shown that a correlation is present, in particular between the angular properties of the leptons, but does not harm the prediction power of the event-mixing technique. However, if there was a possibility to perform the mixing with no correlation at all in the background events – at least from an aesthetic point of view, that method would be preferable.

Instead of starting with the invariant mass calculated from the sum of the Lorentz vectors, also the formulation in terms of energies and angular relation can be used:

$$M_{\ell\ell} = \sqrt{(P_{\ell^+} + P_{\ell^-})^2} = \sqrt{2E_{\ell^+}E_{\ell^-}(1 - \cos\theta_{\ell\ell})}. \tag{5.15}$$
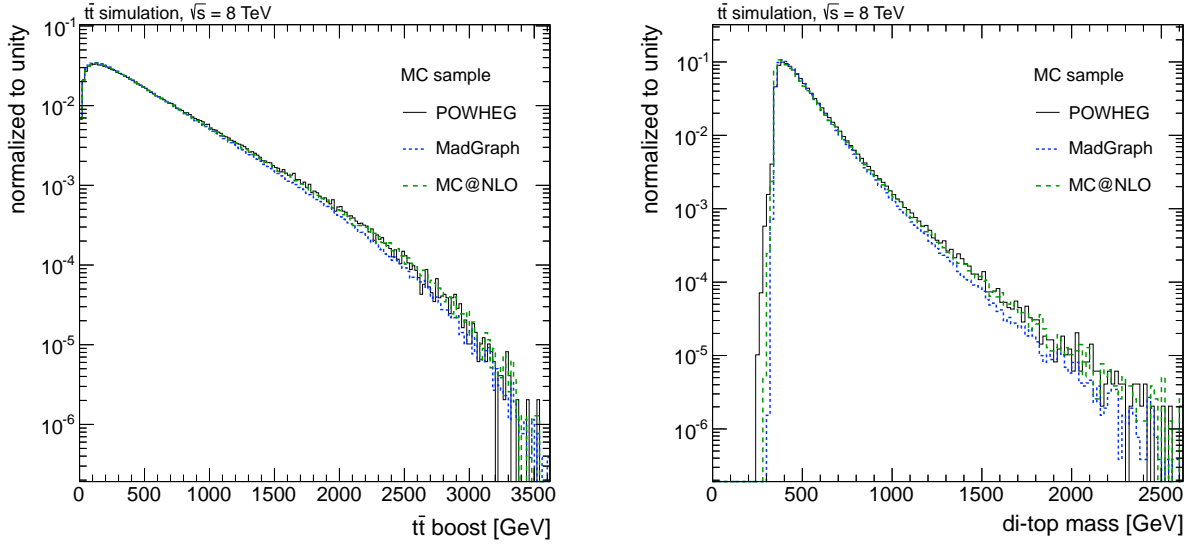
Figure 5.28.: The total boost of the $t\bar{t}$ system and the di-top mass as it is simulated by three Monte-Carlo generators POWHEG, MADGRAPH, and MC@NLO. There is no event selection applied and the histograms are scaled to the unit area. Small differences are visible in the tails of the distributions and at the lower threshold of the di-top mass.

The mixing can then be performed by combining the energy product from one event ($E_{\ell^+} E_{\ell^-}$) with the $\ell\ell$ opening angle from another event ($\cos\theta_{\ell\ell}$).

$$M_{\ell\ell}^{\mathrm{mix}} = \sqrt{2 E_{\ell^+}^{\mathrm{A}} E_{\ell^-}^{\mathrm{A}} (1 - \cos\theta_{\ell\ell}^{\mathrm{B}})}, \tag{5.16}$$

where A and B indicate the two different events.

Obviously, the angular correlation between the leptons in the real events can not be an issue in this type of mixing. Any angular preference in the real events is preserved in the mixing procedure and also present in the mixed events.

Figure 5.29 shows how the prediction fits the real distribution. Compared to the Lorentz-vector mixing (cf. Fig. 5.4) the result is slightly less convincing. Especially in the low energy part of the spectrum the real distribution is underestimated. However, the influence of the boost and the invariant mass of the $t\bar{t}$ system might be decreased, since the distribution of the $\ell^+\ell^-$ opening angle is identical in the real and the mixed events.

In order to study the influence of the $t\bar{t}$ boost on the prediction power of the angle-momenta mixing, the $t\bar{t}$ Monte-Carlo sample is split into two subsamples, one containing only events with small boost, the other only events with high boosts. Additionally all default selection cuts are applied. The mixing is then performed separately in both subsamples. In Fig. 5.30 the results are displayed. The low boost subsample shows a larger deviation between the real and the mixed distributions than the high boost subsample. In the former the mixed distribution is more narrow than the real, in the latter a slight overestimation in the tail can be observed.

For Fig. 5.31 the same is done, but the Monte-Carlo sample is split according to the di-top mass. The lower region shows again the stronger deviation, but here the effect is sort of opposite.

101
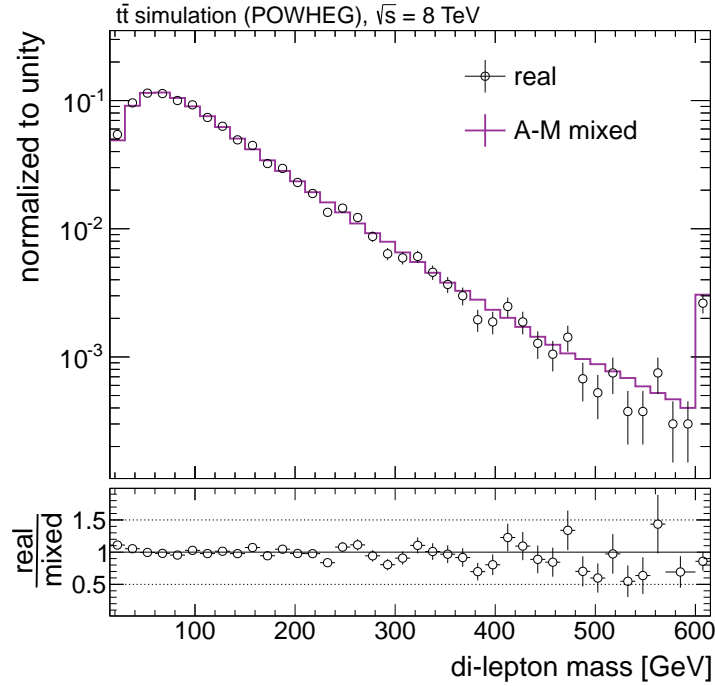
Figure 5.29.: Prediction power of the angle-momenta event mixing in $t\bar{t}$ MC. In the first bins, the mixed spectrum underestimates the real distribution.

The real distribution falls steeply, while the mixed spectrum has a long tail to high di-lepton masses. In the high di-top mass region the distributions differ mainly in the first bins, where the real spectrum is underestimated.

Obviously, even if the angular relation between the leptons is preserved in the mixing, the $t\bar{t}$ boost and the di-top mass have a strong influence on the prediction power of the event-mixing technique. Since any deviation between the real and the mixed distribution is caused by a correlation between the considered variables in the real event, the correlation coefficients ρ are studied. In Table 5.1 ρ between $E_{\ell^+}E_{\ell^-}$ and $\cos\theta_{\ell\ell}$ is listed w.r.t. to the $t\bar{t}$ boost and w.r.t. the di-top mass. At low $t\bar{t}$ boost values the correlation is negative, for higher boost it increases and becomes positive for the highest regions. The di-top mass has the opposite effect: It starts positive at small values and decreases towards larger energies.

The correlation between the variables $E_{\ell^+}E_{\ell^-}$ and $\cos\theta_{\ell\ell}$ and its dependency on the $t\bar{t}$ boost and the di-top mass can be understood from Fig. 5.32. Here the Monte-Carlo sample is binned two-dimensionally w.r.t. the $t\bar{t}$ boost and the di-top mass, and for each bin the correlation coefficient is calculated. At the diagonal the two event energies nearly compensate each other, here the correlations are close to zero. For events with large boosts and small di-top masses (lower right corner) a positive correlation is obtained, if the di-top mass dominates (upper left corner) the correlation is negative.

If the $t\bar{t}$ boost is the dominant energy in the event, the leptons are typically boosted in one hemisphere, i.e. the angles tend to get smaller. The more parallel the boost and the lepton directions are in the $t\bar{t}$ rest frame, the smaller the angle gets and at the same time the leptons gain most energy from the boost. Since a small angle means a large $\cos\theta_{\ell\ell}$, a positive correlation in these events is expected. On the other hand, if the di-top mass is larger than the boost, the
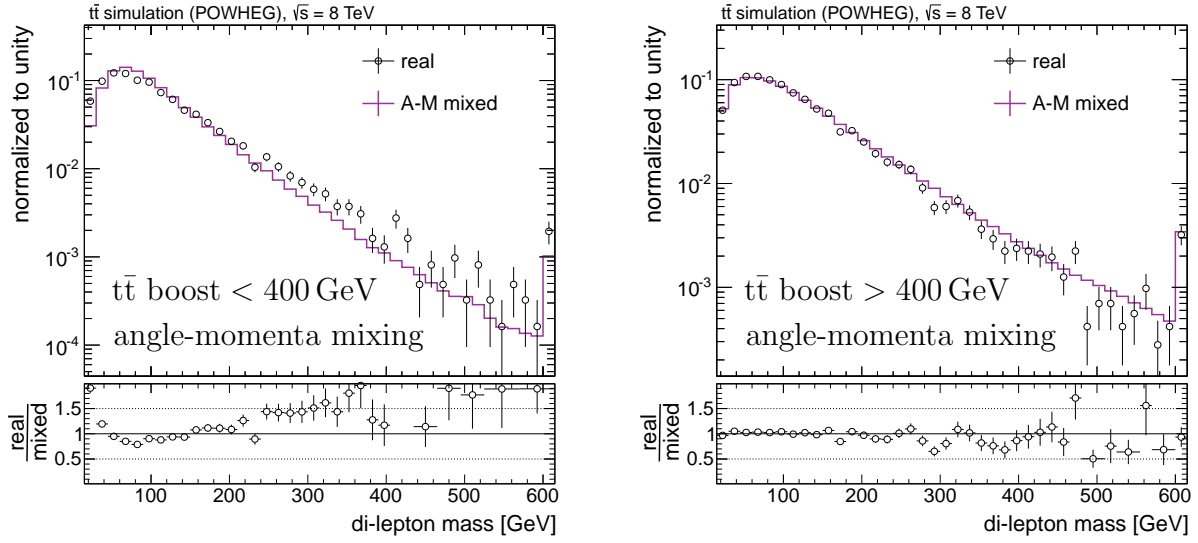
Figure 5.30.: Result of the angle-momenta mixing prediction with two subsets of simulated $t\bar{t}$ event: with only small boosts (left) and only high boosts (right). In the low boost region the shapes of the real and the mixed distributions differ greatly, whereas the agreement in the high boost region is nearly as good as in the whole sample.
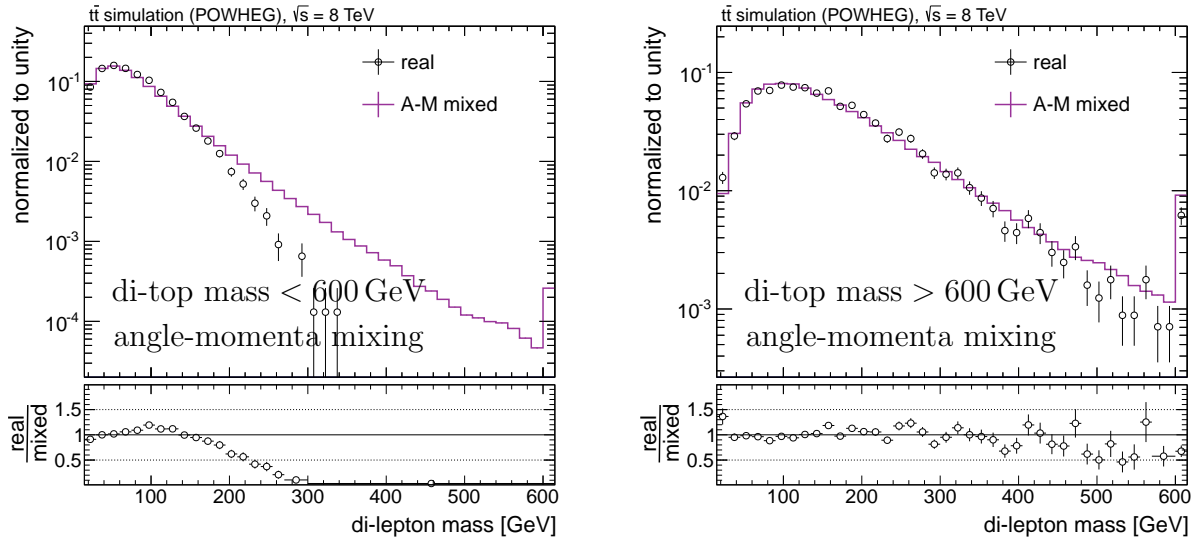
Figure 5.31.: Result of the angle-momenta mixing prediction with two subsets of simulated $t\bar{t}$ event: with only small di-top masses (left) and only high di-top masses (right). Like in the case of the $t\bar{t}$ boost, the low energy region shows a strong disagreement, while the prediction in the high energy region works much better.

Table 5.1.: The correlation coefficient ρ of the two variables $E_{\ell^+}E_{\ell^-}$ and $\cos\theta_{\ell\ell}$ as defined in Eq. 5.5 in different regions of the $t\bar{t}$ boost (left) and the di-top mass (right). The numbers are obtained from the POWHEG $t\bar{t}$ Monte-Carlo sample with no selection cuts applied. The correlation plots can be found in the Appendix E.3.

$t\bar{t}$ boost [GeV]	ρ
$0 - 100$	-0.36
$100 - 200$	-0.33
$200 - 400$	-0.21
$400 - 600$	-0.06
$600 - 1000$	0.11
$1000 - \infty$	0.25
$0 - \infty$	0.17

di-top mass [GeV]	ρ
$0 - 400$	0.30
$400 - 450$	0.29
$450 - 500$	0.27
$500 - 600$	0.25
$600 - 800$	0.16
$800 - \infty$	-0.06
$0 - \infty$	0.17
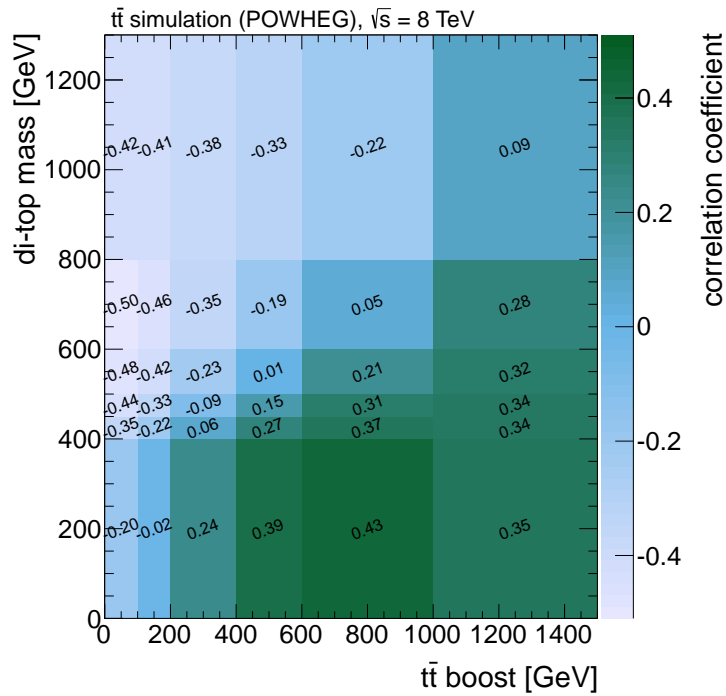
Figure 5.32.: The correlation between $E_{\ell^+}E_{\ell^-}$ and $\cos\theta_{\ell\ell}$ in bins of $t\bar{t}$ boost and di-top mass. The numbers repeat what is also given in terms of color code.

back-to-back topology is dominant. In such events the leptons gain most energy from the di-top mass if they are back-to-back as well, i. e. if the $\cos\theta_{\ell\ell}$ is small, thus the correlation is negative.

Preserving the angle between the leptons in the event mixing turns out to be a less major benefit as one might expect. The proof-of-principle plot is slightly less convincing and the influence from the $t\bar{t}$ boost and the di-top mass can not be fully suppressed. An additional consideration is about the objects that are mixed. In the angle-momenta mixing the objects are simple numbers, but physically a bit complicated, since both contain information of both leptons. In the Lorentz-vector mixing the objects are more complex, but the concept is straightforward.

In the light of these considerations, the Lorentz-vector mixing is chosen to be the main method in this work. However, the angle-momenta mixing has its advantages and might be superior in another context, such as in an analysis with data that is going to be taken after the shut-down. With $13\,\mathrm{GeV}$ or even higher collision energies the insensitivity of the angle-momenta mixing w. r. t. high $t\bar{t}$ boosts and high di-top masses could become crucial.

6. Search Results

In this chapter the results of the search for a supersymmetric signal are summarized. In Section 6.1 the measured di-lepton mass is compared to the event-mixing prediction. The relevant systematic uncertainties are discussed in Section 6.2. In Section 6.3 the result is used for a counting experiment.

6.1. Application of the Event-Mixing Method

The data-driven prediction of the main background in the same-flavor opposite-sign di-lepton mass spectrum generated by event mixing, in comparison to the measured spectrum is shown in Fig. 6.1. Since the event-mixing method predicts the shape of the distribution, but not the total number of expected events, for illustrative reason the mixed shape is scaled to the number of real events. Overall a good agreement can be observed, only in the very first bin and in the region of the Z^0-boson mass a clear underestimation is visible. That is expected since in those regions other backgrounds contribute, which are not predicted by the event-mixing technique; most relevant are $Z^0 \rightarrow \tau^+\tau^-$ decays and di-boson events.

In Fig. 6.2 the selected events are separated in di-muon and di-electron events, and separately the event mixing is performed. The results are very similar. In both channels the data is in agreement with the prediction, apart from the regions where other backgrounds contaminate as mentioned above. The Standard-Model backgrounds are expected to be flavor symmetric, i.e. the $\mu^+\mu^-$ channel should not differ from the e^+e^- channel[1]. In Supersymmetry, however, a difference can be caused by a difference between the smuon and the selectron mass.

Requiring b tags in the events significantly reduces the contamination from the other background processes, in particular Drell-Yan and di-boson. Under the background-only hypothesis a rather clean $t\bar{t}$ sample can be expected after at least one or even two b tags per event are required. Hence, the prediction power of the event-mixing technique should be enhanced. At the same time the sensitivity to SUSY events can be changed. Models predicting many third-generation particles can better be tested with such an event selection. Figure 6.3 depicts the comparison between data and prediction for events with at least one and at least two identified b-quark jets. Expectedly the Z^0 resonance and the low-mass mismatch get strongly reduced. However, the underestimation in the low mass region is still slightly present, even in the two-b-tag sample.

All these results show no obvious deviation between data and the event-mixing prediction. Hence, the recorded and selected event agree with the background expectations and no hints of Supersymmetry can be observed.

A final validation test of the event-mixing technique itself is performed in the *different*-flavor same-sign di-lepton channel. Assuming lepton flavor to be conserved in Supersymmetry, mass

---

[1]One difference emerge from the particle identification in the detector: Muons can be better identified than electrons; electrons can be more easily faked by hadronic objects, thus have to be harder selected. Therefore the di-muon sample is large than the di-electron sample.
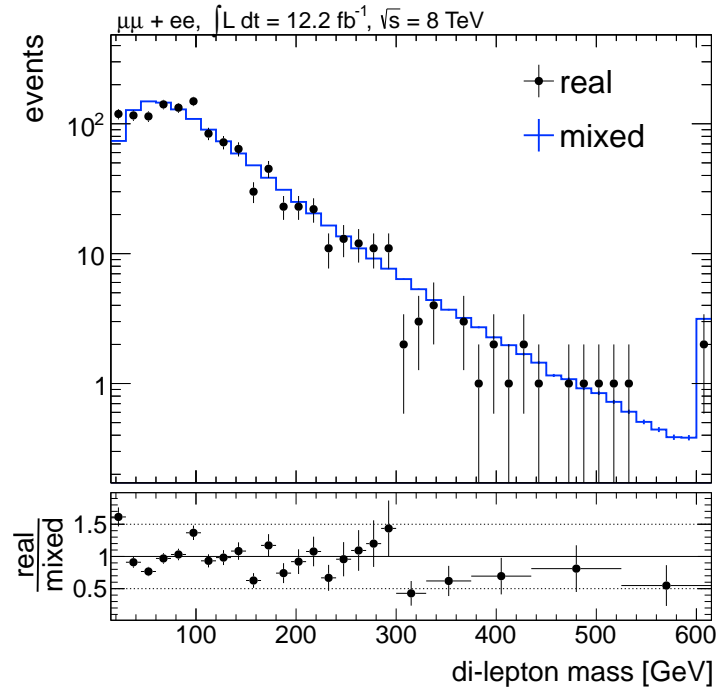
Figure 6.1.: Data compared to the event-mixing prediction in same-flavor channel. The mixed spectrum is scaled to the number of real events. Since the mixed distribution is meant to predict the $t\bar{t}$ contributions, the mismatches at very small di-lepton masses and around the mass of the Z^0 boson are expected because of contributions from $Z^0 \to \tau^+\tau^-$ and di-boson events, respectively.
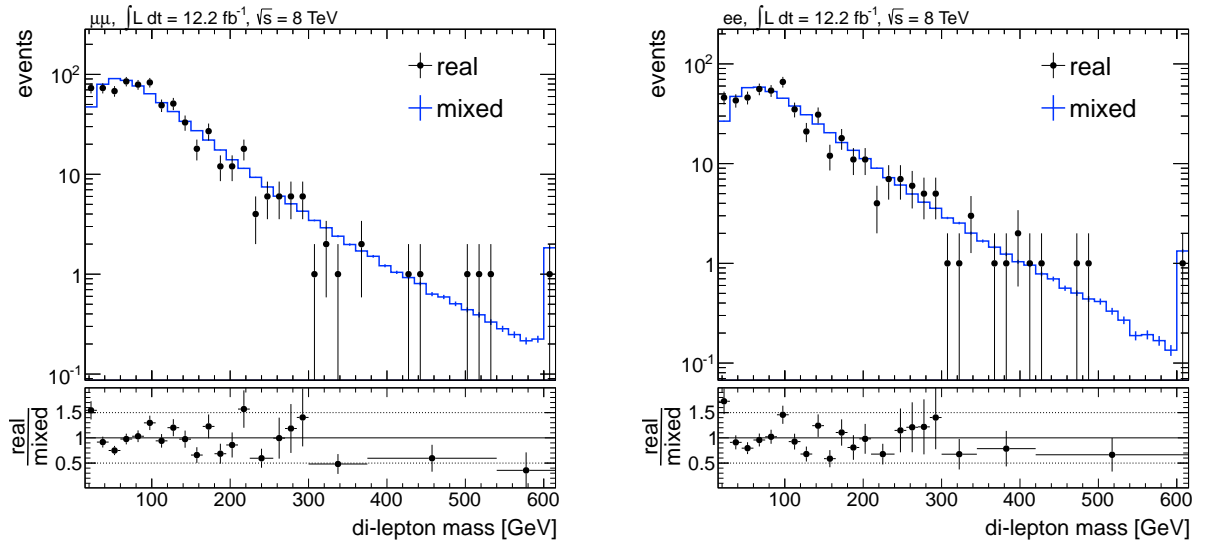
Figure 6.2.: Data compared to the event-mixing prediction separately in $\mu^+\mu^-$ and e^+e^- channels. In both channels the result looks very similar.
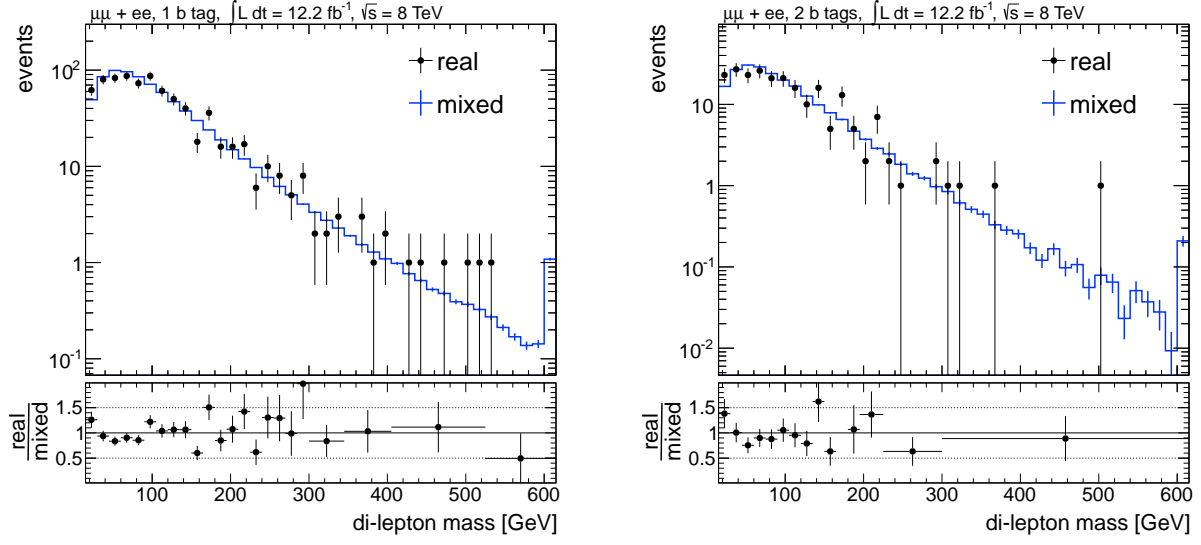
Figure 6.3.: Data compared to the event-mixing prediction in an event sample with an additional requirement of at least one b tag (left) and at least two b tags (right). The overshoot of event in the Z^0 mass region vanishes. Also the measurements in the first bin agree better with the prediction. However, a small mismatch is still present.
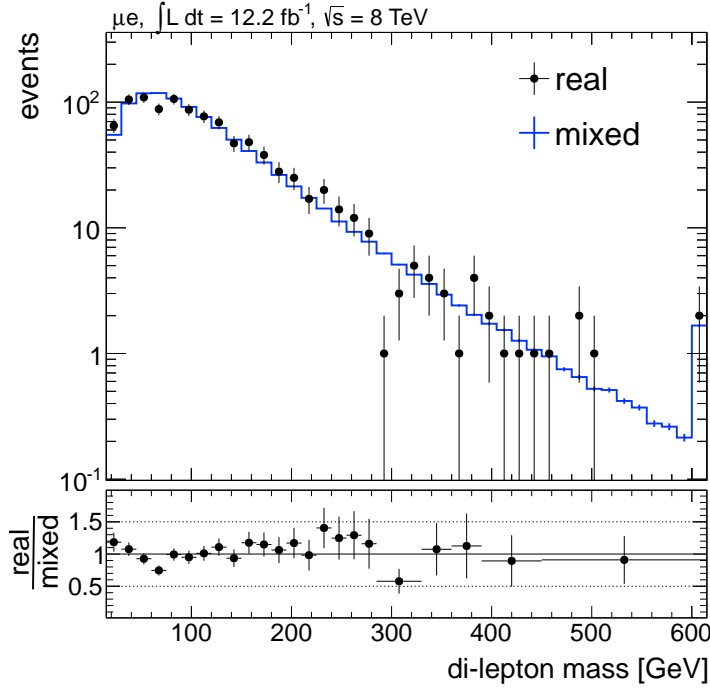
Figure 6.4.: Data compared to the event-mixing prediction in the different-flavor channel. In this event sample no signal is expected, since lepton flavor conservation is assumed to be respected in Supersymmetry.
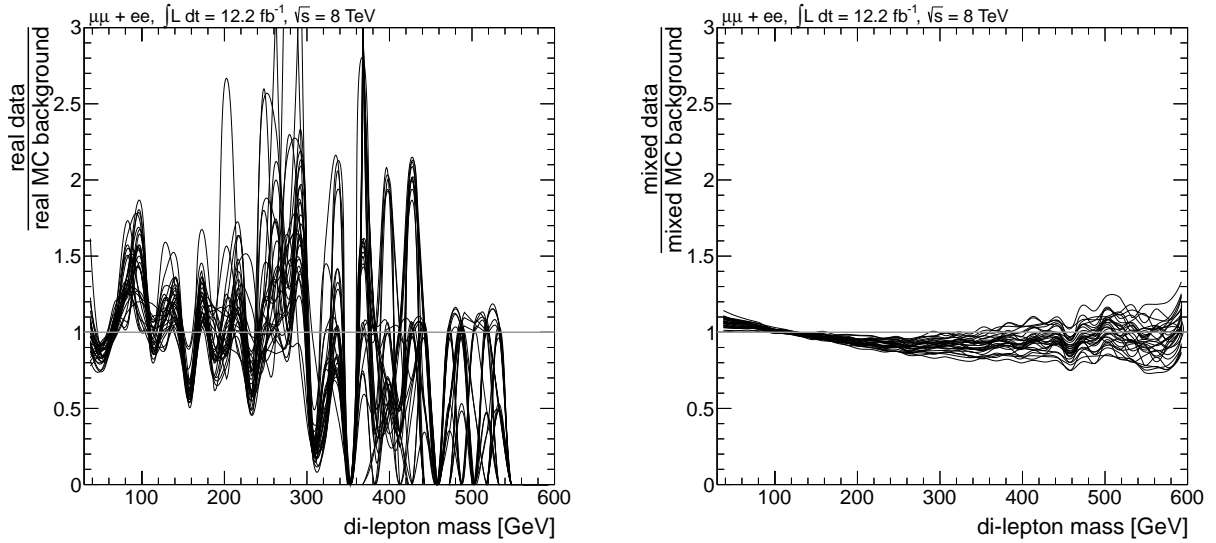
Figure 6.5.: Ratios between data and MC subsamples of real and mixed distributions. The ratio line have all the same numerator (the data distribution) but each has another denominator (the distribution in one of the 30 Monte-Carlo subsamples).

edges are expected only in the same-flavor channel. In that sense the comparison between data and prediction in the μe channel, as shown in Fig. 6.4, can be understood as a cross-check of the method in a signal-free control region *in data*. However, it is not excluded that SUSY events show up in the μe channel, they are just not expected to form an edge shape in the di-lepton mass spectrum. Statistical fluctuations make the interpretation difficult, but the real distributions seems to be slightly broader than the prediction. Alternatively, a deficit of real events in the bulk region might cause this observation. In this case the underprediction at small masses and in the region between $100\,\text{GeV}$ and $300\,\text{GeV}$ is an artifact caused by the normalization of the predicted spectrum. The good data-to-prediction agreement in the tail of the distribution and the flat underprediction between $150\,\text{GeV}$ and $280\,\text{GeV}$ support rather the deficit interpretation than the wrong-width interpretation.

6.1.1. Prediction in Data vs. Prediction in MC

Now, the event-mixing prediction in data is compared to the result of event mixing in Monte-Carlo samples. For this purpose events are randomly picked from the whole Monte Carlo samples in a way that the resulting subsample corresponds to the luminosity of the analyzed data. This is done thirty times, i.e. thirty subsamples are generated reflecting the fluctuations that are expected in data, including the fluctuations in composition of different processes. For each subsample the event-mixing procedure is performed. In Fig. 6.5 two bunches of ratio plots are shown. In the numerator is always the data distribution, in the denominator one of the MC subsamples. On the left the ratios of the real distributions are plotted, the large fluctuations makes is difficult to draw conclusions. But the quality of agreement between the data and the MC prediction was already shown in Fig. 4.13. Here, the comparison of the mixed spectra on the right should be discussed.

Before the ratio between the data mixed and a MC subset mixed distribution is made, both distributions are normalized to unit area. Only the shape differences should be analyzed here. Note, that the single ratio curves are not independent, all of them have the same numerator. However, there seems to be a systematic trend in the ratios of mixed shapes. At small di-lepton masses all MC subsamples underpredict the data (the ratios are above 1), in the region from 150 GeV to 300 GeV all MC subsamples overpredict the data (the ratios are below 1).

Does this observation together with the mismatch found in the different-flavor channel point to a serious problem of the event-mixing technique in data? The wrong-width interpretation in the μe channel suggests that the prediction should be more broader to fit the background in data. Comparing the same-flavor mixed distributions between data and the MC subsamples show however that the prediction in data has already a tendency to be broader. In conclusion, the two observations that might concern point to opposite directions.

Finally, it should be remarked that the ratios on the right in Fig. 6.5 are not assumed to be completely flat. If that was required in order to believe in the event-mixing prediction, the Monte-Carlo prediction could be used directly: Requiring the real MC distribution to be reproduced by the mixed MC distribution *and* requiring the mixed data distribution to agree with the mixed MC distribution is equivalent to requiring the real data events to match with the real Monte-Carlo spectrum. Moreover, the data mixed shape is nearly at the limit of the thirty MC mixed shapes, i. e. in the bunch of curves on the right in Fig. 6.5 there is one curve that agrees very good at small and high di-lepton masses and it is one of the upper curves in the dip region between 200 GeV and 300 GeV. It is not expectable that the data is in the middle of the fluctuations between Monte-Carlo samples; as long as it is "in the range" of the fluctuations they are in agreement.

6.2. Systematic Uncertainties

Every experimental measurement has an uncertainty. Two types of uncertainties can be distinguished, the random uncertainties and the systematic uncertainties. In case the measurement is a count, the random error is due to statistical fluctuations. In this analysis the shape of a frequency distribution is studied. If N events are measured in one bin of this distribution, the statistical uncertainty can be approximated by $\sqrt{N}$. The approximation holds for large numbers of bins, for small values binomial statistics has to be used.

More complicated are systematic uncertainties. Many effects can bias the result of the analysis. In this section several of these are studied. The main source of uncertainties is the transition from simulated to data events. With simulated event samples the background prediction method has been tested, but it cannot be guaranteed that the event mixing works as well on data as on Monte-Carlo events. Some potential systematic effects can directly be studied in data events, e. g. energy scale uncertainties, other uncertainties, e. g. like the choice of the PDF set, is an uncertainty of the simulation and can only be studied there.

Uncertainties that are accessible in data are taken into account by varying the measurement within its error and proceed with the whole analysis. Uncertainties, of which the effect has to be obtained from MC, are applied in terms of corrections to the prediction generated in data. Again the complete analysis is performed with the corrected prediction. The final result of this thesis is – following a conservative approach – the result among all variations that agrees best with the background-only hypothesis.
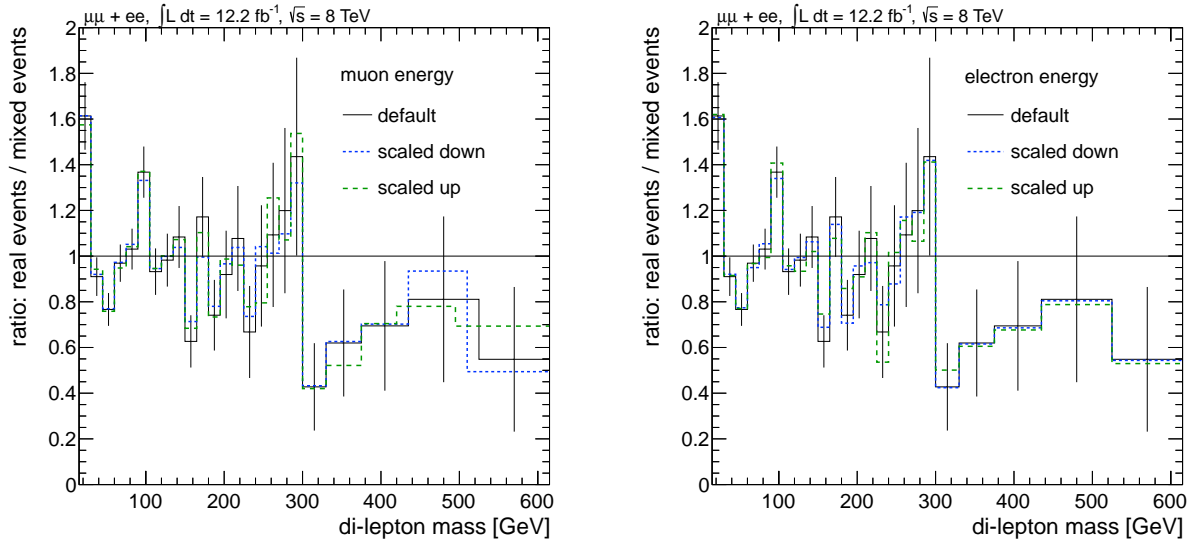
Figure 6.6.: Effect of lepton energy scale on the mixing prediction. The ratios of the real event distributions over the mixed event distributions are plotted. The error bars reflect the statistical uncertainty, they are drawn for the default configuration only. On the left the muon energy scale is varied, on the right the electron energy scale is under investigation. In neither case a systematic effect is visible.

6.2.1. Lepton Energy Scale

Although the energy of a muon or an electron can be measured very accurate with the CMS detector, there is an uncertainty on the absolute energy scale of the lepton measurements. For electrons this is driven by the performance of the electromagnetic calorimeter and found to be 1% in the barrel region and 3% in the endcaps [135]. The momentum scale uncertainty in the case of muons is very small. On the Z^0 peak a 0.2% uncertainty is measured [80]. In order to obtain a conservative estimate and since the event kinematic in $t\bar{t}$ events differ from Z^0 events, a muon energy scale uncertainty of 1% is assumed as systematic uncertainty in this analysis.

The electron and muon energies are scaled up and down independently and the selection and the mixing is repeated. In this way four different results are obtained:

- Muons scaled up, electrons default

- Muons scaled down, electrons default

- Muons default, electrons scaled up

- Muons default, electrons scaled down

An independent variation of the muon and the electron energy scale is justified by the difference in energy determination. The muon energy is derived from its momentum measured by the inner tracker and the muon system. Above 20 GeV the electron energy determination is dominated by the ECAL measurements (cf. Fig. 4.3).

The effect of the lepton energy scaling is illustrated in Fig. 6.6. Relevant for this analysis is not if either the real or the mixed distribution changes due to the energy scale variation.
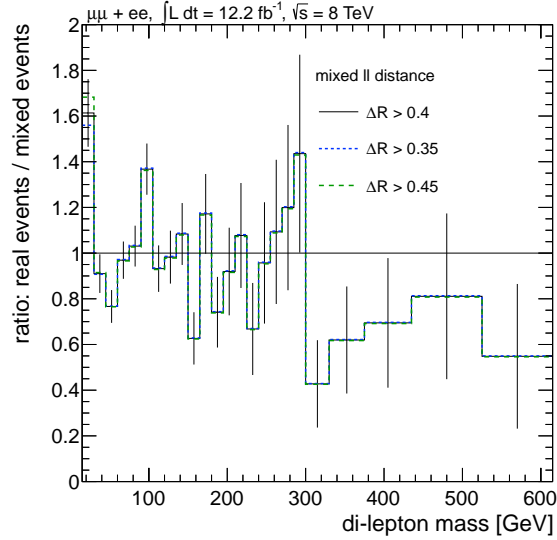
Figure 6.7.: Effect of the minimal allowed distance between the two leptons in mixed events on the prediction. Only in the very first bin a small effect is visible.

Relevant is if the agreement between both change. Therefore the ratios (real over mixed events) are shown. Both in the muon and in the electron case small differences are visible, but no systematic shift or change of the shape. Nevertheless, the systematic uncertainty is accounted for in the results of this analysis.

6.2.2. Lepton-Lepton Spacial Separation

In real events there is a minimal spacial separation between two leptons. The detector resolution defines a lower limit in the distance between two objects to be resolved as two entities. In particular the excellent tracker resolution allows separation of leptons down to very small distances. However, in practice the isolation requirement in the lepton selection sets a much larger limit. The isolation requirement, as discussed in Section 4.3, does not allow any other energetic object in a cone of $\Delta R > 0.4$ around a lepton. Otherwise the lepton is not selected.

In the mixed events the leptons can be arbitrarily close together. Since the angle between the leptons has a direct influence on the di-lepton mass, also in the mixed events a minimal angular distance is required. Otherwise a difference can be expected between the real and the mixed distributions. As threshold the cone size of the isolation requirement is chosen. Obviously, there is still a small difference between real and mixed events. Although the isolation requirement implies a minimal ΔR distance, it is not a strict cut as applied on the mixed events.

To account for the remaining arbitrariness in the ΔR cut, a systematic uncertainty is derived from a variation of the requirement on mixed events by ± 0.05. An illustration is given in Fig. 6.7. Nearly over the whole range the default ΔR requirement leads to exactly the same ratio as the two variations. Only in the very first bin a small deviation is visible. Since parallel leptons have a di-lepton mass of zero, decreasing the ΔR cut adds mixed events with very small di-lepton masses, i.e. the ratio is smaller.

Although this effect is small, it is accounted for in the results of this analysis.
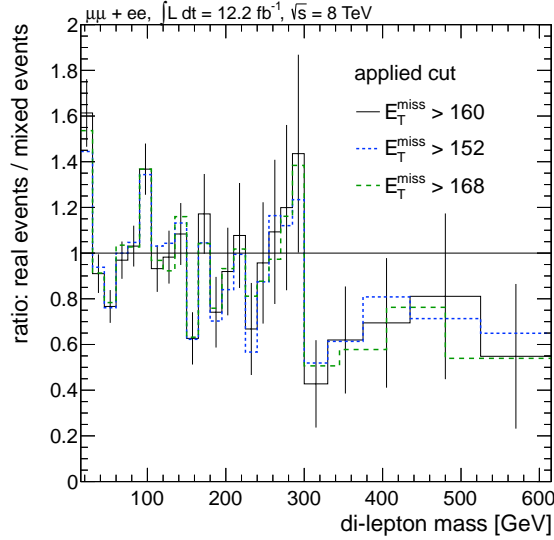
Figure 6.8.: Effect of the E_T^{miss} requirement in the event selection on the mixing prediction. The cut threshold is varied by 5% – corresponding to 8 GeV– up and down.

6.2.3. Selection Cut Variation

In Section 6.2.1 the uncertainty due to the lepton energy scale is discussed. Although leptons are the main objects in this analysis, also the hadronic energy scale might influence the result of the analysis. Since E_T^{miss} and the jet multiplicity are only used for selecting the events, it is sufficient to account for the uncertainties of these variables by varying the cut thresholds. In Section 5.3.5 is discussed that the impact of the jet multiplicity requirement is negligible, while the E_T^{miss} cut effects the event-mixing prediction.

However, the hadronic energy contributes to E_T^{miss} and might therefore be relevant. The jet energy scale uncertainty depends on several jet properties, such as flavor, pseudorapidity, and energy. Overall it is determined to be smaller than 2% [93]. The E_T^{miss} variable is more complex as it is the negative vectorial sum of all particle-flow objects, i.e. the uncertainties of all energy measurements propagate to E_T^{miss}. In order to ensure covering also correlated uncertainties, the E_T^{miss} cut threshold is varied by 5%, and the effects on the result are taken as a systematic uncertainty.

Figure 6.8 illustrates the effect of the 5% (i.e. 8 GeV) variation of the E_T^{miss} cut threshold. The visible differences show no clear structure and seem to be due to statistical fluctuations. However, also this uncertainty is propagated to the results.

6.2.4. Different Monte-Carlo Samples

The event-mixing prediction slightly differs in $t\bar{t}$ event samples generated with different Monte Carlo programs, as shown in Section 5.3.6. Since it is not known which of the used samples describes the data best, all three are taken into account for retrieving a systematic uncertainty. From the comparison of the real and the mixed di-lepton mass distribution the ratio of the two is used as a correction to the mixed distribution obtained in data.

In Fig. 6.9 the ratio plots (real events over mixed events) are shown for three different MC samples. In the POWHEG and MADGRAPH samples a slight overprediction at very small di-
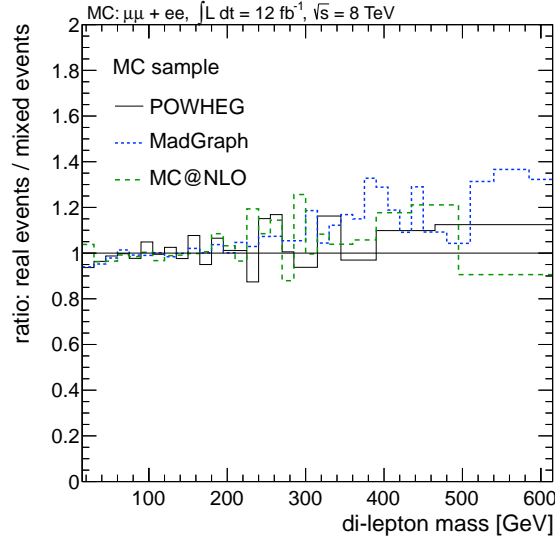
Figure 6.9.: Systematic uncertainty from Monte-Carlo "closure test". Due to the ignorance which MC sample describes $t\bar{t}$ event most truly, three different samples generated with different MC programs are used.

lepton masses is observable, while in the MADGRAPH sample the tail of the distribution is slightly underpredicted.

Each ratio plot is used to "correct" the mixed distribution in data. If they were identical describing the truth perfectly, this correction would lead to a better description of the $t\bar{t}$ background. Since they are different, a systematic uncertainty is obtained.

6.2.5. Uncertainties in MadGraph $t\bar{t}$ Simulation

Two uncertainties in the MADGRAPH simulation of $t\bar{t}$ events are accounted for: the renormalization and factorization scale (Q^2 scale) and the matching threshold between the matrix element calculation and the parton showering. For both uncertainties specific Monte-Carlo samples are used where the scale and the matching is varied. From these variations no effect on the presented analysis is expected. First of all, observables should only slightly depend on these simulation parameters, caused by the hadronic part of the events, but not in the leptonic part. Although leptons are the main objects in this study, via the $E_{\mathrm{T}}^{\mathrm{miss}}$ selection requirement a small influence of jet simulation on the Monte-Carlo closure test may exist.

The possible influence is studied by repeating the closure test with the specific Monte-Carlo samples. In Fig. 6.10 the results are presented. As reference the result obtained in the default MADGRAPH sample as already shown in Fig. 5.27 is plotted. In both figures the two variations follow roughly the pattern in the default MADGRAPH sample: An overprediction at small masses, a tendency to an underprediction in the tail. A systematic effect of the variations is not visible in either case. More detailed comparisons are not possible due to the small statistics, i. e. large fluctuations, of these MC samples.

Although no effects are expected and no effects are observed, the variations are taken into account as systematic uncertainties. The statistical fluctuations prevent a clear statement that the variations of the simulation parameters are negligible.
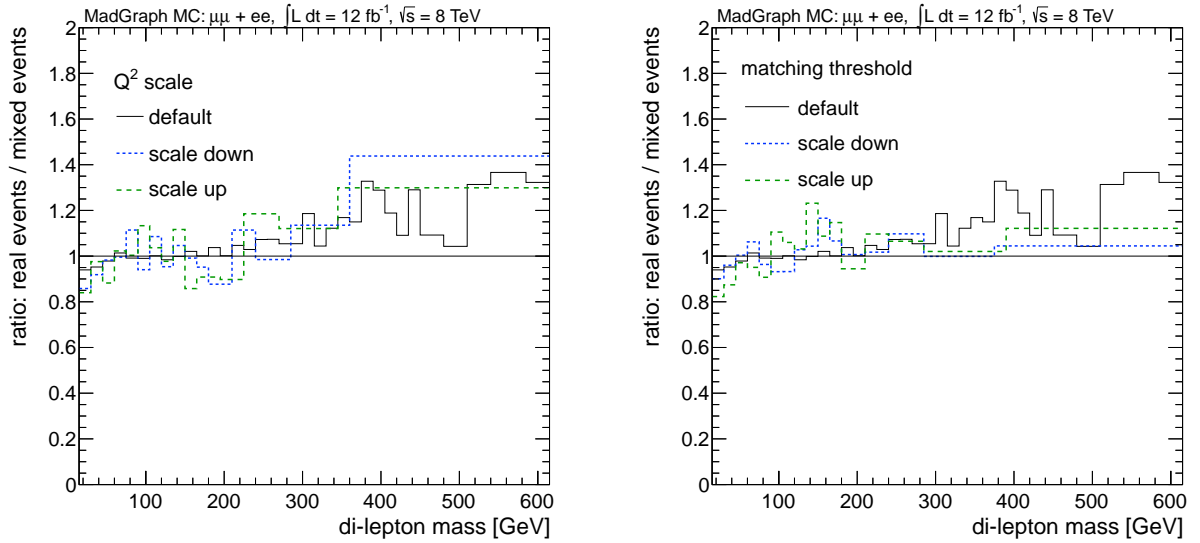
Figure 6.10.: Effect of the Q^2 scale and the matching threshold in MADGRAPH on the event mixing.

6.2.6. Uncertainty on Top Quark Mass

The value of the top mass surely effects the shape of the di-lepton mass distribution. However, only second-order effects are expected to interfere with the prediction power of the event mixing. The $t\bar{t}$ boost and the di-top mass have been found to have a strong impact on the prediction (cf. Section 5.3.1). A different top mass could also change the distributions of these two event energies.

Two MADGRAPH simulated event samples are available with varied assumptions on the top mass. In Fig. 6.11 the according ratio plots are shown. A clear conclusion is again difficult due the limited statistics of the Monte-Carlo samples. In the tail of the distributions one might observe a better performance of the prediction in the case of the reduced top mass. This behavior can be explained by the influence of the di-top mass. As discussed in Section 5.3.1, a smaller di-top mass leads to a harder mixed spectrum compared to the real distribution. If the mass of the top is lower, the di-top mass can be expected to be smaller as well.

Although this explanation is rather speculative and the dominant observation is again the statistical fluctuation in the MC samples, the shown ratio plots are used to obtain a systematic uncertainty.

6.2.7. Arbitrariness of Parton Density Functions

The dependency of the boost and the invariant mass of the $t\bar{t}$ system on the chosen parton density functions (PDF) is shown in Section 5.3.1. Here, a systematic uncertainty from that effect is extracted. For each selected MC event two weights are obtained for the two alternative PDF sets (MSTW 2008 and NNPDF2.1). These weights are meant to reproduce distributions as they are expected if those PDF sets were used in the Monte-Carlo production. For the distributions shown here events are randomly picked out of the whole sample. The probability of being selected is proportional to the weight of the event. This procedure avoids the necessity
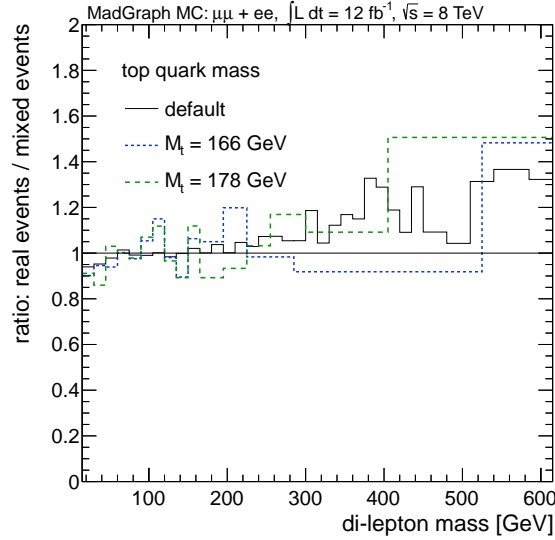
Figure 6.11.: Influence of the top-quark mass on the event mixing.

to extract a weight for a mixed event from the weights of the two real events the leptons are taken from, since all selected events have a weight of one.

Figures 6.12 and 6.13 show the effect of the PDF set on the real di-lepton mass distribution and on the distribution of the mixed events. In Fig. 6.12 the real and the mixed spectra are compared for the two alternative PDF sets. Both show a good agreement, only a very slight under-estimation in the tail of the spectrum is visible for the MSTW weighted events. In Fig. 6.13 the three real distributions are compared and the three mixed ones. The real distributions agree very well, no systematic deviation is visible. The mixed distributions show small differences. The NNPDF spectrum falls slightly steeper than the others.

The choice of the PDF set in the Monte-Carlo simulation has no serious effect on the prediction power of the event-mixing method. Nevertheless, from the ratio plots in Fig. 6.12 corrections are obtained to be applied as systematic uncertainty on the data prediction.

6.2.8. Drell-Yan and Di-Boson Contamination

In Section 5.3.3 the behavior of other Standard-Model processes than $t\bar{t}$ in event mixing is discussed. It is shown that Drell-Yan and di-boson events change the mixed event distribution slightly. Since there could be more or less Drell-Yan and di-boson events in the collected data than it is expected, the nominal Monte-Carlo cross sections might not be the best choice. An additional systematic uncertainty accounts of this ignorance.

Following a conservative approach, the cross sections of all processes that were found to change the mixed distribution (Drell-Yan, Z^0Z^0, $W^\pm Z^0$, and W^+W^-) are simultaneously halved and doubled. A systematic uncertainty is derived from these two extremes. Here, the effect on the mixed distribution itself is relevant, not the effect on the real-over-mixed ratio. The change of the mixed distribution is illustrated in Fig. 6.14 as ratio w.r.t. the mixed spectrum with regular cross sections. A clear effect is visible. Increasing the probability for the electroweak processes leads to a harder mixed di-lepton mass spectrum, halving the cross sections leads to a softer spectrum. Although it is a ratio of two mixed distributions it can be applied in the
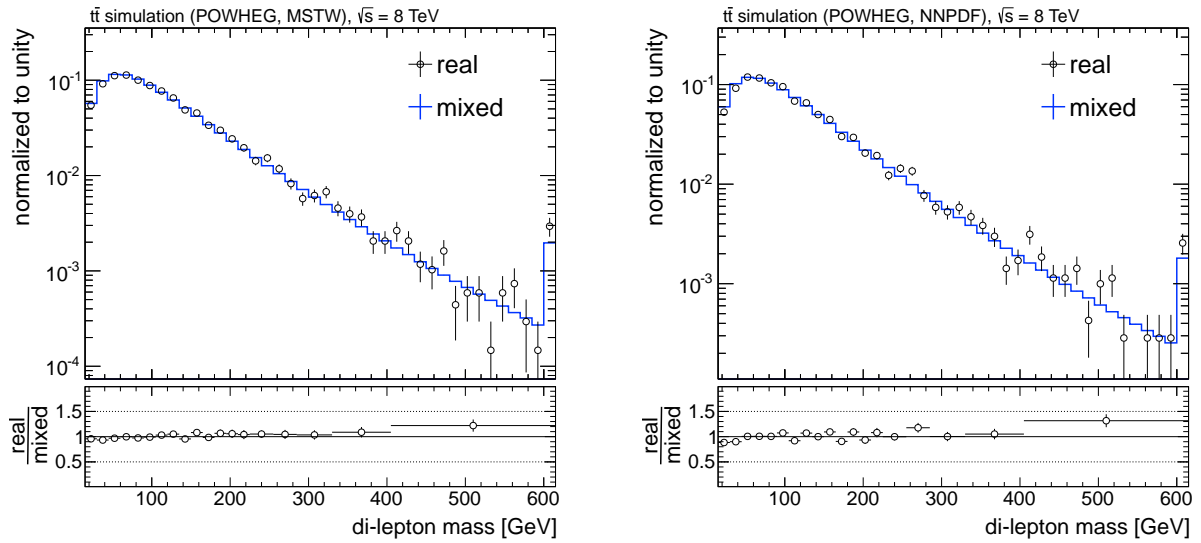
Figure 6.12.: Comparison of the real and mixed distribution after weighting the events according to a different PDF set (left: MSTW 2008, right: NNPDF2.1). The effect of the PDF set is very small, only in the tail of the MSTW spectrum a slight underestimation is visible.
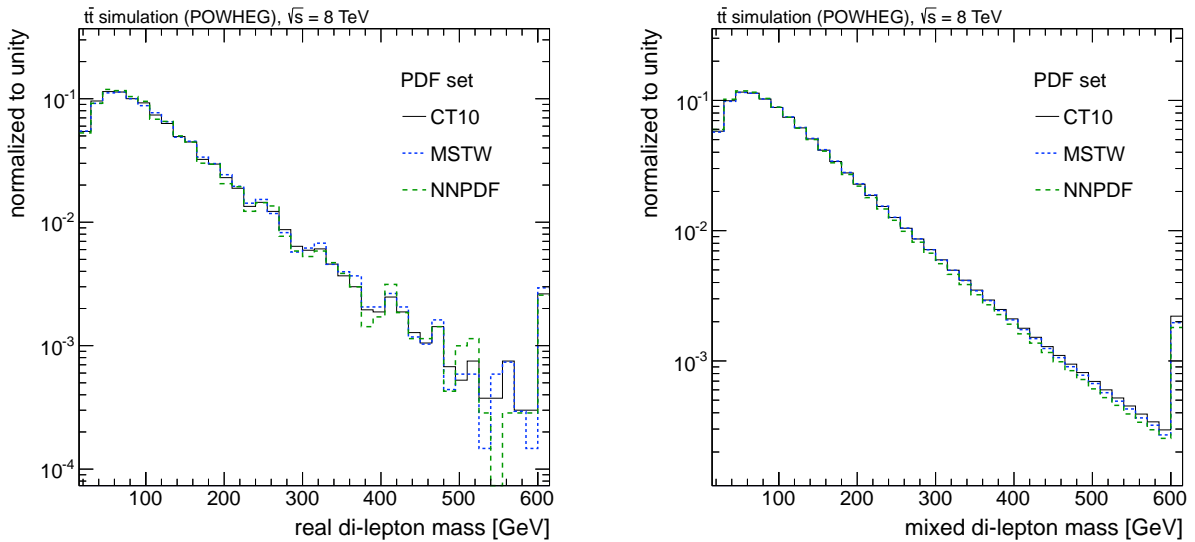
Figure 6.13.: The same spectra as in Fig. 6.12 are plotted again, but this time the real distributions and the mixed distributions are compared. The former comparison shows no deviation besides the statistical fluctuation. The NNPDF mixed distribution is at high masses slightly below CT10 and MSTW, but this might also be due to fluctuations.
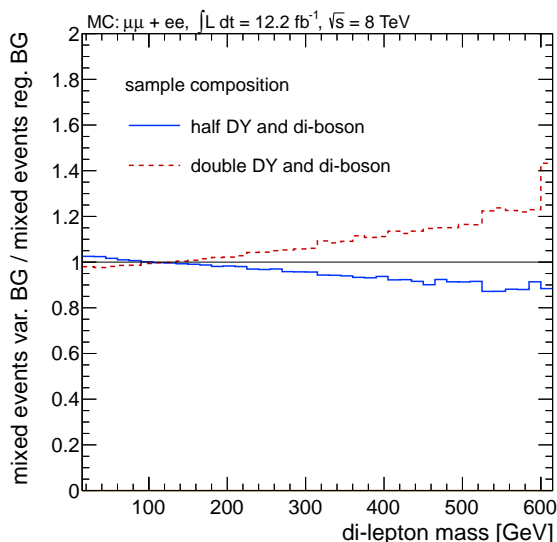
Figure 6.14.: Effect of different assumptions on the cross sections of Drell-Yan and di-boson processes. The shown ratios are different than the ones shown for the other systematic uncertainties: Here also in the numerator is a mixed shape as stated at the y axis.

same way as the previously discussed uncertainties. Multiplying the predicted shape in data with these ratios corrects for an under- or overestimation of electroweak backgrounds.

6.2.9. Summary: Corrections from Monte Carlo

In the previous sections several potential sources of systematic uncertainties are discussed. Some of them can only by studied with simulated events, since they stem from theoretical uncertainties. From these effects corrections are extracted and applied in data. Since this analysis is sensitive to signals showing up in the shape of the di-lepton mass distribution, the corrections have to modify the shape of the prediction.

From each MC effect a ratio plot is made of the real MC distribution over the mixed MC distribution[2]. This binned ratio is linearly interpolated to avoid steps at the bin borders. Finally, the data-driven prediction (i. e. the mixed data distribution) is multiplied by one of the interpolated ratio plots. In this way each effect leads to modified prediction. In the interpretation of the shape analysis, the envelope of all these background prediction that leads to the best agreement with the background-only hypothesis is chosen. The preference of a background-like result follows a conservative search strategy.

6.3. A Counting Experiment

Although the presented analysis is sensitive to deviations from the expected shape of the di-lepton mass distribution, the result can also be used for a counting experiment. Since the event-mixing method predicts only the expected shape of the $t\bar{t}$ background, but not the number of

---

[2]The only exception is the effect of Drell-Yan and di-boson contamination. Here the modified MC mixed distribution over the regular MC mixed distribution is used.
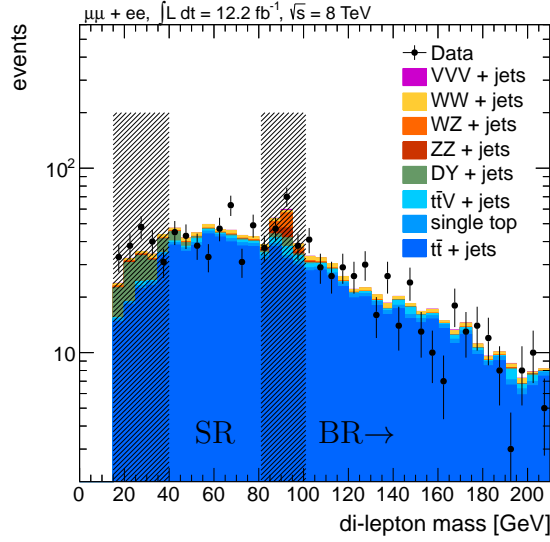
Figure 6.15.: The different regions in the di-lepton mass spectrum defined for the counting experiment. The regions below $40\,\text{GeV}$ and around the Z^0 mass are excluded because the Drell-Yan and di-boson backgrounds are not predicted by the event-mixing method. The signal region (SR) and background region (BR) are labeled. The latter includes also all events with higher masses than shown in this figure.

events, additional assumptions are necessary. Especially in low-mass SUSY scenarios the mass edge can be expected below the Z^0 mass, but also massive SUSY particles can produce such a signature as long as the mass differences of the involved particles are small (cf. Section 5.1). Based on these considerations, two regions in the di-lepton mass spectrum are defined:

- Signal region: $40\,\text{GeV} < M_{\ell\ell} < 81\,\text{GeV}$

- Background region: $M_{\ell\ell} > 101\,\text{GeV}$

Figure 6.15 illustrates the defined regions. The hashed areas are excluded because of contributions from other background processes than $t\bar{t}$. The excluded low-energy area is mainly contaminated with $Z^0 \to \tau^+\tau^-$ events, the region around the Z^0 mass with $Z^0 \to \ell\ell$, $Z^0Z^0 \to \ell^+\ell^-\nu\bar{\nu}$, and $Z^0W^{\pm} \to \ell^+\ell^-\ell\nu$, as pointed out in Section 5.3.3. Since phase space restrictions tend to cause problems in event mixing, the named regions are excluded *after* the event mixing, i.e. all events with $M_{\ell\ell} > 15\,\text{GeV}$ enter the mixing. The resulting contamination by these processes in the mixed distribution is accounted for in terms of a systematic uncertainty.

Assuming no signal events in the background region and no change of the mixed shape due the signal events, the background prediction in the signal region is

$$N_{\text{SR}}^{\text{pred.}} = N_{\text{BR}}^{\text{real}} \cdot \frac{N_{\text{SR}}^{\text{mixed}}}{N_{\text{BR}}^{\text{mixed}}}. \tag{6.1}$$

In the analyzed data the following number are obtained:

$$N_{\text{BR}}^{\text{real}} = 484$$

$$\frac{N_{\text{SR}}^{\text{mixed}}}{N_{\text{BR}}^{\text{mixed}}} = 0.77$$

$$\Rightarrow N_{\text{SR}}^{\text{pred.}} = 371.9 \pm 16.9(\text{stat.})$$

$$\text{to be compared to} \quad N_{\text{SR}}^{\text{meas.}} = 362.$$

The measured number of events in the signal region $N_{\text{SR}}^{\text{meas.}}$ is slightly over-estimated, but within the statistical uncertainty the prediction is still in agreement with the data. For calculating the statistical uncertainty the discussed correlation within the mixed events (cf. Section 5.3.4) is not taken into account. Doing so would increase the error.

From the validation of the method with MC events a correction factor c can be derived. That factor accounts for the slight mis-match of the real and mixed distributions in $t\bar{t}$ MC, and can be calculated from the three different Monte-Carlo samples used through this analysis:

$$c = \frac{N_{\text{SR}}^{\text{MC, real}}}{N_{\text{BR}}^{\text{MC, real}}} \cdot \frac{N_{\text{BR}}^{\text{MC, mixed}}}{N_{\text{SR}}^{\text{MC, mixed}}}$$

$$c_{\text{POWHEG}} = 0.977$$

$$c_{\text{MADGRAPH}} = 0.968$$

$$c_{\text{MC@NLO}} = 0.960$$

The small differences between the Monte-Carlo samples give rise to a systematic uncertainty. The mean correction factor $\overline{c_{\text{MC}}}$ is taken to correct the prediction in data, its error is propagated to the number of predicted events.

The additional systematic uncertainties that are derived from Monte-Carlo simulations are obtained in a similar way: For each systematic variation a correction factor is calculated. Finally the deviations of these correction factors from $\overline{c_{\text{MC}}}$ are summed in quadrature in order to obtain a total MC-induced systematic uncertainty of the prediction.

The systematic variations that are done in data directly lead to variations in the measured and the predicted number of events. In terms of $N_{\text{SR}}^{\text{meas.}} - N_{\text{SR}}^{\text{pred.}}$ all variations are summed in quadrature, forming the second contribution to the total systematic uncertainty.

Figure 6.16 summarizes all systematic uncertainties that are taken into account. In the left plot the simulation uncertainties are shown:

- The mean of the three MC samples is used for correction, the error of the mean as uncertainty.

- The contamination with processes that have been found to change the $t\bar{t}$ prediction ("EW") is discussed in Section 5.3.3. The error is conservatively estimated by halving and doubling their cross sections and applying the change in the mixed distribution to the prediction.

- Specific MADGRAPH MC samples with changed simulation settings (matching up/down, scale up/down, different top masses) are used to estimate these impacts. Since the samples are smaller, there are larger uncertainties on the correction factors. The differences between the variations might also be due to fluctuations (cf. Fig. 6.10).
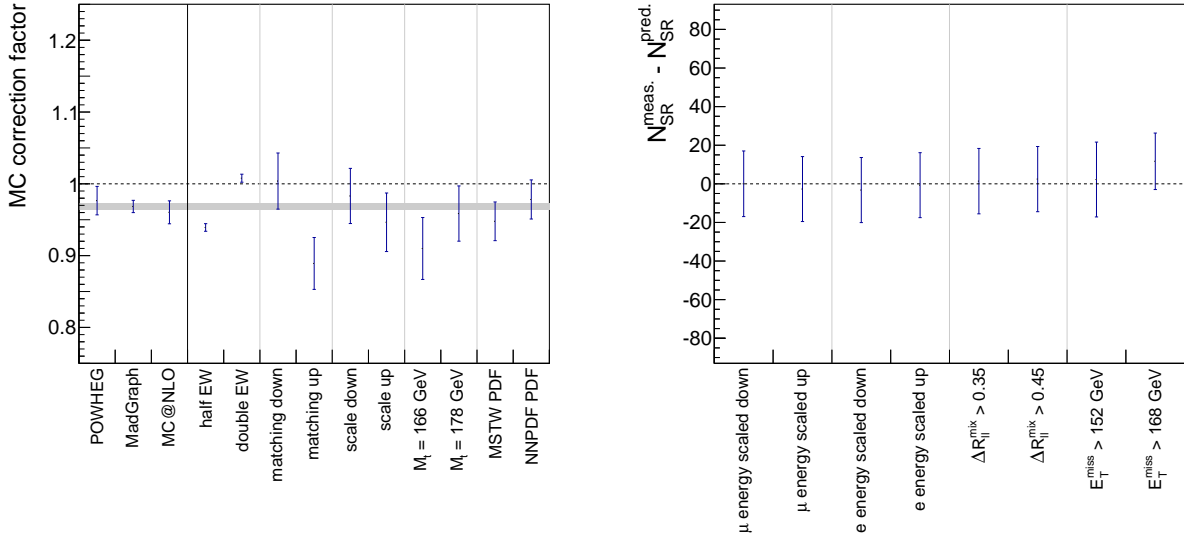
Figure 6.16.: Summary of the systematic uncertainties in the counting experiment. Left: The simulation uncertainties are presented in terms of correction factors to be applied to the number of predicted events in data. The gray band shows the mean factor of the three MC generators, the width represents the error of the mean. Right: The uncertainties in data are presented in terms of measured minus predicted events. The error bars indicate the statistical uncertainty of each variation. The plots are scaled in a way that the shown range in correction factors corresponds to the shown range in number of events, i. e. the variations and error bars in the left and the right plot are comparable.

- The influence of the parton density functions is estimated using the event weighting technique on the POWHEG $t\bar{t}$ sample with two other PDF sets (NNPDF2.1 and MSTW 2008).

The right plot shows the systematic uncertainties in data, the MC correction (mean factor of the three samples) is applied:

- The energy scales of the leptons are varied within their uncertainties. The influence on the prediction is negligible.

- The isolation requirement threshold in the mixed events ($\Delta R > 0.4$) is varied by ± 0.05, but no effect can be seen.

- The E_T^{miss} cut in the event selection is conservatively varied by $\pm 5\%$ (i. e. 152 GeV and 168 GeV).

Adding all systematic uncertainties in quadrature separately for up- and downward deviations delivers the total uncertainty on the prediction. The final result of this counting experiments does not hold the slightest hint of any SUSY signal:

$$\text{Measurement:} \quad N_{\text{SR}}^{\text{meas.}} = 362$$

$$\text{Prediction:} \quad N_{\text{SR}}^{\text{pred.}} = 360.2 \pm 16.9 (\text{stat.}) \, ^{+24.1}_{-40.3} (\text{syst.})$$

The quite large uncertainties on the number of estimated events emphasize that this analysis aims for a shape interpretation.

7. Interpretation

In this chapter the results are interpreted. In Section 7.1 two hypothesis tests are performed, checking whether the Standard-Model prediction describes the data. Then, the Standard-Model hypothesis is contrasted with two different kinds of signal hypotheses: A generic edge shape in Section 7.2.1 and a simplified SUSY model in Section 7.2.2.

7.1. Background Hypothesis Tests

Two common methods are used to quantify the agreement between the measurements and the predicted di-lepton mass shape: a χ^2 test and a Kolmogorov-Smirnov test (cf. e. g. Ref. 136). They are sensitive to different kinds of deviations.

The χ^2 test is based on the sum of the squared residuals. In each bin of the distribution the difference between the measured and the predicted numbers of events is squared and weighted by the uncertainty. The sum of these residuals is called χ^2. It is evaluated using the χ^2 distribution where the number of bins determines the degrees of freedom. The result is the χ^2 probability, which is expected to be evenly distributed between zero and one if the experiment is repeated and the tested hypothesis is true.

In that way an absolute probability how well the data agrees with the prediction can be obtained. Unfortunately, two requirements have to be fulfilled: The data and the prediction must be statistically independent, and the bin uncertainties must by correct and approximately Gaussian. As discussed in Section 5.3.4 there is a correlation between the data and the event-mixing prediction, also the correct error on the mixed events per bin differs from the simple statistical uncertainty. Both problems can be overcome by utilizing the full covariance matrix to calculate the χ^2.

A more practical approach is chosen here. The χ^2 probability is not understood as an absolute measure for the agreement, but is compared to Monte-Carlo results. On the left in Fig. 7.1 the χ^2 probabilities obtained in the thirty MC subsamples as introduced in Section 6.1.1 are plotted as a histogram ("trials"). As expected, it is not evenly distributed, but biased to large values. The χ^2 probability in data is 0.403, which is well in agreement with the Monte-Carlo trials.

The expected deviation between the data and the prediction caused by the contribution from other processes than $t\bar{t}$ is accounted for by excluding di-lepton mass regions from the comparison. As illustrated in Fig. 6.15, these contaminations cluster mainly below 40 GeV and between 81 GeV and 101 GeV (± 20 GeV w. r. t. the Z^0 boson mass). Similarly to the counting experiment in Section 6.3 all selected events with $M_{\ell\ell} > 15$ GeV enter the mixing, but for the comparison only real and mixed event with $40\,\text{GeV} < M_{\ell\ell} < 81\,\text{GeV}$ or $M_{\ell\ell} > 101\,\text{GeV}$ are used. But in contrast to the counting experiment, here both regions are signal regions. A strong feature of the shape analysis is that no background or normalization region is necessary.

Since the χ^2 is just the sum of all squared deviations, the χ^2 test is blind to the positions and the direction of the deviation. No matter if in a certain region of the spectrum one of the distributions is always above the other of if the deviations are in both direction and spread over the whole range, the χ^2 will be the same.
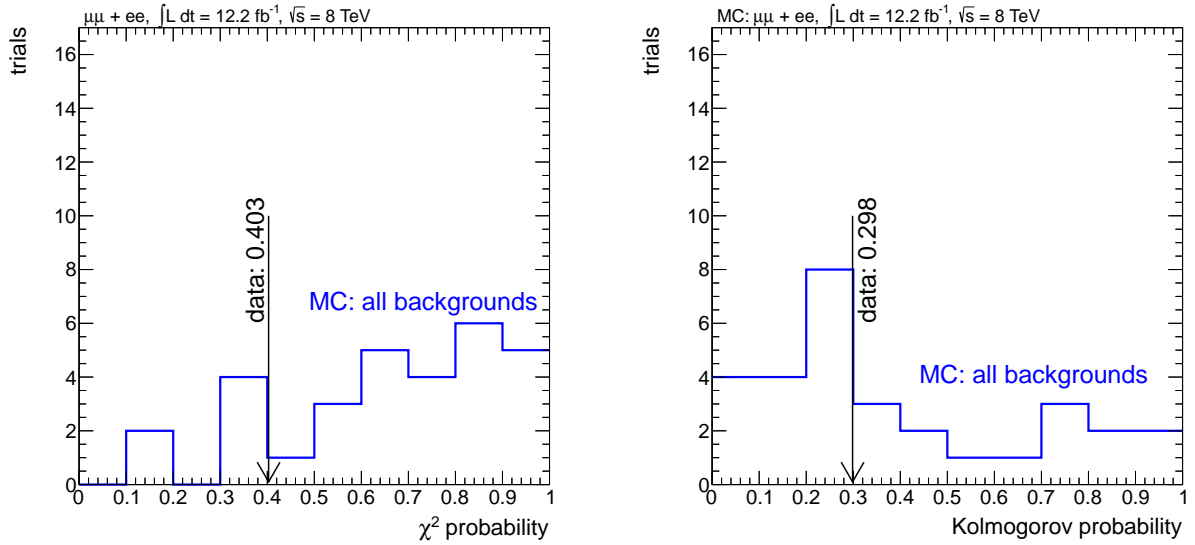
Figure 7.1.: Results of the χ^2 and Kolmogorov-Smirnov tests comparing the measured di-lepton mass distribution with the event-mixing prediction. The p-values in data are compared to 30 Monte-Carlo subsamples that correspond in luminosity and composition to the background-only expectation.

In the Kolmogorov-Smirnov test the normalized cumulative distribution functions of the real and the mixed events are compared. The maximum difference between both distributions that is found at any di-lepton mass is used as test statistic. Hence, the Kolmogorov-Smirnov test is especially sensitive to deviations that cluster in one region of the spectrum and are of the same direction. Another advantage is that the single values of di-lepton masses are used, but not the number of events per bin. The arbitrariness of the binning is avoided, as well as the problems connected with the bin uncertainties and bin correlations.

The test statistic can be translated into a probability using specific tables. Also here a flat probability distribution between zero and one is expected from repeated tests if the prediction is true.

Figure 7.1 shows on the right the distribution of the Kolmogorov-Smirnov probability among the MC subsamples. Here, the MC trials tend to smaller probability values. The probability in data is 0.298, which is well in agreement with the Monte-Carlo expectations. Again, the contaminated regions $M_{\ell\ell} < 40\,\text{GeV}$ and $81\,\text{GeV} < M_{\ell\ell} < 101\,\text{GeV}$ are excluded from the real and the mixed event sample.

7.2. Signal Hypotheses Tests

More powerful tests can be performed if an alternative hypothesis is formulated. In the previous section it was only tested whether the data agrees with the prediction or not. Now, the null or background hypothesis is contrasted with a specific alternative or signal hypothesis. Then the maximum likelihood ratio can be used as test statistic. The alternative hypothesis has one additional free parameter quantifying the amount of signal events. The null hypothesis can be derived from the alternative hypothesis by setting this parameter to zero. In that sense the null
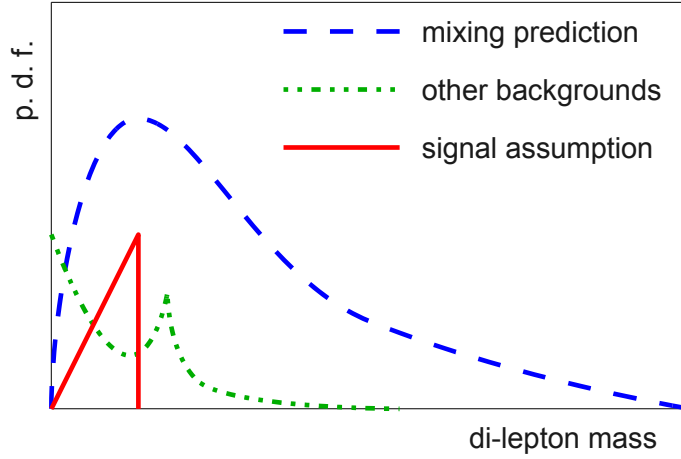
Figure 7.2.: Sketch of the three components of the p. d. f. The main background $t\bar{t}$ is described by the mixed event shape, the shape of the other backgrounds is taken from Monte Carlo, the signal shape is either described by a triangle or taken from simulation. The final p. d. f. is the weighted sum of these components with the weights as free parameters.

hypothesis is a special case of the alternative. Performing the maximum-likelihood-ratio test, the signal parameter and further parameters describing the model, called nuisance parameters $\boldsymbol{\nu}$, are varied to find the maximum likelihood of the alternative hypothesis[1]. The same is done for the null hypothesis, where only the nuisance parameters are varied. The maximum-likelihood test statistic λ can be symbolically written like:

$$\lambda = \frac{\max L\left(\boldsymbol{\nu}, S = 0 | \text{data}\right)}{\max L(\boldsymbol{\nu}, S | \text{data})}, \tag{7.1}$$

where L is the likelihood and S is the signal parameter. The numerator is the maximum likelihood of the data under the null hypothesis $S = 0$, the denominator the maximum likelihood for any S. Obviously, the test statistic is limited to $\lambda \leq 1$, with $\lambda = 1$ if $S = 0$ maximizes the likelihood.

The probability density function (p. d. f.) that is used to construct the likelihoods is composed of two background contributions and one signal contribution, which are sketched in Fig. 7.2:

The event-mixing distribution predicts the $t\bar{t}$ background, which is the main background. The p. d. f. is constructed as the shape of a fine-binned histogram of the mixed di-lepton masses.

The other backgrounds are accounted for by a shape that is derived from Monte Carlo. Drell-Yan, di-boson, tri-boson, single top, and $t\bar{t}$V processes are combined according to their cross sections. The p. d. f. is constructed from the histogram, but a second-order interpolation is applied to avoid sharp edges at bin boarders.

---

[1]Here, a profile likelihood is used to handle the nuisance parameters.

The signal p. d. f. is illustrated here as a triangular edge shape. In Section 7.2.1 such a triangular shape is used, but additionally smeared by a Gaussian to account for detector resolution effects. In Section 7.2.2 Monte-Carlo simulations of a simplified SUSY model are studied. Since the statistics of the MC samples are limited, the signal p. d. f. is constructed with a kernel estimation method [137] from the simulated events.

The final p. d. f. is the weighted sum of the three components:

$$\text{p. d. f.} = B_{\text{t}\bar{\text{t}}} \cdot \text{mixing p. d. f.} + B_{\text{other}} \cdot \text{other backgrounds p. d. f.} + S \cdot \text{signal p. d. f.}, \qquad (7.2)$$

where $B_{\text{t}\bar{\text{t}}}$ and B_{other} are unconstrained nuisance parameters, and S is the already mentioned parameter of interest. In this parameterization the weights $B_{\text{t}\bar{\text{t}}}$, B_{other}, and S are the number of events of the according processes[2]. The shape of the other backgrounds contribution is taken from simulation, but the number of events is a free parameter, whose value is determined in the likelihood maximization.

7.2.1. Generic Mass Edge Scan

The supersymmetric signal is expected to show up in the di-lepton mass spectrum as an edge-like shape, as discussed in Section 5.1. In a model-independent way a generic triangle shape is used here as signal hypothesis. It is not even limited to Supersymmetry. Any new physics model that predicts a decay $X \rightarrow \ell^+\ell^-Y$, where X and Y are on-shell particles can be tested.

The only parameter of this generic edge model is the endpoint of the signal shape. A limitation towards small di-lepton masses is not assumed, hence the lower edge of the triangle is at zero. The triangle is convoluted with a Gaussian (with a width of 1.5 GeV) to account for resolution effects in the di-lepton mass measurement. A scan is performed varying the signal endpoint between 20 GeV and 400 GeV in steps of 5 GeV. For each step the maximum likelihood ratio fit is performed. In Fig. 7.3 the numbers of events that maximize the likelihood are shown. Of course, also the amount and composition of the background depend on the signal hypothesis. Therefore the best fitting numbers of $\text{t}\bar{\text{t}}$ and other background events are also plotted.

At several values of endpoints the signal hypothesis fits better to the data than the background-only hypothesis, most striking at endpoints between 130 GeV and 150 GeV, but also at very small values, slightly above the Z^0 mass, and at 185 GeV. At several higher endpoint masses up to 300 GeV smaller signal contributions are preferred by the fit. Figure 7.4 exemplarily displays the di-lepton mass spectrum with the best fitting process composition for different signal hypotheses.

First the result for the background-only hypothesis is shown. It is notable that the background composition resulting from the fit differs from the Monte-Carlo expectation. From the simulation 983 $\text{t}\bar{\text{t}}$ events and 237 other background events (Drell-Yan, di-boson, tri-boson, single top, and $\text{t}\bar{\text{t}}$V) are expected, under the background hypothesis 881 $\text{t}\bar{\text{t}}$ events and 336 other background events maximize the likelihood. The small overshoot of data events w. r. t. to MC at small di-lepton masses (cf. Fig. 4.13) explains that behavior. If a very narrow signal edge is added to the p. d. f. composition (i. e. at 30 GeV, as shown at the top right in Fig. 7.4) this excess of events is assigned to the signal and the background composition fits better to the MC expectation. The local significance (without accounting for systematic uncertainties) is however only 1.6σ.

---

[2]A so-called extended p. d. f. is used that is not required to be normalized to unity.
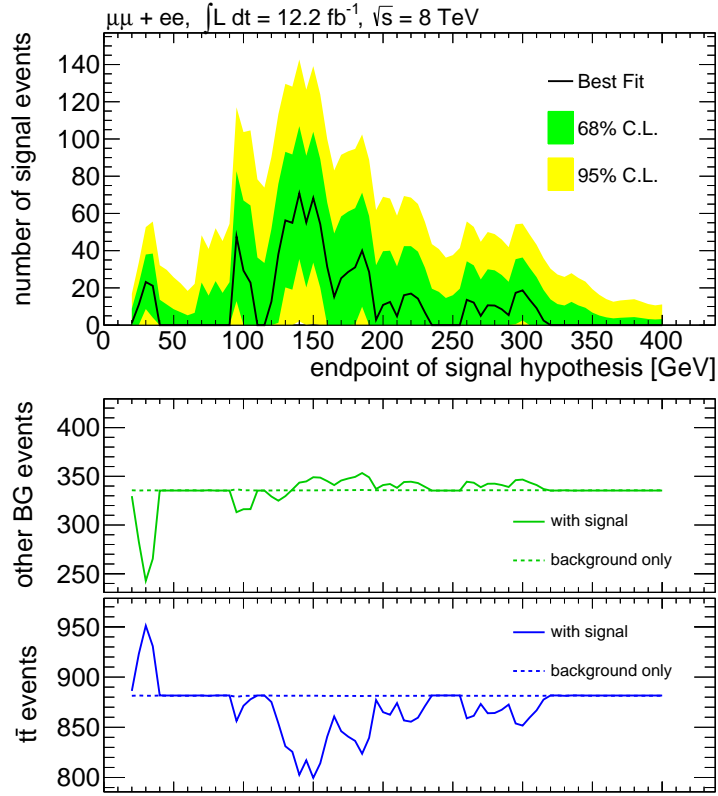
Figure 7.3.: Numbers of signal and background events maximizing the likelihood for different values of the signal endpoint. On the top the number of signal events (i.e. the integral of the triangle shape) together with the 1σ and 2σ uncertainty bands are plotted. Below the numbers of the two background components are shown. The dashed lines show the background composition under the null hypothesis. Systematic uncertainties are not taken into account.

The signal scenario with an endpoint at $95\,\mathrm{GeV}$ leads to a significance of 1.36σ. Here, the signal edge is close to the Z^0 peak and can replace parts of the two backgrounds. The further signal hypothesis shown in Fig. 7.4 coincidence with fluctuations in the data. Most significant is the excess of the edge at $140\,\mathrm{GeV}$ with 2σ. Although the edge shape is less affected by the look-elsewhere effect than a peak shape, especially at the falling background spectrum any upward fluctuation can give rise to a small excess. Taking the look-elsewhere effect as well as systematic uncertainties into account would decrease the stated significances.

From the edge scan summary in Fig. 7.3 as well as from the examples in Fig. 7.4 the different kinds of "leveling" between the p.d.f. components can be studied: If a narrow edge at $30\,\mathrm{GeV}$ is provided to the fit, the excess is at the expense of the other backgrounds, while an increase of the $t\bar{t}$ background compensates for the lack of other background events at higher masses. If the edge is close to the Z^0 peak similar fractions of events from both background components are assigned to the signal. For high-mass signal edges the number of $t\bar{t}$ events is reduced, while more other background events compensate in the low-mass region.

As done in Section 6.1, the event sample can be divided into a di-muon sample and a di-electron sample. Additionally, b tags can be required in order to study third-generation rich
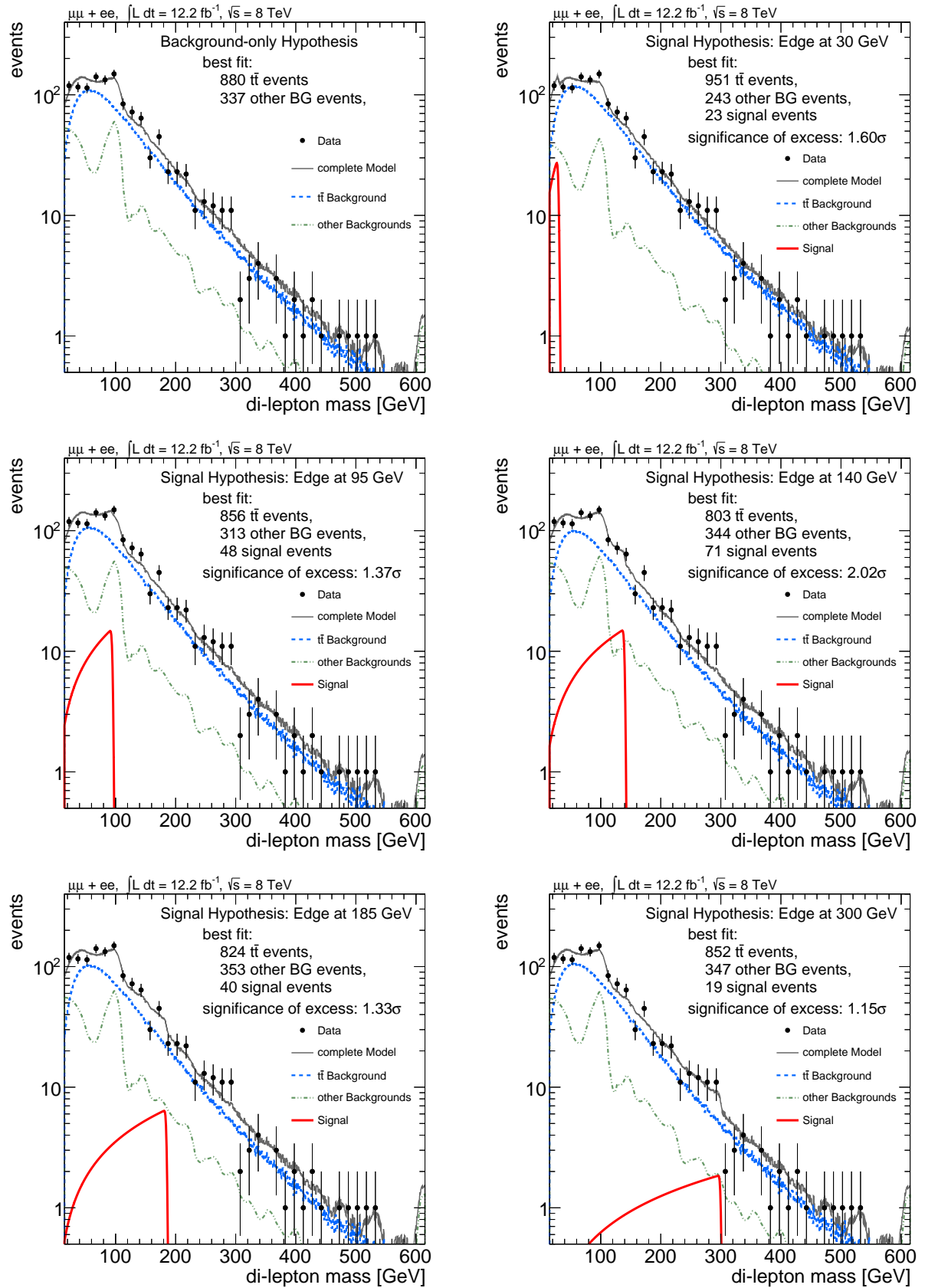
Figure 7.4.: The di-lepton mass spectrum as measured in data faced with the background-only hypothesis (top left) and several signal endpoint hypotheses. The stated significances are local, without accounting for systematic uncertainties.
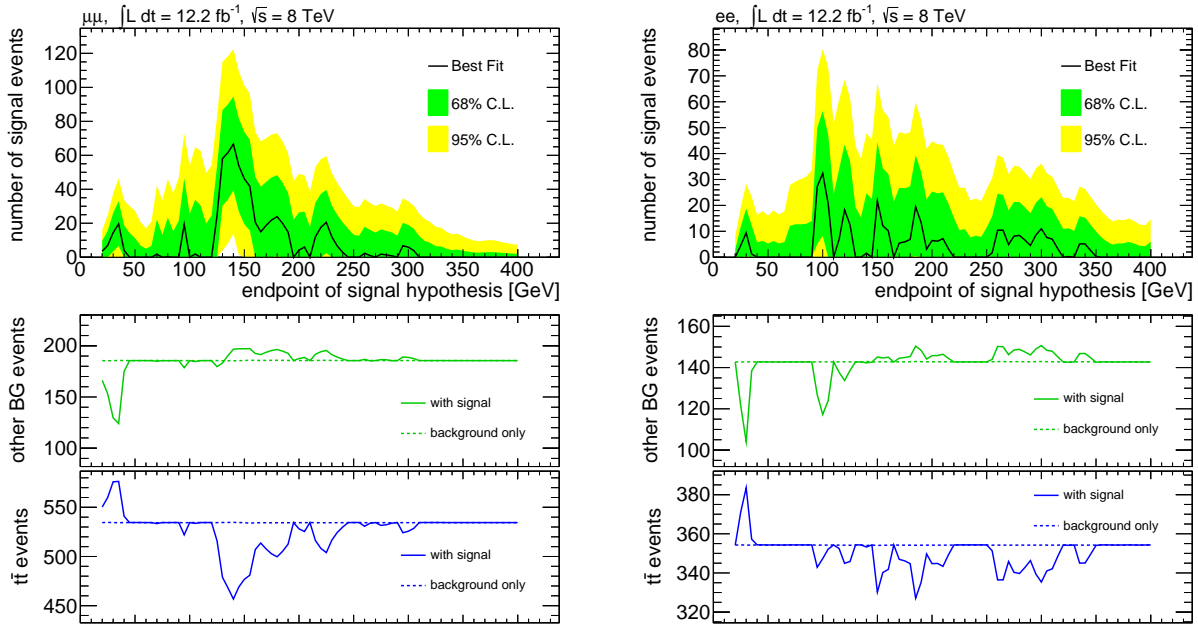
Figure 7.5.: Scan results in the di-muon (left) and in the di-electron (right) channel

SUSY models, but also benefit from a cleaner $t\bar{t}$ sample.

The scan results for the separate di-muon and di-electron scenarios are shown in Fig. 7.5. The most significant excess at 140 GeV is clearly caused by $\mu^+\mu^-$ events, while the signal edge close to the Z^0 peak is more accented in the e^+e^- channel. The situation at small masses is similar in both channels.

Figure 7.6 displays the di-muon and di-electron mass spectra with fitted background and signal compositions, illustrating the background hypothesis as well as the most significant signal hypothesis. The local significance without systematic uncertainties of the 140 GeV excess in the di-muon increases w.r.t. the inclusive channel to 2.49σ, whereas the significance of the excess close to the Z^0 peak is similar in the di-electron channel and the inclusive channel.

The endpoint scan result requiring identified b-quark jets is presented in Fig. 7.7. The small excess at low masses is still present, while the Z^0 excess completely and the 140 GeV excess nearly vanish. Interestingly the two background components change their behavior in the low-mass region. While the signal in the inclusive, the di-muon, the di-electron, and the 1-b-tag sample is at the expense of the other backgrounds with a simultaneously increased number of $t\bar{t}$ events, in the 2-b-tag sample it is vice versa. Here, the other backgrounds are enhanced under the low-mass signal hypothesis and the $t\bar{t}$ background is reduced. This can be explained by the changed shape of the other-background templates. The contribution from $Z^0 \rightarrow \tau^+\tau^-$ is strongly reduced by the b-tag requirement, i.e. the low-mass contribution from the other-background shape is reduced as well. In Fig. 7.8 the di-lepton mass distribution plots with b-tag requirements are shown. The small Z^0 peak in the other background template originates mainly from $t\bar{t}Z^0$ events. In this case the template suffers increasingly from low Monte-Carlo statistics.

Again, the different-flavor channel is analyzed for control reasons. In this channel no signal edge is expected, hence any observed deviations are interpreted as fluctuations. In Fig. 7.9 the numbers of signal and background events that are preferred by the fit are plotted against the
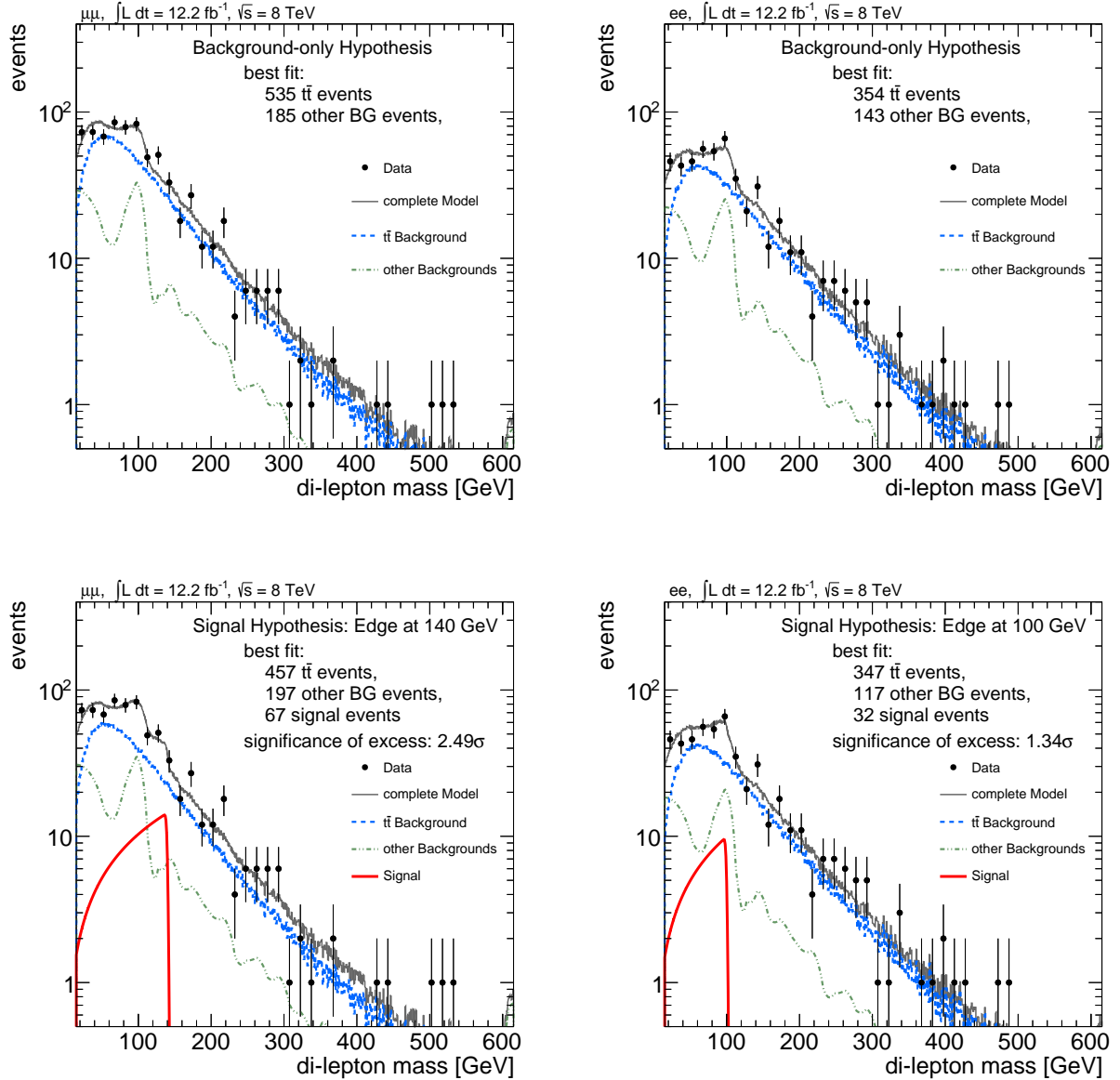
Figure 7.6.: The di-lepton mass spectrum as measured in data faced with the background-only hypothesis (top) and a signal endpoint hypothesis (bottom) in the di-muon channel (left) and the di-electron channel (right). The shown signal examples are the most significant in the according channel. The stated significances are local, without accounting for systematic uncertainties.
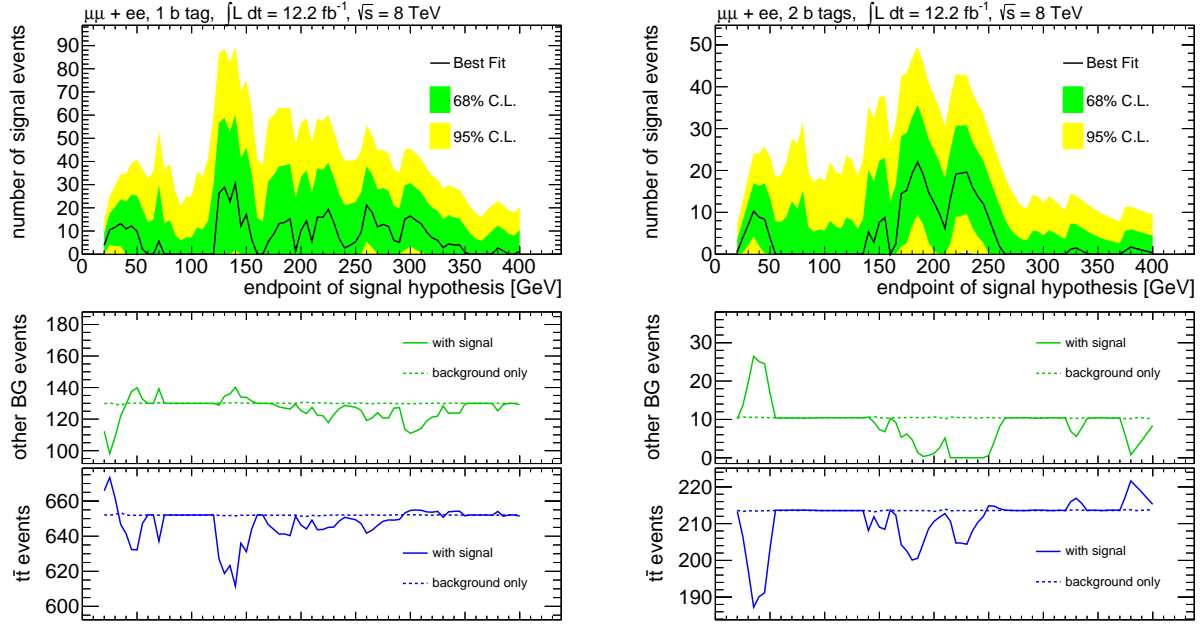
Figure 7.7.: Scan results if additionally b-tagged jets are required: at least one b tag on the left, at least two b tags on the right.

endpoint of the signal hypothesis. Figure 7.10 displays the di-lepton mass spectrum fit under the background-only hypothesis and under the signal hypothesis that shows the most significant excess. The already discussed mismatch between the data and the prediction in the μe channel (cf. Section 6.1) leads to broad region of fitting signals with endpoints between 150 GeV and 300 GeV. But also at very small di-lepton masses a small amount signal events are preferred by the fit.

It can be concluded that the observed "excesses" in the search channels (inclusive OSSF, di-muon, di-electron, at least 1 b tag, at least 2 b tags) are all in agreement with the expectations from Standard-Model processes. The signal search in the μe control channel confirms that quality and quantity of the excesses can be assumed from fluctuations in the data.

Limit Setting

Since none of the tested signal scenarios result in a significant excess w. r. t. the background-only hypothesis, exclusion limits are set. These limits state the minimum number of signal events that are needed to expect a significant excess. That means, all models that predict at a certain endpoint mass more signal events can be excluded with a confidence level (C. L.) of 95%. From the upper bound of the 2σ uncertainty band in Fig. 7.3 a first estimate of the 95% upper limit can be read. However, for the exclusion limits the more trusted frequentist CL_s method [5, 138] is used.

In Fig. 7.11 the 95% C. L. upper exclusion limit is presented. Besides the observed limit curve also the expected limit is drawn. This limit is expected if the null hypothesis is true, i. e. no signal exists that forms a triangle shape in the opposite-sign same-flavor di-lepton mass
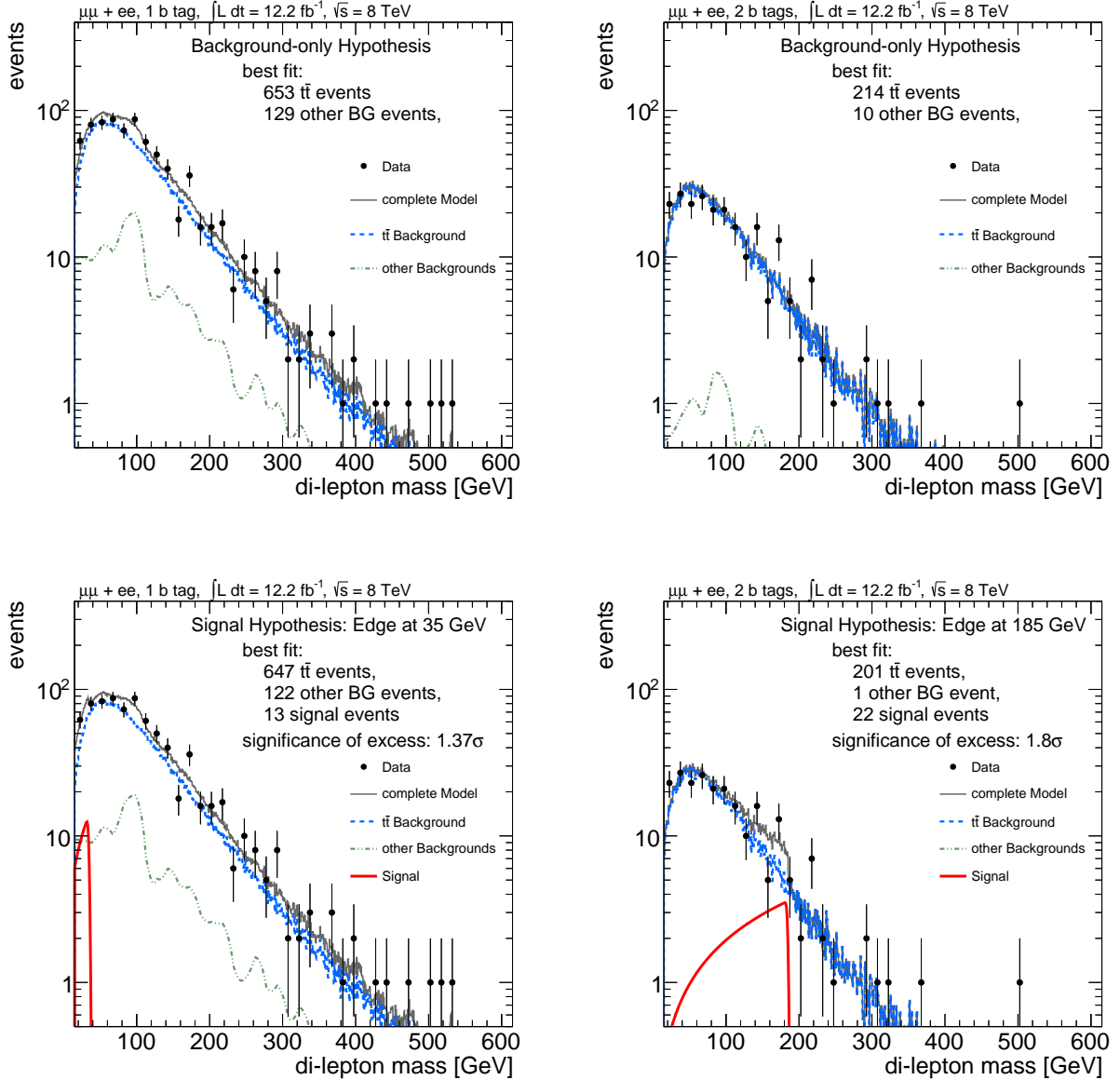
Figure 7.8.: The di-lepton mass spectrum as measured in data faced with the background-only hypothesis (top) and a signal endpoint hypothesis (bottom) with at least one b tag (left) and at least two b tags (right). The stated significances are local, without accounting for systematic uncertainties.
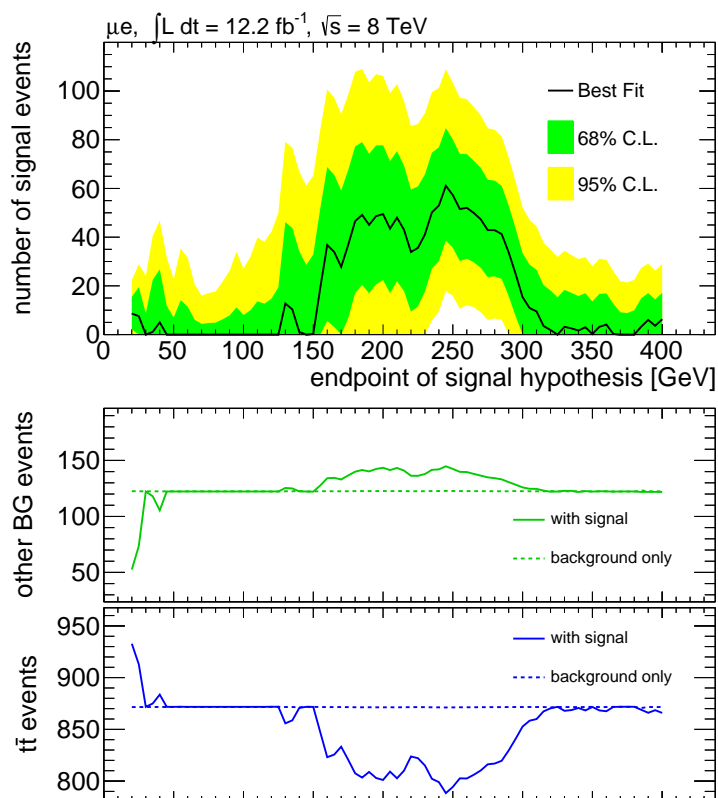
Figure 7.9.: Scan result in the μe control channel.
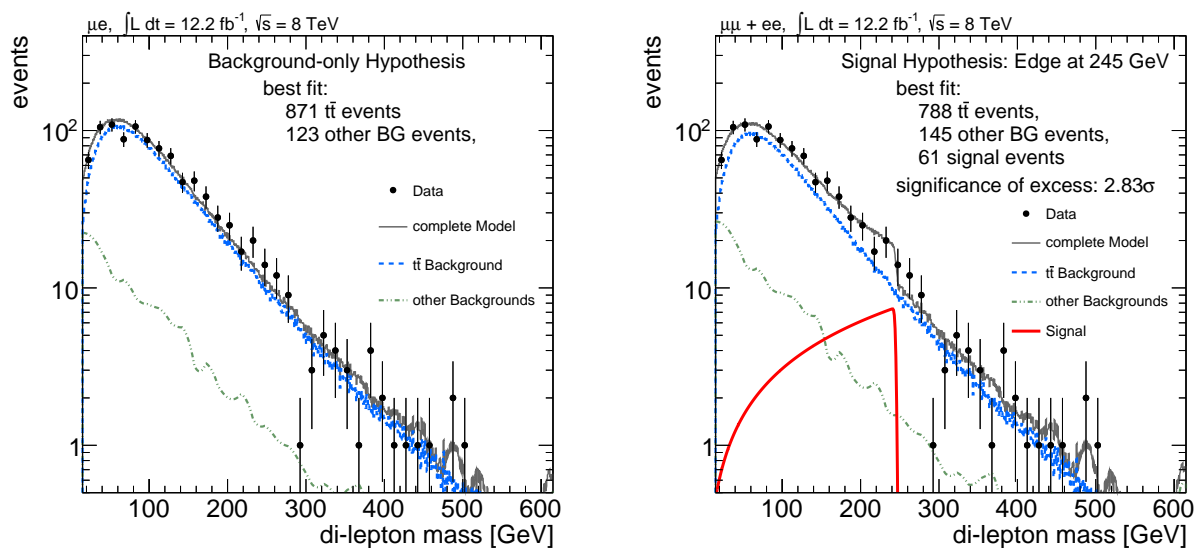
Figure 7.10.: The di-lepton mass spectrum as measured in data faced with the background-only hypothesis (left) and one signal endpoint hypothesis (right).
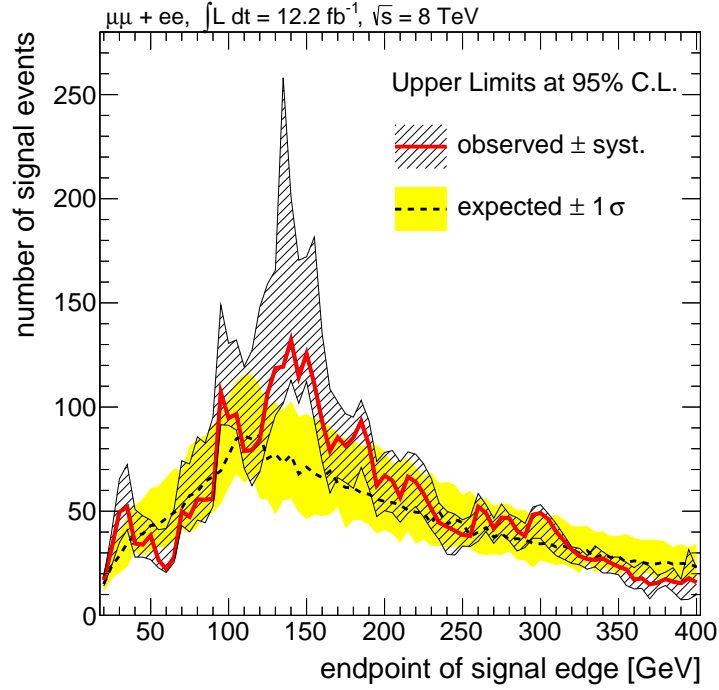
Figure 7.11.: The exclusion limit on the number of signal events distributed in an triangle shape w. r. t. the endpoint of the triangle.

spectrum at the tested endpoints. The rise and fall of the expected limit reflect the sensitivity resulting in the interplay between the different background and signal shapes. The sensitivity is high at small masses where the edge is almost peak-like, it gets worse in the $t\bar{t}$ bulk region where signal hypothesis and background prediction become less distinguishable, and gets better again moving to endpoints at large masses where the distance between the background maximum and the signal maximum is getting larger.

An absolute agreement between expected limit and the observed limit is not expected due to fluctuations is data. The regions where the observed limit is less stringent than the expected are already discussed above. Additionally uncertainty bands are shown: The expected limit is surrounded by the 1σ uncertainty band obtained from fluctuations in the toy experiments that are performed to calculate the limits. The hashed area around the observed limit illustrates the effect of systematic uncertainties. Each variation discussed in Section 6.2 leads to one limit curve. The hashed area is the envelope of all these curves. Conservatively the upper edge of the envelope should be trusted as exclusion limit.

The strong upward fluctuation of the systematic uncertainty band around signal endpoints of 135 GeV is studied in Fig. 7.12. On the left the same limits are shown as in Fig. 7.11, but the systematic variation of the $E_{\mathrm{T}}^{\mathrm{miss}}$ cut threshold is not included in the hashed band. Instead, the observed limits with the varied $E_{\mathrm{T}}^{\mathrm{miss}}$ cut are drawn separately. Clearly, the $E_{\mathrm{T}}^{\mathrm{miss}}$ threshold downward variation causes the large range of the systematic uncertainty. On the left the best-fit result at an endpoint of 135 GeV in the data sample with the lowered $E_{\mathrm{T}}^{\mathrm{miss}}$ cut is shown. The significance of the excess is only slightly larger than in the regular sample. The much weaker limit in the cut varied sample can be partly explained by the total number of events, which is, of course, larger if the $E_{\mathrm{T}}^{\mathrm{miss}}$ cut is lower. Normalized to the same total number of
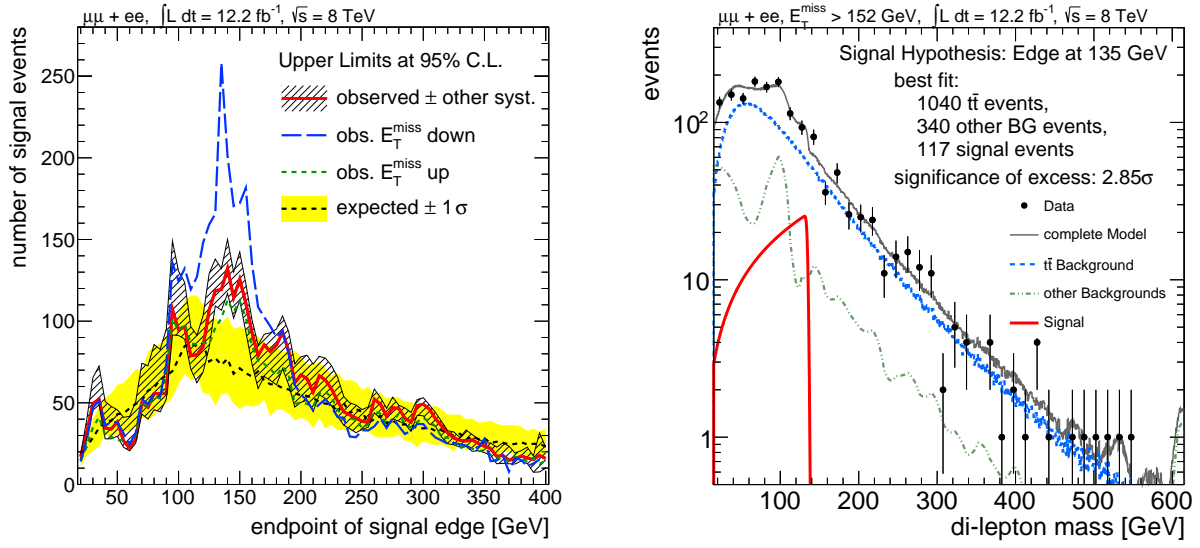
Figure 7.12.: Strong limit fluctuation due to E_T^{miss} uncertainty: Compared to Fig. 7.11, on the left the change of the limit due to the E_T^{miss} cut threshold variation is drawn separately. The limit in the sample with the loosened E_T^{miss} cut is clearly the weakest of all systematic variations. The best-fit plot on the right, however, shows no large difference compared to Fig. 7.4.

measured events, the upper limit of 250 events corresponds to approximately 200 events in the regular data sample with the E_T^{miss} cut applied at 160 GeV. This is still more than what can be excluded in the regular sample, but the E_T^{miss} variation was assumed to be a dominant systematic uncertainty.

In Fig. 7.13 the exclusion limits separately in the $\mu^+\mu^-$ and the e^+e^- channels are shown. The main observation is like before: The excess in the 150 GeV region is only present in the $\mu^+\mu^-$ channel, while the deviation around the Z^0 boson mass is only visible in the e^+e^- channel. However, in the e^+e^- channel the observed and the expected limit agree very well.

The exclusion limits in the one and two b-tag channels are presented in Fig. 7.14. In both samples an underfluctuation at mass edges around 100 GeV is observable. In events with at least two b-tagged jets the excess at low masses is less compensated by the systematic uncertainties. A further deviation between the expected and the observed limit appears at signal endpoints of around 230 GeV.

7.2.2. Exclusion Limits in an SMS Parameter Space

Using the generic mass edge limits every possible model can be tested that produces an edge in the opposite-sign same-flavor di-lepton mass spectrum. However, it is deemed worthwhile to calculate limits in an actual SUSY model as well. For that purpose a *simplified model spectrum* (SMS) of direct gaugino production is chosen.

Figure 7.15 illustrates the process. Via electroweak quark-quark fusion two gauginos are produced, such as $q\bar{q} \rightarrow W^\pm \rightarrow \tilde{\chi}_2^0 \tilde{\chi}_1^\pm$. In contrast to the majority of SUSY searches at the LHC, the sparticles are not produced via strong interaction, thus less hadronic activity in
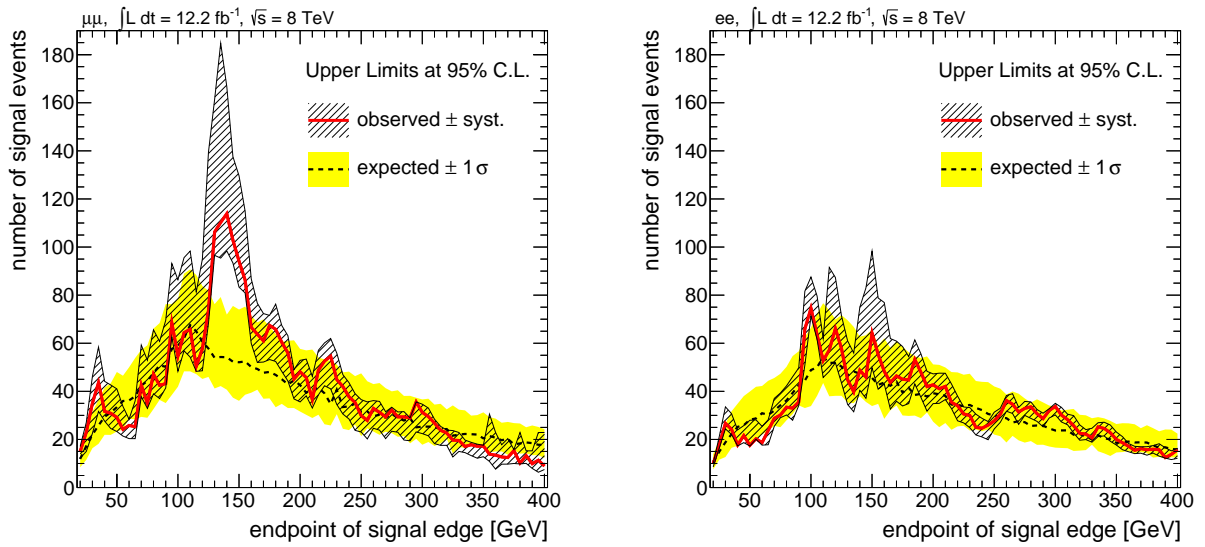
Figure 7.13.: The exclusion limits separately in the di-muon (left) and in the di-electron (right) channel.
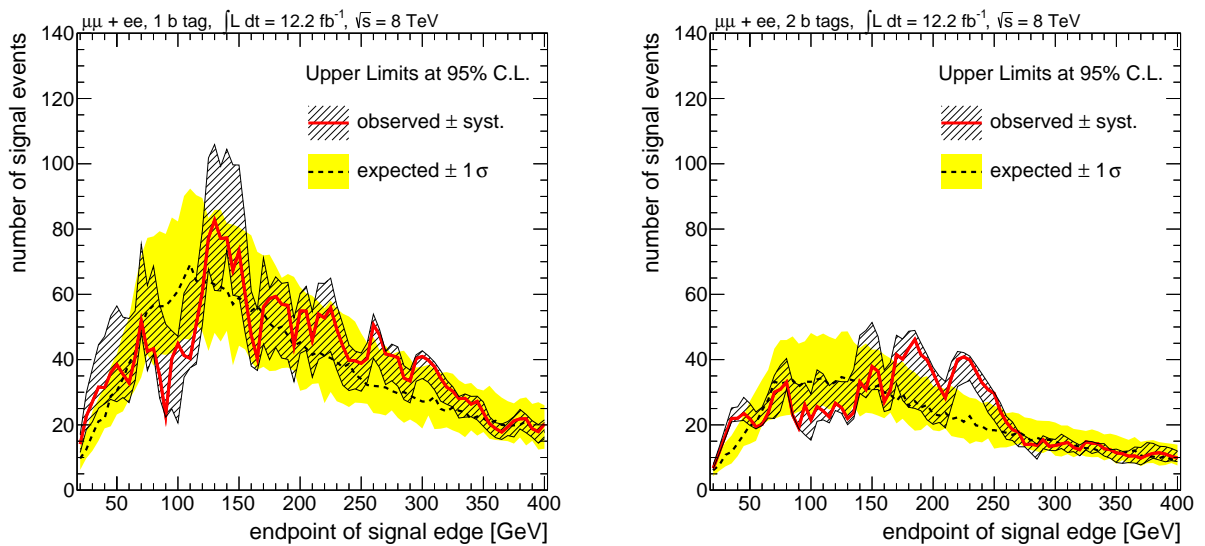
Figure 7.14.: The exclusion limits if additionally b-tagged jets are required: at least one b tag on the left, at least two b tags on the right.
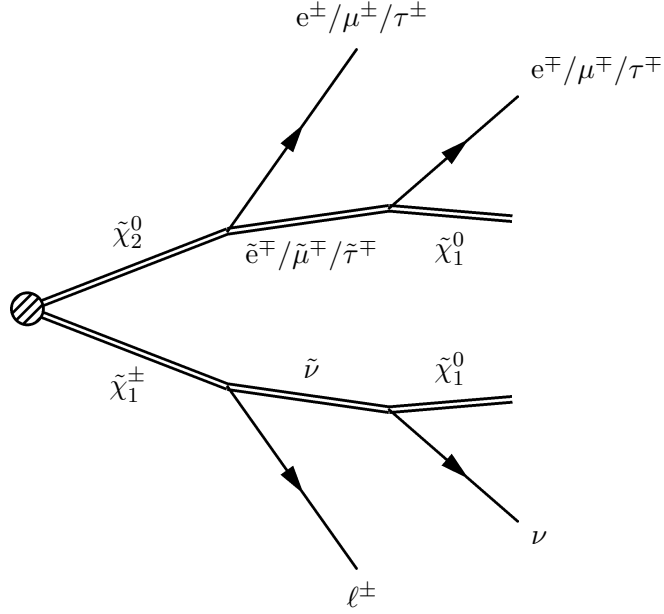
Figure 7.15.: SMS process on which exclusion limits are set. The involved particle masses act as parameters of the model.

the event is expected. The shown process leads to a final state with three lepton and missing transverse energy due to one neutrino and two $\tilde{\chi}_1^0$. Two of the three leptons are correlated in flavor, sign, and kinematics, i.e. they form an edge in the opposite-sign same-flavor di-lepton mass distribution. The third lepton originates from the other decay branch. The event selection used up to now required at least two leptons and at least two jets. Obviously, three leptons and no jet requirement would be more appropriate. However, the background composition would also change. The main background would not be $t\bar{t}$ anymore, but di-boson. Since the heart of this analysis is the $t\bar{t}$ background estimation it is compromised on two leptons as before, but only at least one jet.

The additional jet that is not expected from the diagram in Fig. 7.15 is supposed to originate from initial state radiation. In Table 4.1 it is shown that the fractions of Drell-Yan and di-boson events are increased by omitting the requirement for the second jet, but $t\bar{t}$ is still the dominant background. Table 4.2 shows that the one-jet requirement reduces the number of signal stronger than the number of background events. Nevertheless the cut seems appropriate since it rejects many di-boson events. Performing the analysis with no jet requirement would increase the Monte-Carlo dependency, since the di-boson shape is taken from simulation.

The parameters of the model are the masses of the involved SUSY particles. Parts of this parameter space should be excluded. Three two-dimensional scans are available. The scanned parameters are the masses of the $\tilde{\chi}_2^0$ and the $\tilde{\chi}_1^\pm$, which are assumed to be mass degenerated, and the mass of the $\tilde{\chi}_1^0$. The masses of the intermediate states, i.e. the slepton and the sneutrino, are also assumed to be identical and change with $M_{\tilde{\chi}_2^0, \tilde{\chi}_1^\pm}$ and $M_{\tilde{\chi}_1^0}$. In one scan $M_{\tilde{\ell}, \tilde{\nu}}$ is always in the middle between the two scanned masses, in the second scan it is close to the lighter mass, in the third scan close to the heavier mass. It is parametrized by $x_{\tilde{\ell}}$:

$$M_{\tilde{\ell}, \tilde{\nu}} = M_{\tilde{\chi}_1^0} + x_{\tilde{\ell}} \left(M_{\tilde{\chi}_2^0, \tilde{\chi}_1^\pm} - M_{\tilde{\chi}_1^0} \right), \tag{7.3}$$
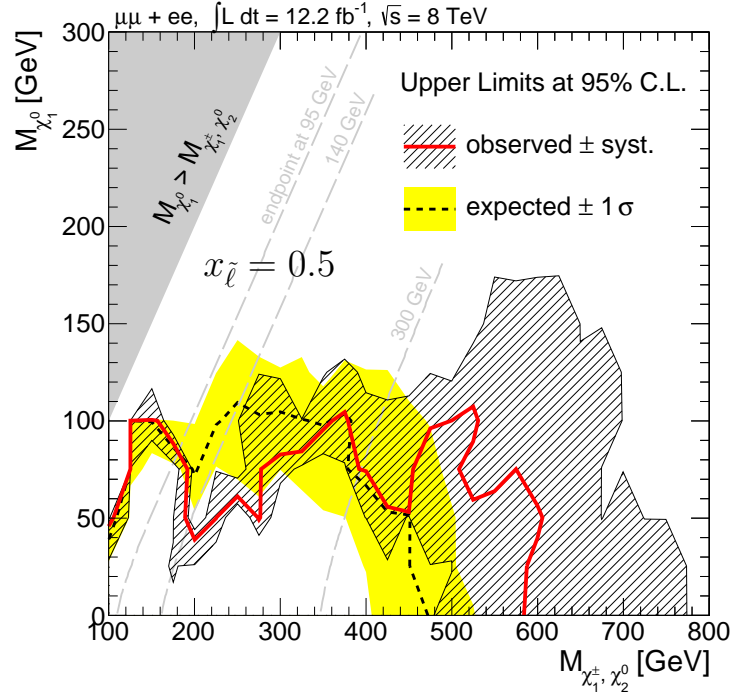
Figure 7.16.: Exclusion limit in the SMS plane with $x_{\tilde{\ell}} = 0.5$. The hashed area is the envelope of all exclusion curves obtained from the systematic variations. Lines of constant position of the mass edge are drawn in dashed gray for some values that are studied in the context of the generic mass-edge scan.

with the values $x_{\tilde{\ell}} = 0.5, 0.05, 0.95$.

In the case of $x_{\tilde{\ell}} = 0.5$ the analysis is most sensitive since the available energy is evenly distributed between the two leptons. The obtained exclusion limit is displayed in Fig. 7.16. In a similar way as before, the uncertainty on the expected limit and the systematic uncertainty on the observed limit are shown. Conservatively, the *lower* edge of the hashed area reaching up to $M_{\tilde{\chi}_2^0, \tilde{\chi}_1^\pm} = 500\,\text{GeV}$ is the final exclusion limit.

In Fig. 7.17 several example parameter points are plotted as well as the fit result under the background-only hypothesis for this modified event selection. The fit with no signal reproduces nicely the background event composition expected from Monte Carlo, which is 1255 $t\bar{t}$ events and 432 other background events. In the region between $M_{\tilde{\chi}_2^0, \tilde{\chi}_1^\pm} = 200\,\text{GeV}$ and $M_{\tilde{\chi}_2^0, \tilde{\chi}_1^\pm} = 300\,\text{GeV}$ the observed exclusion limit is weaker than expected. That means that in this region the signal fits to the data. From the dashed gray lines in Fig. 7.16 as well as from the example fit on the bottom left in Fig. 7.17 it becomes clear that in this parameter region the edge in the di-lepton mass is at values where an excess is also observed in the generic mass scan. However, in parameter regions with edges near the mass of the Z^0 boson and around 300 GeV no deviation between the observed and the expected limit is visible.

In Fig. 7.18 the exclusion limits in the parameter scans with $x_{\tilde{\ell}} = 0.05$ and $x_{\tilde{\ell}} = 0.95$ are plotted. Especially for $x_{\tilde{\ell}} = 0.05$ the limit is much weaker. The reason is the very different distribution of the energy between the two leptons. For $x_{\tilde{\ell}} = 0.05$ the masses of the primary gaugino and the slepton are very similar, i.e. in the $\tilde{\chi}_2^0 / \tilde{\chi}_1^\pm \to \tilde{\ell}\ell$ decay the lepton has only little momentum in the rest frame of the gaugino. The slepton decay into the much lighter $\tilde{\chi}_1^0$
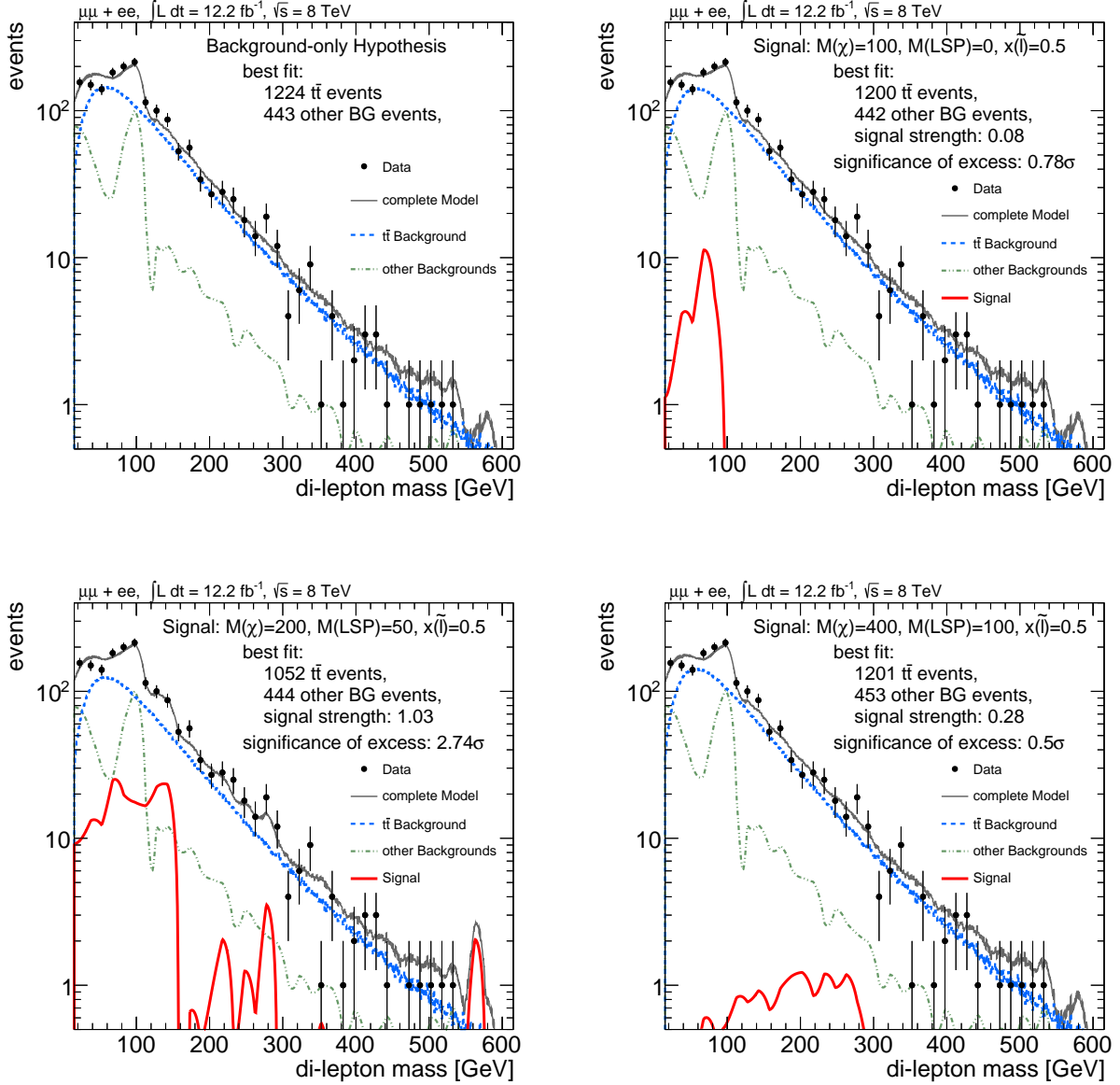
Figure 7.17.: Fit results for the background-only hypothesis and several points in the SMS parameter space. The signal is parametrized in terms of "signal strength", which is the cross section normalized to the expected cross section. The expected positions of the mass edges according to Eq. 5.2 is for the top right scenario 87 GeV, bottom left 143 GeV, and bottom right 286 GeV.
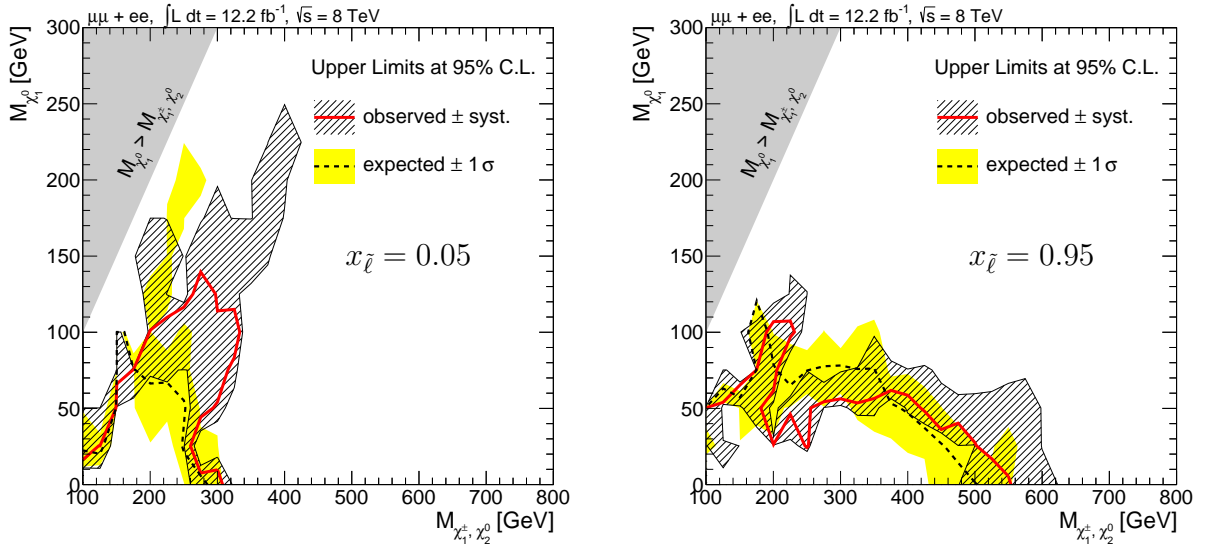
Figure 7.18.: Exclusion limits in the SMS plane with $x_{\tilde{\ell}} = 0.05$ and $x_{\tilde{\ell}} = 0.95$

produces a high-energetic lepton. Consequently, for $x_{\tilde{\ell}} = 0.05$ one of the leptons is expected to be mostly soft and therefore might not surpass the trigger and selection threshold.

For $x_{\tilde{\ell}} = 0.95$ the situation is reverse. The first decay in the cascade produces a high-energetic lepton while the second lepton gets only a small boost in the rest frame of its mother particle, the slepton. The slepton, however, is boosted from the gaugino decay, i.e. also the lepton is expected to be energetic in the laboratory frame. In this case both leptons have a good chance to be selected and the sensitivity is only a little bit weaker than in cascades with a $x_{\tilde{\ell}} = 0.5$ mass hierarchy.

Comparing the exclusion limit of this analysis in Fig. 7.17 with the CMS-published best limit in the SMS with direct gaugino production in Fig. 2.9, other analyses are clearly more sensitive to such a SUSY scenario. However, the comparison might be not really fair. While the CMS-published limit is a combination of several analyses that as particularly designed for such models (most strongest is the tri-lepton analysis), the limit presented here is more or less a by-product. As discussed, the event selection does not really fit to the features of the signal. Requiring only two leptons although three are expected in the signal and requiring a jet that is not expected from the hard process, could be called negligent, if the analysis was aiming for best sensitivity in the presented gaugino-production model. Moreover the CMS-published limit includes also τ events.

The main result of this analysis is the exclusion limit on the generic mass edge presented in Fig. 7.11. It shows the sensitivity of the presented analysis in a very model independent way.

8. Conclusions

Within Supersymmetry and other models of new physics, cascades with two subsequent particle decays each including one lepton are possible. The leptons are expected to be correlated in charge, flavor, and kinematics, resulting in an edge-like structure in the opposite-sign same-flavor di-lepton mass spectrum.

In this thesis an analysis has been presented searching for such a signal in LHC collisions at a center-of-mass energy of $8\,\mathrm{TeV}$ recorded by the CMS detector in 2012. The analyzed data corresponds to an integrated luminosity of $12.2\,\mathrm{fb}^{-1}$. Events with at least two leptons forming an opposite-sign same-flavor pair are selected. Additionally, a transverse imbalance of the momenta and at least one or at least two jets per event are required in order to enrich possible signal events. In the resulting data sample most Standard-Model background events are expected from $t\bar{t}$ processes.

With the event-mixing technique an established background estimation method in particle and nuclear physics has been found to be suitable to predict the $t\bar{t}$ background from data. Since event mixing is a novel technique to estimate the $t\bar{t}$ background, it has been tested and validated with simulated $t\bar{t}$ events. Two event energies have been found to compromise the prediction ability of event mixing: The total boost of the $t\bar{t}$ system and the di-top mass. A reliable simulation of both quantities has been ensured.

Further Standard-Model backgrounds cluster in two distinct regions in the di-lepton mass spectrum: Below $40\,\mathrm{GeV}$ mainly $\mathrm{Z}^0 \to \tau^+\tau^-$ events are expected, around the mass of the Z^0 boson di-boson events are predicted by Monte Carlo to survive the event selection. Two ways handling these backgrounds are chosen: These regions are either excluded from the search or the shape of these backgrounds is taken from simulation.

Systematic uncertainties account for effects that might occur in the transition of the event-mixing technique from Monte Carlo to data. Is has been proven with simulated events that the method works. In addition, a crosscheck performed in the different-flavor channel provides evidence that the data behave as expected in the event mixing.

A counting experiment has been conducted searching for an excess of events with a di-lepton mass below the Z^0 boson mass. The data are found to be very well in agreement with the event-mixing prediction:

$$
\begin{aligned}
&\text{Number of measured events:} \quad 362 \\
&\text{Number of predicted events:} \quad 360.2 \pm 16.9(\text{stat.})\ ^{+24.1}_{-40.3}(\text{syst.})
\end{aligned}
$$

Also general shape comparisons show an agreement between the data and the prediction within expectable fluctuations.

With an edge shape in the di-lepton mass spectrum as signal hypothesis the main results of the analysis have been presented in a generic and model-independent way. Besides expected fluctuations, no excess that could be explained by the signal hypothesis has been found. Additionally, the di-muon and the di-electron channels are studied separately. Moreover, events with

at least one and at least two identified b-quark jets have been analyzed. These event samples have less contaminations from other backgrounds than $t\bar{t}$ processes and are suitable to search for specific signal scenarios. In all mentioned channels exclusion limits on the number of signal events have been set.

Further exclusion limits have been calculated in the parameter space of a simplified model spectrum. The model describes direct $\tilde{\chi}_2^0$-$\tilde{\chi}_1^\pm$ pair production with the common $\tilde{\chi}_2^0$-$\tilde{\chi}_1^\pm$ mass and the $\tilde{\chi}_1^0$ mass as free parameters. The mass of the intermediate slepton is varied in three steps, the best sensitivity has been found if the slepton mass is in the middle between the $\tilde{\chi}_2^0$-$\tilde{\chi}_1^\pm$ mass and the $\tilde{\chi}_1^0$ mass. It this scenario $\tilde{\chi}_2^0$-$\tilde{\chi}_1^\pm$ masses up to $500\,\mathrm{GeV}$ can be excluded if the $\tilde{\chi}_1^0$ is light or massless. The exclusion of $\tilde{\chi}_1^0$ masses reaches up to $75\,\mathrm{GeV}$ for certain $\tilde{\chi}_2^0$-$\tilde{\chi}_1^\pm$ masses.

The presented background-determination method provides a new alternative to established methods, such as a direct use of Monte-Carlo simulations or the different-flavor prediction. The latter exploits that the lepton flavors are uncorrelated in $t\bar{t}$ events. Thus, the $t\bar{t}$ background in the same-flavor channel can be estimated from the different-flavor channel. An advantage of this method is that not only the shape of the distribution can be predicted, but also the number of events. A drawback is the limited statistics for the background prediction. Both, fluctuations in the signal region (same-flavor) and fluctuations in the background region (different-flavor) influence the results. Moreover, a very accurate knowledge of differences between muon and electron reconstruction is required.

The event-mixing technique has the rather unique feature that the data-driven background estimation is not derived from any control or background region, which is assumed to be signal-free, but in terms of background compatible with the signal region. Instead, the same set of events – among which signal events are searched for – is used to generate the prediction.

The different-flavor or the event-mixing technique might be more or less sensitive to a certain signal, depending on the nature of the signal. Searches with one or the other method can complement each other.

8.1. Outlook

The presented analysis can be further improved. Up to now only the $t\bar{t}$ background estimation is determined from data, whereas the shape of the di-lepton spectrum expected from the other backgrounds (mainly $Z^0 \rightarrow \tau^+\tau^-$, di-boson, single top, and $t\bar{t}$ in association with a vector boson) is estimated with Monte-Carlo simulation. Although only the shape is taken from Monte Carlo, but not the number of events, it might be worth to estimate these contributions from data as well. The observed difference between the background composition in Monte-Carlo simulation and in the shape fit might give rise to further investigations.

At several points in the analysis the bin uncertainties of the distribution of the mixed events play a role. Since the mixed events are not completely independent from each other, the statistical error is not a valid quantity. Furthermore, the comparison between the real events and mixed events would benefit from accounting all correlations. Also the estimations of systematic uncertainties could be improved w.r.t. the presented shape analysis: On the one hand they can be assumed to be underestimated in the shape analysis, because their effects are not summed, but the envelope of all effects is taken. On the other hand many effects are accounted although no clear effect is observable. Therefore, fluctuations might blow up the energy band, and the true effect of uncertainties might be overestimated. Control regions with higher statistics in

data and large Monte-Carlo samples could clarify, which of the uncertainties really affect the event-mixing method and which can be omitted.

The question of how different signal characteristics influence the prediction, has been investigated only shortly in this thesis. Studying more signal scenarios in detail could help understanding the dependency of the signal features and the sensitivity of the analysis.

Finally, when a supersymmetric signal will be found, mass-edge analyses provide the great opportunity to not only discover a signal, but directly determine some of its properties. The masses of newly found particles are important quantities to understand the underlying mechanism. Due to the relation between the position of the mass edge and the mass differences of the involved particles, edge analyses are powerful tools for an early determination what kind of signal causes the excess.

A. Lorentz-Vector Components of Leptons in Data and MC
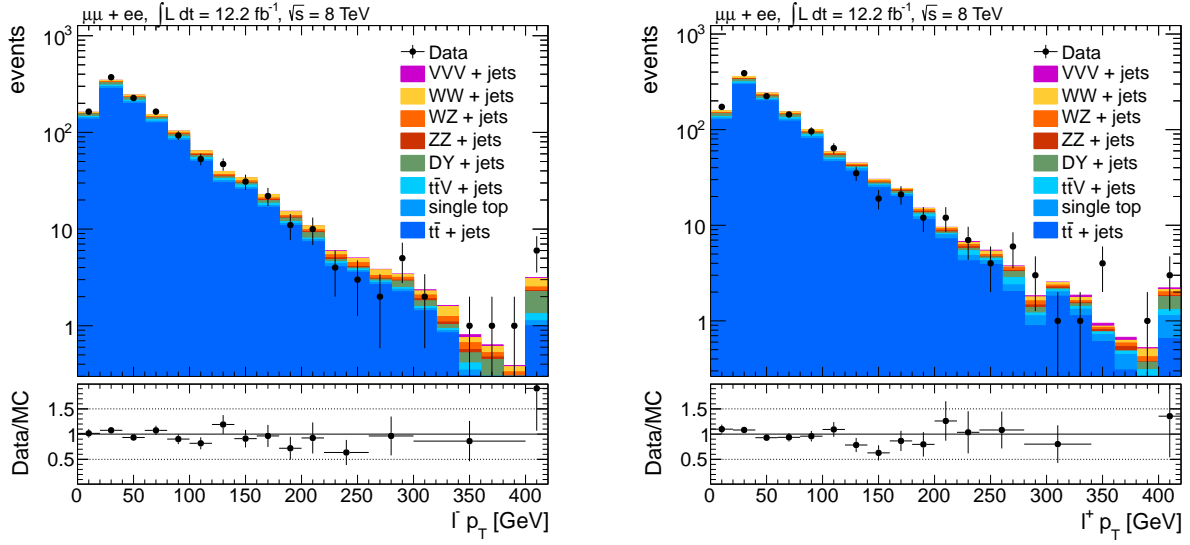
Figure A.1.: p_T of the lepton and of the anti-lepton after the whole event-selection chain.
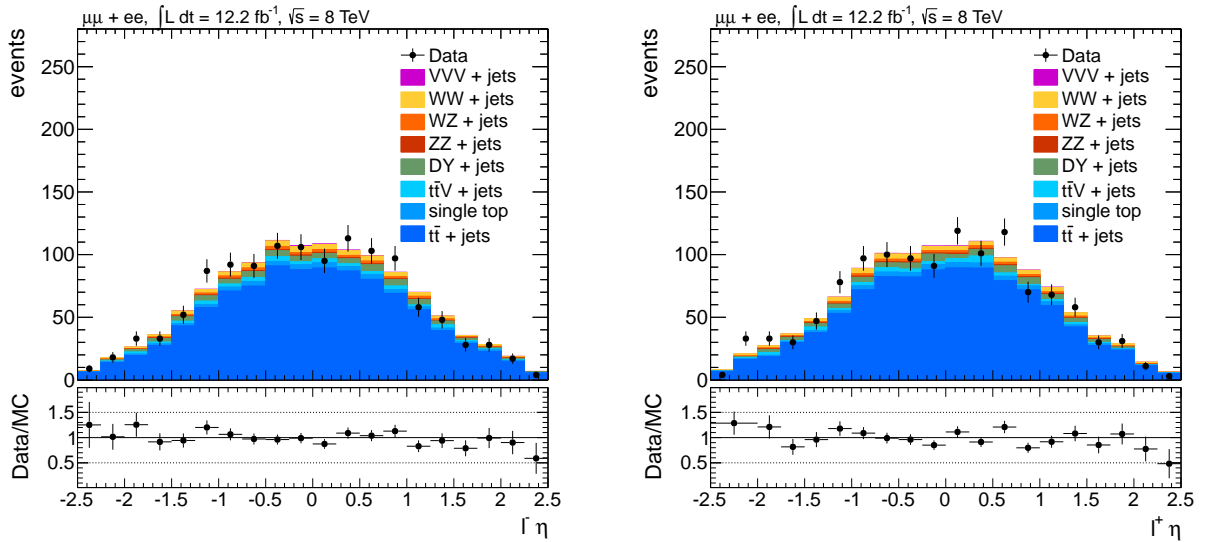
Figure A.2.: η of the lepton and of the anti-lepton after the whole event-selection chain.
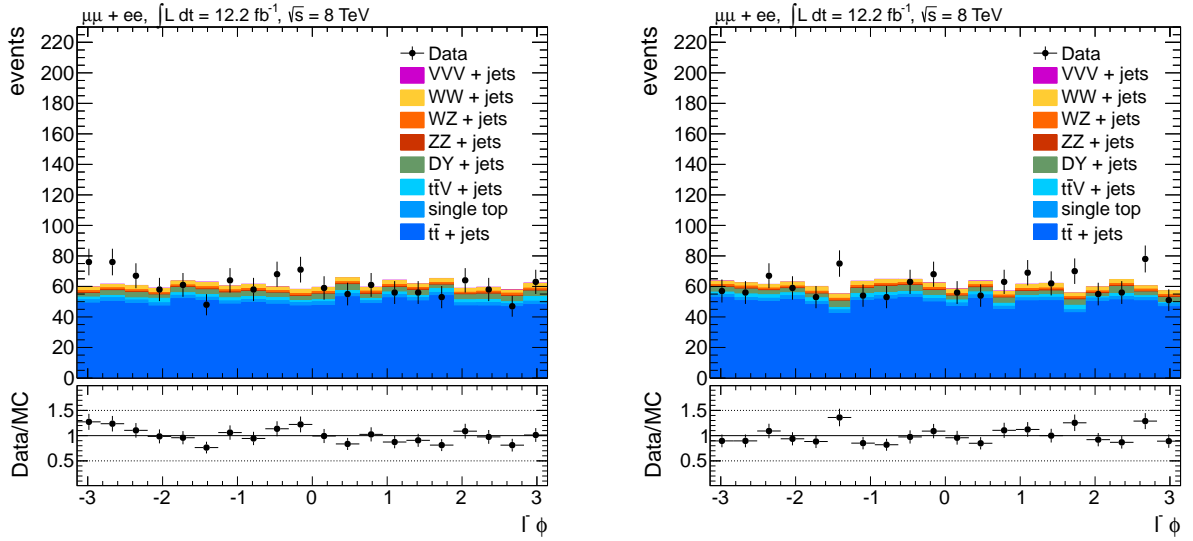
Figure A.3.: ϕ of the lepton and of the anti-lepton after the whole event-selection chain.
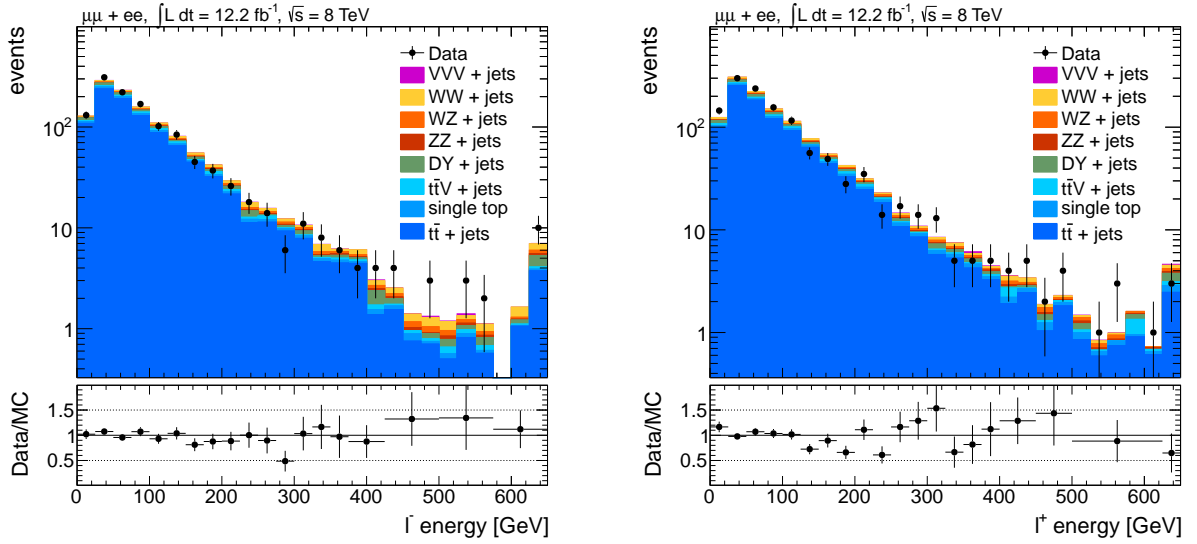
Figure A.4.: Energy of the lepton and of the anti-lepton after the whole event-selection chain.

B. Mass Edges

B.1. Three-Body Decay

In case of the three-body decay the end-point of the di-lepton invariant mass is simply

$$M_{\ell\ell}^{\max} = M_{\tilde{\chi}_2^0} - M_{\tilde{\chi}_1^0}. \tag{B.1}$$

This follows from Lorentz vector conservation:

$$P_{\tilde{\chi}_2^0}^\mu = P_{\ell^+}^\mu + P_{\ell^-}^\mu + P_{\tilde{\chi}_1^0}^\mu \tag{B.2}$$

$$P_{\tilde{\chi}_2^0}^\mu - P_{\tilde{\chi}_1^0}^\mu = P_{\ell^+}^\mu + P_{\ell^-}^\mu \tag{B.3}$$

$$(M_{\tilde{\chi}_2^0} - M_{\tilde{\chi}_1^0})^2 \leq (P_{\ell^+}^\mu + P_{\ell^-}^\mu)^2 \tag{B.4}$$

$$M_{\tilde{\chi}_2^0} - M_{\tilde{\chi}_1^0} \leq M_{\ell\ell} \tag{B.5}$$

Between line B.3 and B.4 it is used that $M_{\ell\ell}$ is maximized if $\tilde{\chi}_1^0$ is produced at rest $(\vec{p}_{\tilde{\chi}_1^0} = \vec{0})$, at the same time the $\tilde{\chi}_2^0$ rest frame is chosen to evaluate the formula $(\vec{p}_{\tilde{\chi}_2^0} = \vec{0})$.

B.2. Two Subsequent Two-Body Decays

In case of two subsequent two-body decays, the situation is slightly more complicated. The whole derivation of the formula can be found in [103], here it is only adumbrated:

Considering the decay $\tilde{\chi}_2^0 \to \ell^+ \tilde{\ell}^- \to \ell^+ \ell^- \tilde{\chi}_1^0$. Again, the $\tilde{\chi}_2^0$ rest frame is chosen.

$$M_{\ell\ell}^2 = 2E_{\ell^+}(E_{\ell^-} + p_{\|,\ell^-}), \tag{B.6}$$

where $p_{\|,\ell^-}$ is the longitudinal momentum component in the $\tilde{\chi}_2^0$ rest frame. With the approximation $m_\ell = 0$ the anti-lepton energy is

$$E_{\ell^+} = \frac{M_{\tilde{\chi}_2^0}^2 - M_{\tilde{\ell}}^2}{2M_{\tilde{\chi}_2^0}}, \tag{B.7}$$

the energy of the lepton in the slepton rest frame looks similar:

$$E_{\ell^-} = \frac{M_{\tilde{\ell}}^2 - M_{\tilde{\chi}_1^0}^2}{2M_{\tilde{\ell}}}. \tag{B.8}$$

After Lorentz transformation of the latter one to the $\tilde{\chi}_2^0$ rest frame

$$E_{\ell^-} + p_{\parallel,\ell^-} = \frac{M_{\tilde{\chi}_2^0}(M_{\tilde{\ell}}^2 - M_{\tilde{\chi}_1^0}^2)}{2M_{\tilde{\ell}}}(1 + \cos\theta^*),$$ (B.9)

where θ^* is the angle between $\tilde{\ell}$ and ℓ^- momentum in the $\tilde{\chi}_2^0$ rest frame. All together:

$$M_{\ell\ell}^2 = \frac{(M_{\tilde{\chi}_2^0}^2 - M_{\tilde{\ell}}^2)(M_{\tilde{\ell}}^2 - M_{\tilde{\chi}_1^0}^2)}{2M_{\tilde{\chi}_2^0}^2}(1 + \cos\theta^*),$$ (B.10)

which is maximized for $\theta^* = 0$. That is the case (like in the three-body decay) if the $\tilde{\chi}_1^0$ is at rest, i. e. the ℓ^- takes the whole $\tilde{\ell}$ momentum. Which leads finally to

$$M_{\ell\ell}^{\max} = \frac{\sqrt{(M_{\tilde{\chi}_2^0}^2 - M_{\tilde{\ell}}^2)(M_{\tilde{\ell}}^2 - M_{\tilde{\chi}_1^0}^2)}}{M_{\tilde{\chi}_2^0}}.$$ (B.11)

C. Additional Material: Kinematic Correlation

C.1. Quantification of the ϕ_1 vs. ϕ_2 Correlation

The correlation between the ϕ components of the two leptons in di-leptonic $t\bar{t}$ decays should be quantified by the linear correlation coefficient ρ (Cf. Eq. 5.5). The ϕ_1 vs. ϕ_2 distribution as it is would result in a negative ρ caused by the two parts of the split accumulation at the by π shifted diagonal. In Fig. C.1 the original distribution is shown in contrast to the same distribution but with ϕ_2 shifted by π.

But still, due to the accumulations in the upper-left and lower-right corners the value of ρ would not reflect the real correlation. In particular, a change in the strength of the correlation might also not be reflected in the number. Since ϕ is invariant under addition of $\pm 2\pi$, the distribution (i. e. ϕ_2) can be transformed in a way that $|\phi_1 - \phi_2| \leq \pi$. The resulting distribution is shown in Fig. C.1. All stated correlation coefficients for ϕ_1 vs. ϕ_2 refer to the modified distribution. Obviously, the price is a bias towards larger positive correlations, but changes in the correlation account for equivalent changes in the coefficient.
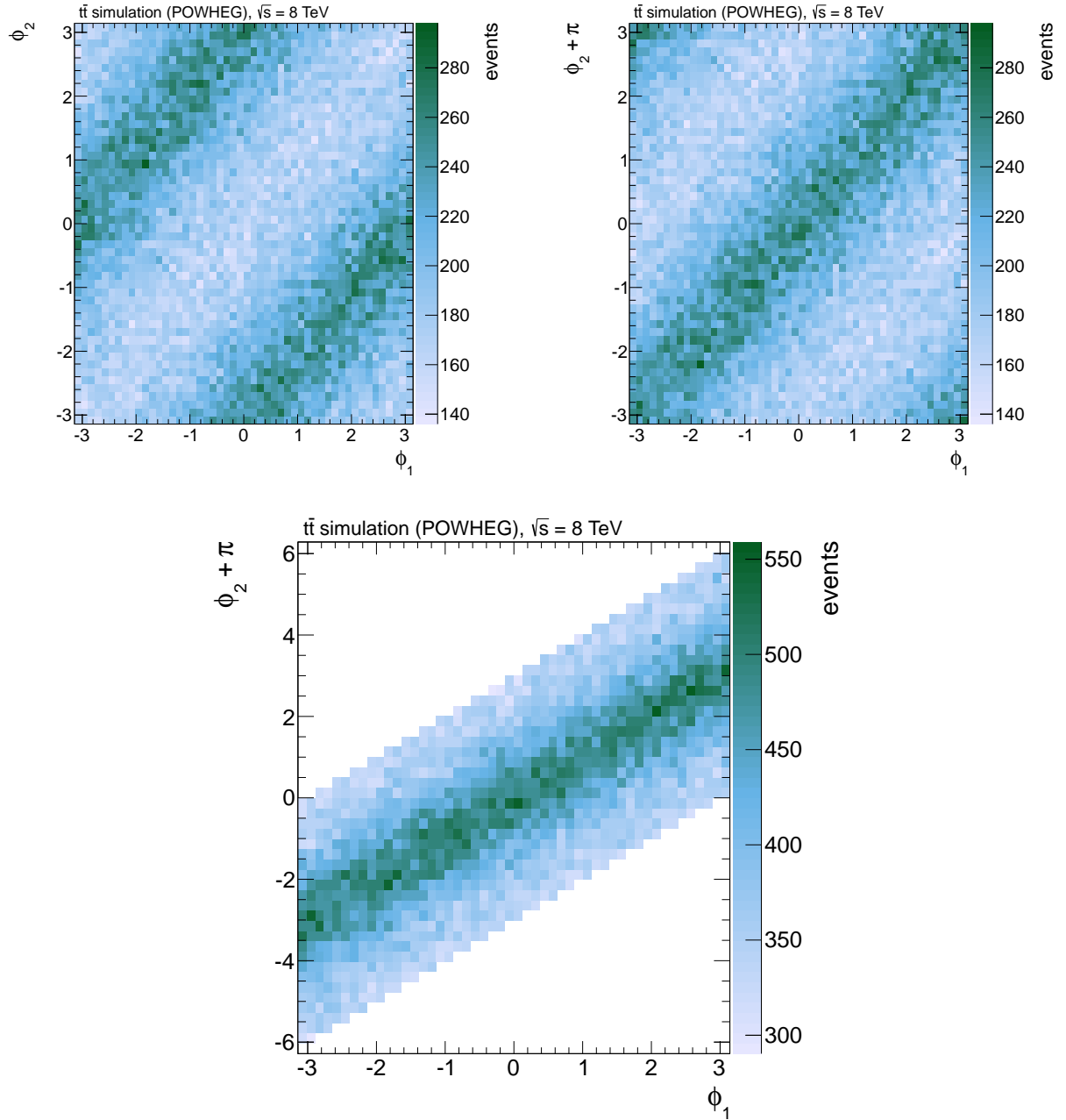
Figure C.1.: Three representations of the ϕ_1 vs. ϕ_2 correlation plot in $t\bar{t}$ MC. The upper left shows the raw distribution in the usual ϕ range from $-\pi$ to π, for the upper right plot ϕ_2 is shifted by π. Additionally, for the lower plot from the equivalent $\phi_2+n2\pi$, with $n=-1, 0, 1$, the one is chosen that results in the smallest value of $|\phi_1 - \phi_2|$. All stated ρ numbers are derived from the latter representation.

C.2. Correlation Coefficients in Bins of tt̄ Boost and Di-Top Mass
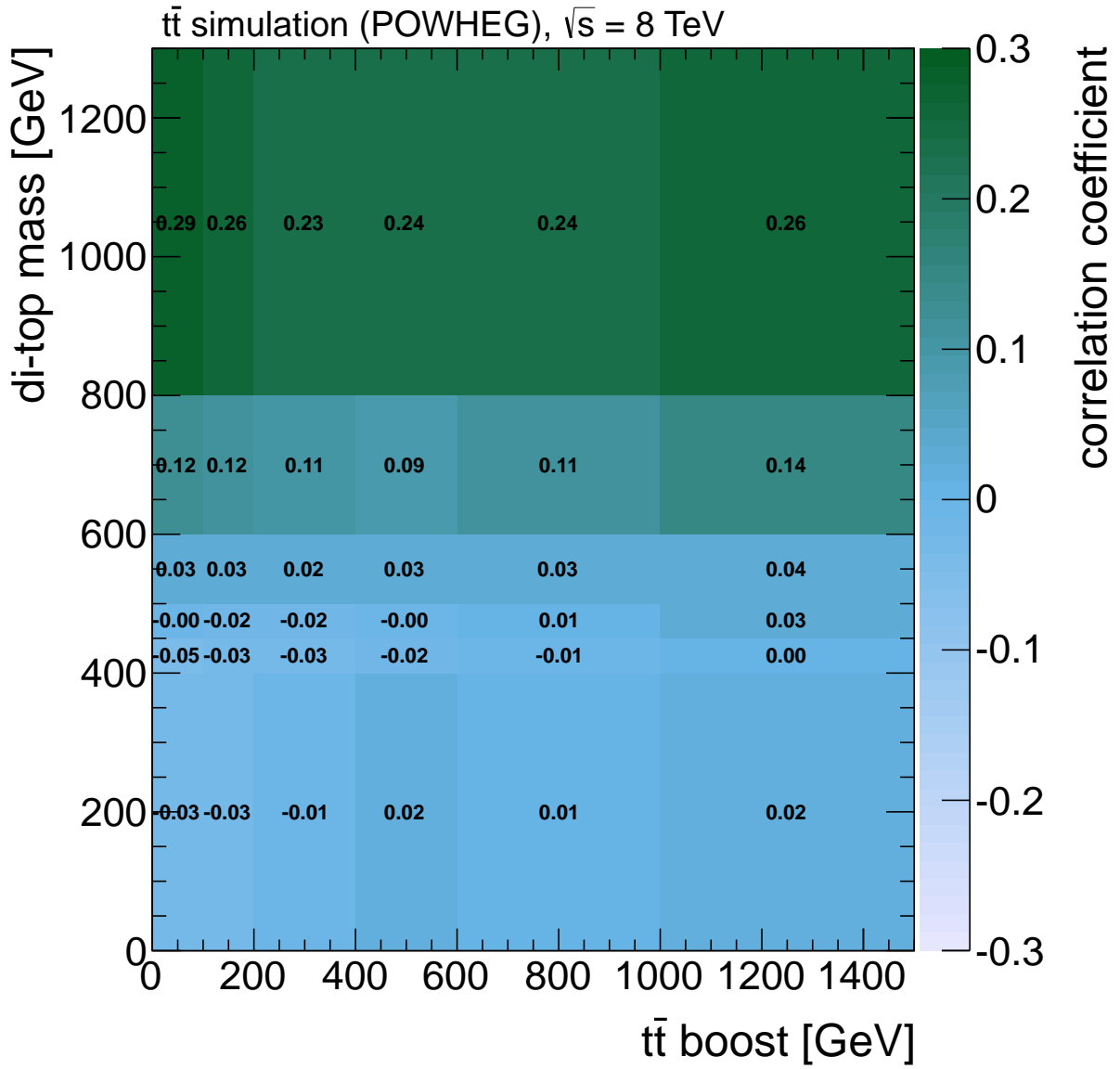
Figure C.2.: $p_{T,1}$ vs. $p_{T,2}$ correlation in bins of the tt̄ boost and the di-top mass. Since the boost is mainly in z direction, the transverse momentum correlation is not effected from it, and the known dependency on the di-top mass is similar in all boost columns.
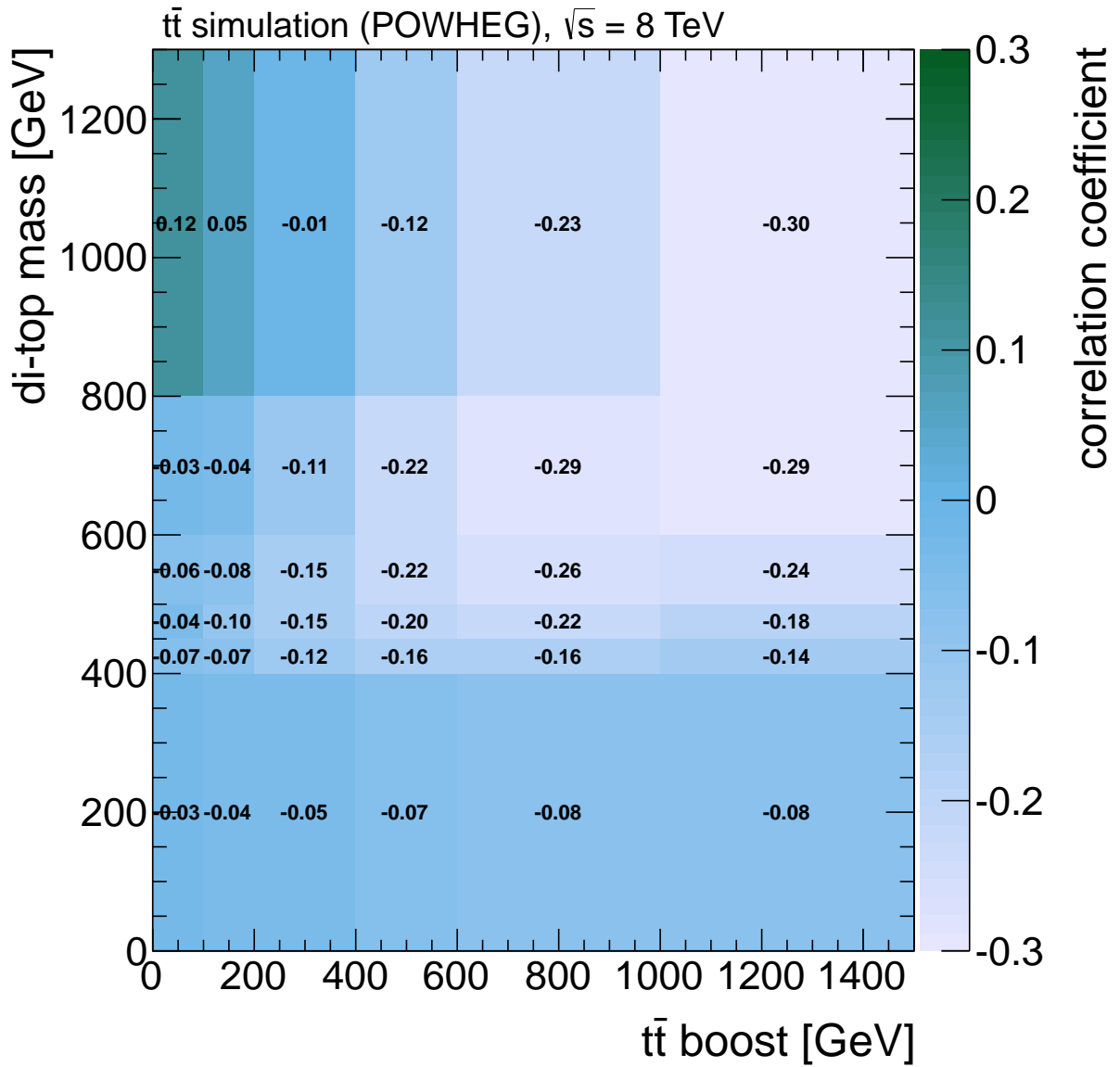
Figure C.3.: E_1 vs. E_2 correlation in bins of the $t\bar{t}$ boost and the di-top mass: Only if the transverse back-to-back topology is pronounced (high di-top mass) the boost changes the correlation. If the boost is high, it is likely that one lepton gains energy (boost and di-top energy add) while the other loses (boost and di-top energy in opposite direction). The resulting negative correlation increases to the upper left corner.
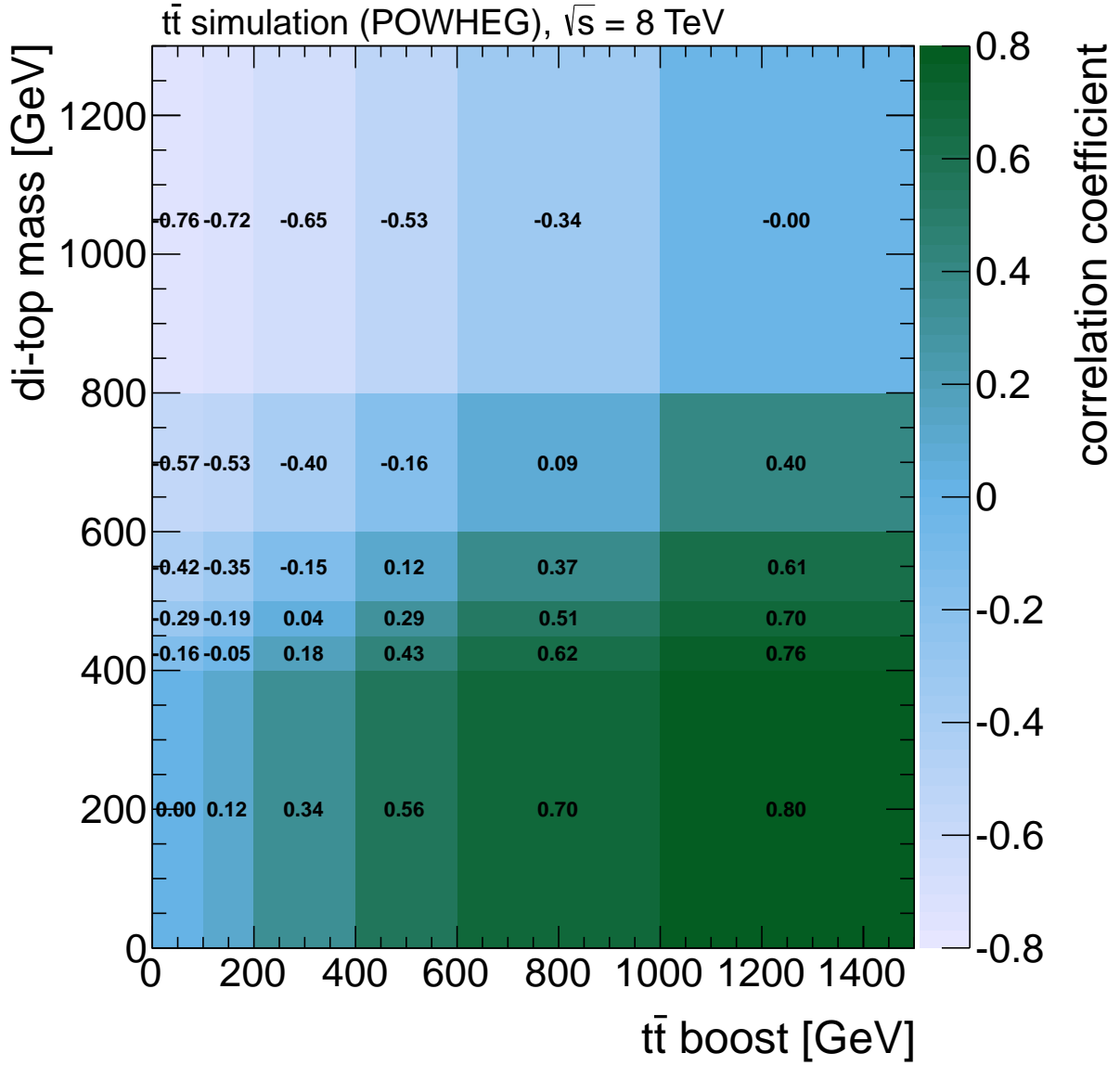
Figure C.4.: η_1 vs. η_2 correlation in bins of the $t\bar{t}$ boost and the di-top mass: In the *eta* correlation the two event energies directly compete. A high boost pushes both leptons into similar η regions, a high di-top mass enhances the back-to-backness, i.e. if one lepton in in one hemisphere, the other is likely to be in the other.
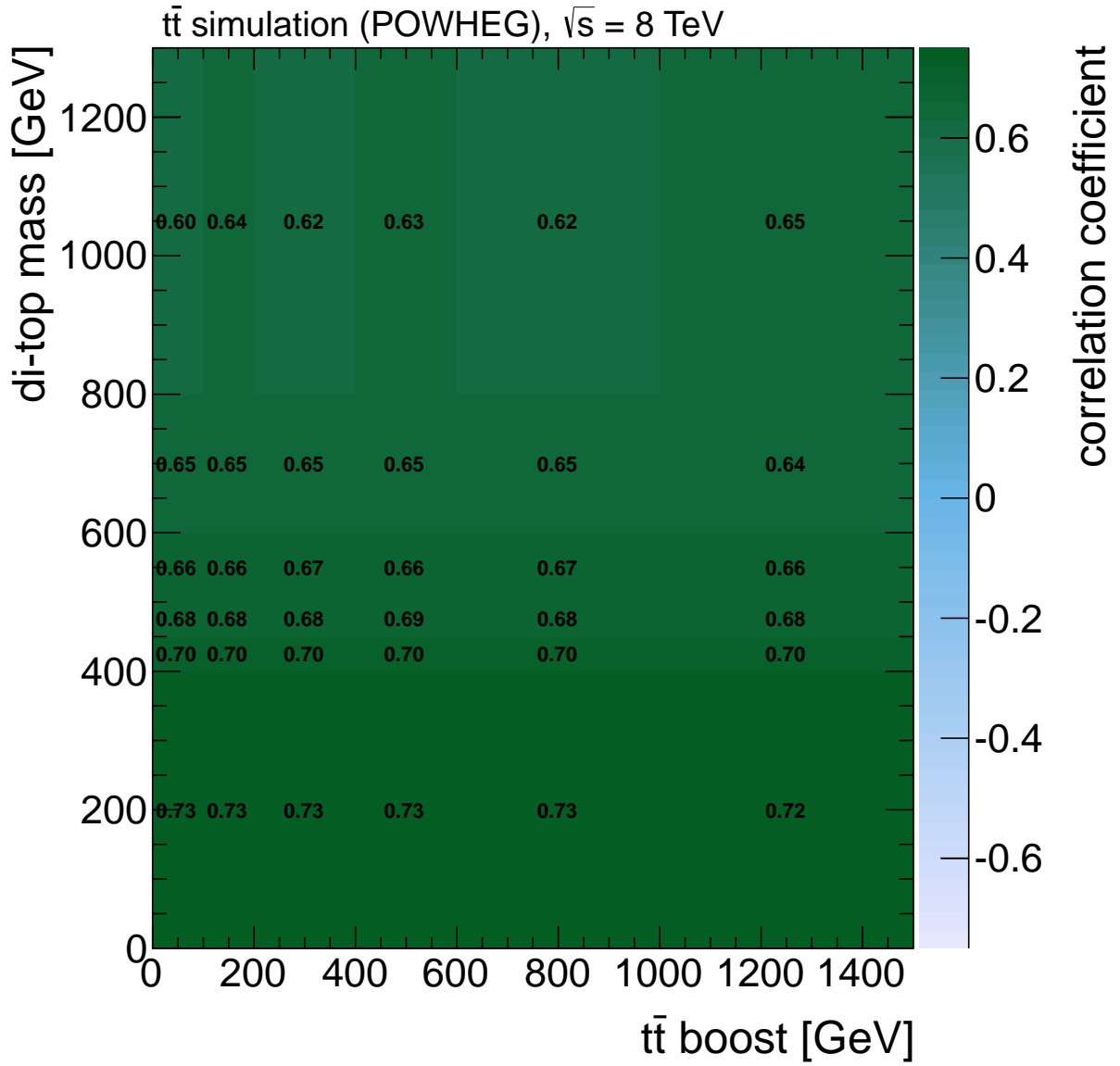
Figure C.5.: ϕ_1 vs. ϕ_2 correlation in bins of the t$\bar{\text{t}}$ boost and the di-top mass: As figured out in Appendix C.1, a large positive ρ means a clear back-to-back preference.

C.3. tt̄ Boost vs. Di-Top Mass Correlation
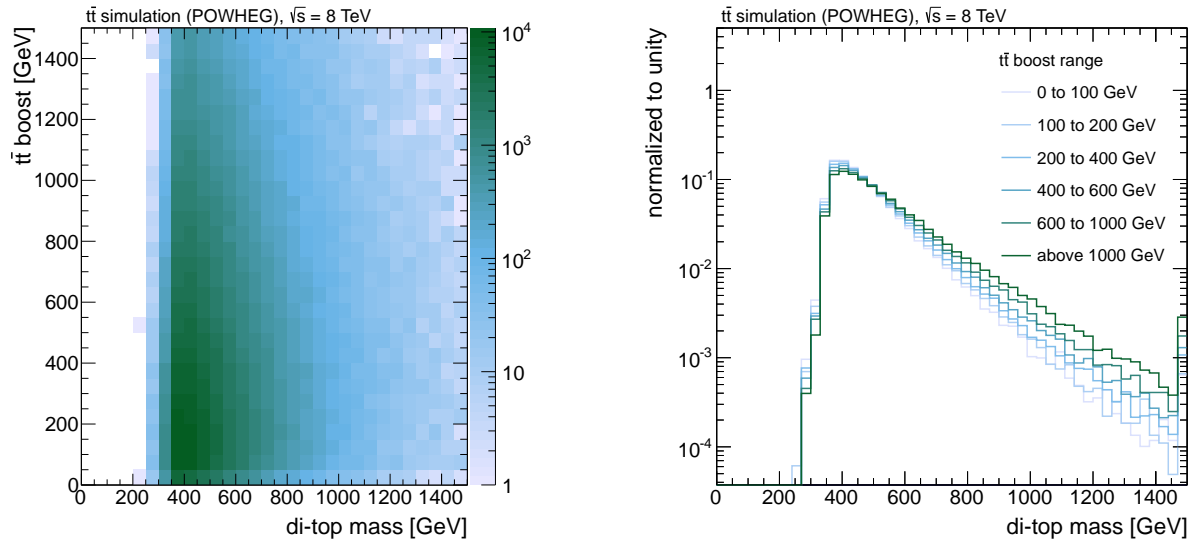
Figure C.6.: Correlation between the two basic event energies in tt̄ events: the boost of the whole tt̄ system and the invariant di-top mass. The normalized di-top spectra in slices of the tt̄ boost (right) show a small positive correlation, which is also indicated by the correlation coefficient of $\rho = 0.12$.

D. Background Contamination Effects in 1-Jet Selection
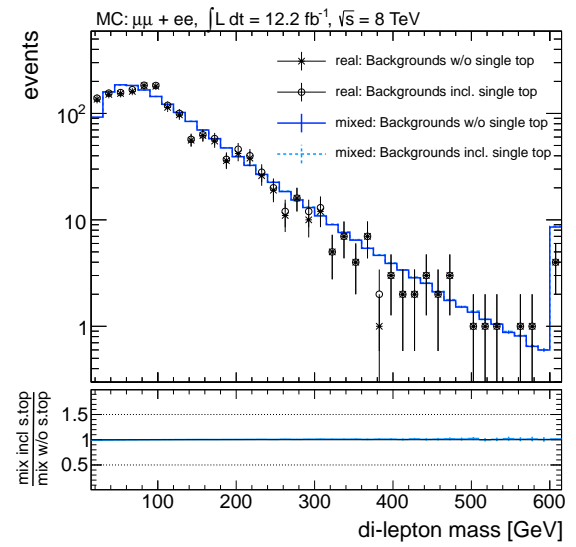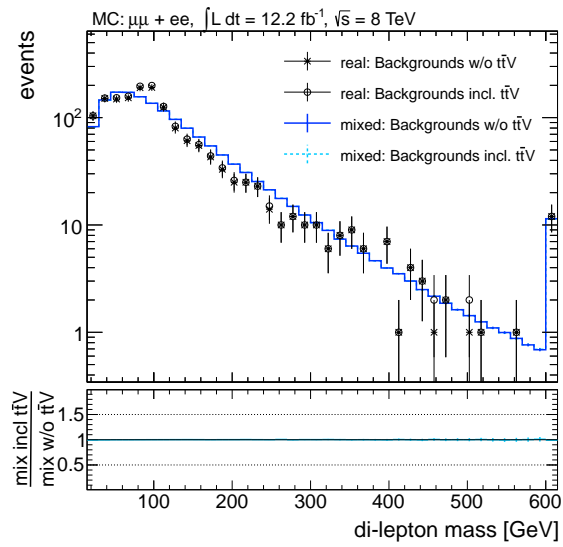
E. Cut Threshold Variations

E.1. Jet Multiplicity
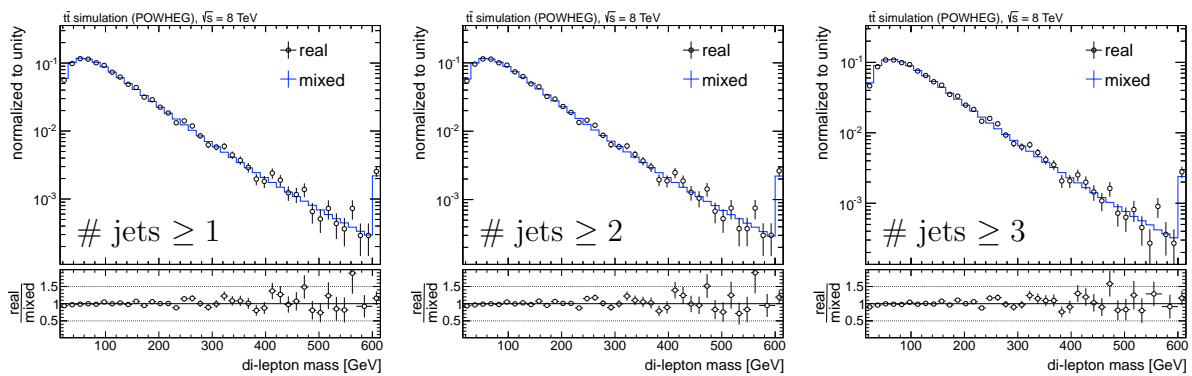
Figure E.1.: Variation of the required number of jets per event: The middle plot represents the nominal cut value, which in loosened on the left and tightened on the right.

E.2. Simultaneous Variations

E.2.1. Lepton p_T vs. $E_\mathsf{T}^\mathsf{miss}$
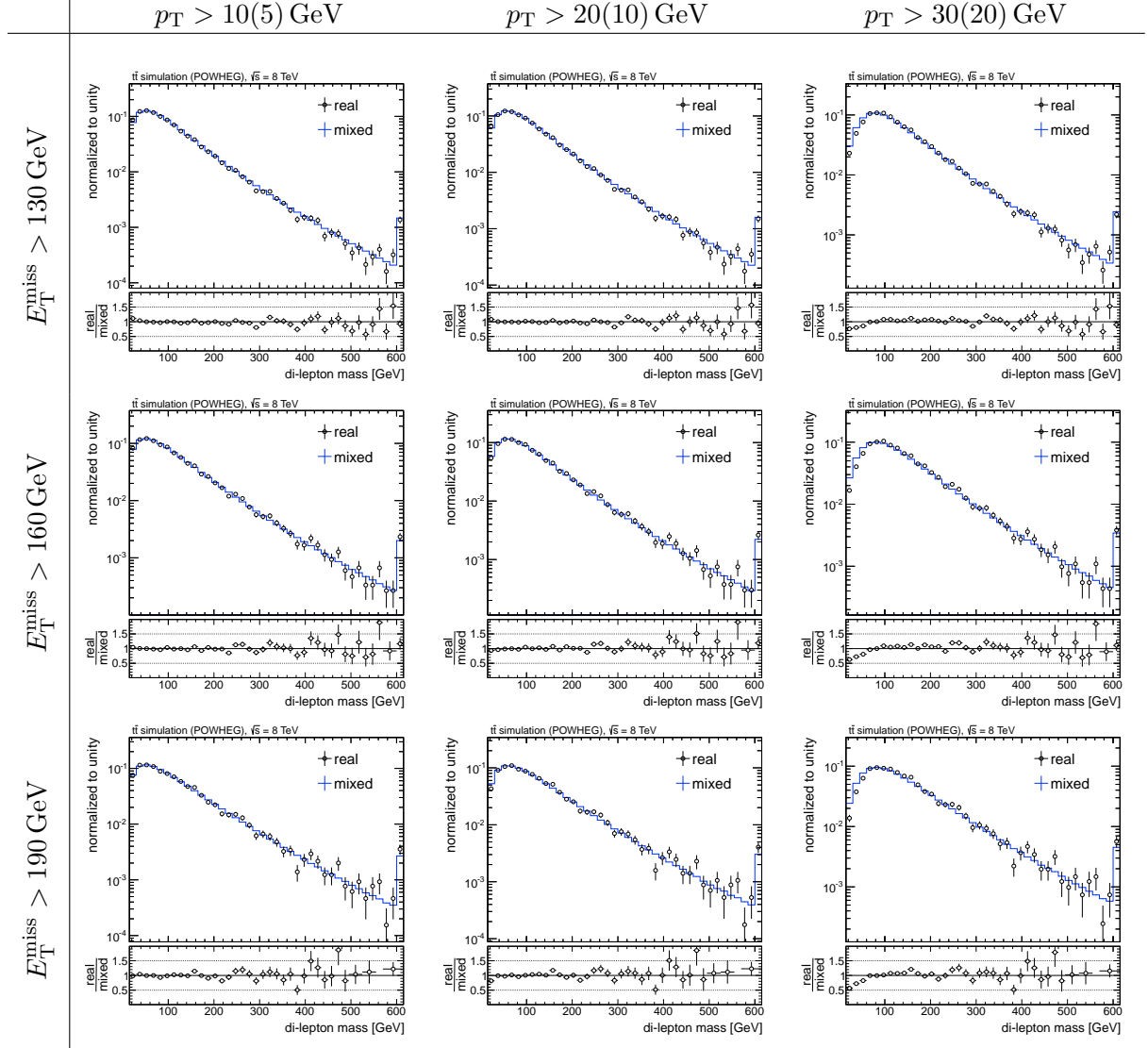
E.2.2. Lepton p_T vs. Lepton η
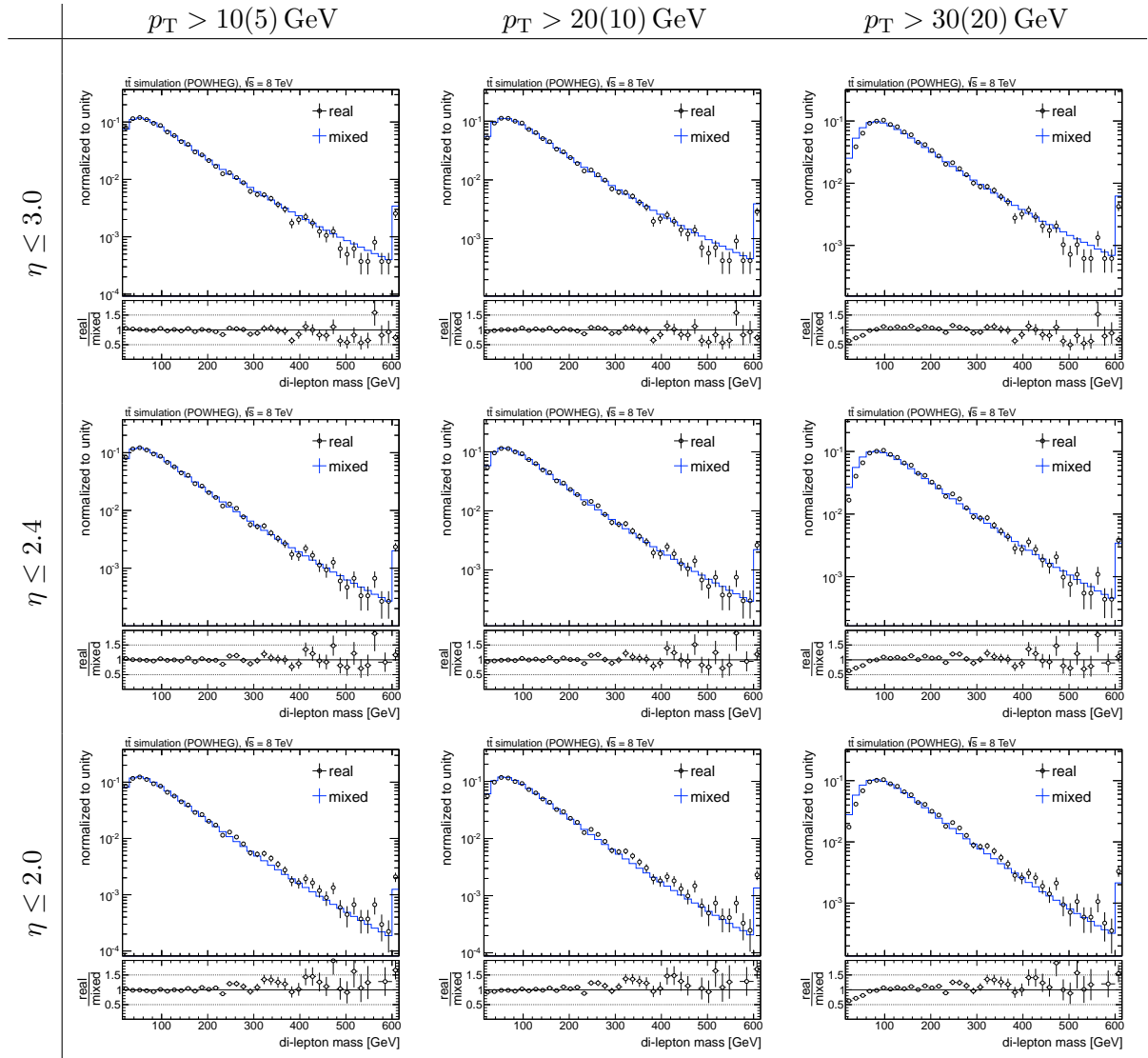
E.2.3. Lepton p_T vs. # Jets
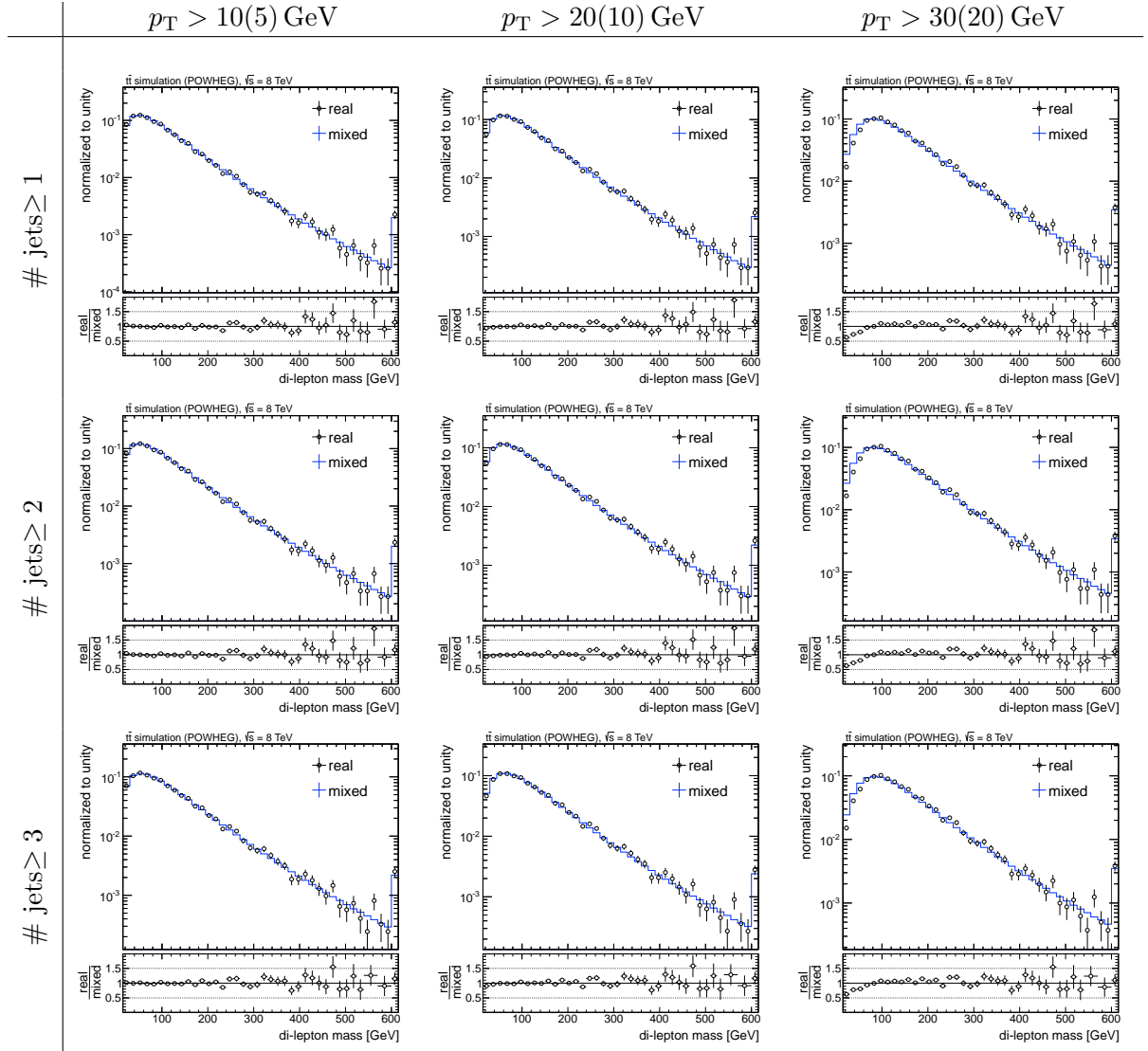
E.2.4. $E_\mathrm{T}^\mathrm{miss}$ vs. Lepton η
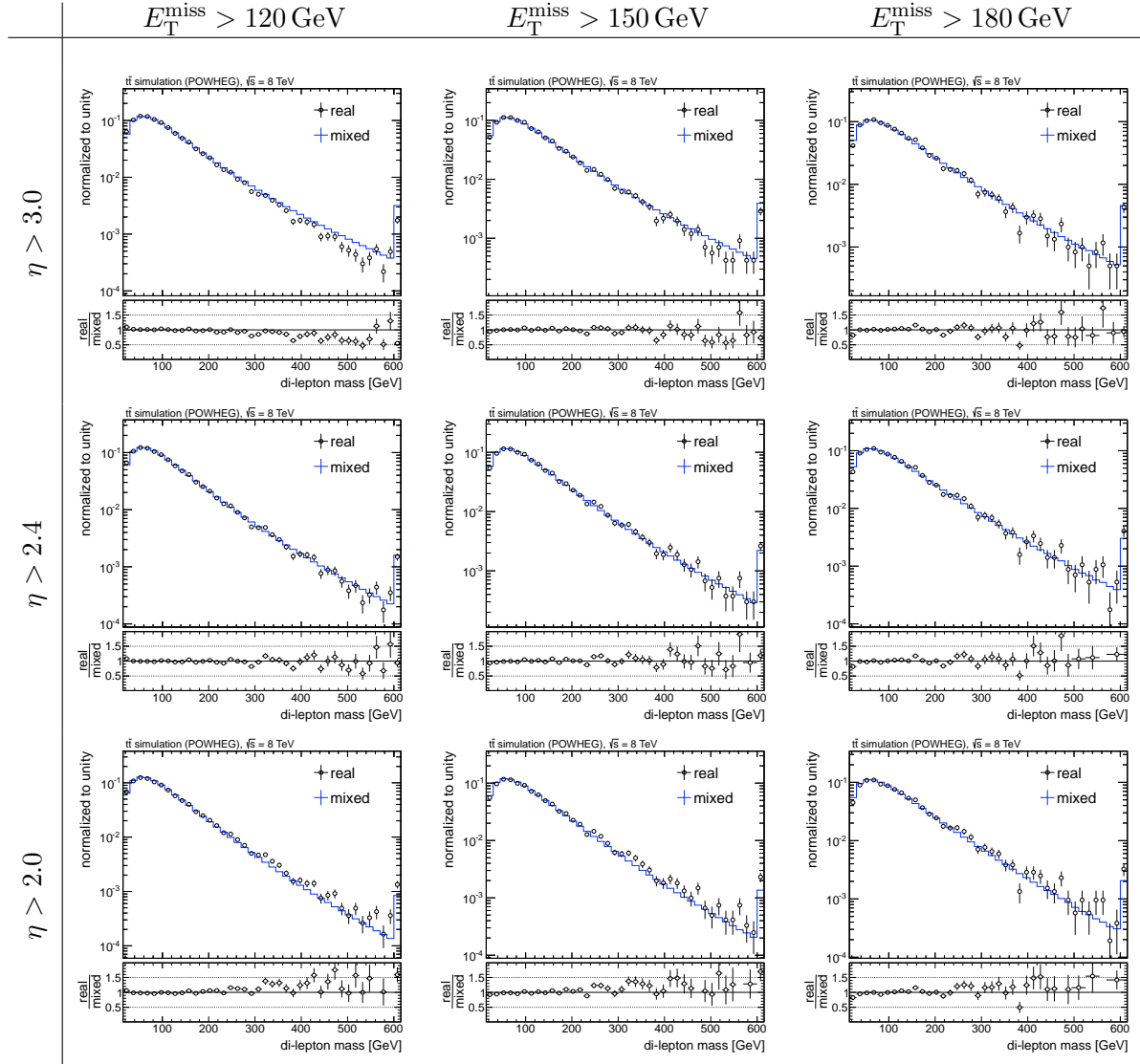
E.2.5. $E_\mathrm{T}^\mathrm{miss}$ vs. # Jets
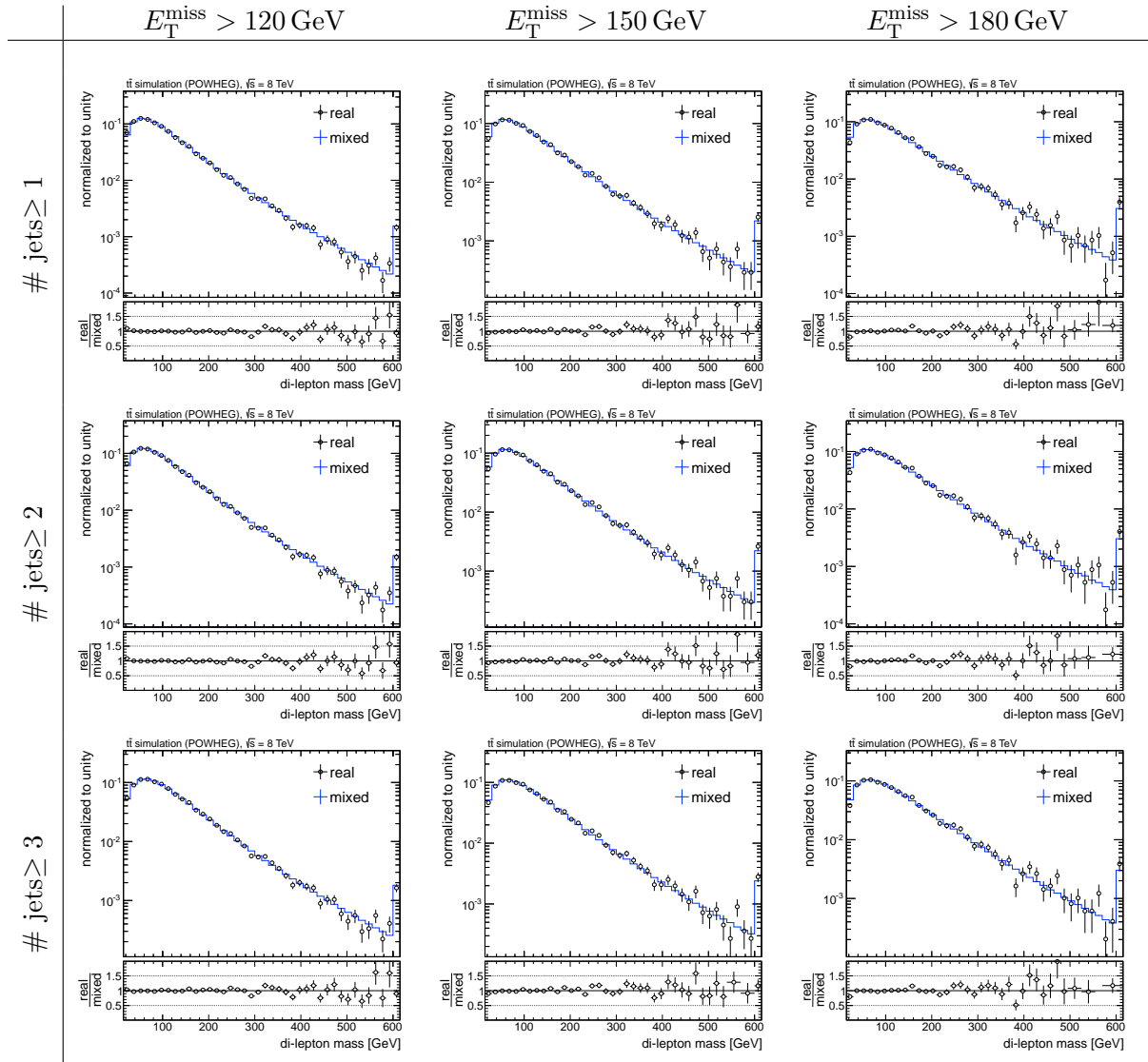
E.2.6. Lepton η vs. # Jets
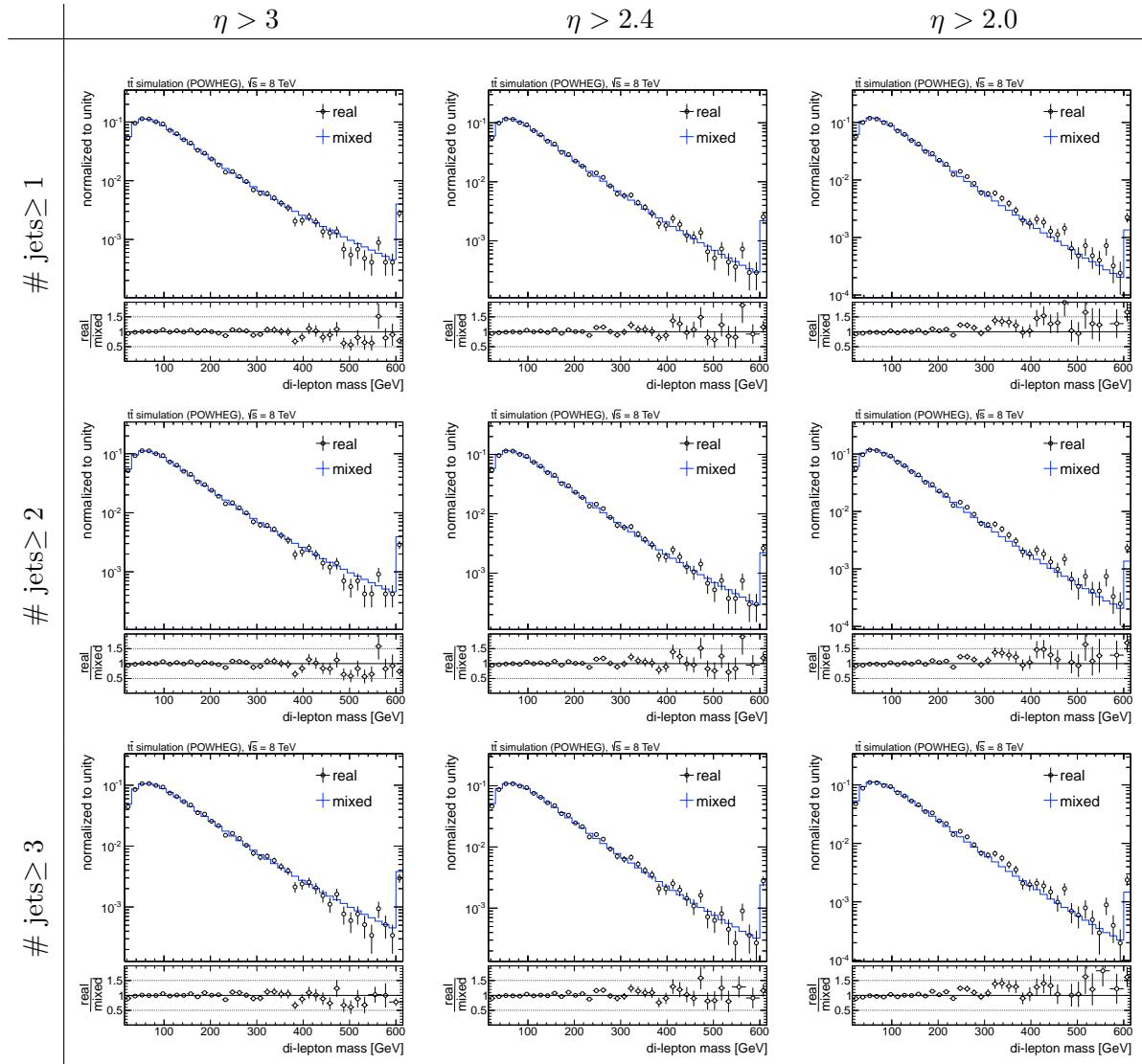
E.3. Angle-Momenta Correlation
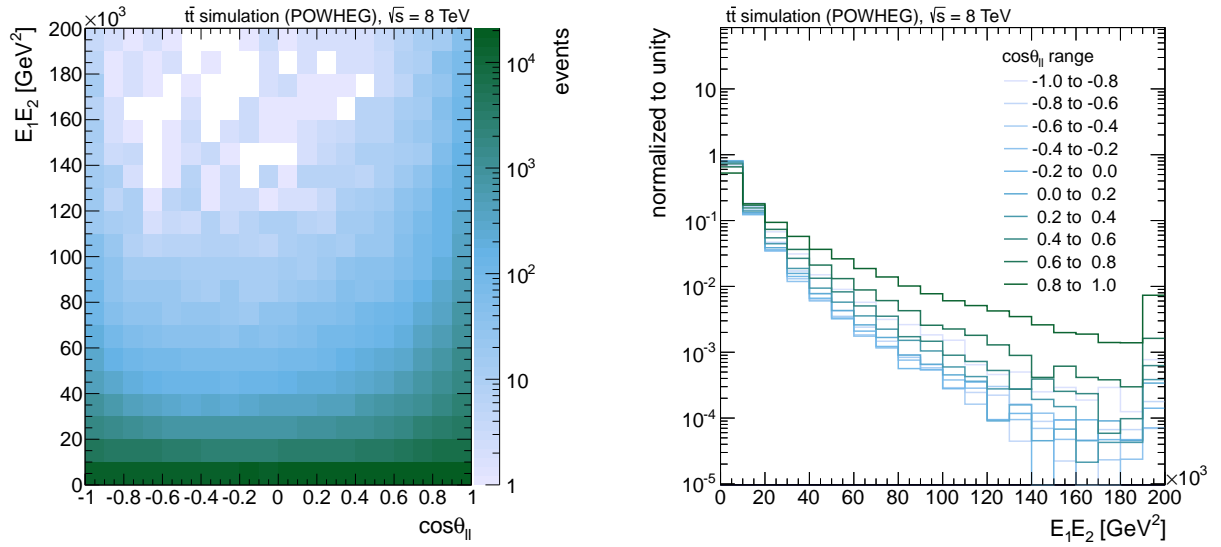
Figure E.2.: Correlation plots between the variables that are used in the angel-momenta mixing: the $\ell\ell$ opening angle and the product of the lepton energies. The right plot shows $E_{\ell^+}E_{\ell^-}$ in slices of $\cos\theta_{\ell\ell}$, normalized to unity. First, the positive correlation stated in Table 5.1 is visible since hardest distribution is for large values of $\cos\theta_{\ell\ell}$, but also very small cosines lead to an increase in energy.

List of Figures

Bibliography

[1] Schmüser, Peter, "Feynman-Graphen und Eichtheorien für Experimentalphysiker". Springer, 1995.

[2] F. Halzen and A. D. Martin, "Quarks and Leptons". John Wiley & Sons, 1984.

[3] V. Barger and R. Philips, "Collider Physics". Froniers in Physics. Addison-Wesley, 1996.

[4] D. Griffiths, "Introduction to Elementary Particles". Wiley-VCH, 2008.

[5] J. Beringer et al. (Particle Data Group), "Review of particle physics", *Phys. Rev.* **D86** (2012) 010001. And references therein. `doi:10.1103/PhysRevD.86.010001`.

[6] S. P. Martin, "A Supersymmetry primer", `arXiv:hep-ph/9709356`.

[7] S. Weinberg, "The quantum theory of fields. Vol. 3: Supersymmetry". Cambridge University Press, 2000.

[8] P. Binetruy, "Supersymmetry: Theory, experiment and cosmology". Oxford University Press, 2006.

[9] H. E. Haber and G. L. Kane, "The Search for Supersymmetry: Probing Physics Beyond the Standard Model", *Phys.Rept.* **117** (1985) 75–263. `doi:10.1016/0370-1573(85)90051-1`.

[10] Z. Liu et al. (Belle Collaboration), "Study of $e^+e^- \to \pi^+\pi^- J/\psi$ and Observation of a Charged Charmonium-like State at Belle", *Phys.Rev.Lett.* **110** (2013) 252002, `arXiv:1304.0121`. `doi:10.1103/PhysRevLett.110.252002`.

[11] M. Ablikim et al. (BESIII Collaboration), "Observation of a charged charmoniumlike structure in $e^+e^- \to \pi^+\pi^- J/\psi$ at $\sqrt{s} = 4.26$ GeV", *Phys.Rev.Lett.* **110** (2013) 252001, `arXiv:1303.5949`. `doi:10.1103/PhysRevLett.110.252001`.

[12] W. Ochs, "The Status of Glueballs", *J. Phys. G* **40** (2013) 043001, `arXiv:1301.5183`. `doi:10.1088/0954-3899/40/4/043001`.

[13] I. Brock. `http://pi.physik.uni-bonn.de/~brock/feynman/ktp_ws1011/chapter16/higgs_pot.eps`. [Accessed June 2013].

[14] J. Goldstone, A. Salam, and S. Weinberg, "Broken Symmetries", *Phys.Rev.* **127** (1962) 965–970. `doi:10.1103/PhysRev.127.965`.

[15] ALEPH Collaboration, CDF Collaboration, D0 Collaboration, DELPHI Collaboration, L3 Collaboration, OPAL Collaboration, SLD Collaboration, LEP Electroweak Working Group, Tevatron Electroweak Working Group, SLD Electroweak and Heavy Flavour Groups, "Precision Electroweak Measurements and Constraints on the Standard Model", `arXiv:1012.2367`.

[16] S. Chatrchyan et al. (CMS Collaboration), "Observation of a new boson at a mass of 125 GeV with the CMS experiment at the LHC", *Phys.Lett.* **B716** (2012) 30–61, `arXiv:1207.7235`. `doi:10.1016/j.physletb.2012.08.021`.

[17] G. Aad et al. (ATLAS Collaboration), "Observation of a new particle in the search for the Standard Model Higgs boson with the ATLAS detector at the LHC", *Phys.Lett.* **B716** (2012) 1–29, `arXiv:1207.7214`. `doi:10.1016/j.physletb.2012.08.020`.

[18] CMS collaboration, "Combination of standard model Higgs boson searches and measurements of the properties of the new boson with a mass near 125 GeV", *CMS Physics Analysis Summary* **HIG-13-005** (2013). `http://cds.cern.ch/record/1542387`.

[19] ATLAS collaboration, "Study of the spin of the new boson with up to 25 fb^{-1} of ATLAS data", *ATLAS Conference Note* **2013-040** (Apr, 2013). `http://cds.cern.ch/record/1542341`.

[20] S. R. Coleman and J. Mandula, "All Possible Symmetries of the s Matrix", *Phys.Rev.* **159** (1967) 1251–1256. `doi:10.1103/PhysRev.159.1251`.

[21] R. Haag, J. T. Łopuszański, and M. Sohnius, "All Possible Generators of Supersymmetries of the s Matrix", *Nucl.Phys.* **B88** (1975) 257. `doi:10.1016/0550-3213(75)90279-5`.

[22] P. Ade et al. (Planck Collaboration), "Planck 2013 results. I. Overview of products and scientific results", `arXiv:1303.5062`. And references therein.

[23] ATLAS Collaboration, "ATLAS Experiment – Physics Results: ATLAS Supersymmetry (SUSY) searches". `https://twiki.cern.ch/twiki/bin/view/AtlasPublic/SupersymmetryPublicResults`. [Accessed July 2013].

[24] CMS Collaboration, "CMS Supersymmetry Physics Results". `https://twiki.cern.ch/twiki/bin/view/CMSPublic/PhysicsResultsSUS`. [Accessed February 2013].

[25] N. Arkani-Hamed, P. Schuster, N. Toro et al., "MARMOSET: The Path from LHC Data to the New Standard Model via On-Shell Effective Theories", `arXiv:hep-ph/0703088`.

[26] D. Alves et al. (LHC New Physics Working Group), "Simplified Models for LHC New Physics Searches", *J.Phys.* **G39** (2012) 105005, `arXiv:1105.2838`. `doi:10.1088/0954-3899/39/10/105005`.

[27] C. Lefèvre, "The CERN accelerator complex". `http://cds.cern.ch/record/1260465`, 2008. [Accessed April 2013].

[28] L. Evans, (ed.) and P. Bryant, (ed.), "LHC Machine", *JINST* **3** (2008) S08001. `doi:10.1088/1748-0221/3/08/S08001`.

[29] O. S. Brüning, P. Collier, P. Lebrun et al., eds., "LHC Design Report. 1. The LHC Main Ring". CERN-2004-003-V-1. 2004. `doi:10.5170/CERN-2004-003-V-1`.

[30] O. S. Brüning, P. Collier, P. Lebrun et al., eds., "LHC Design Report. 2. The LHC infrastructure and general services". CERN-2004-003-V-2. 2004. `doi:10.5170/CERN-2004-003-V-2`.

[31] M. Benedikt, P. Collier, V. Mertens et al., eds., "LHC Design Report. 3. The LHC injector chain". CERN-2004-003-V-3. 2004. `doi:10.5170/CERN-2004-003-V-3`.

[32] J.-L. Caron, "Magnetic field induced by the LHC dipole's superconducting coils". `http://cds.cern.ch/record/841511`, 1998. [Accessed April 2013].

[33] G. Aad et al. (ATLAS Collaboration), "The ATLAS Experiment at the CERN Large Hadron Collider", *JINST* **3** (2008) S08003. `doi:10.1088/1748-0221/3/08/S08003`.

[34] J. Alves, A. Augusto et al. (LHCb Collaboration), "The LHCb Detector at the LHC", *JINST* **3** (2008) S08005. `doi:10.1088/1748-0221/3/08/S08005`.

[35] R. Aaij et al. (LHCb Collaboration), "Evidence for CP violation in time-integrated $D^0 \to h^- h^+$ decay rates", *Phys.Rev.Lett.* **108** 111602. `doi:10.1103/PhysRevLett.108.111602`.

[36] R. Aaij et al. (LHCb Collaboration), "Strong constraints on the rare decays $B_s \to \mu^+ \mu^-$ and $B^0 \to \mu^+ \mu^-$", *Phys.Rev.Lett.* **108** (2012) 231801, `arXiv:1203.4493`. `doi:10.1103/PhysRevLett.108.231801`.

[37] R. Aaij et al. (LHCb Collaboration), "First evidence for the decay $B_s^0 \to \mu^+ \mu^-$", *Phys.Rev.Lett.* **110** (2013) 021801, `arXiv:1211.2674`. `doi:10.1103/PhysRevLett.110.021801`.

[38] K. Aamodt et al. (ALICE Collaboration), "The ALICE experiment at the CERN LHC", *JINST* **3** (2008) S08002. `doi:10.1088/1748-0221/3/08/S08002`.

[39] K. Aamodt et al. (ALICE Collaboration), "Elliptic flow of charged particles in Pb-Pb collisions at 2.76 TeV", *Phys.Rev.Lett.* **105** (2010) 252302, `arXiv:1011.3914`. `doi:10.1103/PhysRevLett.105.252302`.

[40] G. Anelli et al. (TOTEM Collaboration), "The TOTEM experiment at the CERN Large Hadron Collider", *JINST* **3** (2008) S08007. `doi:10.1088/1748-0221/3/08/S08007`.

[41] T. Csörgő et al. (TOTEM Collaboration), "Elastic Scattering and Total Cross-Section in $p + p$ reactions measured by the LHC Experiment TOTEM at $\sqrt{s} = 7$ TeV", *Prog.Theor.Phys.Suppl.* **193** (2012) 180–183, `arXiv:1204.5689`. `doi:10.1143/PTPS.193.180`.

[42] TOTEM Collaboration, "A luminosity-independent measurement of the proton-proton total cross-section at $\sqrt{s} = 8$ TeV", *CERN-PH-EP* **2012-354** (2012). `http://cds.cern.ch/record/1495764`.

[43] O. Adriani et al. (LHCf Collaboration), "The LHCf detector at the CERN Large Hadron Collider", *JINST* **3** (2008) S08006. `doi:10.1088/1748-0221/3/08/S08006`.

[44] O. Adriani et al. (LHCf Collaboration), "Measurement of forward neutral pion transverse momentum spectra for $\sqrt{s} = 7$ TeV proton-proton collisions at LHC", *Phys.Rev.* **D86** (2012) 092001, `arXiv:1205.4578`. `doi:10.1103/PhysRevD.86.092001`.

[45] "SketchUp CMS".
https://twiki.cern.ch/twiki/bin/view/CMSPublic/SketchUpCMS. [Accessed March 2013].

[46] CMS Collaboration, "CMS Physics Technical Design Report, Volume I: Detector Performance and Software", *CERN/LHCC* **2006-001** (2006).
http://cds.cern.ch/record/922757.

[47] V. Karimäki, M. Mannelli, P. Siegrist et al., eds., "The CMS tracker system project: Technical Design Report", volume 5 of *Technical Design Report CMS*. CERN, Geneva, 1998. *CERN/LHCC* **98-6**. http://cds.cern.ch/record/368412.

[48] CMS Collaboration, "Addendum to the CMS Tracker TDR", volume 5 addendum 1 of *Technical Design Report CMS*. CERN, Geneva, 2000. *CERN/LHCC* **2000-016**.
http://cds.cern.ch/record/490194.

[49] CMS Collaboration, "Technical Proposal for the Upgrade of the CMS detector through 2020", *CERN/LHCC* **2011-006** (2011). http://cds.cern.ch/record/1355706.

[50] S. Chatrchyan et al. (CMS Collaboration), "The CMS experiment at the CERN LHC", *JINST* **3** (2008) S08004. doi:10.1088/1748-0221/3/08/S08004.

[51] CMS Collaboration, "Electromagnetic calorimeter commissioning and first results with 7 TeV data", *CMS Note* **2010-012** (2010). http://cds.cern.ch/record/1278160.

[52] S. Chatrchyan et al. (CMS Collaboration), "Performance of the CMS Hadron Calorimeter with Cosmic Ray Muons and LHC Beam Data", *JINST* **5** (2010) T03012, arXiv:0911.4991. doi:10.1088/1748-0221/5/03/T03012.

[53] S. Chatrchyan et al. (CMS Collaboration), "Commissioning of the CMS Experiment and the Cosmic Run at Four Tesla", *JINST* **5** (2010) T03001, arXiv:0911.4845. doi:10.1088/1748-0221/5/03/T03001.

[54] S. Chatrchyan et al. (CMS Collaboration), "The performance of the CMS muon detector in proton-proton collisions at $\sqrt{s} = 7$ TeV at the LHC", arXiv:1306.6905.

[55] CMS Collaboration, "CMS. The TriDAS project. Technical Design Report, Vol. 1: The trigger systems", volume 6.1 of *Technical Design Report CMS*. CERN, Geneva, 2000. *CERN/LHCC* **2000-038**. http://cds.cern.ch/record/706847.

[56] CMS Collaboration, "CMS: The TriDAS project. Technical Design Report, Vol. 2: Data acquisition and high-level trigger", volume 6 of *Technical Design Report CMS*. CERN, Geneva, 2002. *CERN/LHCC* **2002-026**. http://cds.cern.ch/record/578006.

[57] CMS Collaboration, "Data Parking and Data Scouting at the CMS Experiment", *CMS Performance Note* **CMS-DP-2012-022** (2012).
http://cds.cern.ch/record/1480607.

[58] G. Bauer, U. Behrens, M. Bowen et al., "Operational experience with the CMS data acquisition system", *J.Phys.Conf.Ser.* **396** (2012) 012007.
doi:10.1088/1742-6596/396/1/012007.

[59] L. Tuura, A. Meyer, I. Segoni et al., "CMS data quality monitoring: Systems and experiences", *J.Phys.Conf.Ser.* **219** (2010) 072020. `doi:10.1088/1742-6596/219/7/072020`.

[60] CMS Collaboration, "CMS Physics Technical Design Report, Volume II: Physics Performance", *J.Phys.G: Nucl.Part.Phys* **34** (2007) 995–1579. `doi:10.1088/0954-3899`.

[61] S. Chatrchyan et al. (CMS Collaboration), "Measurement of the Inclusive W and Z Production Cross Sections in pp Collisions at $\sqrt{s} = 7$ TeV", *JHEP* **1110** (2011) 132, `arXiv:1107.4789`. `doi:10.1007/JHEP10(2011)132`.

[62] S. Chatrchyan et al. (CMS Collaboration), "Measurement of $W\gamma$ and $Z\gamma$ production in pp collisions at $\sqrt{s} = 7$ TeV", *Phys.Lett.* **B701** (2011) 535–555, `arXiv:1105.2758`. `doi:10.1016/j.physletb.2011.06.034`.

[63] C. Collaboration, "Measurement of the WW, WZ and ZZ cross sections at CMS", *CMS Physics Analysis Summary* **EWK-11-010** (2011). `http://cds.cern.ch/record/1370067`.

[64] C. Collaboration, "Search for a Higgs boson produced in the decay channel $H \to ZZ^{(*)} \to 4l$", *CMS Physics Analysis Summary* **HIG-11-025** (2011). `http://cds.cern.ch/record/1406342`.

[65] C. Collaboration, "CMS Electroweak Public Physics Results". `https://twiki.cern.ch/twiki/bin/view/CMSPublic/PhysicsResultsEWK`. [Accessed February 2013].

[66] C. Collaboration, "Top pair cross section in e/μ + jets at 8 TeV", *CMS Physics Analysis Summary* **TOP-12-006** (2012). `http://cds.cern.ch/record/1461939`.

[67] C. Collaboration, "Measurement of the $t\bar{t}$ production cross section in the dilepton channel in pp collisions at $\sqrt{s} = 8$ TeV", *CMS Physics Analysis Summary* **TOP-12-007** (2012). `http://cds.cern.ch/record/1462235`.

[68] N. Kidonakis, "Differential and total cross sections for top pair and single top production", `arXiv:1205.3453`.

[69] M. Cacciari, M. Czakon, M. Mangano et al., "Top-pair production at hadron colliders with next-to-next-to-leading logarithmic soft-gluon resummation", *Phys.Lett.* **B710** (2012) 612–622, `arXiv:1111.5869`. `doi:10.1016/j.physletb.2012.03.013`.

[70] U. Langenfeld, S. Moch, and P. Uwer, "Measuring the running top-quark mass", *Phys.Rev.* **D80** (2009) 054009, `arXiv:0906.5273`. `doi:10.1103/PhysRevD.80.054009`.

[71] S. Chatrchyan et al. (CMS Collaboration), "Measurement of the $t\bar{t}$ production cross section and the top quark mass in the dilepton channel in pp collisions at $\sqrt{s} = 7$ TeV", *JHEP* **1107** (2011) 049, `arXiv:1105.5661`. `doi:10.1007/JHEP07(2011)049`.

[72] C. Collaboration, "Measurement of the top quark mass in the lepton+jets channel", *CMS Physics Analysis Summary* **TOP-10-009** (2010). `http://cds.cern.ch/record/1356578`.

[73] S. Chatrchyan et al. (CMS Collaboration), "Measurement of the top-quark mass in $t\bar{t}$ events with dilepton final states in pp collisions at $\sqrt{s} = 7$ TeV", *Eur.Phys.J.* **C72** (2012) 2202, `arXiv:1209.2393`. `doi:10.1140/epjc/s10052-012-2202-z`.

[74] S. Chatrchyan et al. (CMS Collaboration), "Measurement of the top-quark mass in $t\bar{t}$ events with lepton+jets final states in pp collisions at $\sqrt{s} = 7$ TeV", *JHEP* **1212** (2012) 105, `arXiv:1209.2319`. `doi:10.1007/JHEP12(2012)105`.

[75] C. Collaboration, "Measurement of the top-quark mass in all-jets final states", *CMS Physics Analysis Summary* **TOP-11-017** (2011). `http://cds.cern.ch/record/1477721`.

[76] CMS Collaboration, "CMS Top Physics Summary Plots". `https://twiki.cern.ch/twiki/bin/view/CMSPublic/PhysicsResultsTOPSummaryPlots`. [Accessed February 2013].

[77] S. Chatrchyan et al. (CMS Collaboration), "Search for heavy narrow dilepton resonances in pp collisions at $\sqrt{s} = 7$ TeV and $\sqrt{s} = 8$ TeV", `arXiv:1212.6175`.

[78] CMS Collaboration, "CMS Physics Results". `https://twiki.cern.ch/twiki/bin/view/CMSPublic/PhysicsResults`. [Accessed July 2013].

[79] CMS Collaboration, "Particle-Flow event reconstruction in CMS and performance of jets, taus and $E_{\mathrm{T}}^{\mathrm{miss}}$", *CMS Physics Analysis Summary* **PFT-09-001** (2009). `http://cds.cern.ch/record/1194487`.

[80] S. Chatrchyan et al. (CMS Collaboration), "Performance of CMS muon reconstruction in pp collision events at $\sqrt{s} = 7$ TeV", *JINST* **7** (2012) P10002, `arXiv:1206.4071`. `doi:10.1088/1748-0221/7/10/P10002`.

[81] W. Adam, R. Fruhwirth, A. Strandlie et al., "Reconstruction of electrons with the Gaussian-sum filter in the CMS tracker at the LHC", *J.Phys.G: Nucl.Part.Phys.* **31** (2005) N9–N20, `arXiv:physics/0306087`. `doi:10.1088/0954-3899/31/9/N01`.

[82] H. Bethe and W. Heitler, "On the Stopping of Fast Particles and on the Creation of Positive Electrons", *Proc.R.Soc. A* **146** (1934) 83–112. `doi:10.1098/rspa.1934.0140`.

[83] S. Baffioni, C. Charlot, F. Ferri et al., "Electron reconstruction in CMS", *Eur.Phys.J.* **C49** (2007) 1099–1116. `doi:10.1140/epjc/s10052-006-0175-5`.

[84] E. Meschi, T. Monteiro, C. Seez et al., "Electron Reconstruction in the CMS Electromagnetic Calorimeter", *CMS Note* **2001-034** (2001). `http://cds.cern.ch/record/687345`.

[85] G. P. Salam and G. Soyez, "A Practical Seedless Infrared-Safe Cone jet algorithm", *JHEP* **0705** (2007) 086, `arXiv:0704.0292`. `doi:10.1088/1126-6708/2007/05/086`.

[86] S. D. Ellis and D. E. Soper, "Successive combination jet algorithm for hadron collisions", *Phys.Rev.* **D48** (1993) 3160–3166, `arXiv:hep-ph/9305266`. `doi:10.1103/PhysRevD.48.3160`.

[87] M. Cacciari and G. P. Salam, "Dispelling the N^3 myth for the k_t jet-finder", *Phys.Lett.* **B641** (2006) 57–61, `arXiv:hep-ph/0512210`. `doi:10.1016/j.physletb.2006.08.037`.

[88] S. Catani, Y. L. Dokshitzer, M. Seymour et al., "Longitudinally invariant K_t clustering algorithms for hadron hadron collisions", *Nucl.Phys.* **B406** (1993) 187–224. `doi:10.1016/0550-3213(93)90166-M`.

[89] M. Cacciari, G. P. Salam, and G. Soyez, "The Anti-k_t jet clustering algorithm", *JHEP* **0804** (2008) 063, `arXiv:0802.1189`. `doi:10.1088/1126-6708/2008/04/063`.

[90] CMS Collaboration, "Jet Energy Corrections and Uncertainties. Detector Performance Plots for 2012", *CMS Performance Note* **CMS-DP-12-012** (2012). `http://cds.cern.ch/record/1460989`.

[91] CMS Collaboration, "Jet performance in pp collisions at $\sqrt{s} = 7$ TeV", *CMS Physics Analysis Summary* **JME-10-003** (2010). `http://cds.cern.ch/record/1279362`.

[92] CMS Collaboration, "Determination of the Jet Energy Scale in CMS with pp Collisions at $\sqrt{s} = 7$ TeV", *CMS Physics Analysis Summary* **JME-10-010** (2010). `http://cds.cern.ch/record/1308178`.

[93] S. Chatrchyan et al. (CMS Collaboration), "Determination of Jet Energy Calibration and Transverse Momentum Resolution in CMS", *JINST* **6** (2011) P11002, `arXiv:1107.4277`. `doi:10.1088/1748-0221/6/11/P11002`.

[94] S. Chatrchyan et al. (CMS Collaboration), "Identification of b-quark jets with the CMS experiment", *JINST* **8** (2013) P04013, `arXiv:1211.4462`. `doi:10.1088/1748-0221/8/04/P04013`.

[95] CMS Collaboration, "Commissioning of the Perticle-Flow reconstruction in minimum-bias and jet events from pp collisions at 7 TeV", *CMS Physics Analysis Summary* **PFT-10-02** (2010). `http://cds.cern.ch/record/1279341`.

[96] CMS Collaboration, "Tracking and Primary Vertex Results in First 7 TeV Collisions", *CMS Physics Analysis Summary* **TRK-10-005** (2010). `http://cds.cern.ch/record/1279383`.

[97] CMS Collaboration, "CMS Luminosity Public Results". `https://twiki.cern.ch/twiki/bin/view/CMSPublic/LumiPublicResults`. [Accessed February 2013].

[98] R. Fruhwirth, W. Waltenberger, and P. Vanlaer, "Adaptive vertex fitting", *J.Phys.* **G34** (2007) N343. `doi:10.1088/0954-3899/34/12/N01`.

[99] T. Speer, K. Prokofiev, R. Frühwirth et al., "Vertex fitting in the CMS tracker", *CMS Note* **2006-032** (2006). `http://cds.cern.ch/record/927395`.

[100] CMS Collaboration, "Electron reconstruction and identification at $\sqrt{s} = 7$ TeV", *CMS Physics Analysis Summary* **EGM-10-004** (2010). `http://cds.cern.ch/record/1299116`.

[101] G. Arnison et al. (UA1 Collaboration), "Experimental Observation of Lepton Pairs of Invariant Mass Around 95 GeV/c^2 at the CERN SPS Collider", *Phys.Lett.* **B126** (1983) 398–410. `doi:10.1016/0370-2693(83)90188-0`.

[102] P. Bagnaia et al. (UA2 Collaboration), "Evidence for $Z^0 \to e^+e^-$ at the CERN $\bar{p}p$ Collider", *Phys.Lett.* **B129** (1983) 130–140. `doi:10.1016/0370-2693(83)90744-X`.

[103] L. Pape, "Kinematics for searches at LHC, Reconstruction of particle masses (with calculation details)". `http://pape.web.cern.ch/pape/kinem.ps.gz`, 2005. [Accessed November 2012].

[104] G. Kopylov, "Like particle correlations as a tool to study the multiple production mechanism", *Phys.Lett.* **B50** (1974) 472–474. `doi:10.1016/0370-2693(74)90263-9`.

[105] G. Jancso, M. Albrow, S. Almehed et al., "Evidence for Dominant Vector Meson Production in Inelastic Proton Proton Collisions at 53-GeV Center-of-Mass Energy", *Nucl.Phys.* **B124** (1977) 1. `doi:10.1016/0550-3213(77)90271-1`.

[106] M. Albrow, B. Alper, J. Armitage et al., "A Search for Narrow Resonances in Proton Proton Collisions at 53-GeV Center-Of-Mass Energy", *Nucl.Phys.* **B114** (1976) 365. `doi:10.1016/0550-3213(76)90438-7`.

[107] P. Higgins, W. Shephard, N. Biswas et al., "ρ^0 production in $\pi^- p$ interactions at 100, 200, and 360 GeV/c", *Phys.Rev.* **D19** (1979) 65. `doi:10.1103/PhysRevD.19.65`.

[108] D. Drijard, H. Fischer, and T. Nakada, "Study of event mixing and its application to the extraction of resonance signals", *Nucl.Instrum.Meth.* **A225** (1984) 367. `doi:10.1016/0167-5087(84)90275-8`.

[109] B. Dutta, T. Kamon, N. Kolev et al., "Bi-Event Subtraction Technique at Hadron Colliders", *Phys.Lett.* **B703** (2011) 475–478, `arXiv:1104.2508`. `doi:10.1016/j.physletb.2011.08.029`.

[110] N. Ozturk (ATLAS Collaboration), "SUSY Parameters Determination with ATLAS", `arXiv:0710.4546`.

[111] U. Bitenc et al. (BELLE Collaboration), "Improved search for D0 - anti-D0 mixing using semileptonic decays at Belle", *Phys.Rev.* **D77** (2008) 112003, `arXiv:0802.2952`. `doi:10.1103/PhysRevD.77.112003`.

[112] R. Seidl et al. (Belle Collaboration), "Measurement of Azimuthal Asymmetries in Inclusive Production of Hadron Pairs in e+e- Annihilation at s**(1/2) = 10.58-GeV", *Phys.Rev.* **D78** (2008) 032011, `arXiv:0805.2975`. `doi:10.1103/PhysRevD.78.032011`.

[113] V. Khachatryan et al. (CMS Collaboration), "Observation of Long-Range Near-Side Angular Correlations in Proton-Proton Collisions at the LHC", *JHEP* **1009** (2010) 091, `arXiv:1009.4122`. `doi:10.1007/JHEP09(2010)091`.

[114] V. Khachatryan et al. (CMS Collaboration), "Measurement of $B\bar{B}$ Angular Correlations based on Secondary Vertex Reconstruction at $\sqrt{s} = 7$ TeV", *JHEP* **1103** (2011) 136, `arXiv:1102.3194`. `doi:10.1007/JHEP03(2011)136`.

[115] CMS Collaboration, "Measurement of differential top-quark pair production cross sections in the lepton+jets channel in pp collisions at $\sqrt{s} = 8\,\text{TeV}$", *CMS Physics Analysis Summary* **TOP-12-027** (2013). `http://cds.cern.ch/record/1523611`.

[116] CMS Collaboration, "Measurement of differential top-quark pair production cross sections in the dilepton channel in pp collisions at 8 TeV", *CMS Physics Analysis Summary* **TOP-12-028** (2013). `http://cds.cern.ch/record/1523664`.

[117] S. Chatrchyan et al. (CMS Collaboration), "Measurement of differential top-quark pair production cross sections in *pp* colisions at $\sqrt{s} = 7$ TeV", *Eur.Phys.J.* **C73** (2013) 2339, `arXiv:1211.2220`. `doi:10.1140/epjc/s10052-013-2339-4`.

[118] H.-L. Lai, M. Guzzi, J. Huston et al., "New parton distributions for collider physics", *Phys.Rev.* **D82** (2010) 074024, `arXiv:1007.2241`. `doi:10.1103/PhysRevD.82.074024`.

[119] A. Martin, W. Stirling, R. Thorne et al., "Parton distributions for the LHC", *Eur.Phys.J.* **C63** (2009) 189–285, `arXiv:0901.0002`. `doi:10.1140/epjc/s10052-009-1072-5`.

[120] R. D. Ball et al. (NNPDF Collaboration), "Unbiased global determination of parton distributions and their uncertainties at NNLO and at LO", *Nucl.Phys.* **B855** (2012) 153–221, `arXiv:1107.2652`. `doi:10.1016/j.nuclphysb.2011.09.024`.

[121] G. Watt, "Parton distribution function dependence of benchmark Standard Model total cross sections at the 7 TeV LHC", *JHEP* **1109** (2011) 069, `arXiv:1106.5788`. `doi:10.1007/JHEP09(2011)069`.

[122] R. D. Ball, S. Carrazza, L. Del Debbio et al., "Parton Distribution Benchmarking with LHC Data", *JHEP* **1304** (2013) 125, `arXiv:1211.5142`. `doi:10.1007/JHEP04(2013)125`.

[123] PDF4LHC Working Group, "Recommendation for LHC cross section calculations". `http://www.hep.ucl.ac.uk/pdf4lhc/`. [Accessed February 2013].

[124] G. Mahlon and S. J. Parke, "Spin correlation effects in top quark pair production at the LHC", *Phys. Rev. D* **81** (Apr, 2010) 074024. `doi:10.1103/PhysRevD.81.074024`.

[125] CMS Collaboration, "Measurement of spin correlation in $t\bar{t}$ events in the dilepton channels in pp collisions at $\sqrt{s} = 7\,\text{TeV}$", *CMS Physics Analysis Summary* **TOP-12-004** (2012). `http://cds.cern.ch/record/1461788`.

[126] ATLAS Collaboration, "Observation of Spin Correlation in $t\bar{t}$ Events from *pp* Collisions at $\sqrt{s} = 7$ TeV Using the ATLAS Detector", *Phys. Rev. Lett.* **108** (May, 2012) 212001. `doi:10.1103/PhysRevLett.108.212001`.

[127] ATLAS Collaboration, "Measurement of spin correlation in $t\bar{t}$ production from *pp* collisions at $\sqrt{s} = 7$ TeV using the ATLAS detector", *ATLAS Conference Note* **2011-117** (2011). `http://cds.cern.ch/record/1376409`.

[128] S. Voloshin, "Fluctuations in the mixed event technique", `arXiv:hep-ph/9407280`.

[129] S. Alioli, P. Nason, C. Oleari et al., "A general framework for implementing NLO calculations in shower Monte Carlo programs: the POWHEG BOX", *JHEP* **1006** (2010) 043, `arXiv:1002.2581`. `doi:10.1007/JHEP06(2010)043`.

[130] T. Sjostrand, S. Mrenna, and P. Z. Skands, "PYTHIA 6.4 Physics and Manual", *JHEP* **0605** (2006) 026, `arXiv:hep-ph/0603175`. `doi:10.1088/1126-6708/2006/05/026`.

[131] F. Maltoni and T. Stelzer, "MadEvent: Automatic event generation with MadGraph", *JHEP* **0302** (2003) 027, `arXiv:hep-ph/0208156`.

[132] J. Alwall, M. Herquet, F. Maltoni et al., "MadGraph 5 : Going Beyond", *JHEP* **1106** (2011) 128, `arXiv:1106.0522`. `doi:10.1007/JHEP06(2011)128`.

[133] S. Frixione and B. R. Webber, "Matching NLO QCD computations and parton shower simulations", *JHEP* **0206** (2002) 029, `arXiv:hep-ph/0204244`. `doi:10.1088/1126-6708/2002/06/029`.

[134] G. Corcella, I. Knowles, G. Marchesini et al., "HERWIG 6: An Event generator for hadron emission reactions with interfering gluons (including supersymmetric processes)", *JHEP* **0101** (2001) 010, `arXiv:hep-ph/0011363`. `doi:10.1088/1126-6708/2001/01/010`.

[135] CMS Collaboration, "Electromagnetic calorimeter calibration with 7 TeV data", *CMS Physics Analysis Summary* **EGM-10-003** (2010). `http://cds.cern.ch/record/1279350`.

[136] G. Bohm and G. Zech, "Introduction to Statistics ans Data Analysis for Physicists". Verlag Deutsches Elektronen-Synchrotron, 2010.

[137] K. S. Cranmer, "Kernel estimation in high-energy physics", *Comput.Phys.Commun.* **136** (2001) 198–207, `arXiv:hep-ex/0011057`. `doi:10.1016/S0010-4655(00)00243-5`.

[138] A. L. Read, "Presentation of search results: The CL(s) technique", *J.Phys.* **G28** (2002) 2693–2704. `doi:10.1088/0954-3899/28/10/313`.

Acknowledgments

Finally, I would like to express my gratitude to all the people who supported me during my studies.

First of all, I would like to thank Dr. Isabell Melzer-Pellmann for advising my thesis and giving me the opportunity to work in this exciting field of science. She supported me in every step giving me the freedom to pursue my own ideas and interests.

I thank Prof. Peter Schleper for the inspiring and motivating discussions and the valuable advises he provided to my work. His enthusiasm for particle physics aroused my interest for this field of research.

I also thank Jun.-Prof. Christian Sander for referring my disputation.

Furthermore, I wish to thank Dr. Dirk Krücker for supporting my analysis in the technical details as well as in the general direction. For many fruitful discussions I thank all former and current postdocs – Drs. Altan Çakır, Dean Horton, and Elías Ron – and PhD students – Dr. Matthias Stein, Niklas Pietsch, Jakob Salfeld, Francesco Costanza, Özgür Şahin, Artur Lobanov, and Karim Trippkewitz. I very much enjoyed the atmosphere in our office and in our working group.

When the first LHC collision data were recorded by the CMS experiment, I had the great opportunity to work in the "SUSY CAF Team" at CERN led by Dr. Henning Flächer. It was an exciting time and I learned a lot about SUSY analyses and even more about the CMS software and about programming. I'm grateful for that.

A great and sincere "Thank You!" goes to my family and my friends. My parents enabled me to follow my studies and to find my way. My friends always provided me a pleasant and refreshing change from the world of physics.

Michelle deserves my deepest gratitude.